INTERACTIVE AND ADSORPTIVE PROPERTY OF METAL NANOPARTICLES

Sikirat Kehinde Sheu

PhD

University of York

Chemistry

July, 2024

Abstract

The existence of heavy metals from water sources is a serious environmental concern around the globe which is caused by an increased in industrial activities and urbanization expansion leading to detrimental state of the environment, including the pollution of land and water. Noxious heavy metals are the existing toxic contaminant to the watercourses and landfills through improper waste management from industries, inadequate farming habits, and metallurgical engineering and processing. Most of the heavy metals like lead and nickel are highly toxic, cancerous and could pose grave danger to life of human beings and aquatic organisms. Hence, finding efficient approaches to monitor and remove heavy metals from the environment is of great importance and has received prominent attention of scientists. The existing practices available to remove noxious heavy metal contamination have a potential set back; however, adsorption is one of the most suitable techniques for the removal of heavy metals.

Over the last decade, nanomaterials are providing lasting solutions in many fields like environment, food sector, and agricultural practices. Nanotechnology is an emerging field which is gaining prominent attention and various nanomaterials have been developed for removal of heavy metals from polluted water bodies such as metal and metal oxides nanoparticles which is due to their intrinsic features such as high surface area, high adsorption potential and excellent optical properties.

In this report, metal nanoparticles based on silver and gold nanoparticles are synthesised using the greener routes and the traditional routes, and characterized by Fourier Transform Infrared spectroscopy, UV-Visible spectroscopy, thermal Analysis, elemental analysis, SEM and TEM and powder X-ray diffraction. The metal nanoparticles were applied towards interaction and adsorption of heavy metals from aqueous solutions. Comparative studies were carried out on the interaction results and adsorption results of each metal nanoparticles synthesized.

Contents

List of Figures

Tables

Abbreviation

FTIR	Fourier transform Infrared
TGA	thermogravimetry analysis
0D	zero-dimension
1D	one dimension
2D	two dimension
3D	three dimension
LSPR	localized surface plasmon resonance
CTAB	cetyltrimethylammonium bromide
CVD	chemical vapor deposition
NPs	nanoparticles
Cys	cysteine
UV	ultraviolet
I	transmitted intensity
I_O	intensity of the incident light
A	absorbance
T	Transmittance

IR	infrared
S/V	surface -volume
TEM	transmission electron microscopy
SEM	scanning electron microscopy
CCD	charge-coupled device
BSE	backscattered electrons
PXRD	powder X-ray diffraction
FTIR	Fourier transform infrared
SEM	scanning electron microscope
CHN	carbon, Hydrogen and nitrogen
TGA	thermogravimetric analysis
NMR	nuclear magnetic resonance
MW	microwave
AuNPs	gold nanoparticles
AuNRs	gold nanorods
NIR	near infrared region
CuNPs	copper nanoparticles
STP	standard temperature and pressure
SPAB	surface plasmon absorption band
Aq-cys-AgNPs	cysteine stabilized silver nanoparticles in aqueous solvents
ETOH-cys-AgNPs	cysteine stabilized silver nanoparticles in organic solvents
Cys-AuNPs	cysteine stabilized gold nanoparticles
PL	peeled cassava
FL	flesh cassava

Aq-PL	aqueous components of peel cassava
Aq-FL	aqueous flesh cassava
AA	ascorbic acids
Cit	citric acids
AA-AgNPs	ascorbic acids stabilized silver nanoparticles
Cit-AgNPs	citric acids stabilized silver nanoparticles
AA-Ag-casNPs	ascorbic acids silver-cassava-nanoparticles
Cit-Ag-casNPs	citric acids silver nanoparticles-cassava
AA-AuNPs	ascorbic acids stabilized gold nanoparticles
AA-Au-casNPs	ascorbic acids -Gold-cassava nanoparticles
GT	Green tea extracts
GT-AgNPs	green tea stabilized silver nanoparticles
GT-AuNPs	green tea stabilized gold nanoparticles
DA-CFE	dried aqueous fraction of cassava flesh extracts
DO-CFE	dried organic fraction of cassava flesh extracts
DA-CPE	dried aqueous fraction of cassava peel extracts
DO-CPE	dried organic fraction of cassava peel extracts

Declaration

Unless stated, all work presented in this thesis is the author's own. Any contribution from others is duly acknowledged at the appropriate points within the text. The results discussed here have not been presented elsewhere, except for aspects of the presentations at conferences. All sources are acknowledged as references.

Dedication

This Research report is dedicated to Almighty Allah for his help throughout the course of the project.

Acknowledgement

Firstly, I would like to thank Dr. Duncan James Macquarie for his unwavering guidance and support he provide for me on the course of supervising my PhD research. Dr. Duncan James Macquarie, encouraged, motivated and inspired me at all length for the successful completion of my study. He has been a positive driving force for me. I am grateful the enabling platform provided to me to attend scientific gatherings and training provided by the University of York.

My profound gratitude goes to Professor, Avtar Mataru for his morally and academic guidance he provides throughout the course of my research study and also giving me the enabling environment to study and thrive well in difficult time.

I appreciate the Chemistry department for the financial Assistance they provide for me and my family when the going was though. I appreciate Professor Helen Sneddon and Professor James Clark for providing enabling environments to carry out my PhD research in Green Chemistry Centre of Excellence. Chemistry department, University of York.

I also acknowledge Dr. Clare Steele-King and Dr. Karen Hodgkinson for the TEM and SEM training. My gratitude goes to all the technician team, Dr. Hannah Briers, Dr. Richard Gammons, Dr. Surujuana and Dr. Emma Dux for the technical assistance they rendered to me throughout my four-year research study.

I would like to thank Oliver Steven, Jutarat Kavinchan, Eksuree Saksornchai, Ewan Ward, Nicholas Garland, Natthamon Inthalaeng, Rashmi Deshpande and all Green Chemistry Students.

Lastly, to my Parents (Father; Sheu Salaudeen and Mother; Sarata Sheu), Husband (Ibrahim Elewu) and amazing daughter (Mubashirah Ibrahim-Elewu). I do appreciate your unmatching affections that heightened me to this level. I am grateful for all you do for me.

AIM OF THE THESIS

The aim of this thesis is to synthesise nanoparticles in a green manner, primarily those made from Ag and Au, fully characterise them, and assess their interaction with trace levels of dissolved metals. This is a first step to developing sensors which can be used to monitor easily and quickly levels of contamination of water, which is a recurring and frequent problem globally. Nigeria is faced with water pollution problems as there exist lacks of monitoring and waste implementations body, industrial waste, sewages and anthropogenic activities of man have been left to find their way to the river body which have a detrimental effect on the aquatic life and the food been grown in the area and thereby having drastic effects on the chain of any man that consume the foods.

The nanoparticles will be synthesised initially using existing lab procedures, which typically involve the use of a reductant such as sodium borohydride, along with a stabilising agent, often cysteine in the case of Ag and Au. Characterisation will involve a number of techniques to assess the particle size, optical properties, quantity of stabiliser present, and nature of the metallic centre. Having done this, the nanoparticles will be used to adsorb a range of dissolved metal ions, with different counterions, and the key kinetic and thermodynamic parameters of the adsorption measured. This will be carried out by UV-Visible spectroscopy; if there are specific features of the adsorption (e.g., the appearance of a new band, or a distinct shift in LSPR position, then this could be a feature that would directly allow sensing of a specific ion. If there is adsorption, but no specific features in the UV-Visible spectrum, then this does not rule out the potential for this adsorption to be measured by other techniques, such as electrochemical sensing, although this is outside the scope of this project).

Where positive results are achieved, we will look at greener alternatives to the synthetic routes, avoiding reagents such as borohydride, and focussing on bio-derived reductants / stabilisers such as green tea extracts, which are phenol and oligosaccharide-rich and may serve as suitable reductants. Similarly, cassava is a very common crop in Nigeria (and more widely in Africa) and as such utilising cassava waste (peels / damaged flesh) as a source or reductants / stabilisers is also investigated and the detectors and the adsorptive property will also be investigated.

1.0 Introduction

Nanoparticles are materials having one dimension in the range 1-100 nm in the minimum, and they tend to possess physicochemical properties that differ to the bulk material.[1] Nanomaterials can be traced to the Roman era by accidental colouration of glass by throwing coins into melts.[2] Due to the unique property of nanomaterials such as intrinsic particle size and high surface to volume area, they found profound applications in the fields of science, industry, biomedical science and medicines.[3-5] Nanomaterials are generally categorized based on the dimensions of the material, in zero-dimensional nanomaterials all the dimensions are measured within the nanoregion, nanoparticles is popular example.

In one-dimensional nanomaterials, one of the dimensions is at the external region in the nanoregion, popular examples are the nanorods. Common examples of 2D nanomaterials are nanolayers and nanofilms as this involved the two of its dimensions are outside the nanoregion.

Three-dimensional nanomaterials (3D): these are classes of nanomaterials that cannot be compressed to the nanoregion in any dimension. Common examples include the nanotubes and multi-nanolayers.[6]

1.1 Localized Surface plasmon resonance

One of the fascinating properties of nanomaterials is the existence of localized surface plasmon resonance (LSPR) in the near-infrared and visible region of the absorption spectrum which makes them excellent candidates for bioimaging and sensors.[7]

The existence of LSPR in noble metal or transition metal nanoparticles is an extensive feature that occurs as a result of the availability of free d electrons in the transition metals, that are readily available to transition through the metallic lattices of the materials. The dimension in noble metallics nanoparticles such as silver is 50 nm on average. Thus, for a nanoparticle with a dimension less than 50 nm, no scattering is expected from the bulk and as a result the interaction of light is only with the surface of the material. A standing resonance is usually obtained if the nanoparticles are less than the incident light. The incident photons are usually in resonance with the oscillation of nanoparticle surfaces - a result which enforces the available d electron to oscillate with the frequency of the light thereby giving rise to the standing oscillation.[7] This phenomenon causes the nanoparticles to have distinctive colours; this unique feature is responsible for the optical properties of the metal nanoparticles. The sizes and shapes of metal nanoparticles strongly affect the positions of the LSPR in the visible region or near

infrared region, information relating to the particles size range of metal nanoparticles can be obtained by observing the shape of the localized surface plasmon resonance[8,9]

Metal nanoparticles synthesised using different traditional routes are often associated with different LSPR owing to the different choice of reducing agents, stabilizing agents and different synthetic routes. A change in the LSPR of metal nanoparticles is an important parameter used in monitoring the response of the interaction of the heavy metal with the synthesized metal nanoparticles. A summary of different localised surface plasmonic resonance for each metal nanoparticles using different synthetic routes are highlighted in Table.1 which shows ranges of LSPR values for each metal NPs.

Metal nanoparticles	**LSPR**	**Reference**
Silver nanosphere	400-480nm	10
Silver Nano prism	600-700nm	10,11
Silver array	500-600nm	12
Silver nano cubes	430nm	13
Gold Nano star	647-700,783nm	14
gold nanorods	700,653-846nm	15,16
Gold nanoring	1058-1545nm	17
Gold nanosphere	520nm	18,19
Gold Nano shell hollow	680nm	18
Gold nano cubes	538nm	16
Copper nanoarrays	540-680nm	20
Copper nanosphere	570nm	21,22
Copper nano cube	580nm	14
copper nanosphere	337nm,340nm	23,24
Nickel nanosphere	384nm,365nm	25-29
Nickel nanosphere	515nm	30
MoS_2 Nanosheets	>340nm	31
MoS_2 nanoparticles	538nm,811nm	32

Table.1: LSPR values of some selected metal nanoparticles

1.2 Applications of Nanomaterials

1.2.1 Nanomaterials as biosensors

Nanomaterials can be used to detect biological analytes as they sense and provide quantitative information regarding the biomolecules. Biosensor generally contains a sensing object, transducer and a catalyst.[33] A biosensor has the ability to rapidly responds and simultaneously sense the biomolecules. The biosensor found potential applications in the area detection of soil and water borne pathogens, food microorganisms, or drug metabolites and heavy metals, the major challenges faced with biosensors is the low detection limit coupled with selectivity and sensitivity generally lows. The major setbacks of biosensors include detection of another analyte alongside with the analytes of interest especially when the analytes are present at low concentration or in a complex matrix. Biosensors designed using metal nanoparticles proffer a rapid response and selectivity.[33]

1.2.2 Nanomaterials in environmental remediation

The world is in dire need of a pollution free environment as it is crucial for the quality of life, pollution from various class such as urbanization and extensive anthropogenic activities of man are the major cause of our environmental deterioration.[34]In petrochemical industries, agricultural and other industries which involve the high usage of chemicals and fertilizers in the course of generation of products,[35-37] some of the pollutants released are noxious and toxic in nature and environmental. Many physiochemical approaches are devised to get rid of these noxious environmental pollutants, such as air stripping, adsorption and membrane filtration. Many of these methods are expensive, long time for pollutants degradation, and may release of secondary by-products to the immediate environment, which brings additional environmental problems.[38-40] Recently, the photocatalytic technique has been used in the degradation of many non-degradable organic pollutants. Photocatalysis accelerates the photoreaction rate in the presence of a catalyst.[34] Using photocatalysis, the harmful organic compounds disintegrate to H_2O and CO_2, reduces toxic metal ions to nontoxic states, kills the microorganisms, and degrades air pollutants like NO_2.[36]

1.2.3 Adsorption

The major application of NPs covered in this thesis relates to the adsorption of trace metal ions from solution, as a first step towards developing a sensor to detect the ions rapidly and cheaply.

An understanding of the adsorption process is therefore needed, and this section discusses the various models that can be used to develop that understanding.

Adsorption process involve the retainment of atoms, ions or molecules from a gas, liquid or dissolved solid to a surface of a solid material rather in the bulk of the material.[41] This process thus creates a film of the adsorbate on the surface of the adsorbent. This process differs from absorption, in which the adsorbate is dissolved by or permeates the adsorbent.[42]Adsorption is a surface phenomenon and the adsorbate does not penetrate through the surface and into the bulk of the adsorbent, while absorption involves transfer of the adsorbate into the volume of the material, although adsorption does often precede absorption.[43]The term sorption encompasses both adsorption and absorption, and desorption is the reverse of adsorption.

In a bulk material, all the bonding condition such as ionic or covalent bonding of the constituent's atoms of the material are fulfilled by the other atoms present in the material. However, surface atoms on the adsorbents are surrounded by other adsorbent atoms and thus can attracts among the adsorbates, the true nature of the bonding depends on the details of the ions involved. Adsorption are characterized by physisorption or chemisorption and can also occur due to electrostatic force of attraction .[44-45] The adsorption type affects the structure of the adsorbates.[46]

Adsorption is widely used in industrial applications such as heterogeneous catalysts,[47,48], synthetic resins and water purification.

1.2.3.1 Adsorption isotherm Models

The adsorption of solutes and gases are described through adsorption isotherms, i.e., the amounts of adsorbed ions or atoms on the adsorbents as a function of its pressure for gas molecules or concentration for liquid phases sorbates at constant temperature. To date up to 15 different adsorption isotherm models have been devised.[46]

1.2.3.2 Freundlich isotherm model

In 1906, Freundlich and Kluster was the first to published a mathematical fit to an isotherm a purely empirical formular for a gases adsorbates:

$x/m=kP^{1/n}$

where x is the adsorbate mass, m is the adsorbent mass, p is the pressure of adsorbed ion (this can be changed to concentration if investigating solution rather than gas), and k and n are empirical constants for each adsorbent–adsorbate pair at a certain temperature.

1.2.3.3 Langmuir isotherm model

Irving Langmuir derived a scientifically based adsorption isotherm in 1918 as the first to design a mathematical model.[49]The model is applicable adsorption of gas molecules to a solid surface to gases adsorbed on solid surfaces. It is It is based on four assumptions:

1. All of the adsorption sites are uniform, and only one molecule can be accommodated at each site.
2. The adsorbent surface is homogeneous, and adsorbates do not interact.
3. Phase transitions do not occur.
4. Adsorption occurs on localized sites on the adsorbent surface and not with other adsorbed molecules. At the adsorption maximum, only a monolayer is formed.

Langmuir assumes that adsorption occur via this mechanism: A+S(g), -AS where A is a gas molecule, and S is an adsorption site. The direct and inverse rate constants

K=k/k-1=0/(1-A) P

are k and k−1. If we define surface coverage, 0, as the fraction of the adsorption sites occupied, where P is the partial pressure of the gas/ the molar concentration of the solution. For very low pressures. A=KP, and for high pressures. A=1.

1.2.3.4 Temkin isotherm model

The Temkin adsorption model assumes that the heat of adsorption decreases linearly with an additional increase in the surface coverage due to adsorbate–adsorbent interaction.[50]This is likely to be a more realistic assumption that that in the Langmuir isotherm. Temkin adsorption isotherm is valid only for a fairly low to medium range of concentrations.[51] adsorption model in a non-linear form is expressed below:[52]

$Qe=RT/b\ (\ln A_T C_e)$

Its linearized form can be obtained as

$Qe=RT/b\ LnA_T+(RT/b)\ \ln C_e$

$B = RT/b.$

$Qe=RTBlnA_T+ RTBlnC_e$

where A_T (L /g) is the Temkin isotherm equilibrium binding constant, *b* (J/ mol) is the Temkin isotherm constant, *R* is the universal gas constant, *T* is the temperature, and *B* is the constant related to the heat of adsorption. The Temkin parameters can be obtained by a plot of adsorption capacity at equilibrium (q_e) *versus* ln C_e, and the Temkin parameters (b) and (A_T) are obtained AS the slope (b) and intercept (A_T) from the plot.[51,53]

1.2.3.5 The Dubinin–Radushkevich isotherm model

The Dubinin–Radushkevich isotherm model expresses that the process of adsorption is related to the volumes of pores in the adsorbents. In the DR model, the pores structures in adsorbent are considered and it is appreciable for heterogeneous surfaces.[54,55] The DR isotherm model is popularly used to describe physical or chemical adsorption processes.[56] The corresponding equation is:

$Qe=qm\ DR\text{Ɛ}^{-K_{DR}\varepsilon^2}$

$\text{Ɛ}DR=RT(1+1/C_E)$

where qm, DR is the maximum adsorption capacity of the DR isotherm model, KDR is constant of the DR isotherm model (mol^2/kJ^2), εDR is Polanyi potential DR isotherm model ($kJmol^{-1}$).

1.2.3.6 Henry adsorption model

Henry adsorption isotherm model is the most basic adsorption isotherm for liquid and gaseous systems, respectively.[57]The Henry adsorption constant is the constant appearing in the linear adsorption isotherm, which formally resembles Henry's law; as a result, named Henry

adsorption isotherm. It described as the simplest form of adsorption isotherm in that the amount of the adsorbate present at the surface of the adsorbent is proportional to the partial pressure of the adsorptive gas or concentration for a solution.[57]

$QE=K_{HN}C_E$

$QE=K_{HN}P$

where K_{HN} is defined as the Henry adsorption constant

1.2.4 Adsorption kinetics

In addition to the equilibrium data obtained from isotherms, the rate of adsorption/ equilibration is also an important factor. Kinetics of adsorption are typically presented by constructing plots of the adsorbed quantity as a function of time. The nature of the adsorption process is usually indicated by the shapes of the plot. Adsorption kinetics have been analysed by pseudo-first order and pseudo-second order models.

1.2.4.1 Pseudo first -order kinetics

The pseudo-first order equation shown by eqn (2) was proposed in 1898 by Lagergren[58]and is still widely applied for characterizing adsorption processes:[59]

$(Logqe-qt) =logqe^{-(K1/2.303)\ t}$

In the above equation qt (mg /g) and qe (mg /g) represent the adsorbed species concentration at time t (min) and equilibrium, respectively. k1 (mg /g/min) represent the pseudo-first order reaction constant. Ho and McKay have discussed two important aspects of this equation: the adsorption kinetic parameter does not give information on the number of adsorption sites. The log(qe) term does not equate the log value of the adsorbed material equilbrum concentration (ce).[60] The pseudo-first order model has been discussed extensively by Azizian in his work on activated adsorption/desorption[61] as well as by Rudzinski and Plazinski in their work on statistical rate theory derivation[62] to reconcile the physical meaning corresponding to adsorption kinetics and the various parameters in the equation. Rudzinski and Plazinski have discussed that the pseudo-first order model can be derived for both intraparticle diffusion-controlled processes and surface reaction-controlled processes but, the physical meaning of the rate constants is not the same in the two process types.[62] Azizian's report states that the pseudo-first order model only holds in scenarios where the change in the bulk solution concentration of the adsorbate is negligible.

1.2.4.2 Pseudo-second order kinetic model

The pseudo-second order model has been applied on several metals adsorption data for Metal-based adsorbents.[63-68] eqn as proposed by Blanchard et al.[69] shows the rate equation for the pseudo-second order.

$Dqt/dt=K_2(qe-qt)$

$1/qt=1/qe+1/qe^2$

Here K_2 (g/mg/ min) - the pseudo-second order apparent rate constant.

The use of the pseudo-second order equation have been used extensively in the context of polymer, and heavy metal removal from polluted water system.[70,71-74]The adsorption kinetic by pseudo second-order fitting suggest surface-reaction limited adsorption process.[63-66]

1.2.5 Adsorption thermodynamics

Adsorption thermodynamics is an important parameter in the adsorption study and essentials in adsorption mechanisms. According to the laws of thermodynamics, the standard change in Gibbs free energy (ΔG°) is directly calculated from Eq. 1.

$\Delta G° = -RTLnK°eq$……. eq.1

After rearranging, Eq. 1 becomes:

$K°eq = \in -\Delta G°/RT$……eq.2

$\Delta G° = H - T\Delta S$……..... eq.3

Assuming ΔH° and ΔS° is independent of temperature, the relationship between the ΔG° parameter and the others (ΔH° and ΔS°) is expressed as follows:

$K°eq = \in -\frac{\left(\Delta H°\overline{R}\right)1}{T} + \Delta S°/R$……eq.4

After Eq. 2 had been substituted into Eq. 1 the non-linear form of the van't Hoff equation was obtained as Eq. 3 [52,53]. In this case, the standard changes in enthalpy (ΔH°) and in entropy (ΔS°)

were directly calculated from Eq. 2. Similarly, (Eq. 3) was obtained by substituting Eq. 1 into Eqn 3. From this linear form, ΔH° and ΔS° were obtained from the slope and intercept of the plot of lnK against 1/T (Eq. 4), respectively.

$$lnK°eq = \ K°eq = \in -\frac{\left(\Delta H° \frac{}{R}\right)1}{T} + \Delta S°/R$$

where R is the universal gas constant; T is the absolute temperature in kelvin (K); and $K°eq$ is the standard thermodynamic equilibrium constant of adsorption which is dimensionless.

The thermodynamic equilibrium constant is defined in Eq. 23 [75,77], and its derivation was reported in the literature.[78]

$$K°eq = \frac{Kmodel * C° \ adsorbate}{\gamma(adsorbate)}$$

where K Model (L/mol) represents for the equilibrium constant of the adsorption isotherm model; C° $adsorbate$ (mol/L) is the adsorbate standard concentration; and $\gamma \ adsorbate$ is the adsorbate activity coefficient which is dimensionless.

1.3 Synthesis of nanomaterials

There are two generic approaches to synthesis of nanomaterials; namely the "top-down" and "bottom-up" approach.[79] In bottom-up synthetic approach, the atoms, molecules or other sub-nanometre species assemble together to generate the nanoparticle. In contrast, the top-down approach involves the dissociation of bulk solids with large particle size into nanoscale pieces provides the route to nanoparticle formation. The two different synthetic routes play a significant role for different applications. This variety is very important for different application fields, for example, in engineering, science, and medicine. Latter approaches play key role in current industrial nanotechnology. In each of these generic approaches, nanomaterials can be synthesized using different synthetic route: mechanical, co-precipitation chemical, hydrothermal and pyrolysis etc.

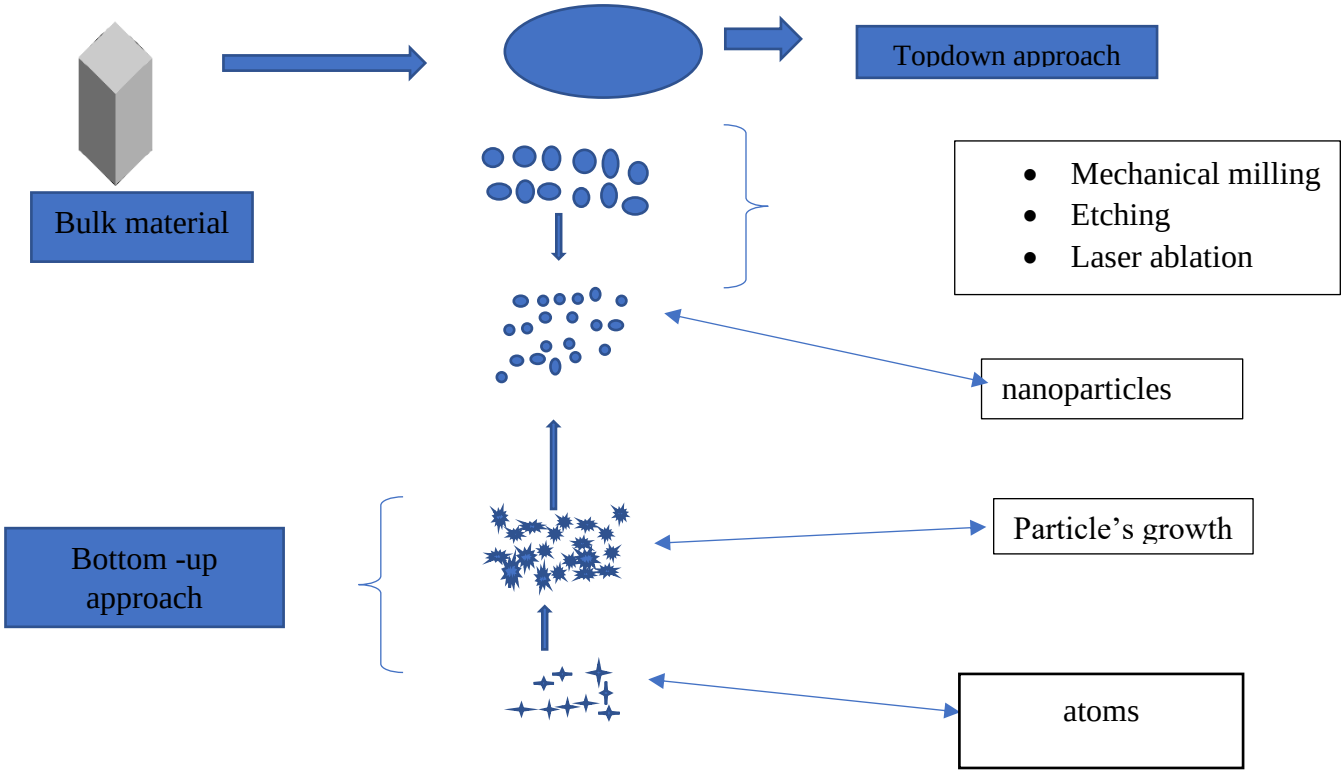

Figure 1.0: synthetic pathways of metal nanoparticles

1.3.1 Top-down synthetic route

The top-down approach involves the production of the nanoparticles starting with larger molecules/crystals/materials and crack/rupture these down to different molecules in the Nano region to obtain the material in nanoregion. To obtain nanoregion form of molecules in this method, first, a bulk material that is 2 to 3 times bulkier in one or two dimensions than the nanoregion demanded is synthesized and then nanopatterning methods are involved in order to obtain a smaller bite. Top-down synthetic approach was introduced firstly by and have been used in semiconductor industry. Several options are available.

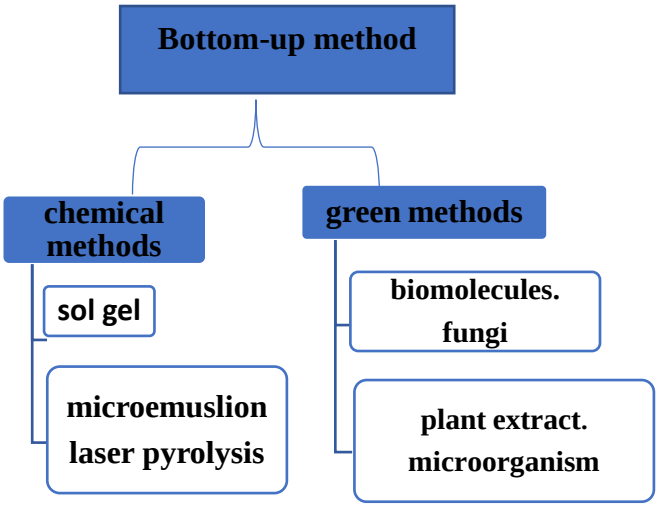

Figure 1.1. – Schematic of bottom-up synthetic routes

This type of synthesis approach involves the construction of nanomaterials from smaller units such as atoms, clusters or molecules, and building them up to make the nanomaterial. The process of bottom-up include gas-state and liquid-state approach. For two synthetic methods, the synthesis of nanoparticles growth can be controlled starting from the individual atom or group of atoms. Self-assembling of atom is a crucial method that need to be considered when optimising the growth of bottom-up assembly of the materials in the nanoregion into other form of nanomaterials such as tubes and nanoelectronics [80]

1.4 Characterization of Metal Nanoparticles

In order to establish the structure of metal nanoparticles, they are analysed using several physiochemical techniques which will be discussed in detail:

1.4.1 UV-Visible spectroscopy

The UV-Vis spectrophotometer is widely employed to confirm the formation of nanomaterial in a colloidal solution using the localized surface plasmon resonance phenomenon of metal nanoparticles, Nanomaterial is associated with the existence of LSPR in the visible region of the UV/Visible spectroscopy and this makes UV/Visible spectroscopy as a suitable characterization technique for investigating the existence of LSPR and monitors the changes in the LSPR resonance band. These optical features of the material depend on the size, shape,

concentration, and agglomeration state of the nanoparticles, thus UV-Visible spectroscopy can be used to provide information on these parameters.

UV-Visible spectroscopy deals with electronic transitions of an electron, once a molecule or ion absorbs UV light the electrons are excited from the ground state to an excited state. The operation of this analytical tool is straight forward as it involve a prism or difrating grating are used to separates a beam of UV or Visible light source into its component wavelength, each individual wavelength beam is further splitted into two equal beams of intensity by a half-mirrored device.

One beam, the sample beam, passes through a small transparent container usually cuvette containing a solution of the compound to be analysed in a clear solvent. The other beam, the reference, passes through a similar cuvette usually containing only the solvent used in the preparation of the compound to be analysed. Electronic detectors are used in the measurement of the intensities of the two light beams and compared I_0 is usually sued for the representation of the intensity of the reference beam, The intensity of the sample beam is defined as I. Over a short period of time, the spectrometer automatically scans all the component wavelengths in the manner described. The region of 200-400 nm is usually used to described the ultraviolet region and a region of 400-800nm are used to describe the visible region. when the intensity of the sample equals the intensity of the reference sample I.e., $I = 1_0$ it shows there is no absorbtion of light by the sample in a given wavelength and when the intensity of sample less than the intensity of reference i.e. $I > 1_0$ it indicates the absorbtion of light by the sample, the difference in these results can be on a graph of absorbance versus wavelength. Light absorbance is usually presented as Transmittance ($T = I/I_0$) or absorbance ($A = \log Io/I$). and $T = 1.0$, $A=0$ in the absence of absorption.

1.4.2 Fourier transform infrared spectroscopy

Infrared Spectroscopy is techniques that deals with the analysis of interaction of infrared light with a sample molecule, this interaction is usually interpreted in three ways by measuring, emission, reflection and absorption. These techniques found optimal usage in inorganic and organic field of chemistry and are been used by scientist to investigate the existence of functional group present and the type of functional group present in a sample compound. IR

Spectroscopy measures the vibrations of groups of atoms, and based on this it is possible to determine the functional groups. Generally, stronger bonds and light atoms will vibrate at a high stretching frequency (wavenumber). The condition necessary for a molecule to absorbed infrared light include the change in dipole moment of the molecule during the vibration must be non-zero and also the energy of light impinging on the molecule must equal the difference in vibrational energy levels in the molecule. Molecules that satisfy these conditions are said to be infrared active[81]

Infrared light is guided through the sample, the distribution of IR light that passes through the interferometer are usually alter by a moving mirror inside the instruments apparatus. ``interferogram (the signal directly recorded) is a representation of the light outputs as a function of the mirror position with the absorption plotted as a function of time .A data processor called Fourier transform turn this raw data into the desired result, which is absorbance versus frequency: the dispersive method is another methods used in the taking of spectra ,here single wavelength passes through the sample at a time .These methods is more pronounced in the UV-Visible spectroscopy and less pronounced in the infrared than the Fourier Transform infrared spectroscopy. The much more rapid Fourier transform method allows for multiple scans to be added together before processing. This improves the signal to noise ratio and gives better spectra. This could be done with the dispersive method but it takes far longer.[82]

1.4.3 Powder x-ray powder diffraction

Powder diffraction is a technique that employs electron, neutron and x-ray on sample (usually powder) in order to establish a structure for the sample compound. Diffractogram are used for the representation of PXRD data and are obtained; the intensity diffracted is shown either as a function of the scattering vector or scattering angle A.[83]Electromagnetic radiation associated with a specific frequency and wavelength are usually release by the diffractometer and are generally determined by the source of the x-ray. Common sources include electrons and neutrons. When a sample is exposed to x-ray and the electromagnetic waves reach the sample, it either the beam is been reflected off the surface or can enter lattice and be diffracted by the group of atoms present in the sample

When the electromagnetic waves reach the sample, the incoming beam is either reflected off the surface, or can enter the lattice and be diffracted by the clusters of atoms in the sample.

If the groups of atoms are arranged symmetrically with a separation distance d (as in a crystal lattice), constructive interference will only occur when the difference in path-length 2dsinθ is equal to an integer multiple of the wavelength, leading to a diffraction maximum in accordance with Bragg's law. Destructive interference occurs at points between the intersections where the waves are out of phase, and lead to rough spots in the diffraction pattern.[84]

1.4.4 Transmission electron microscopy (TEM)

Transmission electron microscopy (TEM) is analytical techniques that involves the passage of electron beams through an ultra-thin specimen as, it passes it interacts with the particles present in the specimen the image is produced as a result of the interaction between the electron and the atom of the specimen. A sensor such as charge-couple device(CCD) camera or the beam can be focused on fluorescent screen to provide an image .[85]one of the optimum condition required to obtain a better image is the specimen needs to be very thin generally lower than 100nm in thickness .The best sample for transmission electron microscopy for nanoparticle size analysis is one with a higher quantity of single particles in nanoregion within the desired transmission electron microscope micrograph field of view, without huge number of agglomeration or nanoparticles crowding. Transmission electron microscopy performance features are usually affected by the physio-chemical attribute of the nanomaterial such as structure and texture. Transmission electron microscopic often produces 2D images of nanomaterials from these images number-based size distributions can be produced or generated, but nanoparticles have all three external dimensions on the nanoregion.[62] Typically, the estimated sizes are expressed as a sphere diameter that the particle has the same projected area as the projected image. In order to get a clearer image, the sample preparation is usually elaborated and is slow with few particles being analysed.[86]

1.4.5 Scanning electron microscope

A scanning electron microscope (SEM) is a technique that generate image of a sample by passing a focused beam of electrons to scan the surface of the sample as it scanning the sample there exist an interaction with the electron and the sample atoms and thus generating signals with information regarding the morphology of the surface and sample composition. The electron beam is scanned in a raster scan pattern, and the intensity of the signal detected and beam position is combined to generate an image. In contrast to TEM, SEM quantify sample by measuring the scattered radiation from the sample surface, rather than that which is transmitted through the sample.

The types of signals produced by SEM are derived from secondary electrons, back scattered electrons, characteristics X-rays light such as cathode luminescence, specimen current and transmitted electrons. These types of signals required specialized detectors. Secondary electron detectors are common in all scanning electron microscope but no single machine would have detectors for all possible signals. The signals result from interaction of the electron beam with atoms at or near the surface of the sample.[87]

Scanning electron microscope functions on voltages between 2-50 kV and its beam diameter that scans the specimen sample is in the range of 5 nm-10μm. Secondary and back scattered electrons are classified according to their energies. When the energy of the transmitted electrons is less than about 50 eV, it is referred to a secondary electron and backscattered electrons (BSE) are often used in analytical scanning electron microscopy along with the spectra made from the characteristics X-rays. BSE images provide information about the distribution of elements.

1.4.6 Thermal analysis

Thermal analysis provides information regarding the physiochemical features of a sample compound and are typically measured as a function of elevating temperature (with constant heating rate), or as a function of time. Likewise. TGA is commonly used to investigate selected properties of materials that exhibit either mass loss or gain due to decomposition, oxidation, or loss of volatiles.[88] In the process of the thermogravimetric analysis, the mass of the sample is examined as a function of the heating suffered, and the result shows a decomposition curve whose analysis gives the loss of volatiles upon thermal decomposition (in an inert atmosphere) or the oxidation temperature (in air) and the residual mass of the sample. For nanomaterials, the volatiles are generally the organic stabilisers on the surface, and the residual mass could be (largely) due to inorganic residues (for example gold nanoparticles are not volatile over the temperature range typically used in TGA – up to 900 ^{o}C), residual involatile components from the synthesis of the material (e.g.B species if borohydride has been used), carbonaceous residues form the organic components, or contaminant inside the sample. Thus, mass loss can be used to estimate the quantities of stabilising organic groups on the surface, or adsorbed contaminants. Thermal analysis under air can be used to measure the thermal resistance to oxidation .[89]The most significant drawbacks of Thermal Gravimetric Analysis are that it is a destructive technique whose sample cannot be retrieved back after the analysis, and it can be excessively costly.

1.5 Literature review on various synthetics routes of metal nanoparticles

1.5.1 Silver nanoparticles (AgNPs)

Silver nitrate $AgNO_3$ has been employed as precursor salt of Ag, which can be reduced to silver nanoparticles using different reducing agents such as sodium citrate, sodium borohydride, hydrazine and a range of alcohol[90-100] $NaBH_4$, which is a one of the stronger reducing agents, results in NPs of smaller size. Suitable stabilizing or capping agents include surfactants, ligands, or polymeric surfactants such as polyvinylpyrrolidone (PVP), sodium oleate and collagen are added to control the growth of the NPs and to form the desired shapes.[101,102]

The citrate nanoparticles reduction approach has been the widely used methods used in the fabrication of silver nanoparticles, the methods reduced the silver nitrate to zerovalent silver, in this approach the citrate ion plays a dual function of reduction and stabilizing the zerovalent silver[103,104.] Furthermore, these methods of silver nanoparticles result in the production of silver nanoparticles of various diverse shapes and sizes. Since then, a broad range of fabricating approaches that make use of hydrogen and greener chemicals as reducing agents have been reported for the synthesis of AgNPs.[105,106]

Puntes and co-workers devised an effectives and kinetically controlled seeded fabricating approach that involves the cleavage of two reductant, such as sodium citrate and tannic acid, to produce monodisperse AgNPs in the size range from 10 to 200 nm.[107]this synthetic steps has also lead to production of stable AgNPs with narrow size distribution ,which allows for further functionalization with other groups and thus making them a better fits in the field of biomedicine[108,109] Another synthetic approach devised by Creighton et al., has been frequently used for the fabrication of nano-silver using $NaBH_4$ as a reductant.[110] The elucidation of the mechanistic route for the synthesis of AgNPs by $NaBH_4$ is accredited to Van Hyning and Zukoski.[111]$NaBH_4$ as the reducing agent resulted into AgNPs with narrow size distribution. In this context, Emmerling and co-workers successfully demonstrated a wet chemical synthetic method for a size-controlled synthesis of AgNPs, in this approach ,silver perchlorate ($AgClO_4$) was reduced by $NaBH_4$ with various kinetically controlled reaction parameters that eventually affected the growth mechanism of the AgNPs.[112]This profound mechanistic understanding enabled the authors to produce, for the first time, well directed and size-controlled AgNPs with the radius ranging from 4 to 8 nm, this being carried out without the involvement of any stabilizers.

1.5.2 Gold NPs

Like other systems, AuNPs demonstrate a greater flexibility permitting appropriate size selections, structure and assembly. This unique feature of AuNPs allows for the fine-tuning of NPs properties which leads toa wide range of applications. Synthetic methods used for AuNPs production have been devised and employed since antiquity to make coloured glasses. In 1908, the different colour of gold colloids is explained by Mie by correlating the optical absorption of spherical objects with their dimensions. [113] Therefore, the frequency of plasmon resonance can be utilized to estimate NPs' dimensions. The major setbacks of particles size estimation of AuNPs were overcome with the advents of electron microscopes, which directly visualized the fabricated NPs, this allows for the checking of results of different synthetic methods and conditions.

The electron microscope was widely employed by Turkevich et al. to estimate the AuNPs produced by reducing tetra chloroauric acid using different reductant.[91]To gain a better particle size control, Frens et al. revised the Turkevich method by selecting the optimal citrate/gold concentrations.[114] However, the dispersibility and stability of gold colloid NPs were still challenging, preventing extensive scale-up of the production process. In 1994 Brust *et al.* proposed a new fabricating approach based on using alkanethiols as stabilizers.[115] This approach is scalable and led to a narrow distribution of AuNP sizes peaking at ∼3 nm. Next, other strategies were proposed to improve the Au colloid monodispersity, such as digestive ripening. Small monodisperse AuNPs are produced at the expense of sizeable polydispersed gold colloids.[116]

A wide range of other shapes of AuNPs can be obtained besides the common spherical shapes using the gold metal salts.[117]The first example of the synthesis of anisotropic AuNPs dates back to 1989 when Wiesner and Wokaun produced rod-shaped AuNPs by adding Au seeds to solutions of gold(III) chloride ($HAuCl_4$).[118] In 2001, the Murphy group described the synthesis of gold nanorods (AuNRs) by the addition of citrate-capped AuNPs to Au(I) obtained from the reduction of Au(III) using ascorbic acid in the presence of cetyltrimethylammonium bromide (CTAB).[119] Besides seed-mediated methods used to synthesize specific shapes with high yields, bulk solution methods are also possible, although low yields are obtained for specific shapes.[120]Popularly known methods such as electrochemical and sonochemical methods using templates, and other.[117] Nevertheless, the optical properties are essential to qualify anisotropic

AuNPs. The Mie theory can be extended to anisotropic NPs, where a spherical shape leads to the absorption of longer wavelengths.[121]

Chapter two

2.0 Materials and methods

All chemicals were of analytical grade and were used as obtained, silver nitrate (Fisher chemical), gold chloride, cysteine, sodium citrate tribasic, magnesium nitrate, copper nitrate trihydrate, sodium chloride, sodium borohydride, sodium chloride, nickel sulphate hexahydrate, citric acid, were source from Sigma Aldrich, sodium chloride anhydrous (ARGOS), nickel nitrate trihydrate (Alfa Aesar) and EDTA (Fluka analytical).Ahmad Jasmine Green tea bag was sourced from a friend which gifts as a present. Cassava was obtained from Amazon. Solvent includes deionized water and ethanol

2.1 Chemical synthesis of metal nanoparticles

2.1.1 Synthesis of cysteine stabilized silver nanoparticles (in aqueous solvents)

silver nitrate(0.068g ,0.0004 mmol) in 800ml of deionized water, sodium borohydride (0.037g, 0.0009 mmol) in 100 ml deionized water and cysteine(0.08g, 0.0066 mmol) in 100 ml deionized water all were added in the following order to in a 1L round bottom flask stirred at 800 rpm 0.0004 mmol silver nitrate followed by the addition of 0.0009 mmol sodium borohydride and 0.0066 mmol cysteine at a room temperature and stirred for 5 minutes, The addition of sodium borohydride changed the solution from colourless to yellow, addition of cysteine the reactant mixture increased the intensity of the yellow colour towards a reddish brown which indicate the formation of cysteine stabilized silver nanoparticles.[122] the resulting cysteine stabilized silver nanoparticles in aqueous solvents were analysed using UV/Visible spectroscopy

2.1.2 Synthesis of cysteine stabilized silver nanoparticles (in organic solvents)

$AgNO_3$ (0.0168g, 0.001 mmol) in 800 ml of ethanol in a 2 L round bottom flask was placed in an ice bath and stirred for 45 minutes after which 5 ml of 0.0008 mmol of cysteine solution (0.01g, 0.0008 mmol) are added No visual changes were observed and the stirring was continued for another 5 minutes after which 0.03 mmol $NaBH_4$ (0.1342g, 0.03 mmol) in 200 ml of ethanol was added to the solution. Dropwise addition of 0.03m sodium borohydride to the mixture solution change from colourless to yellow and after all the sodium borohydride was added, the solution turns to light black, the resulting cysteine stabilized silver nanoparticles were analysed using UV/Visible spectroscopy.

2.1.3 Synthesis of cysteine stabilized gold nanoparticles

sodium citrate tribasic (5.8g, 0.02 mmol) was dissolved in 994 ml of deionized water and heated at 100 ^{o}C until it started boiling. Then 5 ml of gold(III) chloride (0.02g, $6.6x10^{-5}$ mmol) in deionized water was added drop wise to the solution till a purple red colour was observed and 1 ml of 0.008 mmol cysteine solution (0.01g, 0.0008 mmol) was then added at a stirring rate of 800 rpm. The intensity of the purple-red increased as the cysteine was added and was left stirring for 5 minutes and the heating was stopped.[123] The solution was then analysed using UV/Visible spectroscopy.

2.2 Green synthesis of metal nanoparticles using tea bags

2.2.1 Green Synthesis of gold nanoparticles using jasmine green tea extracts

To a 1000 mL round bottom flask was added 600 mL of doubly deionized water, followed by the addition of 5 bag of jasmine green tea leaves. The reaction mixture was stirred continuously at room temperature, after which the extract of the green tea was allowed to cool down and then filtered. To the stirred mixture was added 100 mL gold(III)chloride solution (0.02g, $6.6x10^{-5}$ mmol) in deionised water. The colour of the mixture turned purple-red from pale yellow within 5 minutes after the addition indicating the formation of gold nanoparticles. The reaction mixture was stirred. The colloidal jasmine green tea stabilized gold nanoparticles were then freeze dried for the collection of the product.[124]

2.2.2 Green Synthesis of silver nanoparticles using jasmine green tea extracts

The method used by Ajitha *et al.,*[124] was slightly modified-; To a 1000 mL vessel was added 600 ml of doubly deionized water (DI), followed by the addition of 5 bags of green tea leaves (Green Tea). The reaction mixture was stirred continuously at elevated temperature (~ 100 °C) for 5 min, after which the hot green tea extract was allowed to cool and filtered through a filter paper ,100 ml of the tea extract was stirred on the hot plate stirrer and into the stirred mixture was added 100 mL of $AgNO_3$ solution (0.068g ,0.0004 mmol) at 60 ^{0}C for 60 minutes. The colour of the mixture turned light yellow to pale brown instantly indicating the formation of silver nanoparticles. The reaction mixture was stirred for an additional 5 minutes.

2.3 Green synthesis of metal nanoparticles using cassava waste peels and cassava flesh

2.3.1 Extraction of the cassava extracts

50 g of chopped cassava flesh were extracted in 150 ml deionized water at 100 ^{0}C for 60 minutes. The extract is allowed to cooled down before decantation.

The same procedure was repeated for the extraction of cassava peel.

2.3.2 Synthesis of silver nanoparticles using cassava flesh extracts

10 ml of cassava flesh extract are stirred and boiled at 100 ^{0}C for 30 minutes-.,10 ml of aqueous $AgNO_3$(0.068g, 0.0004mmol) was added with further stirring and heating for 30 minutes. The synthesized silver nanoparticles thus formed were collected by freeze drying method and stored for analysis.

2.3.3 Synthesis of silver nanoparticles using cassava peels extracts

10 ml of cassava peels extract are stirred and boiled at 100 ^{0}C for 30 minutes-.,10ml of aqueous $AgNO_3$ (0.068g, 0.0004mmol) in deionized water was added with further stirring at 800 rpm and further heating for 30 minutes.[125] The silver nanoparticles thus formed were collected by freeze dried method and stored for analysis.

2.3.4 Synthesis of gold nanoparticles using cassava flesh extracts

10 ml of cassava flesh extract are stirred and boiled at 100 ^{0}C for 30 minutes -.,10ml of aqueous $AuCl_3$(0.02g, 0.00007 mmol) in deionized water was added with further stirring at 800 rpm and heating for 30 minutes.[125] The gold nanoparticles thus formed were collected by freeze dried method and stored for analyzation.

2.3.5 Synthesis of gold nanoparticles using cassava peels extracts

10 ml of cassava peels extract are stirred and boiled at 100 ^{0}C for 30 minutes-.,10 ml aqueous $AuCl_3$ (0.02g, 0.00007 mmol) in deionized water was added with further stirring at 800 rpm and heating for 30 minutes.[125] The gold nanoparticles thus formed were collected by freeze dried method and stored for analyzation.

2.4 Separation of the aqueous fraction of the cassava extracts

50g of cassava flesh were extracted in 150 ml deionized water at 100 ^{0}C for 60 minutes, the aqueous extract was extracted with 50 ml ethyl acetate for the separation and purification of the extract-., The organic fractions and the aqueous fractions were separated, dried and collected for further characterization and use. The dried aqueous fraction is referred to as DA-CFE, and the dried organic fraction as DO-CFE

The same procedure was repeated for the separation of aqueous fractions of cassava peel extracts giving, DA-CPE and DO-CPE.

2.4.1 Synthesis of silver nanoparticles using the DA-CFE

0.01 g of DA-CFE were dissolved in 30 ml deionized water and boiled at 100 ^{0}C for 30 minutes ,0.00004 mmol, $AgNO_3$ (0.068g, 0.00004 mmol) solution was added with further stirring, heating and visual observation.[122] The silver nanoparticles thus formed were collected by freeze dried method and stored for analyzation.

2.4.2 Synthesis of silver nanoparticles using the DA-CPE

0.01 g of DA-CPE was dissolved in 30 ml deionized water and boiled at100 ^{0}C for 30 minutes, $AgNO_3$ (0.068g, 0.00004 mmol) was added with further stirring, heating and visual observation.[122]The silver nanoparticles thus formed were collected by freeze dried method and stored for analyzation.

2.4.3 Synthesis of the AuNPs using the DA-CFE

The method used by Adelare *et al.*,[125]were optimized during the synthesis of the gold nanoparticles 4 ml of gold(III) chloride (0.03g, 0.0001 mmol) and 1.5 ml of prepared DA-CFE (0.01 g in 10 ml) was added and left standing with visual monitoring.[125] The gold nanoparticles thus formed were collected by freeze dried method and stored for analyzation.

2.4.4 Synthesis of the AuNPs using the DA-CPE

4 ml of gold chloride (0.03g, 0.0001 mmol) and 1.5 ml of prepared aqueous phase of cassava peel extracts (0.01g in 10 ml) was added and left standing with visual monitoring.[125]The gold nanoparticles thus formed were collected by freeze dried method and stored for analyzation.

2.5 Green synthesis of metal nanoparticles with the involvement of auxiliary reagents (citric acid and ascorbic acid)

2.5.1 Synthesis of citric acid assisted cassava- AuNPs and citric acid-AuNPs

2 ml of citric acid (0.192g, 0.001 mmol) ,4 ml of gold(III)chloride (0.03g, 0.0001 mmol) and 0.5 ml of a solution of 0.125 g of cassava dissolved in 10 ml deionized water are added into a 10 ml glass vial are left into standing for 1 hour without any perturbation, The solution colour changes from light yellow to purple red after 1-hour reaction times.[126]

2.5.1.2 Synthesis of citric acid- AuNPs

2 ml of citric acid (0.192g, 0.001 mmol) ,4 ml of gold(III) chloride (0.03g, 0.0001 mmol) are added into 10 ml glass vial and left into standing for 1 hour without any perturbation, The solution mixture changes from light yellow to purple red after 1-hour reaction times.[126]

2.5.2.1 Synthesis of citric acid assisted cassava -AgNPs

2 ml of citric acid (0.192g, 0.001 mmol),4 ml of silver nitrate (0.068g, 0.00004 mmol) and 0.5 ml of aqueous phase of cassava extracts are added into 10ml glass vial and left standing for 1 hour without any perturbation, The solution colour changes from colourless to radius brown after 2 hours reaction time.[126]

2.5.2.2 Synthesis of citric acid-AgNPs

2 ml of citric acid (0.192g, 0.001 mmol) and 4 ml of silver nitrate (0.068g, 0.00004 mmol) are added into 10 ml glass vial and left standing for 1 hour without any perturbation, The solution colour changes from colourless to reddish brown after 2 hours reaction time.[126]

2.5.3.1 Synthesis of ascorbic acid assisted -AgNPs

1 ml of ascorbic acid (10.6g, 0.06 mmol) and 12 ml of silver nitrate (0.068g, 0.00004 mmol) were added into 10 ml glass. The solution colour changes from colourless to yellow after 5 minutes of reaction time. The solution is then analysed using UV/Visible spectroscopy.[126]

2.5.3.2 Synthesis of ascorbic acid assisted -AgNPs

1 ml of ascorbic acid, (10.6g, 0.06 mmol) 12 ml of silver nitrate (0.068g, 0.00004 mmol) and 0.5 ml of aqueous phase of cassava extract were added into 10 ml glass vial are left into standing for 1 hour without any perturbation. The solution colour changes from colourless to yellow and the solution were then analysed using UV/Visible spectroscopy.[126]

2.5.3.3 Synthesis of ascorbic acids assisted -AuNPs

12 ml of gold (III) chloride (0.03g,0.0001 mmol) and 1ml of (10.6g,0.06 mmol) ascorbic acids were made in a glass vial. The solution colour changes from light yellow to pink red after the addition of ascorbic acid. The solution was analysed using UV/Visible spectroscopy. [126]

2.5.3.4 Synthesis of ascorbic acids assisted -AuNPs-cassava

12 ml of gold(III) chloride (0.03g, 0.0001 mmol), 1 ml of (10.6g, 0.06 mmol) ascorbic acid and 0.5 ml of cassava extract were mixed in a glass vial. The solution colour changes from light yellow to pink red after the addition of ascorbic acid. The solution is analysed using UV/Visible spectroscopy.[126]

2.6 Heavy metal detection by synthesized green tea metal nanoparticles

The colorimetric measurement of heavy metals such as copper nitrate trihydrate, nickel chloride anhydrous and gold(III) chloride are carried out by preparing 2-20 ppm solution of each heavy metal. From it 2 ml of each heavy metal concentrations were added to a 20 ml glass vial and 2 ml of the synthesized metal nanoparticle solution were added and left to stand for 5 minutes after which the solution was analysed using UV/Visible spectroscopy.

This procedure was adopted for all the sensing experiments by each metal nanoparticles.

2.7 Adsorption experiments

The adsorption of heavy metals by metal nanoparticles was carried out using 0.1 g of the synthesized metal nanoparticles .1000 ppm of the stock solution of each metal ion was prepared and from it different concentration ranging from 0.5-20 ppm were prepared by successive dilution with deionized water into these solutions was added 0.1g of synthesized metal nanoparticles was added and agitated in orbital shaker at room temperature for 2 hours

after which the solution was centrifuged and the supernatant analyzed using UV/Visible spectroscopy. The same procedure was used for each metal nanoparticle.

2.7.1 Complexation of the Ni(EDTA)

1M stock solution of the three-metal salt of nickel namely nitrates(2.36g, 1M) sulphates (2.62g, 1M) and nickel chloride anhydrous (1.3g, 1M) were prepared and transfer into conical flask after which a pinch of Murexide powder was added to the solution and 10 ml of Ammonium chloride solution(0.5g, 0.1M) were also added after which the solution was titrated with EDTA(3.36g, 1M) solution and as the titration progress another 10ml of 0.1M Ammonium chloride solution was added and the titration was stopped at the end point.[127]

2.7.2 Physiochemical parameter study

2.7.2.1 The influence of initial concentration of heavy metals on the adsorption of heavy metal

0.5-20 ppm of each metal ions was prepared by successive dilution with deionized water after which 0.1 g of cysteine stabilized silver nanoparticles was added to the solution and agitated in the shaker for 2 hours after which the solution was filtered and the supernatants analysed using UV/Visible spectroscopy. The same procedure was repeated for all other metal nanoparticles adsorption of heavy metals. The optimal contact time was determined for each heavy metal. This is defined as the time at which the adsorbent had sufficiently removed the adsorbate from the solution and no further adsorbate could be remove by the material after this time.

2.7.2.2 Effect of contact time

A range of different initial concentration of each metal ions was prepared and 0.1 g of cysteine stabilized silver nanoparticles were added and agitated for 5-1440 minutes after which the solution was filtered and supernatants was analysed using UV/Visible spectroscopy. The same procedure was repeated for all other metal nanoparticles adsorption of heavy metals. The optimal contact time was determined for each heavy metal by using the following equation

$$Qe = \frac{(Co - Ce)V}{W}$$

Where Co is the initial concentration, Ce is the equilibrium concentration at time T(minutes), V is the working Volume and W is the weight of the adsorbent.

2.7.2.3 Effect of adsorbent dose

Optimal initial concentration of each metal ions was prepared for optimal time of respective metal ions and the doses of cysteine stabilized silver nanoparticles ranging from 0.01-0.05 g were added and agitated for the optimal time of each respective metal cation. At the end of the experiment, the solution was filtered and analysed using UV/Visible spectroscopy. The optimal dose of adsorbent was determined for each heavy metal .by using the following equation

$$Qe = \frac{(Co-Ce)\ V}{W}$$

Where Co is the optimal initial concentration, Ce is the equilibrium concentration at time T(minutes), V is the working Volume and W is the weight of the adsorbent.

2.7.2.4 Effect of pH

optimal initial concentration was prepared for all the metal ions for the optimal time and dose of each metal ions across a pH range of 3-12, the solution pH was adjusted using 0.1 M HCl and 0.1 M NaOH solution and optimal dose of cysteine stabilized silver nanoparticles for respective metal ions were added and agitated for the optimal time of each metal ion, after which the solution was filtered and the supernatant were analysed using UV/Visible spectroscopy.

2.7.2.5 Effect of temperature

optimal initial concentration was prepared for all the metal ions at optimal dose of respective metal ion solution and optimal pH and agitated for the optimal time of each metal ions across a temperature ranging from 30 ^{0}C-90 ^{0}C, after the incubation time the solution were filtered and analyse using UV/Visible spectroscopy.

2.8 Characterization of the synthesized metal nanoparticles

All metal nanoparticles sample were obtained in colloidal state and were freeze dried in order to obtain the powdery form, except for the UV/Visible spectroscopy characterization which was performed directly on the aqueous solution of each metal nanoparticles (with appropriate dilution where necessary).

2.8.1 UV–VIS spectrophotometric analysis

An UV–VIS spectrophotometer (vision lite model) was used to identify the presence of LSPR in the synthesized cassava metal nanoparticles. For each of the cassava metal nanoparticles, the sample was diluted with deionized water and taken in a small plastic corvettes cell for the recording the UV–VIS absorption spectrum at wavelength of 300–800 nm.

2.8.2 X-ray diffraction (XRD) analysis

Powder XRD was used to identify the crystalline phase and particle size of the prepared material. The sample was placed on a grid of XRD instrument and the diffraction patterns were recorded at 40 kV and 40 mA of voltage with Kβ filter 1D for Cu. X-ray diffraction can be used to determine the size of crystal with phase certain. The determination refers to the main peaks of the pattern diffractogram through approach Debye Scherrer's equation formulated in Equation below.

$D=K\lambda/\beta \cos \emptyset$

where D is the crystallite size, K is the Scherrer constant (0.9nm), λ is the wavelength of the X-rays used (0.154, β is the Full Width at Half Maximum, radians), and $\emptyset$ is the peak position (radians)s.[12]

2.8.3 Fourier transform infrared (FT-IR) analysis

The functional groups that stabilize the metal nanoparticles surfaces are observed using FTIR, FT-IR spectra of synthesized cassava metal nanoparticles and both fractions of crude cassava peels and flesh extract were recorded. FT-IR spectra of the samples were recorded from 650 to 4000 cm^{-1} with a FT-IR ATR Spectrometer (OPUS software application.) Resolution was 4 cm-1 and 10 scans were carried out as standard.

2.8.4 Thermogravimetry analysis

Thermogravimetric analyses were performed using Stanton Red croft STA 625 under nitrogen atmosphere in a low flow rate, and at a heating rate of 10 ^{o} C / min.

2.8.5 Scanning electron microscopy

5 mg of each metal nanoparticles were submitted to the Imaging and cytometry department, University of York for analysis of the morphology and structure of each metal nanoparticles.

2.8.6 Transmission electron microscopy

5 mg of each metal nanoparticles were submitted to the Imaging and cytometry department, University of York for analysis of the morphology and structure of each metal nanoparticles. Each of the nanoparticle's colloids suspended in deionized water in the presence of stabilizing agents was deposited and air dried on the specimen grid and observed with a transmission electron microscope (TEM: JEOL – JEM 1010). Transmission electron microscope specimens consist of carbon or collodion coated copper grids. Transmission electron microscope images have been recorded with a JEOL standard software.

2.8.7 HPLC analysis

5 mg of the cassava peel, cassava flesh and aqueous phase of the cassava peel and cassava flesh are dissolved in 1.5 ml of deionized water and submitted for HPLC analysis in GCCE chemistry department University of York.

CHAPTER THREE

Results and discussion on cysteine stabilized silver nanoparticles (AgNPs) and application towards the detection and removal of heavy metals from aqueous solutions

Cysteine-stabilised silver nanoparticles were prepared following a literature procedure[122]both in aqueous solution (leading to aq-cys-AgNPs) and in ethanolic solution (org-cys-AgNPs)

3.1 Cysteine stabilized AgNP in aqueous solvents

The synthesized AgNPs were freeze dried in order to obtain the nanoparticles in the solid state. Structural analysis of the aq-cys-AgNPs were carried out using UV/Visible spectroscopy, microanalysis, FTIR, TGA, PXRD, SEM and TEM. The resulting aq-cys-AgNPs were used for the adsorption and interaction of heavy metals in aqueous solution. The addition of cysteine solution to the reduced silver atom further increases the intensity of the colour of the synthesized silver nanoparticles. (Figure.3.0)

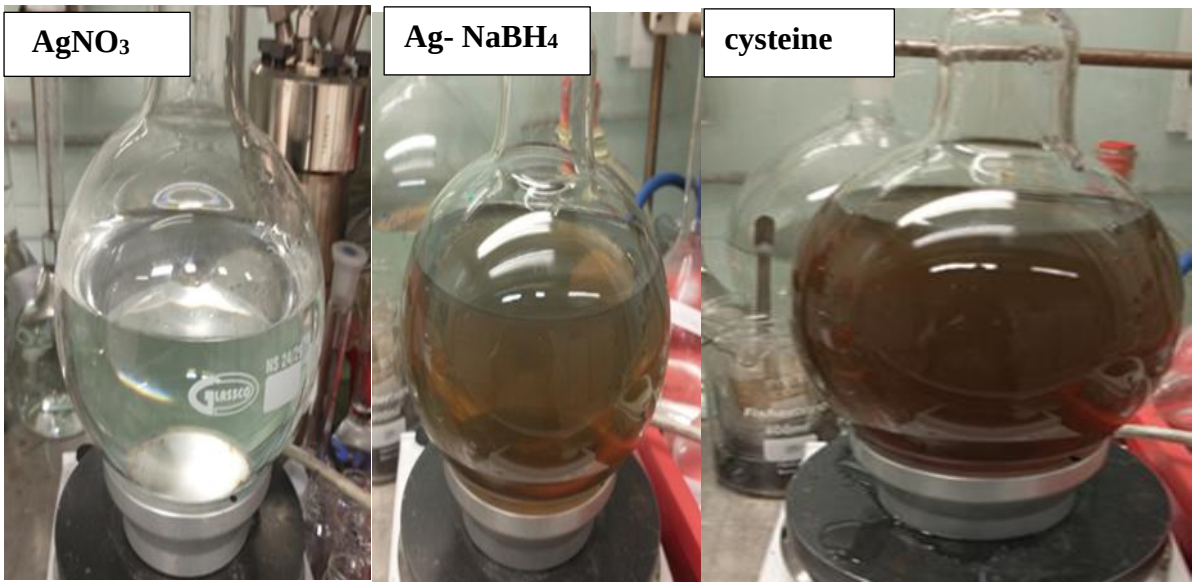

Figure 3.0: Synthetic process of aq-cys-AgNPs in aqueous solution

3.1.1 UV/Visible Characterization of aq-cys-AgNP in aqueous solvents

The resulting aq-cys-AgNPs were characterized using Uv/visible spectroscopy. Typically, 5 ml aliquots of the aq-cys-AgNPs in aqueous solvent were taken in single vials and the UV–Visible absorption measurements are recorded. The LSPR appears at 401 nm and tends to be stable over time (Figure 3.3). The UV/Visible spectra were recorded at 10-minute intervals for 100 minutes in order to assess the stability of the nanoparticles.

The reduction of the silver ions to the elemental state was primarily by sodium borohydride as indicated in the UV/Visible spectra of the (silver sodium) borohydride, there has also been a shift in the absorption spectra of the aq. $AgNO_3$ after the reduction steps (from 268 nm to 388 nm) depicted in Figure 3.1-3.2. The stabilization of the nanoparticles by cysteine leads to a significant change in the size of the LSPR (Figure 3.3). Such an effect is generally considered to relate to an increase in NP size of the aq-cys-AgNPs. According to previously published works of Paramelle et al.[128] and Alula et al.[129], smaller sized nanoparticles, approximately 10 nm in diameter, produce a maximum absorption band around 392 nm while larger sized nanoparticles such as those 30 nm in diameter exhibit absorption peak around 406 nm.

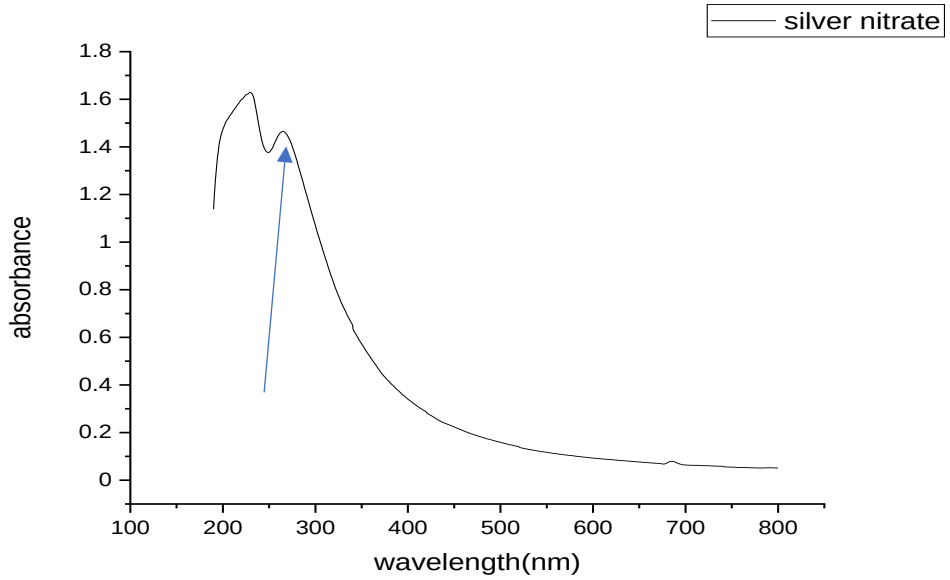

Figure.3.1: UV/Visible spectra of Aq. $AgNO_3$

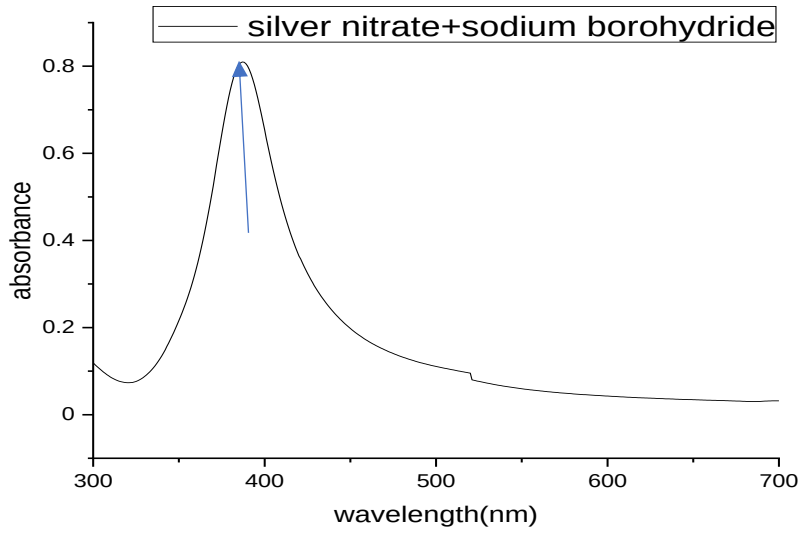

Figure.3.2: UV/Visible spectra of $AgNO_3$-$NaBH_4$

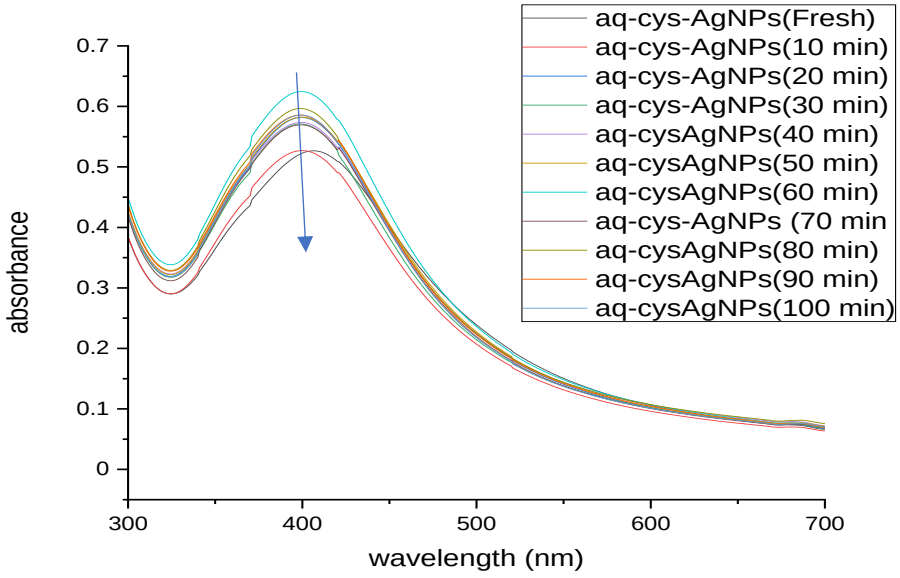

Figure.3.3: UV/Visible spectra of aq-cysAgNPs in aqueous solvent with absorbance stability over time (10-100 minutes) at 10 minutes interval

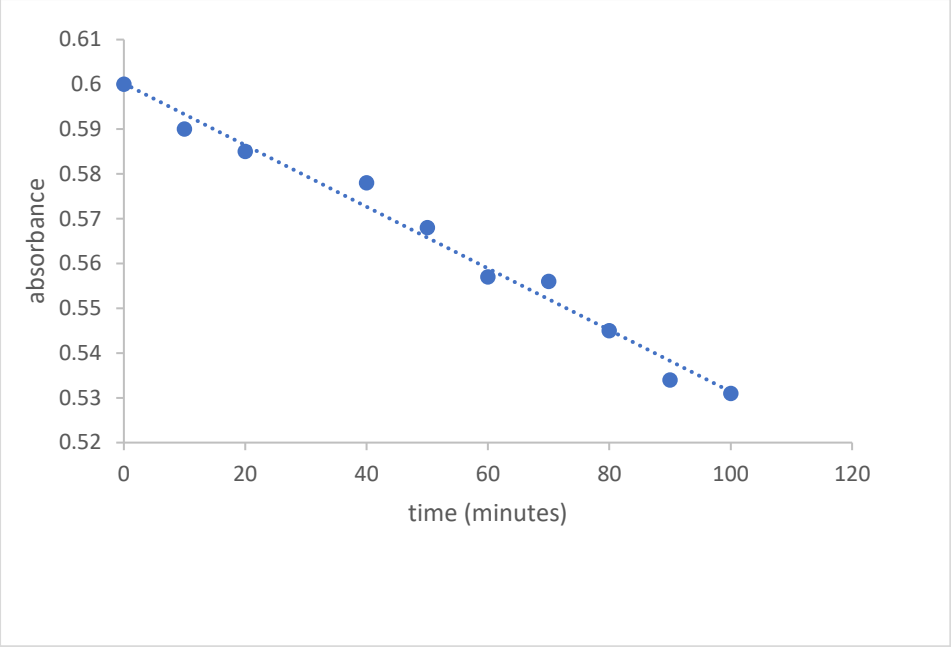

Figure.3.4: A plot of aq-cys-AgNPs LSPR peak height versus time

3.1.2 Fourier transform infrared spectra of aq-cys-AgNP

The binding of cysteine on the surface of the aq-cys-AgNPs was confirmed by FT-IR measurements. The FT-IR spectra of free cysteine and aq-cys-AgNPs are displayed in figure 3.2. The band observed at 2554cm^{-1} in the figure may be attributed to the S-H vibration of cysteine [130]. However, this band was not observed for aq-cys-AgNPs. It indicates the possibility of binding of cysteine to the surface of the aq-cys-AgNP via the thiol group. The weak carbonyl band at 1754 cm^{-1} in the cysteine spectra has shifted to 1732cm^{-1} in the spectra of aq-cys-AgNPs. The weak band at 1524 cm^{-1} in the band of cysteine also shifted to 1558 cm^{-1} and now more intense in the spectra of aq-cys-AgNPs. Characteristic spectra of cysteine are found in the finger print region of the spectra of cysteine stabilized AgNPs suggesting the presence of cysteine in the synthesized nanoparticles., There is a complex hydrogen bonding network of cysteine on the surface of the NPs which leads to the broad and strong band centred on 3047 cm^{-1} and this differs from the complex H-bonding of cysteine in the solid state and this is consistent with the shift in C=O vibration noted earlier.

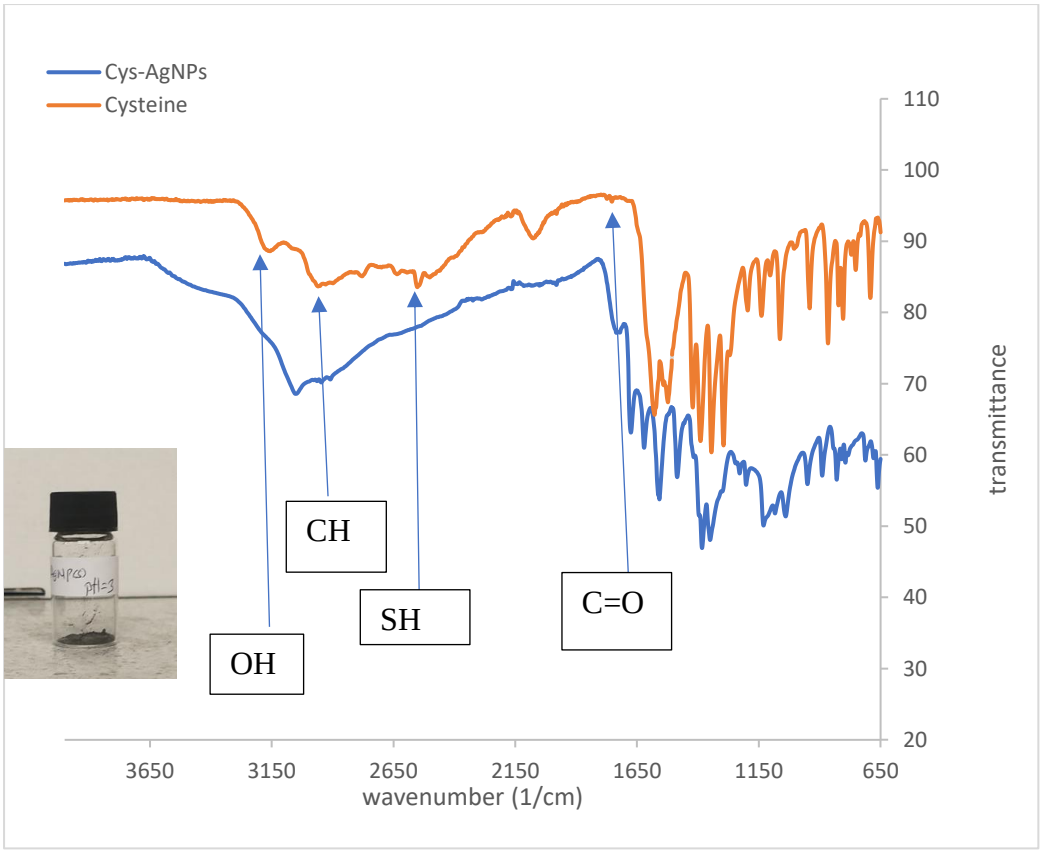

Figure.3.5: Fourier transform infrared spectra of cysteine and aq-cys-AgNPs

3.1.3 Thermal analysis of aq-cys-AgNPs.

The thermal decomposition of aq-cys-AgNPs is depicted in figure 3.6 This result revealed a decomposition pattern consisting of an overall mass loss of 63% between room temperature and 600 ^{0}C, consisting of two distinct mass losses - a sharp loss between ca. 185 ^{0}C and ca. 200 ^{0}C, a broader mass loss from ca. 210, ^{0}C to ca. 350, ^{0}C, followed by a very gradual loss up to 600 ^{0}C. As silver is not volatile in this temperature range, the result show that there is a high amount of cysteine or cysteine-derived organics at the surface of the aq-cys-AgNPs. While TGA itself does not identify the volatile species, the first mass loss is consistent with decarboxylation (expected mass loss 14 % compared to the measured 15 %). This is consistent with the thermal decomposition of pure cysteine reported by Weiss et al. over the range 50-300 ^{0}C, where CO_2 was the only volatile reported.[131] In our case, the mass loss is at a significantly lower temperature, possibly indicating loss of stability due to a lack of crystallinity of the cysteine, or perhaps a destabilising role of Ag.

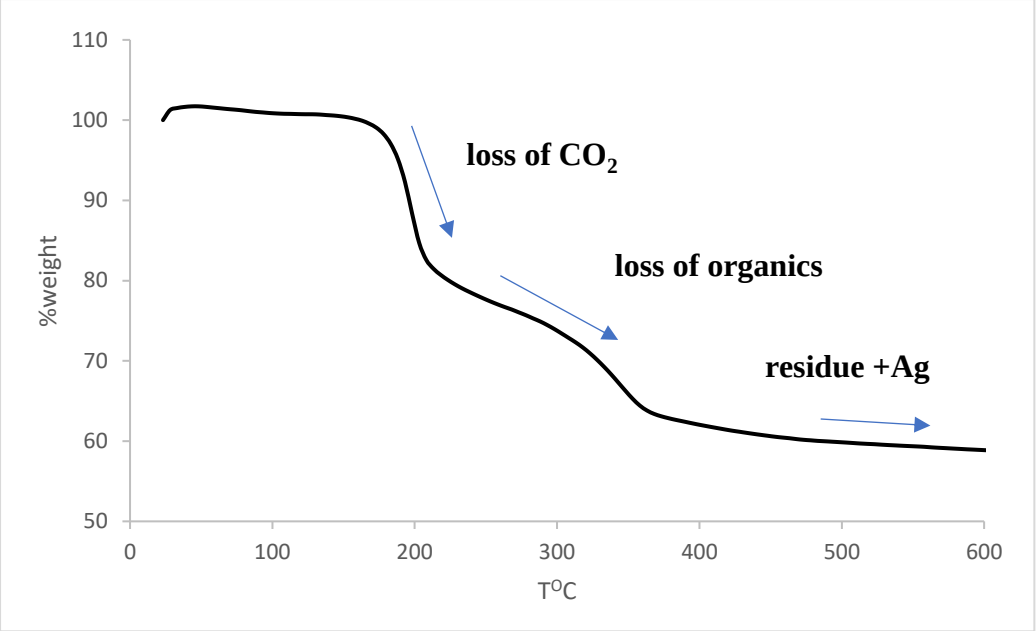

Figure 3.6: Thermal analysis of aq-cys-AgNPs

3.1.4 Elemental composition of aq-cys-AgNPs.

The CHN microanalysis of the fabricated AgNP in aqueous solvents revealed that the percentage organic material, consistent with cysteine (15.79 % C, 7.61 % N,13.4 % S) was found to be 39.84 %, corresponding to 53.23% cysteine – $C_3H_7NO_2S$, while the remainder (Ag and O) was found to be 60.156 % (Table.2). The results were found to be in good agreement with the thermogravimetry analysis result, and suggests that there is residual organics left at 600°C.

sample	%C	%H	%N	%S	%O	%Remainder
aq-cys-AgNP	15.79	3.044	7.61	13.393	-	60.156

Table.2: Microanalysis of aq-cys-AgNPs

3.1.5 Powder x-ray diffraction of aq-cys-AgNPs.

The powder x-ray diffraction data result (Figure 3.7) implies that the aq-cys-AgNP were highly crystalline, the particle sizes estimated using Debye-Scherer equation and was found to be 48

nm, consistent with the LSPR position. The 2θ values were taken from 20° to 90° and the Bragg reflections were observed at 38.52º, 45.8º, 64.93º and 77.2º which correspond to the indexed planes of crystals of Ag (111), (200), (220) and (311)[132]. The cell parameter was found to be in good agreement with the database of JCPDS Card no. 04-0783[132,133]. There was no evidence of cysteine crystallites on the surface of the NPs.The extra Bragg reflections observed between 20º -37 º could be attributed to the peaks of cysteine as this was compared to the diffractogram of ET-OH-cys-AgNPs where few amounts of cysteine were present at the surface of the ET-OH-cys-AgNPs. (Figure.3.7)

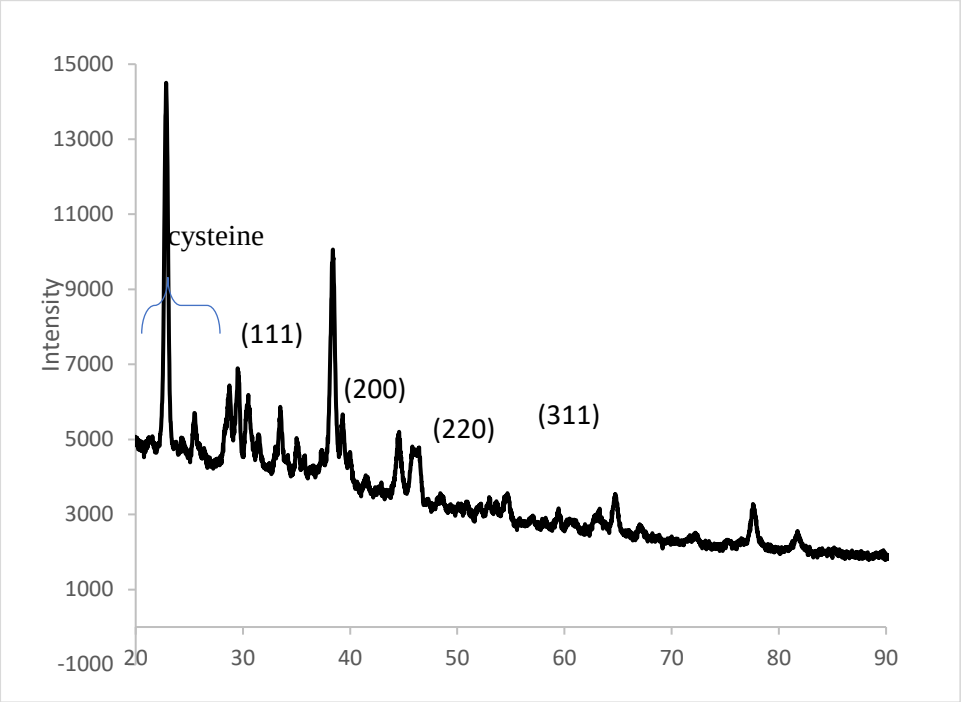

Figure 3.7: PXRD of aq-cys-AgNPs

3.1.6 Scanning electron microscopy (SEM) of aq-cys-AgNPs.

The SEM result (Figure 3.8 and 3.9) revealed the bulk morphology of the aq-cys-AgNPs to be predominantly dominated by cluster of smaller particles. The nanoparticles also show a degree of aggregation in the structure.

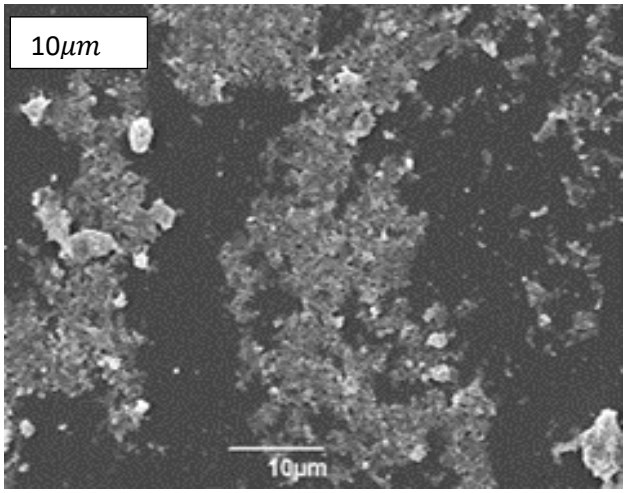

Figure 3.8: SEM of aq-cys-AgNPs (10μm)

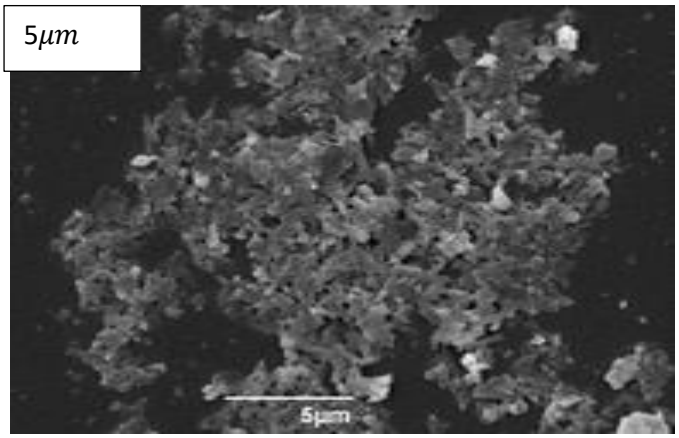

Figure 3.9: SEM of aq-cys-AgNPs (5μm)

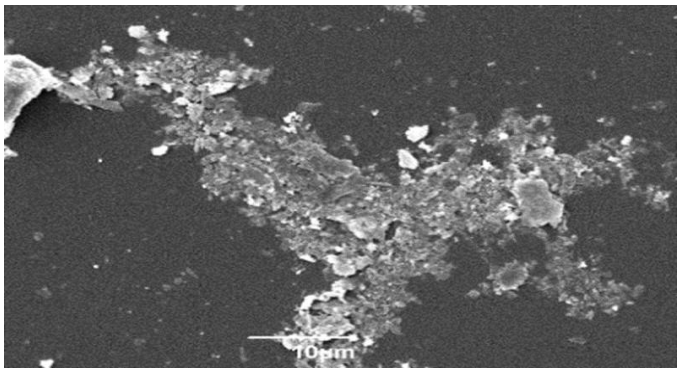

Figure 3.10: SEM of aq-cys-AgNPs (10μm)

3.1.7 Transmission electron microscopy (TEM) of aq-cys-AgNPs.

The transmission electron microscopy (Figure 3.11) aq-cys-AgNPs revealed the morphology of the aq-cys-AgNPs to be spherical like. The nanoparticles also show a degree of aggregation in the structure.

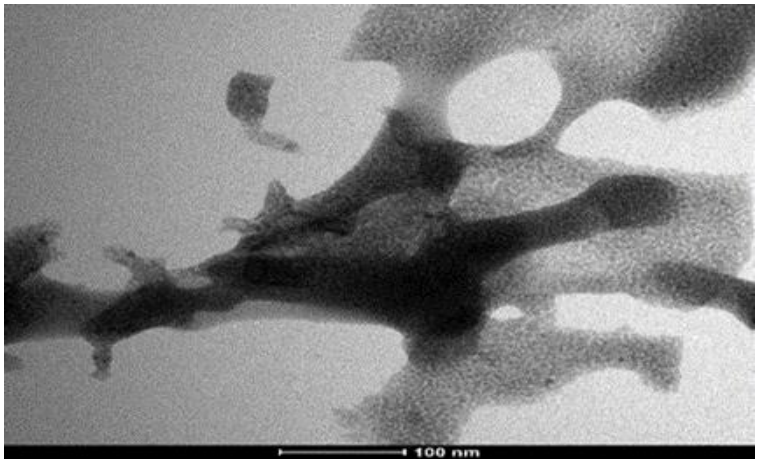

Figure 3.11: TEM of aq-cys-AgNPs (100μm)

Thus, in summary, a range of analyses have demonstrated the successful fabrication of aq-cys-AgNPs, with particle size in the range 5-40 nm, with UV/Visible spectroscopy, PXRD suggesting particle size in 30-40 nm which is consistency with the TEM, The TEM image shows some large NPs consistent with the UV/Vis and pXRD data (around 40 nm) but also much smaller NPs, typically 5 nm can be seen". Aq-cys-AgNPs possess organic content of ca. 50 mass %. TGA, microanalysis and FTIR suggest the cysteine remains intact and is likely to bound to the Ag surface via Ag-S bonds. pXRD shows the presence of crystallinity in the Ag but not in the adsorbed cysteine. There is evidence for a bimodal distribution of nanoparticle size.

3.1.8 Potential structure of the aq-cys-AgNPs.

FTIR spectra suggest the coordination of the thiol group with the aq-cys-AgNPs and also the presence of organic molecules in the synthesized cysteine stabilized silver nanomaterial which is also confirmed by the microanalysis and the thermal analysis. (Figure 3.12.)

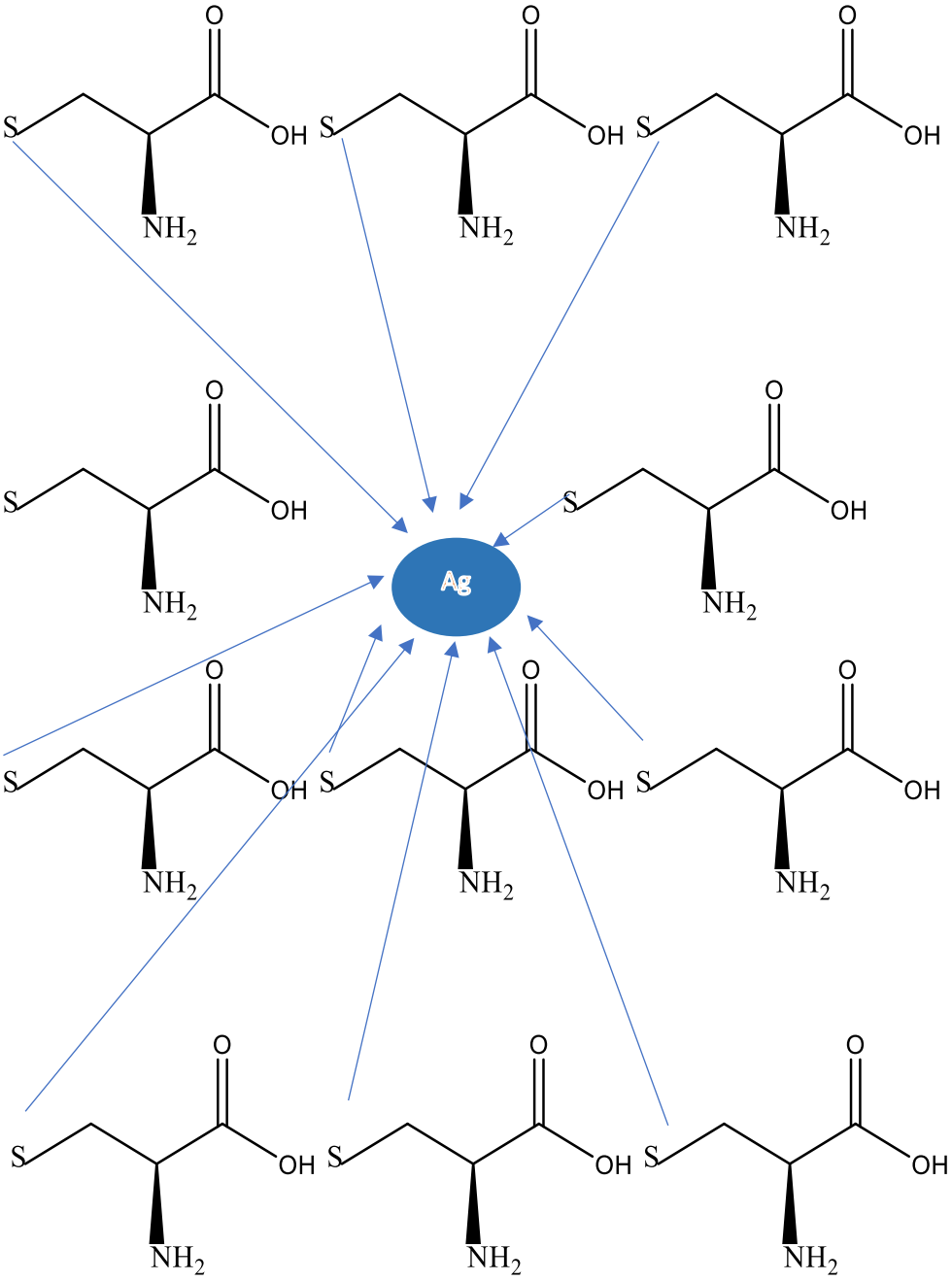

Figure 3.12: Suggested structure of aq-cys-AgNPs

3.2 Heavy metal ion determination using colorimetric technique

3.2.1 Adsorption of Cu(II) and Ni(II)

For the colorimetric detection approach, 2 ml of 8-20 ppm of copper nitrate trihydrate and nickel(II) chloride anhydrous solutions were prepared into two different 10 ml glass vials after which 2 mL of synthesized aq-cys-AgNPs was added., The mixture was allowed to stand for 5 min equilibration and the reaction progress was monitored by the spectral behaviour of the suspension from 200 to 800 nm using a UV/Vis spectrophotometer. Other metal ions such as (Cd(II), Ni(II), Cu(II), Pb(II) and Ni(II)EDTA) were also exposed to cysteine stabilized AgNP in aqueous solvents at a concentration of 2-6 ppm to compare and quantify the selectivity of the detection techniques. After 5 minutes, a golden yellow colour appears for Ni(II) and Cu(II), the intensity of the yellow colour for Cu(II) increasing as the concentration increases (fig.3.14). Surface plasmon resonance in the case of Cu(II) shifted from 402 nm-412 nm. (figure.3.13) whereas a slightly red shift in the surface plasmon resonance (402 to 405 nm) was observed for Ni(II) with peaks becoming broader in this case. A possible rationale behind the observed behaviour is that the association of NPs into larger clusters with bridging Ni^{2+} ions (that results in the formation of a "superlattice" [134]) can cause the shift in Surface plasmon resonance. On such a premise, the first part of the curve in Figure.3.13 represents the slow formation of a small lattice of silver NPs in the presence of low concentration of Ni(II) (the lag phase, low-sensitivity region). Next, as the Ni(II) concentration increases, a mild tendency towards agglomeration of a higher number of additional nanoparticles is seen. This phenomenon results in a superlattice that is associated with fairly or no change in the absorbance spectrum and less sensing ability of the detector at the range of metal ion concentration tested.

Next, upon further increase in Ni(II) concentration, the NPs-Ni(II) cluster reaches a critical mass and these leads to collapsing of the superlattice.

It has been reported in literature that the colour of nanoparticles depends on their shape, dimension, composition, and dielectric constant[135], and differences in the degree of agglomeration of metal nanoparticles; the interparticle distance between agglomerates shifts in the surface plasmon absorption band (SPAB) with respect to monodisperse ones[136,137]. The principle for detection of heavy metals via a colorimetric sensor developed by metal nanoparticles is based on the dependence of SPAB on the degree of agglomeration.[138.]

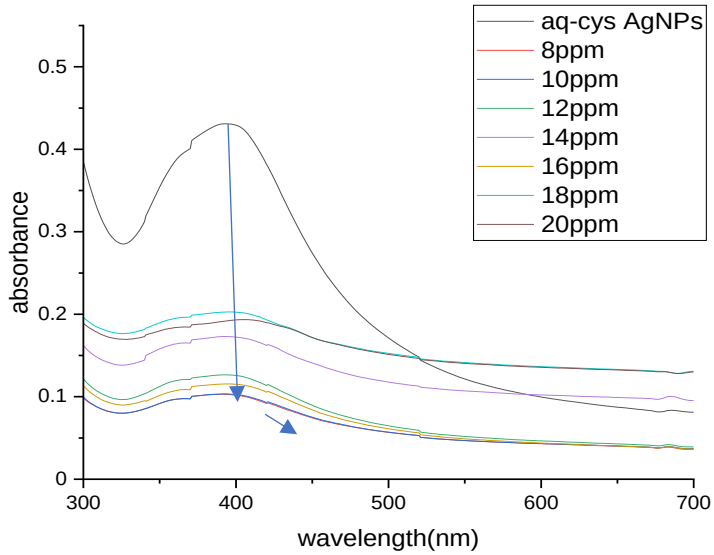

Figure.3.13: UV/Visible spectra of detection of Ni(II) by aq-cys-AgNPs and nickel (8-20 ppm)

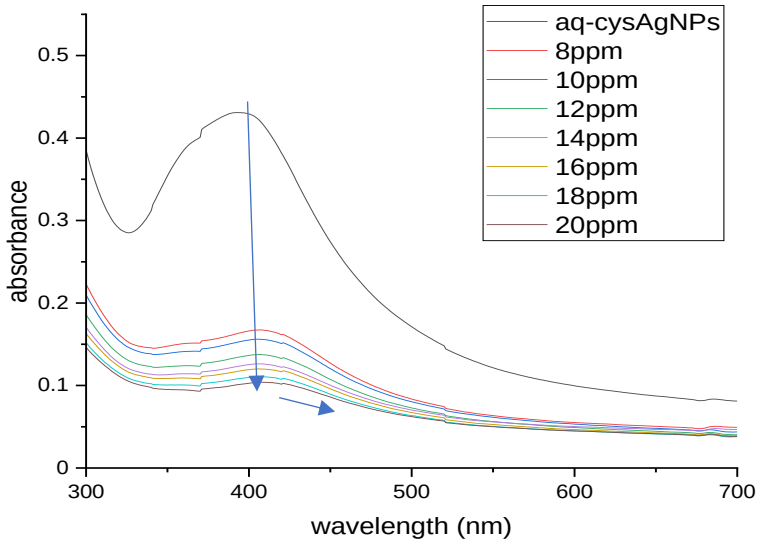

Figure.3.14: UV/Visible spectra of detection of Cu(II) by aq-cys-AgNPs and copper (8-20 ppm)

3.2.2 Detection of Cu(II), Ni(II), Cd(II), Pb(II) and NiEDTA (2-6 ppm) by aq-cys-AgNPs

The detection of Cu(II), Cd(II), Pb(II) and NiEDTA by aq-cys-AgNPs at 2-6 ppm shows a slight bathochromic shift for each metal ion tested (Figure 3.15-3.17)

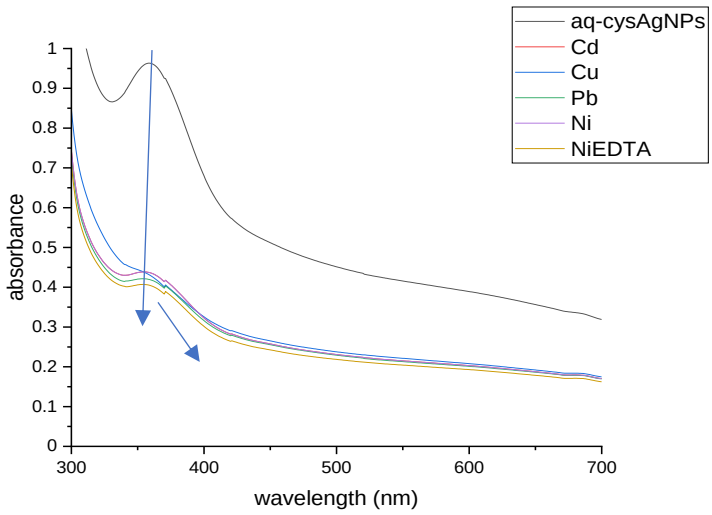

Figure.3.15: **UV/Visible spectroscopy of aq-cys-AgNPs and copper, nickel, cadmium, lead and NiEDTA at 2 ppm**

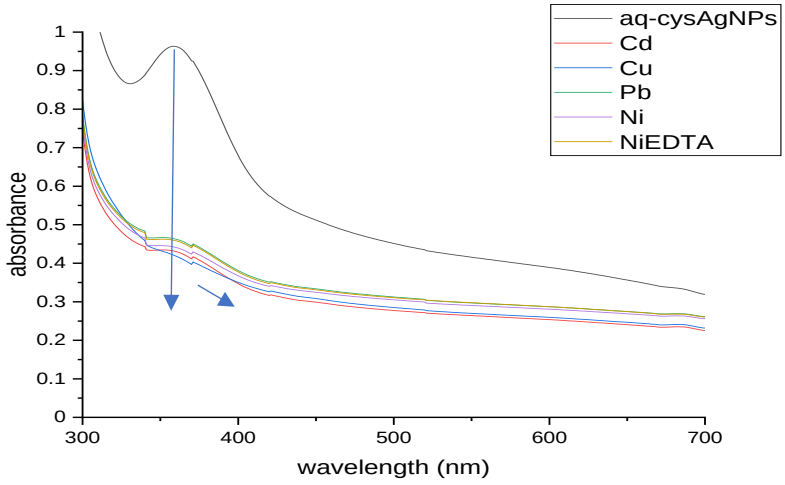

Figure.3.16: **UV/Visible spectroscopy of aq-cys-AgNPs and copper, nickel, cadmium, lead and NiEDTA at 4 ppm**

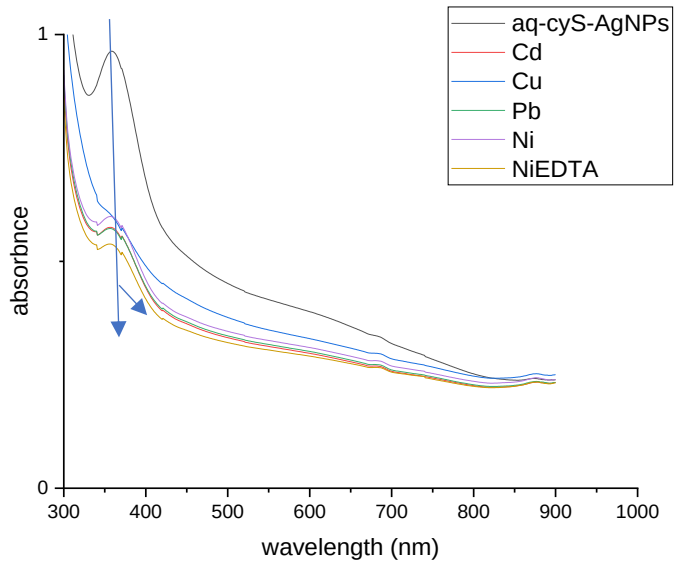

Figure.3.17: **UV/Visible spectroscopy of aq-cys-AgNPs and copper, nickel, cadmium, lead and NiEDTA at 6 ppm**

3.2.3 Detection of gold by aq-cys-AgNPs

The detection of gold by aq-cys-AgNPs shows an intense yellow coloration after 5 minutes, the intensity also decreases as the concentration increases. The appearance of the shape of the LSPR of the new batch of aq-cys-AgNPs retains the narrowness but tends to be slightly broader towards a higher concentration of gold ions, and a slight red shift is also observed form 388 nm to 391 nm in the spectra. (Figure 3.18)

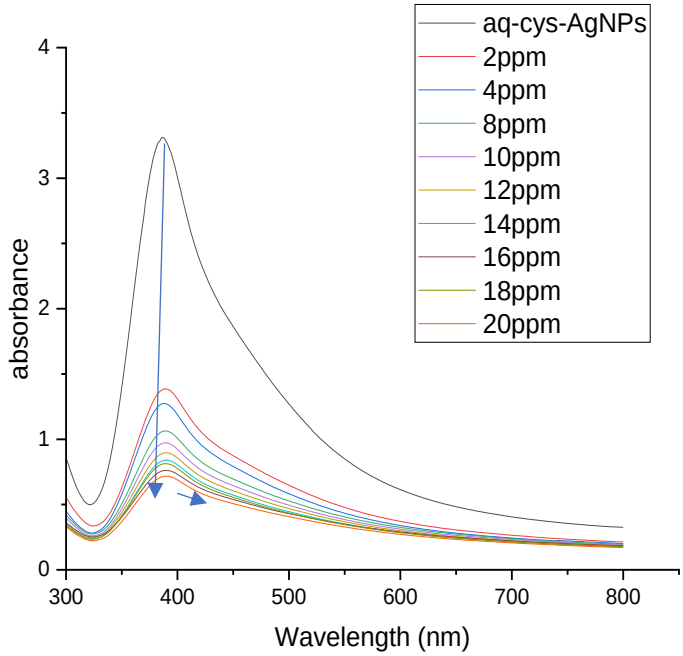

Figure.3.18: Detection of gold (2-20 ppm) by aq-cys-AgNPs by UV/Visible spectroscopy

3.3 Quantitative analysis of the adsorption of heavy metals by aq-cys-AgNPs

Out of all the heavy metals analysed two of the metals were selected for the majority of the adsorption experiments, copper and nickel due to time factor. The concentration tested for each metal are in the range of 2- 20 ppm. The range of metals concentrations investigated for each of the metal salts and gave a suitable R^2 value.

3.3.1 Effect of initial concentration

The quantity of Cu(II) and Ni(II) ions adsorbed by aq-cys-AgNPs increases linearly with the initial concentration at room temperature at pH of 4.65 for copper and 5.60 for nickel (figure.3.18). The qe values are calculated using the formula. (Figure.3.19)

Qe= ((Co-Ce) V) ÷W

Where Co -is the initial concentration of the metal ions, Ce is the equilibrium concentration obtained from the calibration curve results, V is the working Volume and W is the weight of the adsorbents.

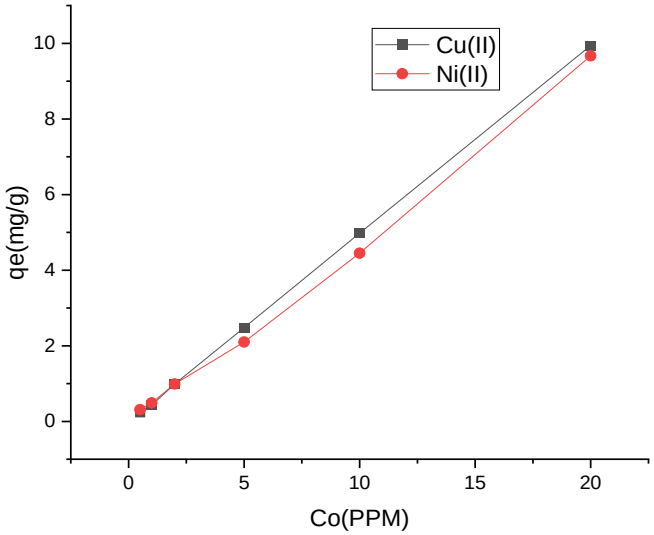

Figure. 3.19: Effect of initial concentration of Cu(II) and Ni(II) by aq-cys-AgNPs

3.3.2 Effect of contact time at optimal initial concentration 20 ppm

The adsorption of copper by aq-cys-AgNPs occurs at a rapid time, being essentially complete after 5 minutes, but then drifts slowly upwards to reach equilibrium at 60 minutes. Subsequently, the quantity of copper ions adsorbed then remains stable over 24 hours. The adsorption of nickel by aq-cys-AgNPs tends to be slower, reaching equilibrium at 20 minutes with a lower qe (mg/g) compared to the qe value of copper at 60 minutes and then remains stable till 24 hours. (Figure. 3.20)

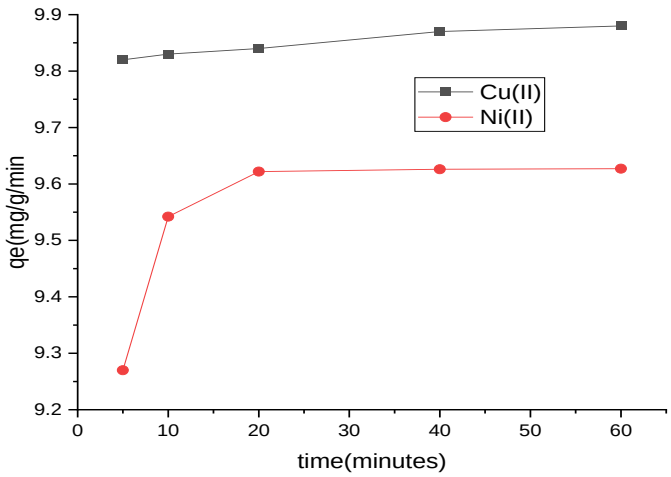

Figure. 3.20: Effect of contact time of Cu(II) and Ni(II) by aq-cys-AgNPs over 60 minutes(top) and 1440 minutes (down) all experiment runs at initial concentration of 20 ppm

3.3.3 Effect of nanoparticle dose at optimal initial concentration of 20 ppm

The quantity of metal ions adsorbed (qe) decreases for both copper and nickel (Figure 3.21) as the number of NPs increases due to all the metal absorbing with the lowest amount of adsorbent, so adding more has no effect as there is nothing left to adsorb, this was confirmed by treating the ETOH-cys-AgNPs with high amount of metal concentration and the results revealed optimal adsorption at 400 ppm with 0.01 g of the ETOH-cys-AgNPs, leading to a maximum qe of 111.76 mg/g.

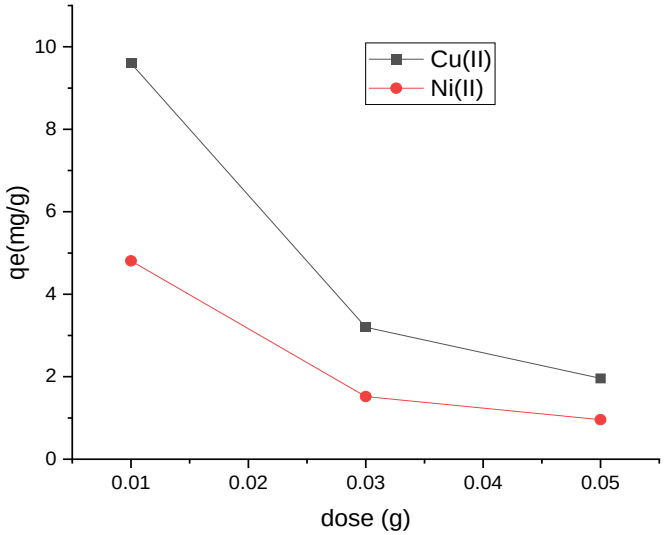

Figure. 3.21: Effect of nanoparticle dose of Cu(II) and Ni(II) by aq-cys-AgNPs at initial concentration of 20 ppm

3.3.4 Effect of pH at optimal initial concentration of 20 ppm

0.1M HCl and 0.1M NaOH are used for the tuning of the pH. The quantity of Ni(II) removed by aq-cys-AgNPs increases as pH increases which is common for metal cations owing to the improving electrostatic interaction between unlike charges in the surface of the aq-cys-AgNPs and the Ni(II) (Figure 3.22). The point of zero charge (PZC) for cysteine is 5.3, and Sangeetha et al.2013[117] has demonstrated that the PZC of cysteine supported on Fe_3O_4 nanoparticles is very similar (between X and Y). Thus, it is expected that cysteine capped AgNPs will be positively charged below pH 5.3 and increasingly negatively charged above this pH. The speciation of Ni(II) in dilute aqueous solution has been described by Sangeetha et al.2013.[139] They showed that increasing pH up to around 9 retains predominantly positively charged Ni species; largely $Ni(H_2O)_6^{2+}$ until close to pH 9 where some $Ni(H_2O)_5OH^+$ occurs. At the highest pH, significant participation from $Ni(OH)_2$ is seen, which has limited solubility, and can precipitate onto the NPs, consistent with the significant rise in adsorption seen at the highest pH. The relatively low drop in adsorption at low pH – expected as the NPs should be predominantly positively charged – may be due to either the presence of sufficient carboxylates even at pH 3 (there is a large excess of cysteine to Ni(II)) or to the ability of the increasing Cl ion concentration at low pH leading to ligation of chloride, reducing the charge on Ni.

Copper, on the other hand has a relatively uniform and relatively high qe across the whole range. The higher affinity of Cu for amine ligands, compared to Ni, may be partly responsible for this behaviour, meaning that carboxylate and amine can both participate, possibly "smoothing" the variation in surface chemistry and Cu speciation.

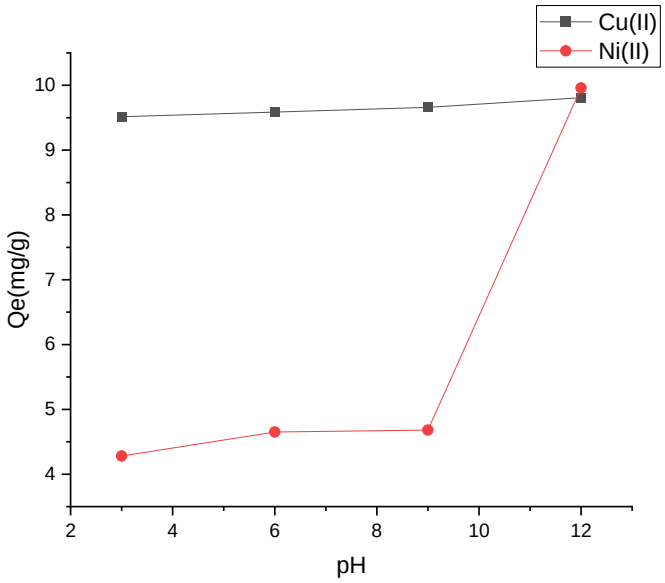

Figure. 3.22: Effect of pH on the adsorption of Cu(II) and Ni(II) by aq-cys-AgNPs at initial concentration of 20 ppm

3.3.5 Effect of temperature at optimal initial concentration of 20 ppm

The quantity of Ni(II) adsorbed by aq-cys-AgNPs increase with temperature; the same behaviour is seen in the qe values for Cu(II), albeit it is much less pronounced. (Figure. 3.23.)

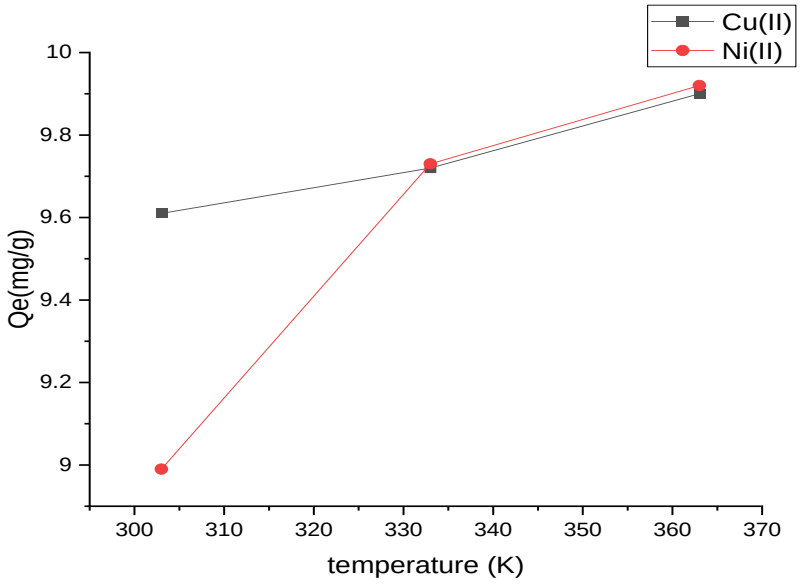

Figure.3.23: Effect of temperature of Cu(II) and Ni(II) by aq-cys-AgNPs at initial concentration of 20 ppm

3.3.6 Adsorption thermodynamics

Thermodynamic parameters such as standard free energy (ΔG), standard enthalpy (ΔH) and standard entropy (ΔS) provide information regarding the inherent energetic changes associated with adsorption. The values of ΔH, ΔS and ΔG are calculated by using

$$\ln K = -\Delta H/RT + \Delta S/R \quad \ldots\ldots(1)$$

$$\Delta G = \Delta H - T\Delta S \quad \ldots\ldots(2)$$

The adsorption thermodynamics of Cu(II) and Ni(II) adsorption by aq-cys-AgNPs shows that the adsorption process is spontaneous in both cases, as confirmed by the negative values of ΔG and the ΔH values. This suggests an exothermic reaction process, a positive value for the ΔS. A list of values of change in heat of enthalpy and entropy are depicted in Table. 3.2 and Figure. 3.24. The significantly negative enthalpy suggests the formation of bonds or strong electrostatic interactions, while the significant and positive entropy values are consistent with the loss of some ligands around the adsorbed species during the adsorption process.

Metals	**ΔH (kJ mol^{-1})**	**ΔS (J mol^{-1} K^{-1})**	**ΔG (kJ mol^{-1})**
Cu(II)	-58.5	170.5	-50.9
Ni(II)	-40.0	137.2	-38.5

Table. 3.2: Adsorption thermodynamics of Cu(II) and Ni(II) adsorption by aq-cys-AgNPs

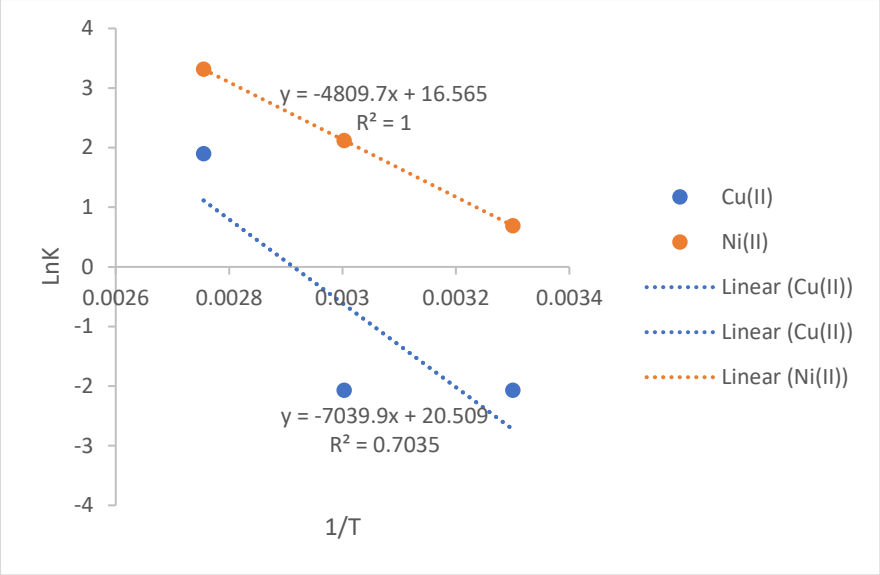

Figure.3.24: Adsorption thermodynamics of Cu(II) and Ni(II) adsorption by aq-cys-AgNPs

3.4 Adsorption kinetics

The pseudo first-order kinetic model is based on solution concentration, and used for the initial adsorption process or the adsorption period close to equilibrium. The pseudo second-order kinetic model is based on the adsorption equilibrium capacity, and it assumes that there is a proportional relationship between the adsorption capacity and the number of active sites on the surface of an adsorbent. The fitting parameters of pseudo first-order and pseudo second-order adsorption kinetic models are listed below. The fitting degrees of the pseudo first order model (R^2) were in the range from 0.1 to 0.2. The R^2 values of the pseudo second-order kinetic model have been discussed in detail in Chapter 1 of the thesis and are both equal to 1, which indicates that the heavy metal ions adsorption process fit the pseudo second-order kinetic model very well. Depicted in Table.3.3 and Figures 3.25 and 3.26.

metals	**Pseudo-first order kinetic**	**Pseudo-second-order kinetic**
Cu(II)	0.1174	1
Ni(II)	0.1939	1

Table. 3.3: Table of R^2 value of Cu(II) and Ni(II) adsorption by aq-cys-AgNPs

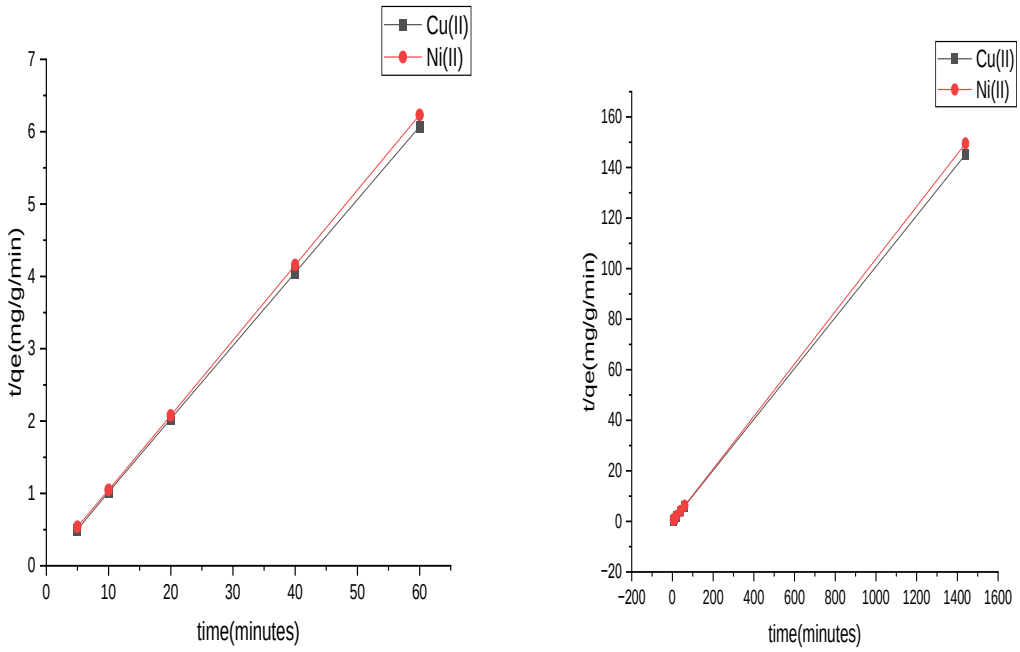

Figure.3.25: Pseudo second -order kinetic of Cu(II) and Ni(II) adsorption by aq-cys-AgNPs at 5-60 minutes and 1440 minutes

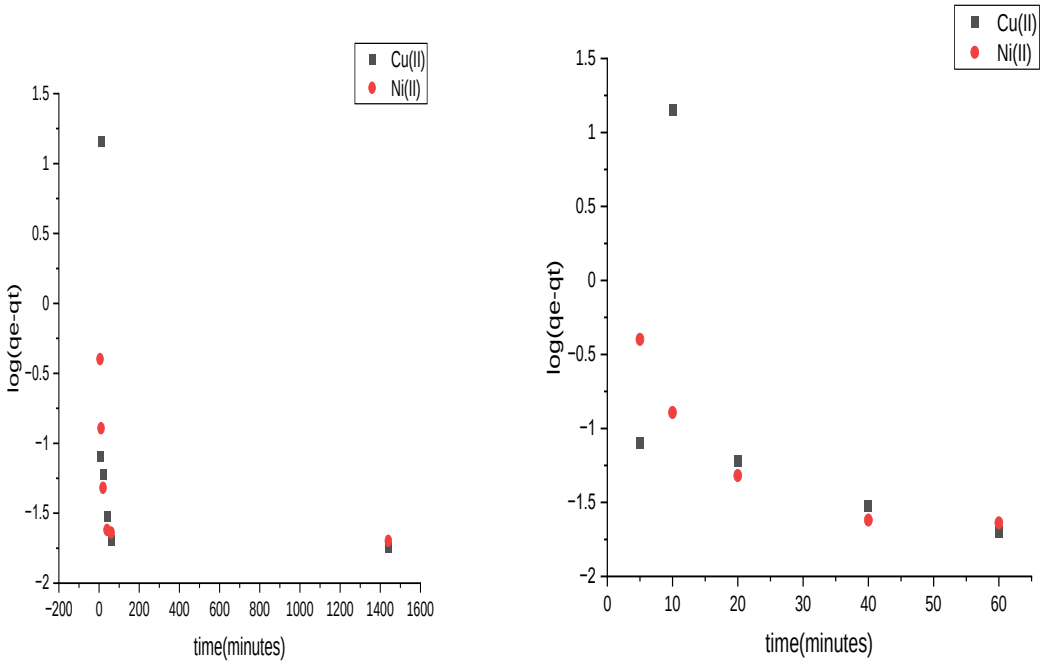

Figure. 3.26: Pseudo first -order kinetics of Cu(II) and Ni(II) adsorption by aq-cys-AgNPs at 5-60 minutes and 1440 minutes

3.5 Adsorption isotherm

Adsorption models are used for the mathematical description of the adsorption equilibrium of the metal ions on to the aq-cys-AgNPs. The results obtained on the adsorption of copper and nickel were analysed by the popularly known models given by Langmuir and Freundlich,[140,141]Henry,[142] Temkin[143] and Dubinin-Raduskevich.[144]As can be seen form Table.3.4, the adsorption of Cu(II) and Ni(II) by aq-cys-AgNPs fits best using the Henry isotherm model as this model is recognised to work very well at low solute concentration. Henry adsorption isotherm assumes that the surface adsorbate is be proportional to the concentration of the solute:[142]It is typically taken as valid for low surface coverages, and the R^2 Henry fitting shows that the adsorption energy is independent of the surface coverage i.e., lack of inhomogeneities on the surface. (Table. 3.4 and Figure. 3.27).

heavy metal	**Henry isotherm R^2**	**Freundlich isotherm R^2**	**Temkin isotherm R^2**	**Langmuir isotherm R^2**	**D-R Isotherm R^2**
Cu(II)	0.9666	0.1476	0.7327	0.2351	0.6508
Ni(II)	0.9586	0.9319	0.5728	0.0001	0.2865

Table. 3.4: Table of adsorption isotherm R^2 value of adsorption of Cu(II) and Ni(II) by aq-cys-AgNPs

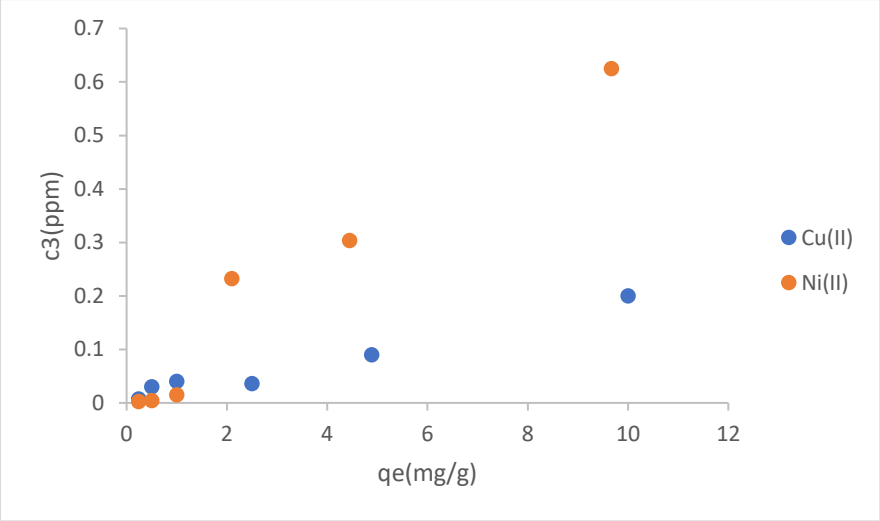

Figure. 3.27: Henry adsorption isotherm model of Cu(II) and Ni(II) adsorption by aq-cys-AgNPs

3.6 Summary of results on Aq-cysAgNPs

Fabrication of cysteine stabilized silver nanomaterial in aqueous solvents was successfully achieved by bottom-up synthesis using sodium borohydride as reductant, and cysteine as the surface coating. Characterization revealed the presence of significant amounts of surface bound cysteine in the fabrication of cysteine stabilized silver NPs in aqueous solution, with the nanoparticles being in the range 30-40 nm, with some smaller (ca. 5nm) NPs also being evident by TEM. The nanoparticles were shown to adsorb copper and nickel ions very effectively from solution, with reductions in SPR intensity as a function of initial metal ion concentration. The strong and rapid adsorption shows that the NPs could potentially be used as a sensor for copper and nickel.

3.7 Discussion on cysteine stabilized AgNP synthesised in ethanol (EtOH-cysAgNPs))

Cysteine stabilized AgNP were synthesized using ethanol and characterized using several analytical techniques, the synthesized EtOH-cysAgNPs were used for the adsorption study of heavy metals and interaction of the EtOH-cysAgNPs in organic solvent with the heavy metals. This is section here to have a comparison with the one in the aqueous solvents.

3.7.1 Synthesis and physical appearance of EtOH-cysAgNPs

The addition of cysteine solution to the silver nitrate did not cause any significant change in the UV/Visible spectra of silver solution (Figure.3.28-3.29) - the dramatic change is observed upon addition of the sodium borohydride to the mixture. (Figure 3.30) This leads to the appearance of the LSPR which tends to be stable after 10 minutes of synthesis. (Figure. 3.30).

Addition of sodium borohydride to the mixture solution caused an initial yellow coloration and subsequently to light black. The resulting solutions were analysed using UV/Visible spectroscopy. (Figure. 3.30), The colloidal solutions were dried at 60 ^{0}C in order to obtained the nanoparticles in solid form.

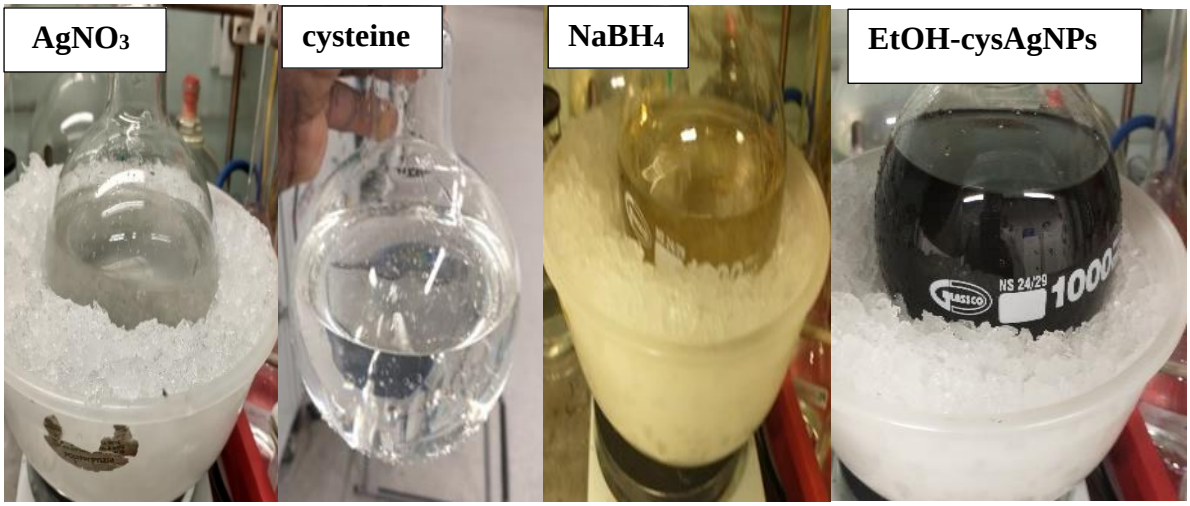

Figure. 3.28: JPEG of synthetic process of EtOH-cysAgNPs

3.7.2 UV/Visible characterization of EtOH-cysAgNPs

The resulting EtOH-cysAgNPs were characterized using Uv/visible spectroscopy. Typically, 5 ml aliquots of the EtOH-cysAgNPs were taken in single vials and the UV-Vis absorption measurements recorded. The localized surface plasmon resonance appears at 410 nm as observed previously. It tends to be broader, compared to the aqueous system. The UV/Visible spectroscopy were recorded at 10 minutes interval for 100 minutes in order to assess the stability of the synthesized silver NPs. UV-Vis and stability data are shown in Figure 3.31. The initially formed NPs are less stable, with LSPR intensity dropping significantly in the first 10 minutes, but then being relatively stable.

Comparing the UV/Visible spectroscopy of the nanoparticles synthesised in water and in ethanol, it is distinctly clear that the medium has influence on the particle size formation of the cys-AgNPs and it could be concluded from the UV/Visible spectra results that the EtOH-cys-AgNPs are dominated by a large particle size compared to the aq-cys-AgNPs.

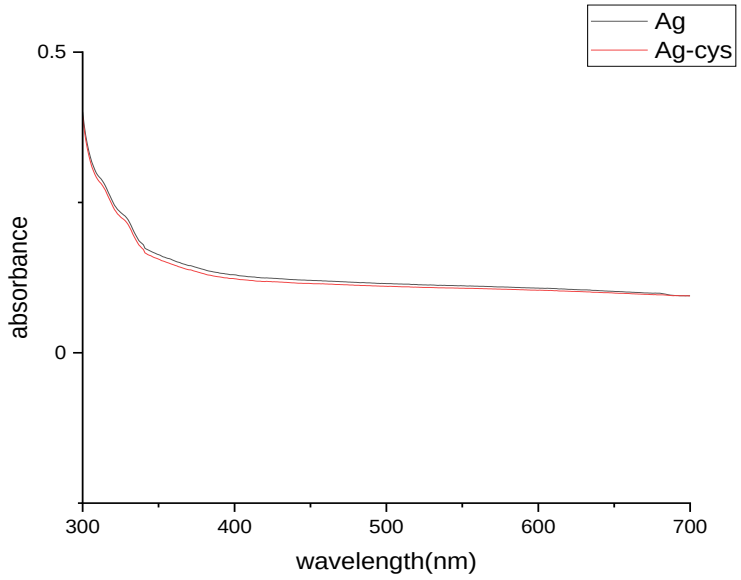

Figure.3.29: UV/Visible spectra of silver nitrate solution, and silver nitrate-cysteine solution

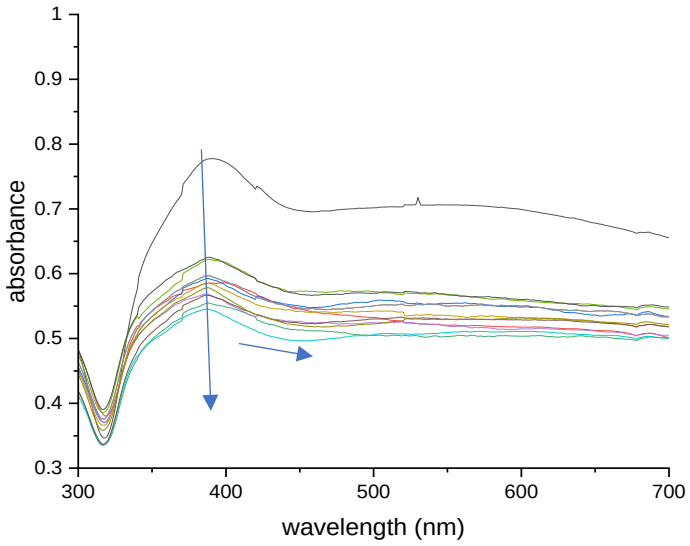

Figure 3.30: UV/Visible spectra of EtOH-cysAgNPs and its absorbance stability measurements with time

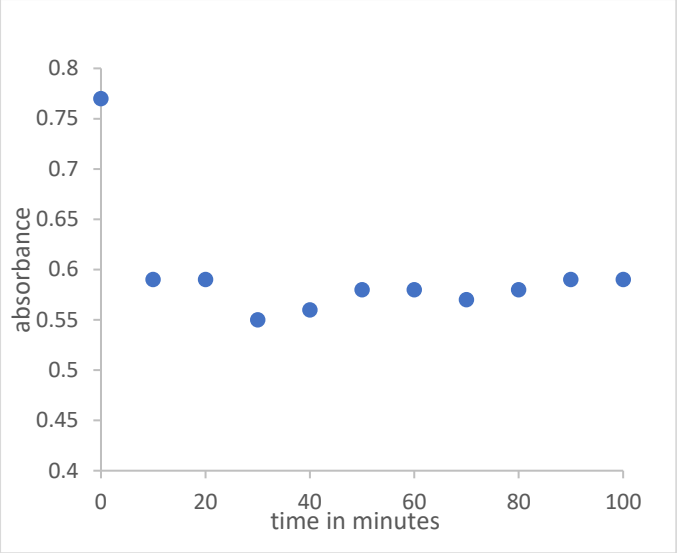

Figure 3.31: A plot of absorbance maximum of EtOH-cysAgNPs against time

3.7.3 Thermal decomposition of EtOH-cysAgNPs

Thermogravimetric analysis was undertaken to evaluate the thermal stability of the EtOH-cysAgNPs. The thermograms (Figure. 3.32) revealed significantly less weight loss over the studied temperature range than the NPs produced in aqueous solvents, indicating significantly lower amounts of organic material present at the surface of the NPs. The weight loss at the transition from room temperature to 120 °C is most likely to the evaporation of physically adsorbed water molecules or ethanol, followed by decarboxylation a loss of organics. These account for 4% weight loss and remnant of 96% remnants.

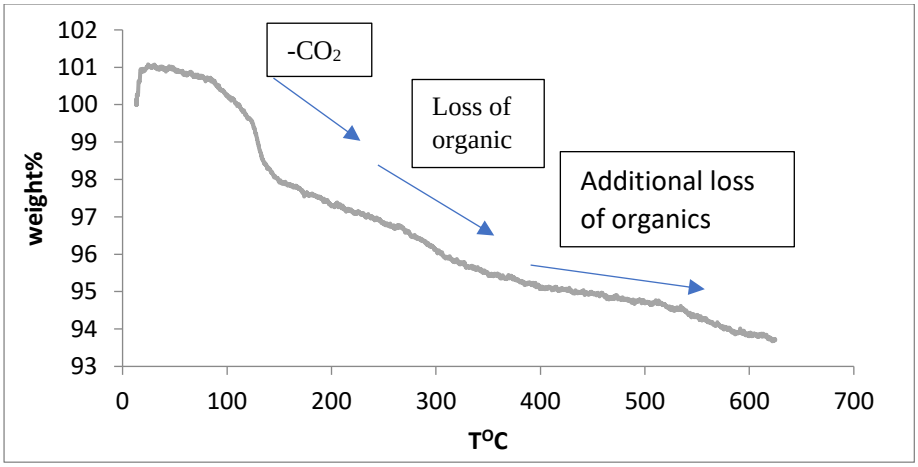

Figure. 3.32: Thermogram of EtOH-cysAgNPs

The weight loss from 200 to 430 °C might be assigned to the organic compounds. Additional weight loss between 500 and 600 °C may be due to the gradual decomposition of organic

fragments. It is significant to consider that the higher residual organic weights of the synthesized nanoparticles were attributable to the functionalized AgNP because the metal nanoparticles are not anticipated to volatilise at the subjected temperatures. The thermal analysis confirmed the present of ca. six percent organic compound present in the nanoparticles (significantly lower than the ca. 63% present with the aqueous synthesis) and this is also consistent with the very weak Fourier transform infrared spectroscopy spectra of the synthesized AgNPs (Section 3.7.5).

The thermal analysis of EtOH-cysAgNPs revealed that the synthesized nanoparticles contain little organic materials and this was also confirmed by the elemental analysis. The thermogram suggests ca. 6% of the cysteine stabilized AgNP in organic solvents and 94% inorganic presumably silver atoms This is in contrast with the aq-cys-AgNP with 63% organic material at the surface.

3.7.4 Microanalysis of EtOH-cysAgNPs

The microanalysis results (Table. 3.5) revealed the elemental composition of the synthesized EtOH-cysAgNPs contains 0.3% S and 0.14% N, suggesting that there is a very small amount of cysteine on the surface – the ratio of N:S is correct, and would suggest only 1 – 1.5% cysteine. The %C is much higher, suggesting some other organic species (probably EtOH) is present. Given this, the remainder (Ag plus O associated with the organic component) would suggest around 85% Ag.

Thus, microanalysis of both cysteine stabilized nanoparticles in aqueous and organic solvents confirms the presence of gar less cysteine in the EtOH-synthesised nanoparticles compared to the aqueous product. This is consistent with the FTIR spectra and TGA as well as the different signal strepgths for the pXRD patterns of both nanoparticles.

Sample	% C	% H	% N	% S	% Remainder
EtOH-cysAgNPs	8.01	2.01	0.18	0.3	89.5

Table 3.5: Microanalysis of EtOH-cysAgNPs

3.7.5 Fourier Transform Infrared Spectroscopy of EtOH-cysAgNPs

The infrared spectroscopy of the cysteine and EtOH-cysAgNPs shows the incorporation of trace amounts of organic molecules in the spectra of the EtOH-cysAgNPs. It also shows that

the -S-H- band present in the cysteine spectra has disappeared in the spectra of the cysteine stabilized AgNP and these suggest possible coordination at the thiol sites and the formation of Ag-S bonds, although the low cysteine incorporation and the relatively weak S-H band makes this less definitive as with the aqueous system. Characteristics spectra of the cysteine can be found in the finger print region of the spectra of cysteine stabilized AgNP suggesting the presence of cysteine in the synthesized AgNP but are weak. The short narrow N-H band at 3149 cm $^{-1}$ in the spectra of cysteine was is no longer visible as a discrete band and now forms part of the larger OH / NH band, consistent with the TGA suggesting significant water / EtOH content in the spectra of EtOH-cysAgNPs. The broad C-H- band at 2949 cm^{-1} in the spectra of cysteine has moved to 2972 cm^{-1} and appears to be relatively sharp in the spectra of EtOH-cysAgNPs. It is likely that this band also indicates the presence of EtOH. (Figure. 3.33)

Consequently, the spectra of aq-cysAgNPs revealed the presence of higher number of organic molecules which might be as a result of the higher concentration of synthetic process while the spectra of EtOH-cysAgNPs suggest the incorporation of trace amounts of organic molecules in the spectra and which is as a result of the lower amount of cysteine used in the fabrication process.

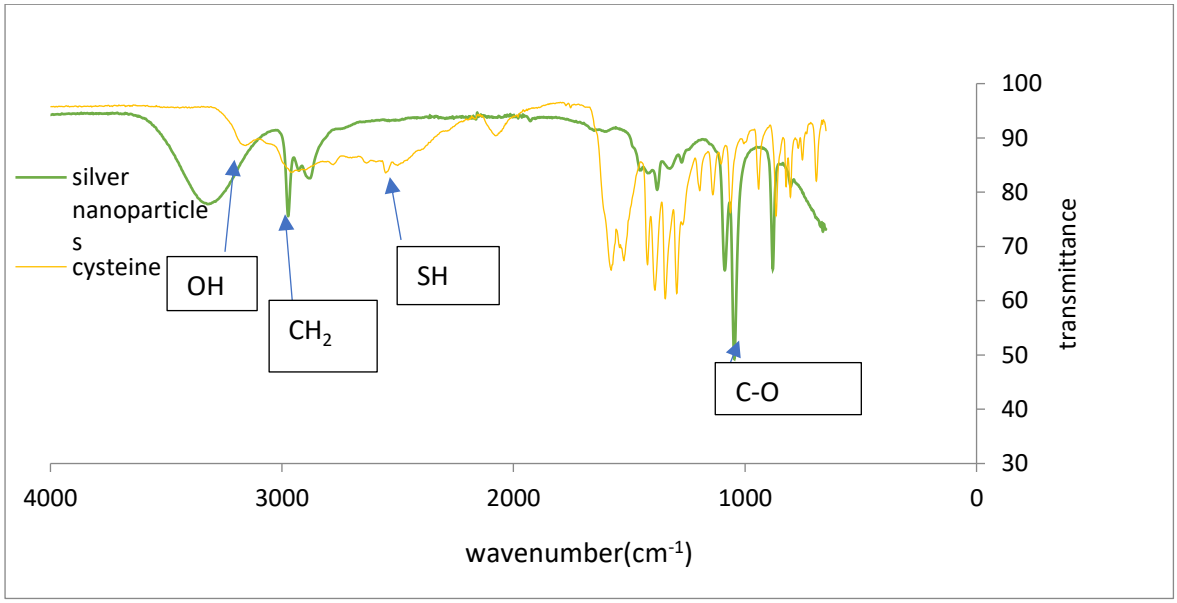

Figure. 3.33: FT-IR of cysteine and EtOH-cysAgNPs

3.7.6 Powder X-ray Diffraction of EtOH-cysAgNPs

The powder x-ray diffraction spectrum analysis of the AgNP showed four Bragg reflections at 2 θ =38.24, 44.46, 64.85, and 77.98 (Figure 3.34). These reflections correspond to the facets

of the face-centred cubic crystal of AgNP and it in good agreement with the results published by (Prakash et al. 2013) and (Jyoti et al.2016)[145,146]. The particle size is estimated by the Debye-Scherer equation and estimated to be 4 nm. The diffractogram demonstrate absent of additional peaks between 20-37^0 due to the few amounts of cysteine used during the fabrications of the EtOH-cysAgNPs.

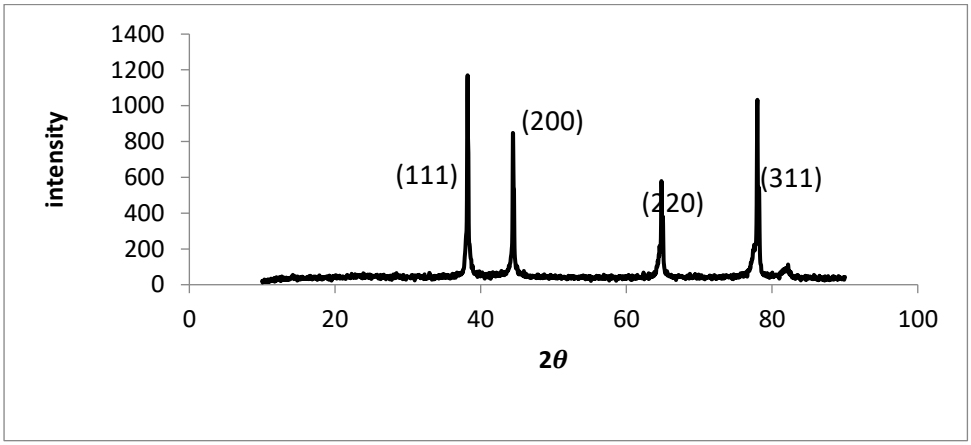

Figure.3.34: PXRD of ETOH-cysAgNPs

3.7.7 Scanning electron microscopy of EtOH-cysAgNPs

Scanning electron microscopy was done to study physical appearance of the synthesized AgNP and gives structural morphology of the synthesized nanoparticles, and the study revealed that the samples contained regular agglomerates of particles around 150-200 nm in size. (Figure 3.35)

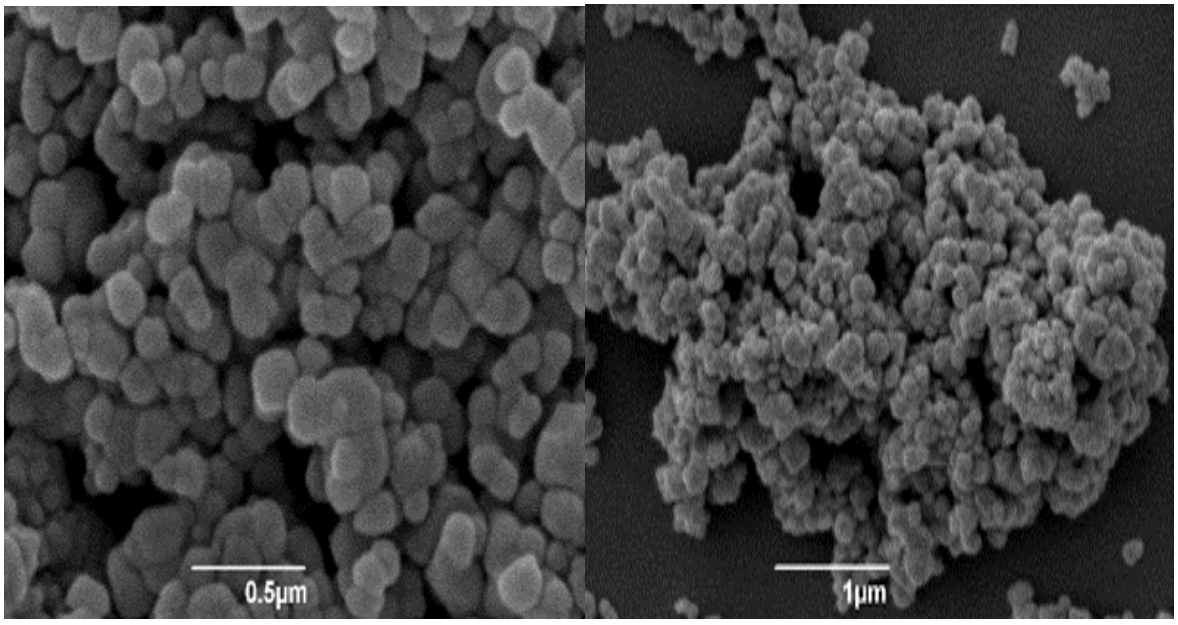

Figure.3.35: SEM of EtOH-cysAgNPs at 0.5μm and 1μm

3.7.8 Transmission electron microscopy of EtOH-cysAgNPs

The TEM images showed features which were spherical and of relatively uniform size ranging from 4-10 nm, consistent with the size calculated above using the Debye-Scherer equation (Figure. 3.36). In the literature, transmission electron microscope of cysteine capped silver nanoparticle suggested to have diameter ranging from 5 nm-40 nm and spherical geometry. Khan et al. reported that those were prepared by chemical reduction method using l-cysteine as a capping agent.[147] (The structure of the cysteine stabilized AgNP appears to be mono-distributed which might be as a result of the lower amounts of organic molecules at the surface of the nanoparticles therefore the cysteine stabilized AgNP are majorly dominated by the silver itself, and less by organic ornamentation on the surface).

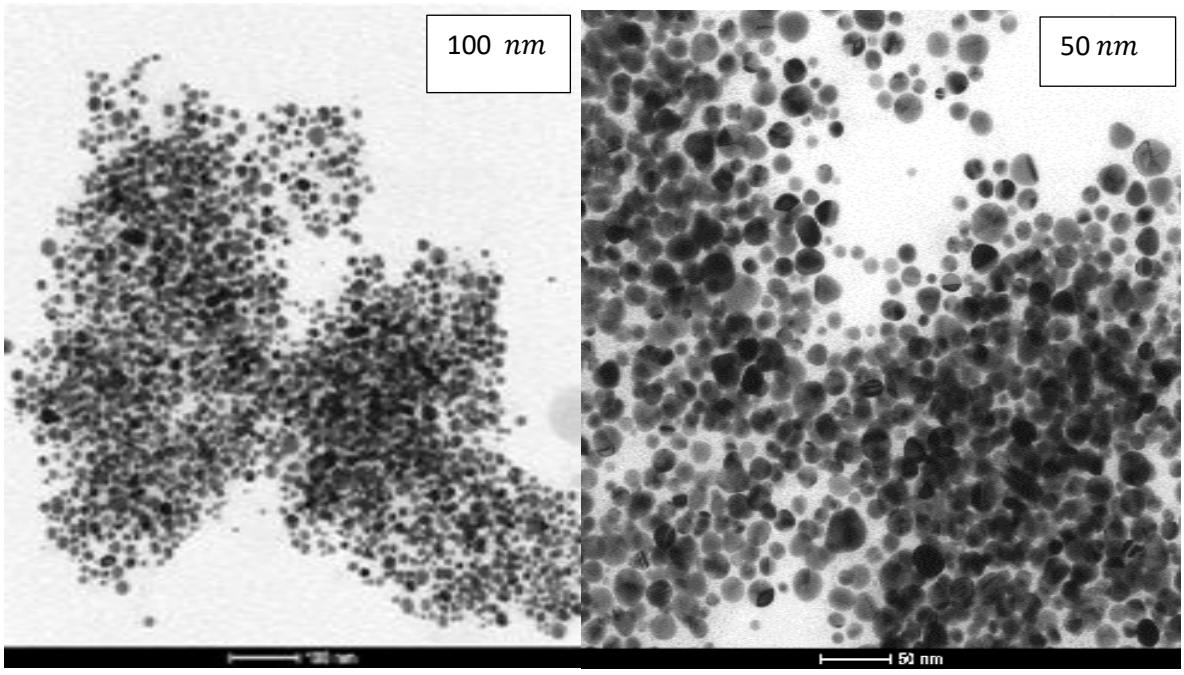

Figure.3.36: SEM of EtOH-cysAgNPs at 100μm and 50μm

Thus, in comparison to the aqueous route, the ethanol route provides AgNPs with much lower organic surface ornamentation, but with a relatively uniform size and morphology, while the aqueous route has a much higher organic surface ornamentation predominantly much larger nanoparticle

3.8 Detection of heavy metals using EtOH-cysAgNPs

The detection of Cd(II), Cu(II), Ni(II), NiEDTA, Mg(II), Na(I), (Na+Pb),(Mg+Pb) at 2 ppm of each metal ion by cys-AgNPs (in organic solvents) was investigated. EDTA was also included as a control, in order to probe the variation in behaviour between a metal ion and its EDTA

complex. Similarly, Pb(II) was tested alone and in the presence of Mg and Na ions to simulate fresh and brackish water samples.

There exists a change in LSPR for all the metal ions investigated, a blue shift in the LSPR for Cu(II), NiEDTA, Mg, Na, EDTA and Cd(II), the LSPR shifting from 414 nm to 386 nm, 384 nm ,386 nm, 385 nm, 392 nm and 384 nm respectively. The LSPR underwent a red shift for Pb(II), Ni(II), (Na+Pb) and (Mg+Pb) to 484 nm, 428 nm, 471 nm and 505 nm respectively at 2ppm .

System	**LSPR (nm)**	**Blue shift**	**Red shift**
Alone	414	n/a	
+ Cd(II)	384	-30	
+ Cu(II)	386	-28	
+ Ni(II)	428		+14
Ni(II)EDTA	384	-30	
+Mg(II)	386	-28	
+Na(I)	385	-29	
+ Na/Pb(II)	471		+57
+ Mg/Pb(II)	505		+91
+EDTA	392	-22	
Pb(II)	484		+70

Table 3.6 summary of changes in LSPR position on addition of metal ions

The addition of Pb(II) to the solution of magnesium and sodium drags the LSPR towards a red shift suggesting the dominant influence of lead in two-metal systems containing Na(I) and Mg(II) ions by EtOH-cysAgNPs and also the presence of Na(I) and Mg(II) ions would not be a major issue for looking for lead (Figure. 3.37). Similar trends were noted at 4 ppm and 6 ppm concentrations of the various salts (Figure.3.38-3.39). Overall, however, trends are hard to see, with most M(II) ions giving very similar blue shifts, while Ni(II) and Pb(II) give significant red shifts. (Figures 3.37 – 3.39)

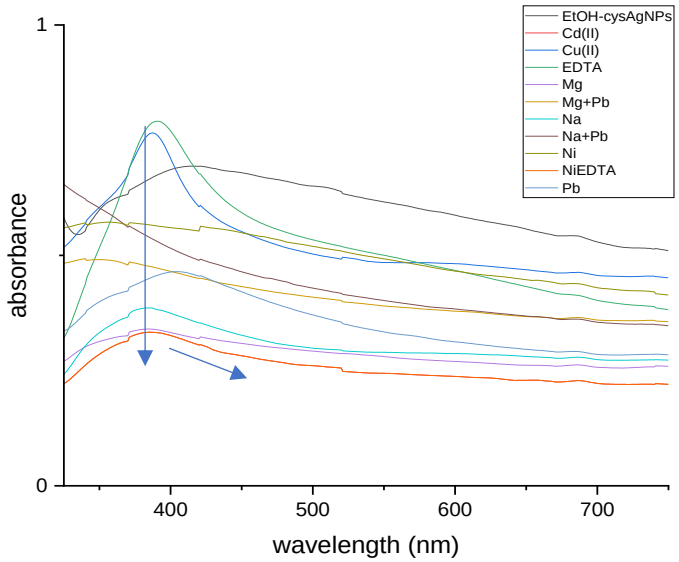

Figure. 3.37: UV/Visible spectra of heavy metals at 2 ppm and EtOH-cys-AgNPs

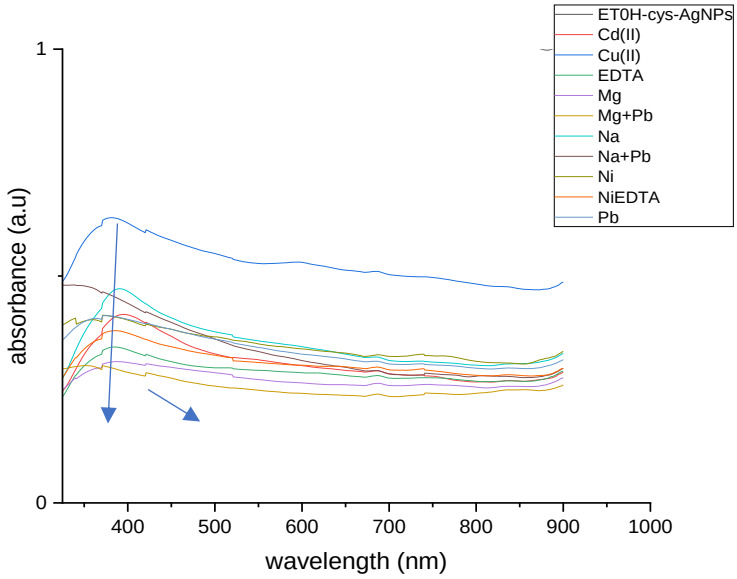

Figure. 3.38: UV/Visible spectra of heavy metals at 4 ppm and EtOH-cys-AgNPs

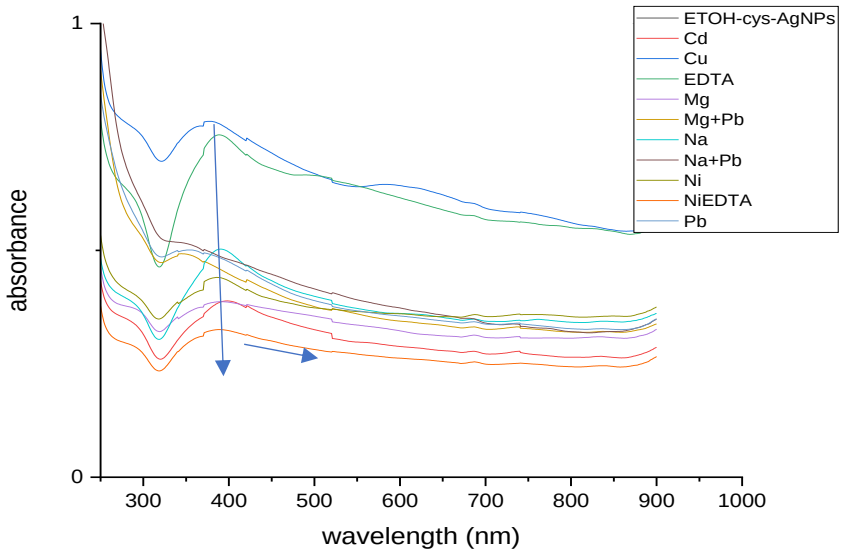

Figure. 3.39: UV/Visible spectra of heavy metals at 6 ppm and EtOH-cys-AgNPs

The detection experiments of Cu(II) and Ni(II) by EtOH-cysAgNPs was extended to 20 ppm while all other metal ions stopped at 6 ppm of detection, after 5 minutes a dark-grey colour appears for nickel and the UV/Visible spectroscopy showed there is a red shift and appearance of new surface plasmon resonance at 526 nm for nickel (Figure 3.40). For copper the intensity of the colour for copper increases as the concentration increases. Surface plasmon resonance shifted from 380 nm to 572 nm (Figure. 3.41). The colour changes from light black to red after 5 minutes of reaction.

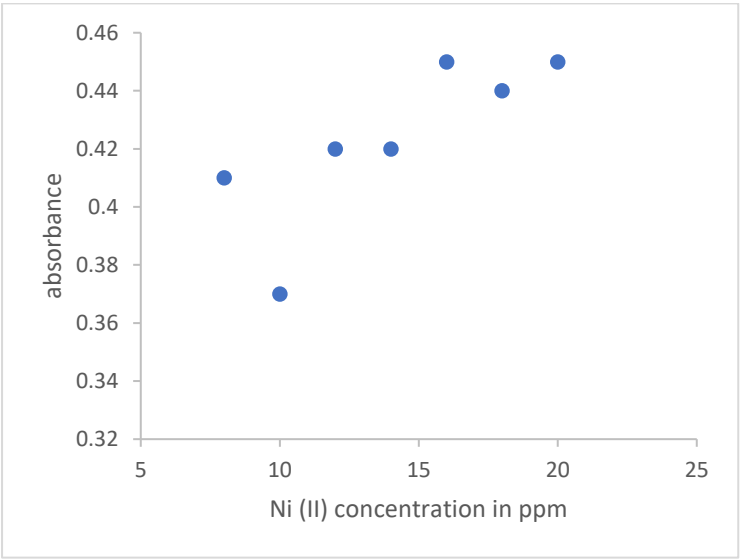

Figure. 3.40: UV/Visible peak height of nickel (8-20 ppm) of EtOH-cysAgNPs with Ni(II) at 393 nm

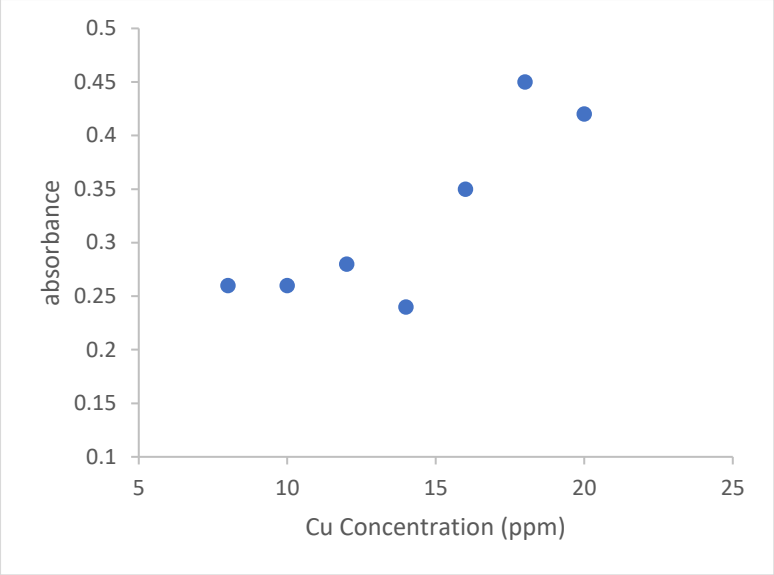

Figure. 3.41: A plot of peak height of copper (8-20 ppm) of EtOH-cysAgNPs with copper at 572 nm

3.8.1 Adsorption of Cu(II), Cd(II), Pb(II) and Ni(II) by EtOH-cysAgNPs

Effect of initial concentration

The result of adsorption of copper, cadmium, lead and nickel shows the same trend in their adsorption pattern and similar quantities of each metal ion are adsorbed by EtOH-cysAgNPs, increasing approximately linearly over the range studied (Fig.3.42).

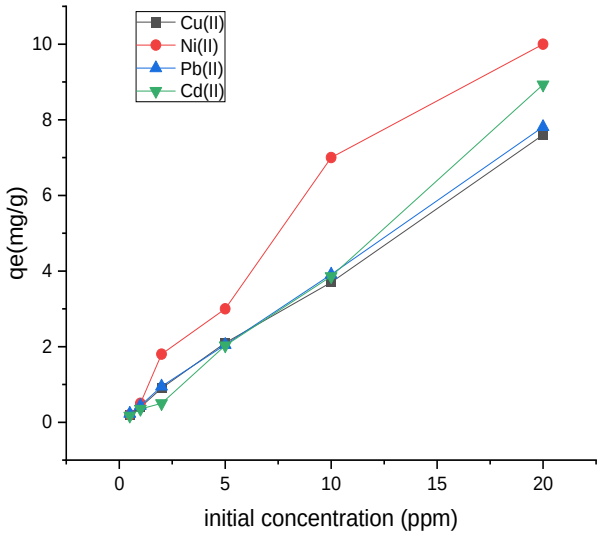

Figure. 3.42: Effect of initial concentration of heavy metals on equilibrium adsorption by EtOH-cysAgNPs

3.8.2 Effect of contact time at optimal initial concentration of metal ions

The adsorption of copper and nickel, cadmium and copper by EtOH-cysAgNPs is fast at the beginning and reaches equilibrium at 40 minutes for all the metal ions and tends to be stable subsequently from 60 minutes till 24 hours. After 40 minutes, the value of qe became relatively constant (the second stage), indicating that equilibrium was reached. The phenomena of this two-stage adsorption might be attributed to the available active sites on the EtOH-cysAgNPs. (Figure. 3.43). Except for lead whose adsorption is quite slow initial and then rapid as the adsorption is not quite finished after 40 minutes and then remain stable till 24 Hrs or It could also be that there is a rapid adsorption, followed by a slower process that gradually frees up more sites.

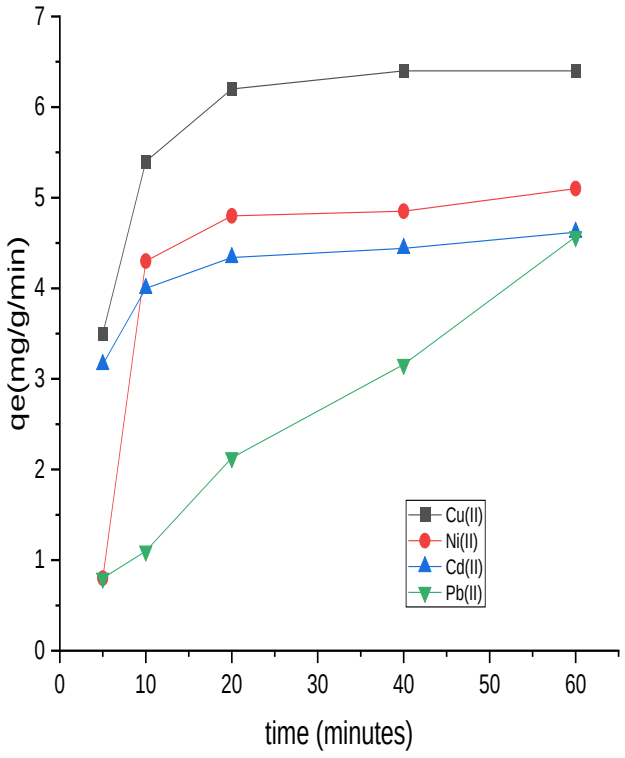

Figure. 3.43: Effect of contact times of heavy metals at 20 ppm by EtOH-cysAgNPs up to 60 minutes

3.8.3 Effect of dose at optimal initial concentration of metal ions

As adsorbent dosage increases, Cd(II), Pb(II), Ni(II) and Cu(II) ion uptake per unit mass decreases as shown in the Figure. 3.44 which simply means that 0.01g of the EtOH-cysAgNPs is enough to adsorb all metal ions over the concentration of the metal ions tested.

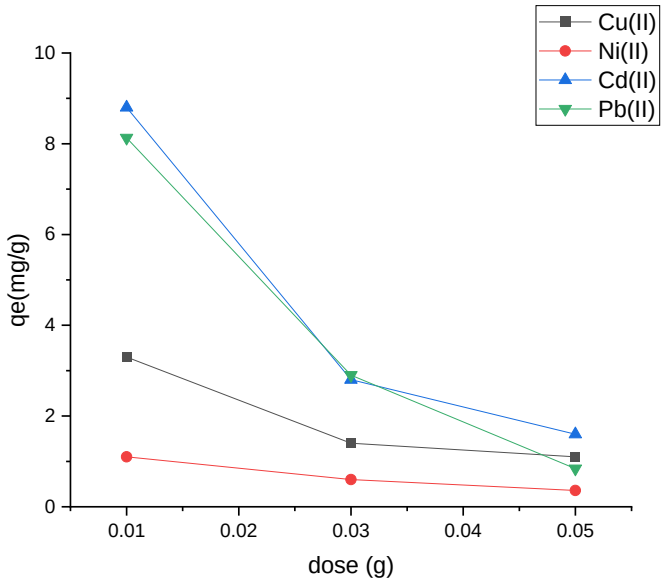

Figure. 3.44: Effect of dose of heavy metals at 20 ppm by EtOH-cysAgNPs

3.8.4 Effect of pH at optimal initial metal concentration of metal ions

The qe value for each metal ion increases with the pH. As the pH was varied from 3 (with HCl) to 12 (with NaOH), adsorption efficiency increases as shown in Figure 3.45 for all species except Cd, which showed the opposite trend.

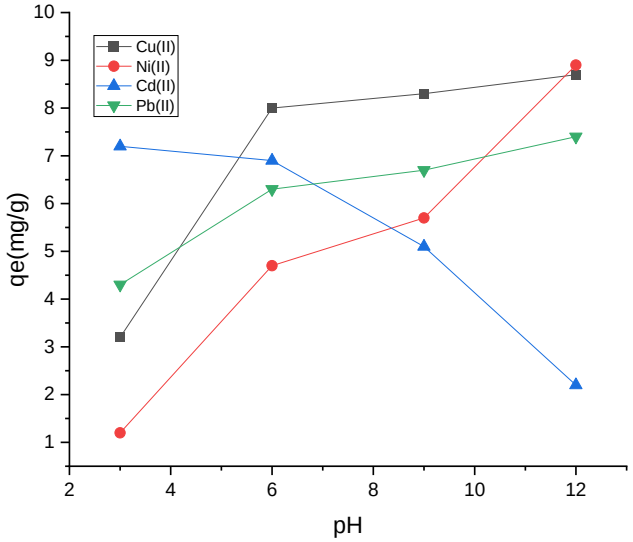

Figure. 3.45: Effect of pH on adsorption of heavy metals at 20ppm by EtOH-cys-AgNPs

Optimum pH was at 12 for all other metal ions and all other experiments were done at this pH. As pH increases the surface of EtOH-cys-AgNPs become more negatively charged. This causes increased attraction between the positive charge of the metal cations and EtOH-cys-AgNPs. Hence the removal efficiency increases with increase in pH. Except for Cd(II) which exists predominantly as a negative $Cd(OH)_3^-$ ion in solution, thereby being repelled from the surface of the EtOH-cys-AgNPs thereby leading to a decrease in the qe adsorbed. This result is consistent with results reported by Ozer et al. for the adsorption of cadmium on sugar beet pulp[148]where they found the optimum pH was 6.3. Bhattachary and Venkobachar also found the optimum pH was 6.6 for removal of cadmium on Gridih coal[150]. Mathialagan and Viraraghava[149] observed that the optimum pH for cadmium adsorption by perlite was 12. The decrease in the adsorption capacity in the range of pH from 6 to 11 might be attributed to the formation of $Cd(OH)_3^-$ ions taking place as a result of dissolution of $Cd(OH)_2$.

The effect of pH on the other three ions are qualitatively similar to each other. While all the species will tend to move from positive (+2) charge to +1 and 0 as hydroxide competes as a ligand, this is less pronounced than with Cd, which forms -1 charged species at unusually low pH.

3.8.5 Effect of temperature

The qe value increases for all the metal ions as the temperature is increased from 303-363 K. The maximum qe values of Cu(II), Cd(II), Pb(II) and Ni(II) ions adsorbed by EtOH-cys-AgNPs are 8.4 mg/g, 9.3 mg/g, 9.86 mg/g and 12.1 mg/g respectively (Figure. 3.46)

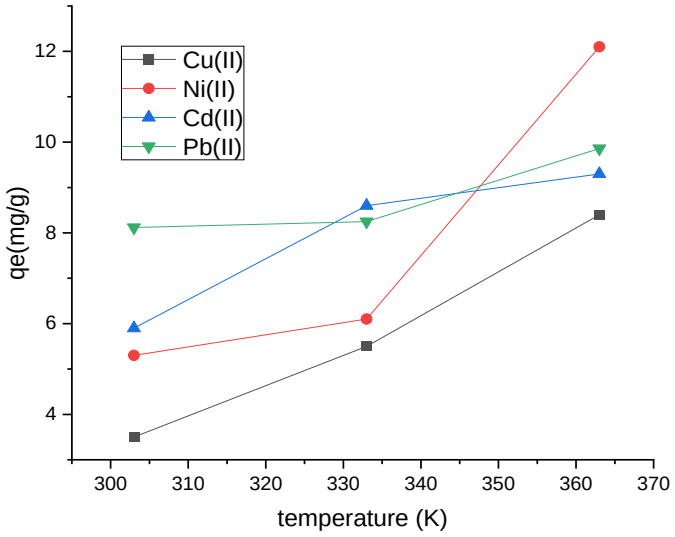

Figure. 3.46: Effect of temperature on the adsorption of heavy metals at 20 ppm and optimal pH of each metal by EtOH-cys-AgNPs

3.8.6 Adsorption thermodynamics

The thermodynamics of adsorption were measured at temperature 303-363 K and suggest a spontaneous adsorption process for Cd(II), Cu(II), Pb(II) except for Ni(II) ions which progress via a non-spontaneous process with a positive value for entropy. (Table.3.7and figure.3.47). these are generally similar to those found for the aq-cys-AgNPs system might suggests a similar mechanism of adsorption, given the vastly different amounts of cysteine.

metals	**ΔH (kJ/mol)**	**ΔS(J mol^{-1} K^{-1})**	**ΔG(kJ/mol)**	**slope**	**intercept**
Cd(II)	-56.79	219.5	-122.17	-6831	26.399
Cu(II)	-51.03	197.9	-109.95	-6139	23.803
Pb(II)	-31.31	151.2	-76.36	-3767	18.187
Ni(II)	10.28	29.6	1.45	1228.8	3.5672

Table. 3.7: adsorption thermodynamic parameters for Cd(II), Cu(II), Pb(II) and Ni(II) adsorption by EtOH-cys-AgNPs

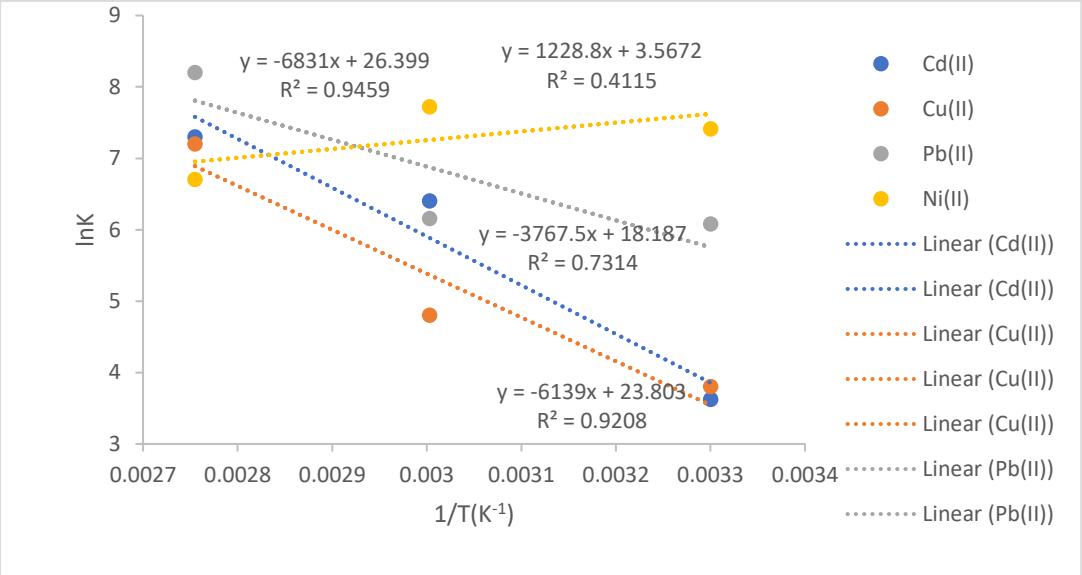

Figure. 3.47: Adsorption thermodynamics of Cd(II) and Cu(II) adsorption by EtOH-cys-AgNPs

3.9 Adsorption kinetics

The adsorption kinetics were carried out at 298 K and pH 12 on 20 ppm solutions. As was seen for the aq-cys-AgNPs, the data fit better to pseudo second-order kinetics than pseudo -first order kinetic model for all ions studied. This is consistent with the process of adsorption being a chemisorption. Table of R^2 values for adsorption of Cd(II) and Cu(II) ions by EtOH-cys-AgNPs are highlighted in Table. 3.8, and graphs in Figure 3.38. Pb(II) is the least well-fitting to pseudo second order, and was significantly slower in uptake than the other three ions, as was evident in Figure 3.48

metals	**Pseudo-first-order kinetics**	**Pseudo-second-order kinetics**
Cu(II)	0.203	1
Cd(II)	0.1174	0.9996

Table. 3.8: Adsorption kinetic R^2 value of adsorption of Cd(II), Cu(II), Pb(II) and Ni(II) at 20 ppm by EtOH-cys-AgNPs

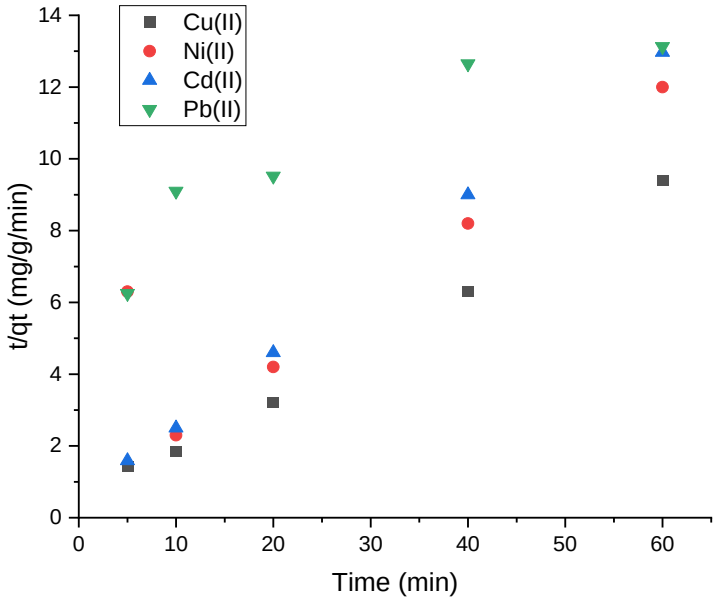

Figure. 3.48: Pseudo second order kinetic on the adsorption of cadmium, nickel, lead by EtOH-cys-AgNPs at 60 minutes

3.10 Adsorption isotherm model of adsorption of Cd(II), Ni(II), Cu(II) and Pb(II) by EtOH-cys-AgNPs

The adsorption data was fitted to several isotherm models and, - the results of R^2 values are listed in Table 3.9 The results suggest a better R^2 fitting with Henry adsorption isotherm for all ions investigated, although Cd(II) is slightly less good fit that the other three. As before, the good performance of the Henry isotherm might simply be as a result of the low concentrations ranges of the heavy metal ions being adsorbed on the EtOH-cys-AgNPs as the linearity of the Henry isotherm can be used to describe the initial part of many practical isotherms which has been typically taken as valid for low surface coverages, with the adsorption energy being independent of the coverage/lack of inhomogeneities on the surface in this range. Other Isotherms such as Langmuir, Freundlich, Temkin and Dubinin-Radushkevich isotherm have been used to describe the adsorption process and prove not to be suitable as the R^2 values fall well below the expected ranges. (Table. 3.9 and Figure. 3.49-3.)

heavy metal	Henry isotherm R^2	Freundlich isotherm R^2	Temkin isotherm R^2	Langmuir isotherm R^2	D-R isotherm R^2
Cu(II)	0.9734	0.8805	0.7534	0.1664	0.4554
Ni(II)	0.9804	0.1267	0.6557	0.4047	0.0439
Pb(II)	0.9932	0.786	0.7866	0.663	0.65
Cd(II)	0.9342	0.7632	0.5167	0.3571	0.5331

Tables. 3.9: R^2 values of Adsorption isotherm model for Cu(II), Cd(II), Pb(II) and N(II) ions adsorption by EtOH-cys-AgNPs

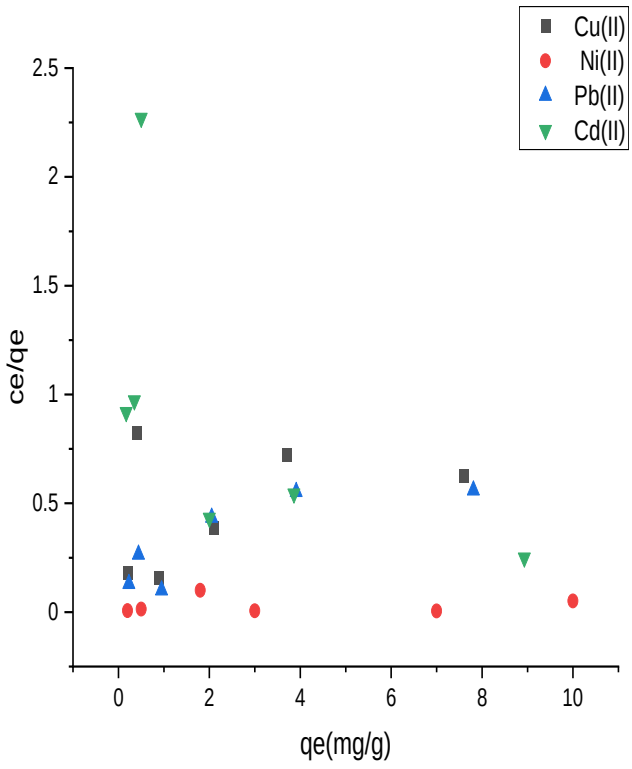

Figure 3.49: Langmuir isotherm plot of Cd(II), Pb(II), Ni(II) and Cu(II) adsorption by EtOH-cys-AgNPs in organic solvents

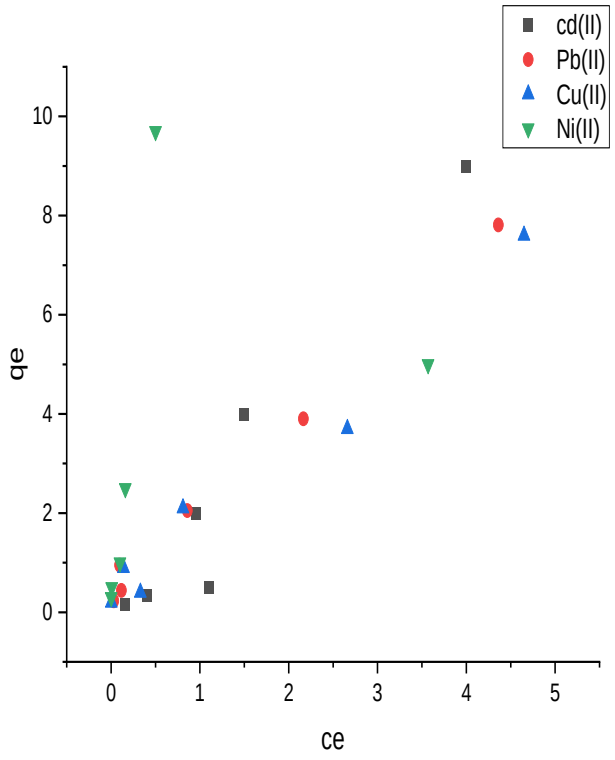

Figure 3.50: Henry isotherm plot of Cd(II), Pb(II), Ni(II) and Cu(II) adsorption by EtOH-cys-AgNPs in organic solvents

3.11 The influence of chelating agent on the adsorption of Ni $(NO_3)_2$, $NiCl_2$ and $NiSO_4$ and their respective EDTA chelates

EDTA often remains in the washed soil and impacts the effectiveness and mobility of toxic metals. Therefore, attention should be paid to the residual EDTA in soil after remediation, especially their forms and lability. Many previous studies have studied EDTA adsorption behaviour on the water-mineral interface in the EDTA solution system, or single metal-EDTA chelate system, where [metal]: [EDTA] = 1:1. However, the stoichiometrically excessive chelating agent is generally used in soil washing practices, where the free EDTA and metal-EDTA chelates coexist. In this study, adsorption of $Ni(NO_3)_2$, $NiCl_2$ and $NiSO_4$ and their respective EDTA chelates on EtOH-cys-AgNPs were studied. The formation of the chelate were carried out by titration of nickel salts (nickel nitrate. trihydrate, nickel sulfate hexahydrate and nickel chloride against 1M of EDTA solution, 12.6 ml of EDTA were used for complete complexation of nickel nitrate with EDTA, 12.8 ml were used for complete complexation of

nickel sulphate hexahydrate and 13.1 ml of EDTA were used for the complete chelation of nickel chloride with EDTA.

Suitable plot of absorbance versus initial concentration was carried out in order to know the suitability of the metal salt for the adsorption results, a R^2 values ranging from 0.92-0.97 were obtained for each metal.

3.11.1 Effect of initial concentration on adsorption of Ni {nitrate, chloride, sulfate} and Ni {nitrate, chloride, sulfate}-EDTA by EtOH-cys-AgNPs

The adsorption of Ni salts by EtOH-cys-AgNPs increases as the initial concentration increases. The maximum adsorption capacities of Ni{NO_3^-, SO_4^{2-}, Cl_2^-} were 9.6 mg/g, 10 mg/g, and 9.5 mg/g respectively, (Figure. 3.40**)** similar behaviour were seen with the Ni-EDTA systems over the same range of concentrations (0.5- 20 ppm) and Ni{NO_3^-, SO_4^{2-}, Cl_2^-}-EDTA EtOH-cys-AgNPs were 17.5 mg/g, 18.4 mg/g and 17.5 mg/g respectively, i.e. approximately double that of the uncomplexed ions. Thus, the chelation of the metal with EDTA adsorbed increased quantity of metal ion adsorbed for all the three salts. (Figure. 3.51).

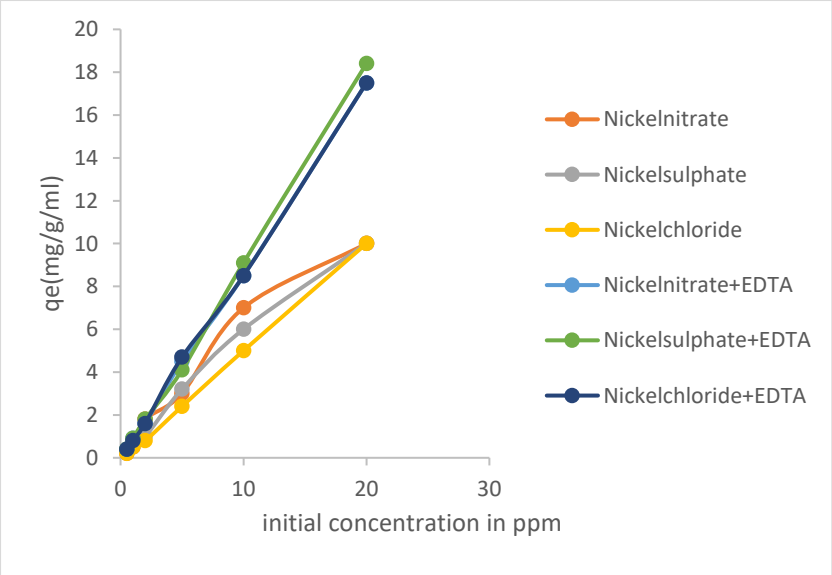

Figure. 3.51:Effect of initial concentration on adsorption of Ni {nitrate, chloride, sulfate} and Ni {nitrate, chloride, sulfate}-EDTA by EtOH-cys-AgNPs

3.11.2 Effect of contact time

Adsorption of Ni salts by EtOH-cys-AgNPs were practically complete after 40 minutes with qe values of 2.9 mg/g, 5.9 mg/g and 5.6 mg/g for sulphate, chloride and nitrate respectively

and 19.2 mg/g, 19.4 mg/g and 19.2 mg/g for the corresponding EDTA complexes. The adsorption of Ni {NO_3, Cl_2, SO_4}-EDTA appeared to reach equilibrium slightly faster than the uncomplexed system. (Figure. 3.52). The EDTA systems continue to increase beyond 60 minutes compared with the system without the EDTA systems.

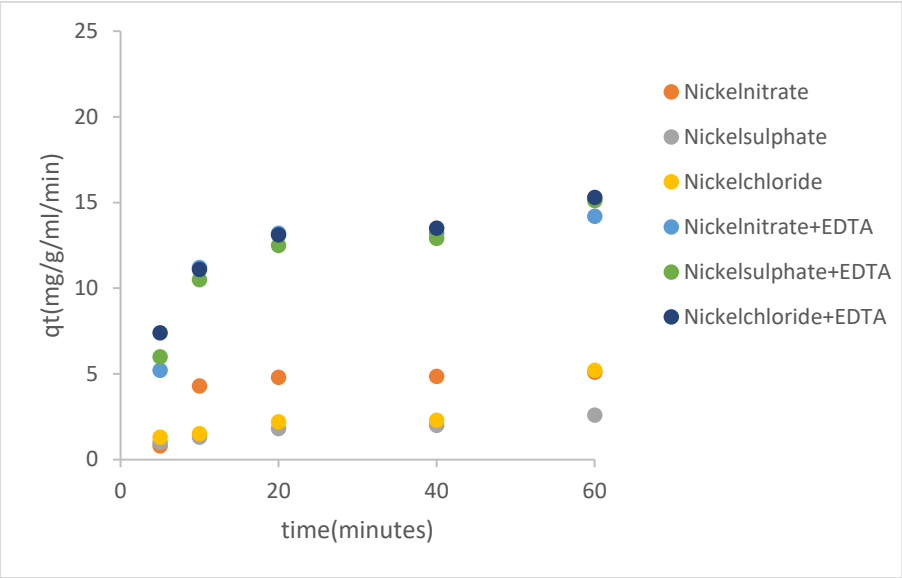

Figure. 3.52: Effect of contact time on adsorption of Ni {NO_3, Cl_2, SO_4} and Ni {NO_3, Cl_2, SO_4}-EDTA by EtOH-cys-AgNPs at 5-60 minutes

3.11.3 Effect of Dose

For the Ni{NO_3, Cl_2, SO_4} and Ni{NO_3, Cl_2, SO_4}-EDTA adsorption by EtOH-cys-AgNPs the quantity of metals decreases with increasing dose of EtOH-cys-AgNPs (Figure 3.53). A similar observation was made for the adsorption of Ni{NO_3, Cl_2, SO_4}-EDTA adsorption by EtOH-cys-AgNPs at 24 hours whose time of equilibrium extends to 1440 minutes.

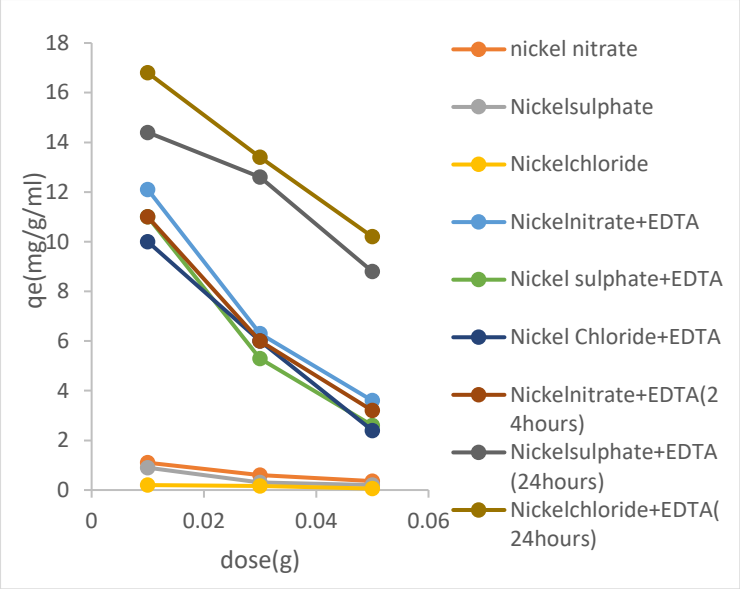

Figure. 3.53: Effect of dose on adsorption of Ni{NO_3, Cl_2, SO_4} and Ni{NO_3, Cl_2, SO_4}-EDTA by EtOH-cys-AgNPs

3.11.4 Effect of pH

The quantity of Ni{NO_3,Cl_2,SO_4} adsorbed by by EtOH-cys-AgNPs increases with the pH more so for the sulfate and nitrate than chloride, and this increase is consistent with an electrostatic interaction of metal cation and the EtOH-cys-AgNPs (Figure 3.54). The adsorption of the corresponding Ni-EDTA complexes by EtOH-cys-AgNPs is less pH dependent, with significant adsorption at relatively low pH values, in contrast to the uncomplexed cations. This much more constant adsorption behaviour may be attributed to the anionic behaviour of $NiEDTA^{2-}$ over a wide range of pH and thus getting higher adsorption at a low pH due to NPs carrying some positive charge at these pH values.

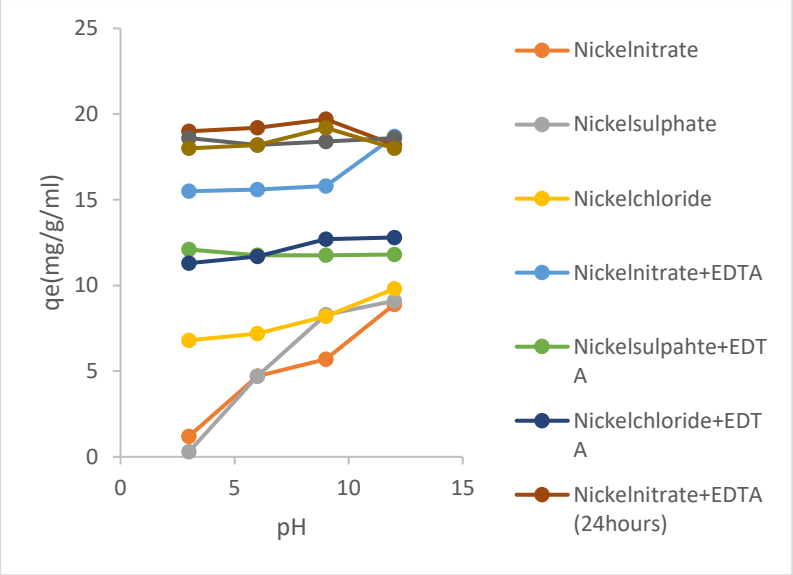

Figure. 3.54: Effect of pH on adsorption of Ni{NO_3, Cl_2, SO_4} and Ni{NO_3, Cl_2,SO_4}-EDTA by EtOH-cys-AgNPs

3.11.5 Effect of temperature

Increasing the temperature has been found to enhance the adsorption of a range of metals onto the AgNPs, this behaviour was also seen here, although the temperature dependence was much lower for the EDTA complexes. (Figure. 3.55)

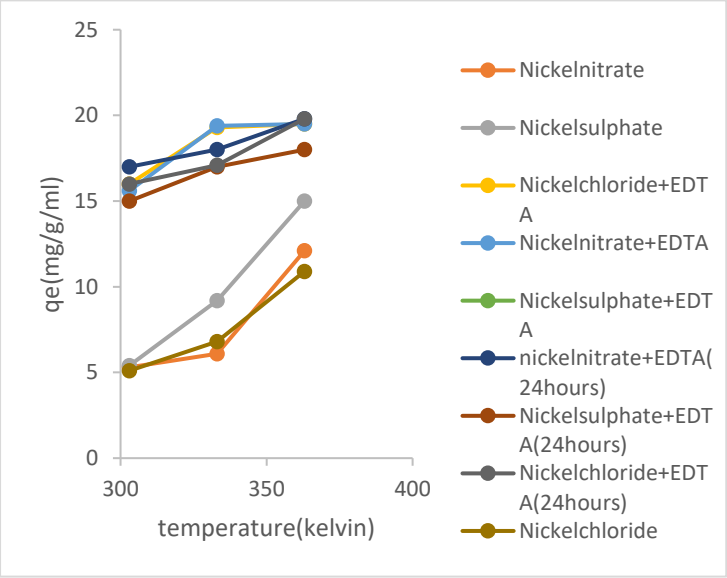

Figure. 3.55: Effect of temperature on adsorption of Ni{NO_3, Cl_2, SO_4} and Ni{NO_3, Cl_2,SO_4}-EDTA by EtOH-cys-AgNPs

3.11.6 Adsorption thermodynamics

The adsorption processes are spontaneous for the Ni{Cl_2,SO_4} and Ni{Cl_2,SO_4}-EDTA adsorption by EtOH-cys-AgNPs as confirmed by the negative values of the Gibbs free energy and there exists an increase in randomness in the adsorption process for all the metals as confirmed by the positive values of the entropy of the system .The adsorption of $Ni(NO_3)_2$ and Ni{NO_3,Cl_2,SO_4}-EDTA (24Hrs) are characterized by a spontaneous adsorption process but with an exothermic reaction process except for nitrate which is endothermic reaction process. Values of the adsorption thermodynamics parameters are highlighted in Table 3.10 and the plot of LnK versus 1/T are depicted in Figure. 3.56

Metals -Ni (II)	**ΔG kJ/mol**	**ΔH kJ/mol**	**ΔS J mol^{-1} K^{-1}**	**slope**	**intercept**
NO_3	-8.63	10.36	29.2	1246.5	3.5103
NO_3-EDTA	-41.02	-25.96	138	-3123	16.65
Cl_2	-100.95	-91.22	338.37	-10972	40.709
Cl_2-EDTA	-102.89	-95.66	347.6	-11507	41.481
SO_4	-88.42	-76.91	296.46	-9251.1	35.659
SO_4-EDTA	-82.13	-72.45	275.54	-8714	33.142

Table. 3.10: Adsorption thermodynamic of Ni{NO_3^-, Cl^-, SO_4^{2-}} and Ni{NO_3,Cl_2,SO_4}-EDTA by EtOH-cys-AgNPs

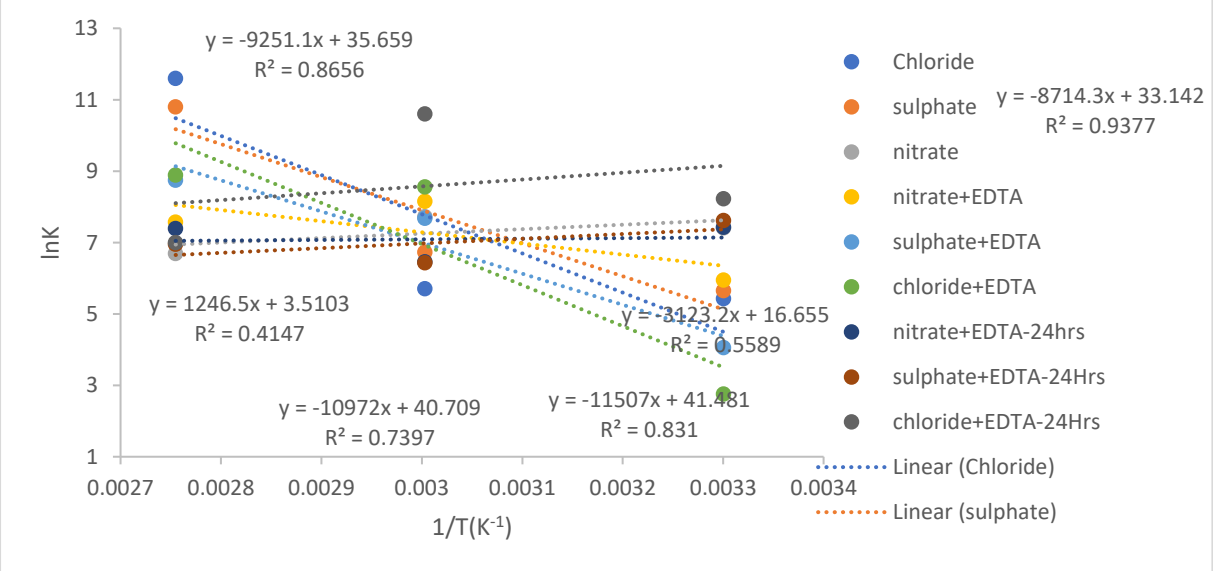

Figure. 3.56: Adsorption thermodynamics of Ni{NO_3,Cl_2,SO_4} and Ni{NO_3,Cl_2,SO_4}-EDTA by EtOH-cys-AgNPs

3.11.7 Adsorption kinetics

In order to investigate the kinetics models of Ni {NO_3^-, Cl^-, SO_4^{2-}} and Ni{NO_3^-, Cl^-, SO_4^{2-}}-EDTA adsorption by EtOH-cys-AgNPs, the linear pseudo first order and pseudo-second order kinetics models were tested to fit the experimental data. The kinetics of the adsorption of the six s by EtOH-cys-AgNPs are presented in Figure. 3.57) and fitted by the pseudo-first- and -second-order kinetic models. As shown, the corresponding adsorption reaction could approach adsorption equilibrium within 40 min in Ni{NO_3^-, Cl^-, SO_4^{2-}} and reaches adsorption equilibrium at 60 minutes with of Ni{NO_3^-, Cl^-, SO_4^{2-}}-EDTA by EtOH-cys-AgNPs, kinetic analysis was carried out on the first 60 minutes of contact time, after which equilibrium had been reached. Based on the comparison of the fitting coefficient (R^2) and Qe value the adsorption behaviour of both the free ions and their EDTA complexes by EtOH-cys-AgNPs were more consistent with the pseudo-second-order kinetics model (Figure 3.57 and Table. 3.11). EtOH-cys-AgNPs has a high capacity for rapid adsorption of Ni{NO_3, Cl_2, SO_4}-EDTA in the solution, whether in the mixed systems or not. However, the adsorption performance of EtOH-cys-AgNPs the single system was markedly better at a high pH.

Metal Ni (II)	**R^2-Pseudo-firstorder kinetic model-60 minutes**	**R^{2-}Pseudo second-order kinetic model-60 minutes**
Nickel nitrate	0.2413	0.7489
Nickel sulphate	0.4994	0.9724
Nickel chloride	0.6228	0.5939
Nickel nitrate+EDTA	0.4601	0.9869
Nickel sulphate+EDTA	0.7455	0.9914
Nickel chloride+EDTA	0.441	0.9941

Table.3.11: R^2 value of adsorption of Ni {NO_3^-, Cl^-, SO_4^{2-}} and Ni {NO_3^-, Cl^-, SO_4^{2-}}-EDTA by EtOH-cys-AgNPs

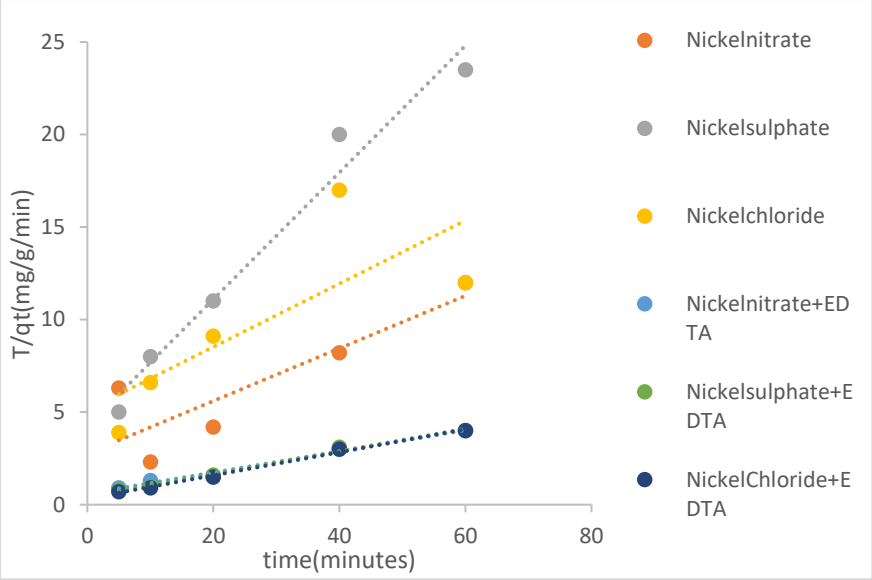

Figure. 3.57: Pseudo - second-order kinetic model of Ni {NO_3^-, Cl^-, SO_4^{2-} } and Ni {NO_3^-, Cl^-, SO_4^{2-}}-EDTA by EtOH-cys-AgNPs at 60 minutes

3.11.8 Adsorption Isotherm of Ni {NO_3^-, Cl^-, SO_4^{2-}} and Ni{NO_3^-, Cl^-, SO_4^{2-}}-EDTA by EtOH-cys-AgNPs

All the adsorption isotherm of Ni{NO_3^-, Cl^-, SO_4^{2-}} and Ni{NO_3^-, Cl^-, SO_4^{2-}}-EDTA by EtOH-cys-AgNPs fit best with Henry isotherm except for the sulfate and sulfate-EDTA which also fit very well with the Freundlich isotherm and D-R isotherm, both suggesting inhomogeneity of the surface of the EtOH-cys-AgNPs may play a significant role in these systems. (Table. 3.12 and Figures 3.58-3.60).

Metal(Ni (II))	(Henry Isotherm) R^2	Temkin isotherm R^2	D-R isotherm Plot R^2	Langmuir isotherm R^2	(Freundlich isotherm) R^2
SO_4	0.95	0.86	0.95	0.6	0.99
Cl_2	0.95	0.56	0.52	0.1	0.66
NO_3	0.95	0.92	0.8	0.037	0.83
SO_4-EDTA	0.96	0.844	0.98	0.55	0.97
Cl_2-EDTA	0.96	0.955	0.94	0.017	0.903
NO_3-EDTA	0.96	0.84	0.82	0.52	0.81

Table.3.12.: Adsorption Isotherm R^2 values of Ni{NO_3^-, Cl^-, SO_4^{2-}} and Ni{NO_3^-, Cl^-, SO_4^{2-}}-EDTA by EtOH-cys-AgNPs

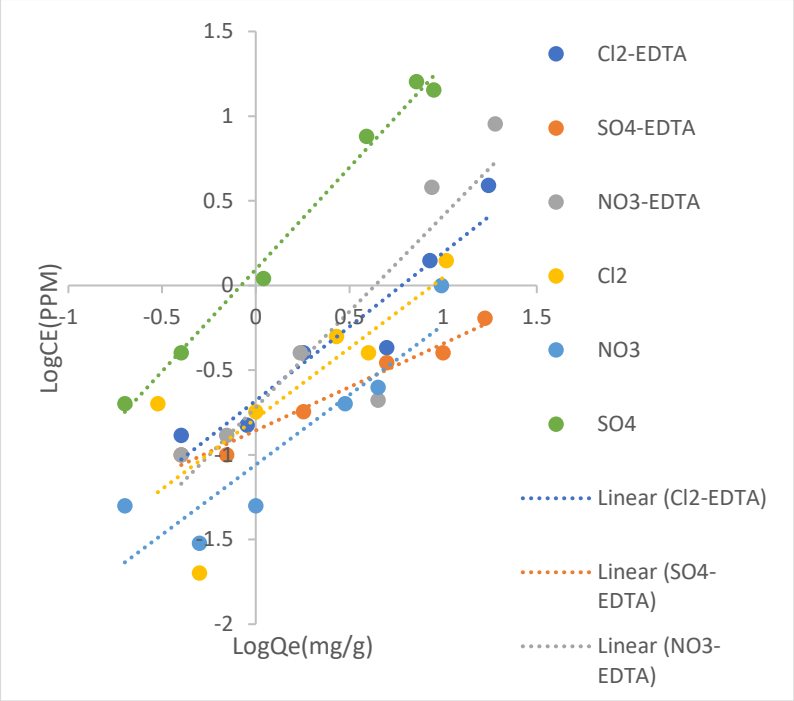

Figure. 3.58: Freundlich isotherm of Ni{NO_3^-, Cl^-, SO_4^{2-}} and Ni{NO_3, Cl_2, SO_4}-EDTA by EtOH-cys-AgNPs

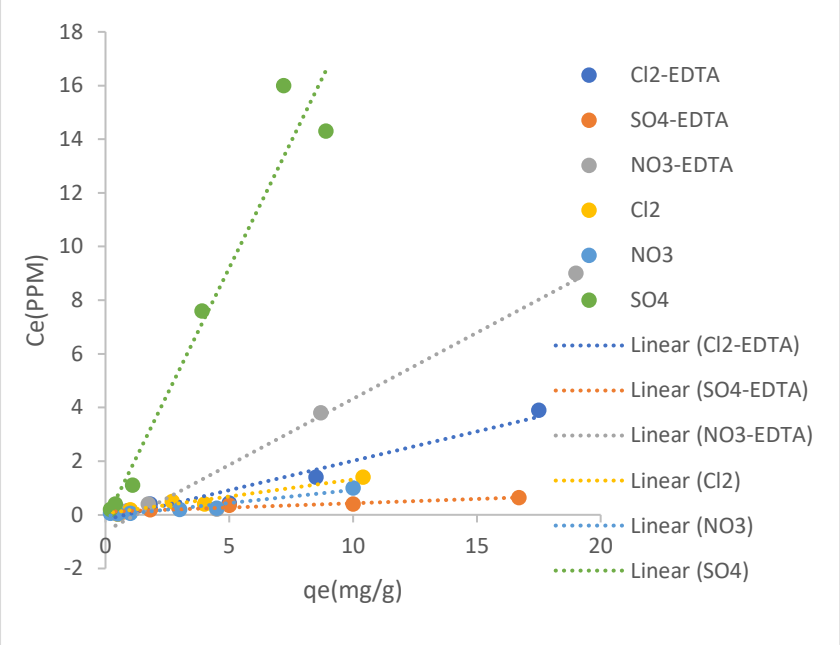

Figure. 3.59: Henry isotherm of Ni{NO_3^-, Cl^-, SO_4^{2-}} and Ni{NO_3, Cl_2, SO_4}-EDTA by EtOH-cys-AgNPs

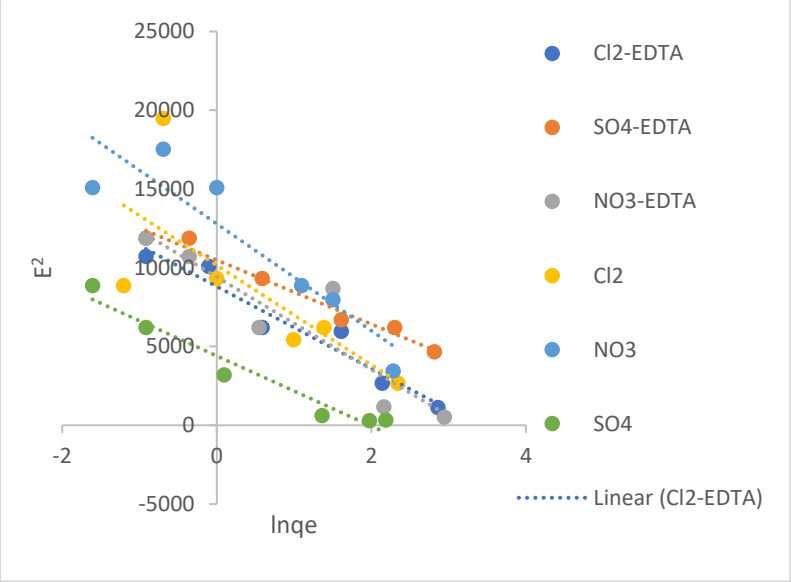

Figure. 3.60: D-R adsorption isotherm of Ni{No_3^-, Cl^-, SO_4^{2-}} and Ni{No_3, Cl_2, SO_4}-EDTA by cys-AgNPs in organic solvents

3.12 The adsorption of EDTA and NiEDTA by EtOH-cys-AgNPs at higher initial concentration (50 ppm) of EDTA and NiEDTA

In order to understand the adsorption behaviour of EDTA in the previous experiments further adsorption experiments were carried out at a higher concentration of the EDTA and the NiEDTA using Nickel nitrate trihydrate. The adsorption of EDTA and NiEDTA by EtOH-cys-AgNPs was carried out at 10 ppm - 50 ppm of each species. The calibration curve obtained show the metal salt are suitable for the experiments.

3.12.1 Effect of initial concentration

The quantity of EDTA adsorbed by EtOH-cys-AgNPs increases with the initial concentration suggesting the availability of more vacant site on EtOH-cys-AgNPs. The same observation is observed with the NiEDTA as well. From this result it can be noted that there is a co-adsorption of EDTA and Ni (II) ions on the surface of EtOH-cys-AgNPs accounting for the increase in the qe value of Ni {NO_3^-, Cl^-, SO_4^{2-}}-EDTA adsorption by EtOH-cys-AgNPs in the previous experiments. (Figure. 3.61). No evidence of Ni(II) adsorption at this concentrations as no experiments were carried out on Ni(II) at this concentration.

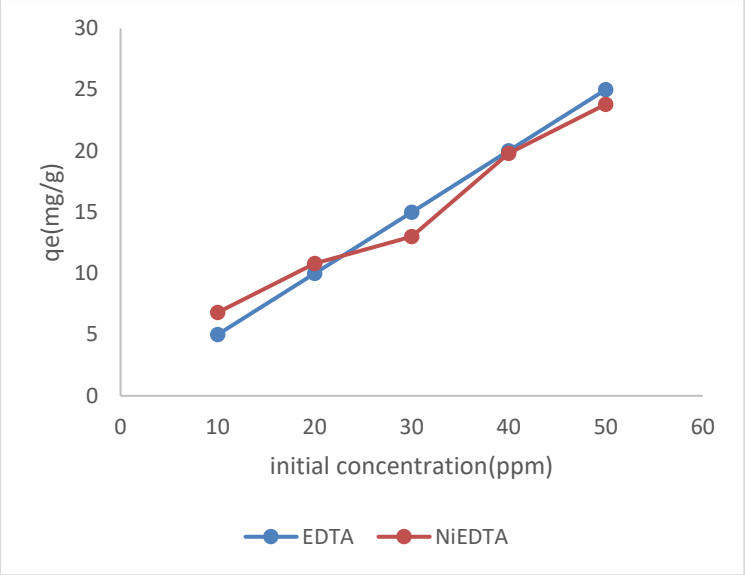

Figure. 3.61: Effect of initial concentration of EDTA and NiEDTA adsorption by EtOH-cys-AgNPs

3.21.2 Effect of contact time

The adsorption of EDTA and NiEDTA by EtOH-cys-AgNPs was rapid at the initial stage of adsorption and reaches equilibrium at 40 minutes remaining constant till 1440 minutes. (Figure. 3.62-3.63). The results explained there might be possible co-adsorption of EDTA by EtOH-cys-AgNPs as the qe value for EDTA increases with the time of the experiments and reaches equilibrium at 40 minutes and became stable till 24Hrs.

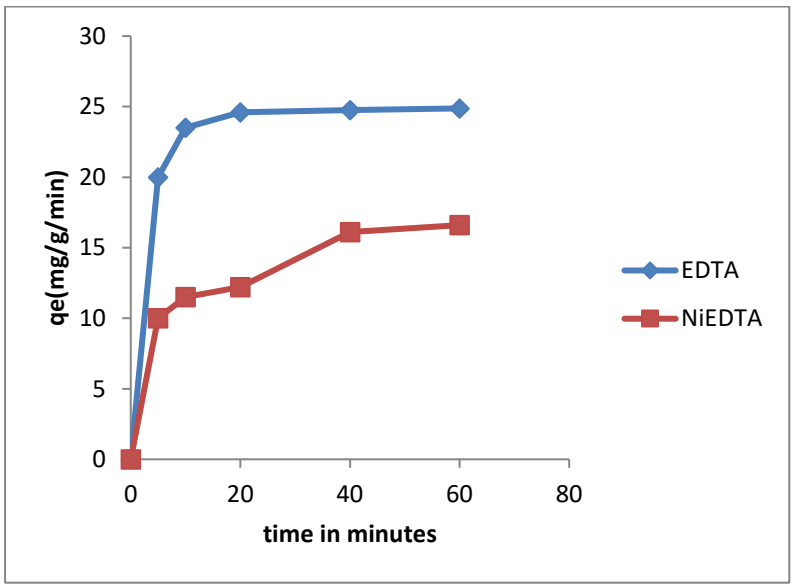

Figure. 3.62: Effect of contact times of EDTA and NiEDTA adsorption by EtOH-cys-AgNPs at 5- 60 minutes at 50 ppm of EDTA and NiEDTA

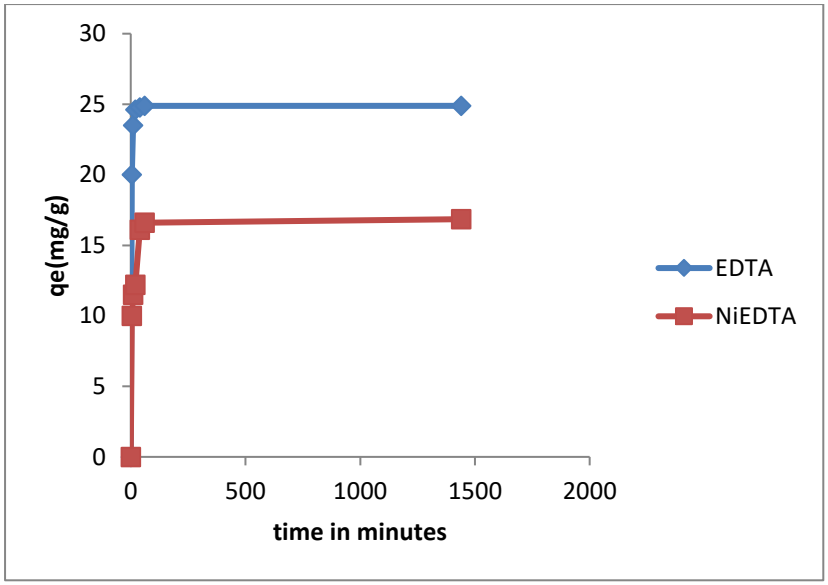

Figure. 3.63: Effect of contact times of EDTA and NiEDTA adsorption by EtOH-cys-AgNPs at 5- 1440 minutes at 50 ppm of EDTA and NiEDTA

3.12.3 Effect of Dose

The same trend observed in the adsorption of of Ni{NO_3^-, Cl^-, SO_4^{2-}} and Ni{NO_3^-, Cl^-, SO_4^{2-}}-EDTA by EtOH-cys-AgNPs was also observed maximum uptake of EDTA and NiEDTA by EtOH-cys-AgNPs were 14.2 mg/g and 15.8 mg/g respectively. The qe value tends to decrease with dose of EtOH-cys-AgNPs. (Figure. 3.64).

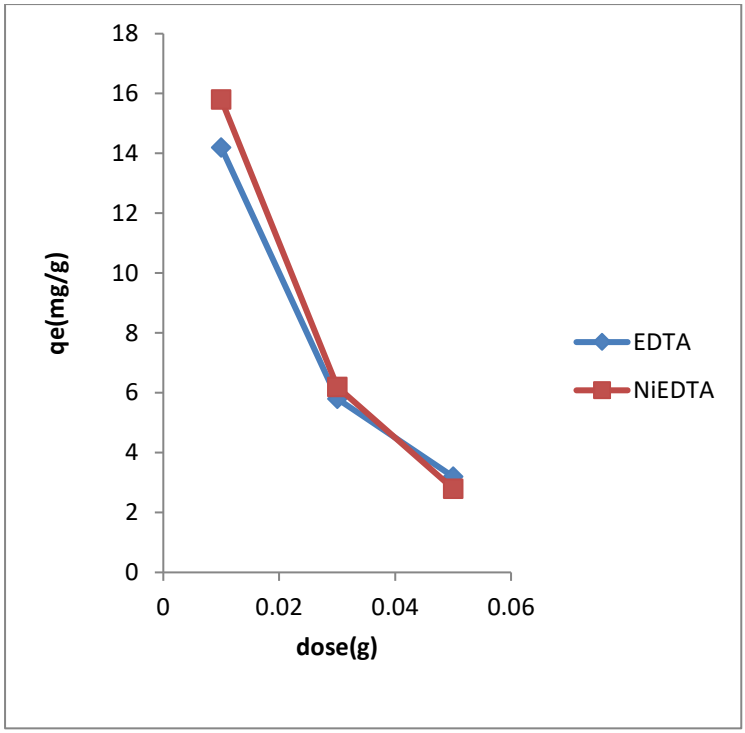

Figure. 3.64: Effect of dose of EDTA and NiEDTA adsorption by EtOH-cys-AgNPs

3.12.4 Effect of pH

The adsorption of EDTA and NiEDTA by EtOH-cys-AgNPs increases with PH and there exist a little change in the adsorption of NiEDTA by EtOH-cys-AgNPs (Figure.3.65)

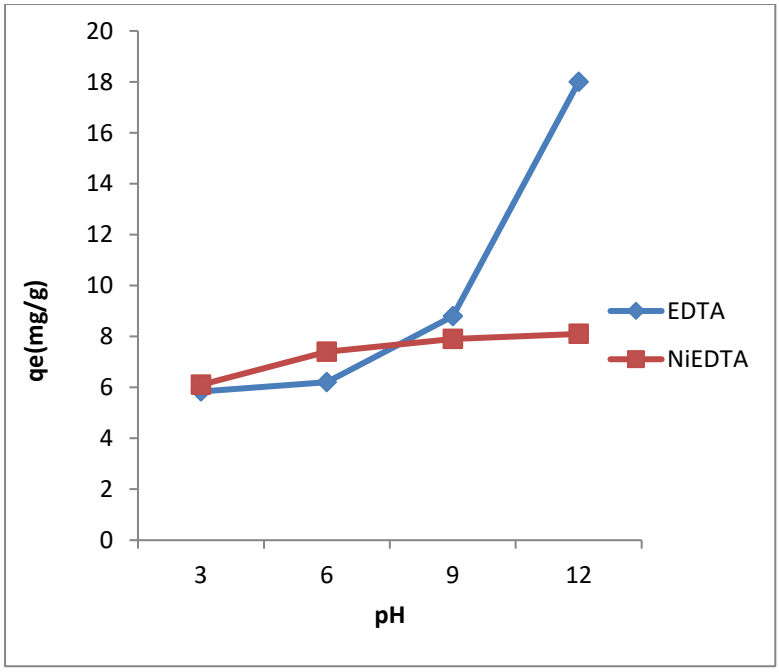

Figure. 3.65: Effect of pH of EDTA and NiEDTA adsorption by EtOH-cys-AgNPs

3.12.5 Adsorption thermodynamics

Increasing temperature increases adsoeption for both EDTA and NiEDTA with quantity of metal adsorbed (Figure 3.66).

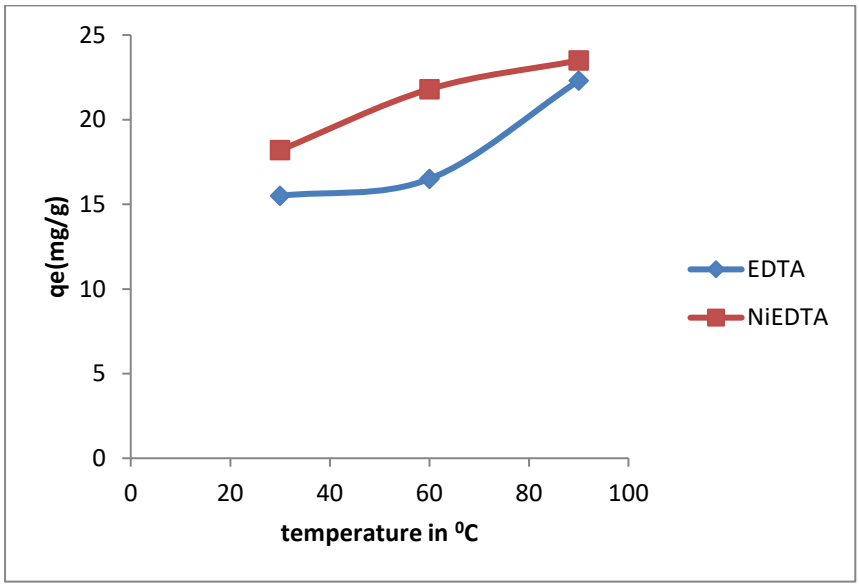

Figure. 3.66: Effect of pH of EDTA and NiEDTA adsorption by EtOH-cys-AgNPs

The values of Gibbs free energy and enthalpy are both negative for EDTA and NiEDTA adsorption by EtOH-cys-AgNPs suggesting a spontaneous process with a positive values for entropy.(Table 3.13 and figure 3.67).

species	ΔG (kJ/ mol)	ΔH (kJ/mol)	ΔS (J mol^{-1}K^{-1})	slope	intercept
EDTA	-89.63	-41.25	162.35	-4962.2	19.527
NiEDTA	-64.3	-24.37	134.3	-2932	16.154

Table. 3.13: Adsorption thermodynamic of EDTA and NiEDTA adsorption by EtOH-cys-AgNPs

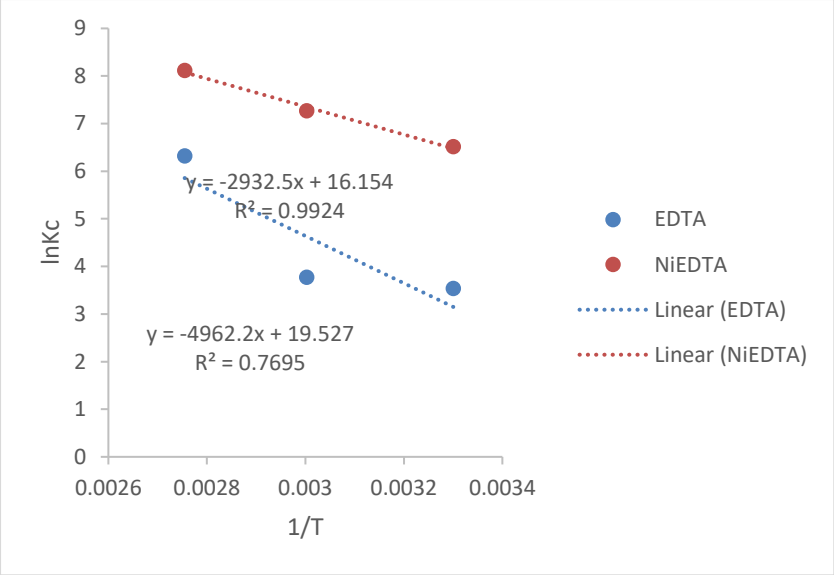

Figure.3.67: Adsorption thermodynamic of EDTA and NiEDTA adsorption by EtOH-cys-AgNPs

3.12.6 Adsorption kinetics

The adsorption kinetic fits best to pseudo second-order kinetic model with R^2 values close to 1 in contrast with 0.2-0.3 R^2 values which were observed for the pseudo first order adsorption model for both EDTA and NiEDTA respectively. The adsorption kinetic of EDTA and NiEDTA adsorption by EtOH-cys-AgNPs suggested that the mechanism of reaction to be chemisorption. (Figure. 3.68 and Table 3.14).

Adsorption kinetics	**R^2 pseudo first-order model**	**R^2 pseudo second-order model**
EDTA	0.2311	0.9998
NiEDTA	0.3067	0.9908

Table 3.14: Adsorption kinetics R^2 values of EDTA and NiEDTA by EtOH-cys-AgNPs

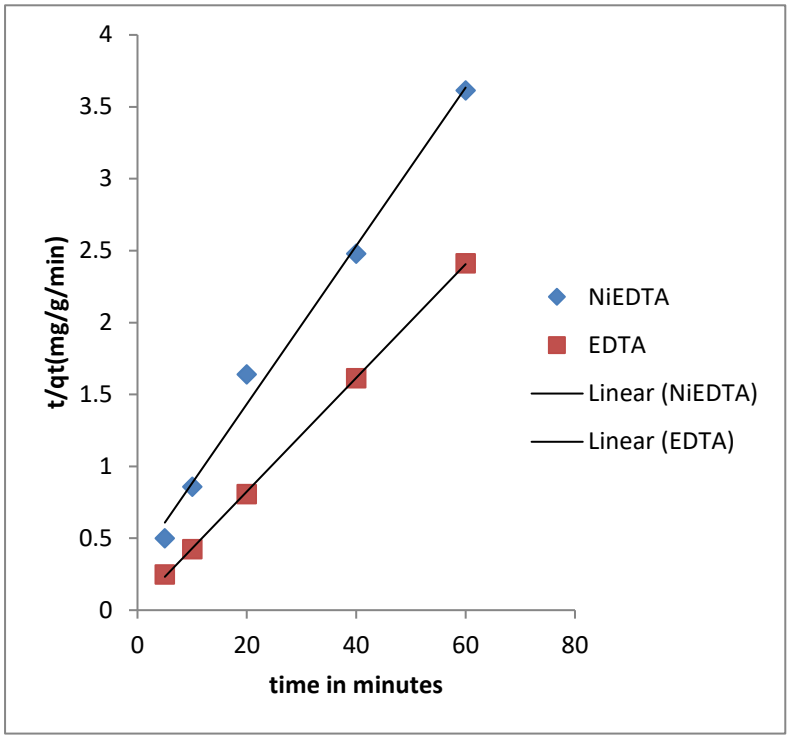

Figure. 3.68: Pseudo second order kinetics of adsorption of EDTA and NiEDTA by cys-AgNPs in organic solvents at 5- 60 minutes

3.12.7 Adsorption isotherm

The adsorption of EDTA and NiEDTA by EtOH-cys-AgNPs fit best to the Henry isotherm which suggest that the adsorption energy is surface coverage independent. Other isotherm models such as Freundlich, Temkin, Dubinin-Raduschkevich and Langmuir isotherm model were also tested and gave lower R^2 values and are highlighted in the Table.3.15 and Figure.3.69.

Table of R^2 values

Metal	Henry isotherm	Freundlich isotherm	Temkin isotherm	Langmuir isotherm	D-R isotherm
EDTA	0.9978	0.084	0.6406	0.762	0.2195
NiEDTA	0.9519	0.8992	0.8991	0.7241	0.6552

Table. 3.15.: R^2 values of adsorption isotherm model of EDTA and NiEDTA adsorption EtOH-cys-AgNPs

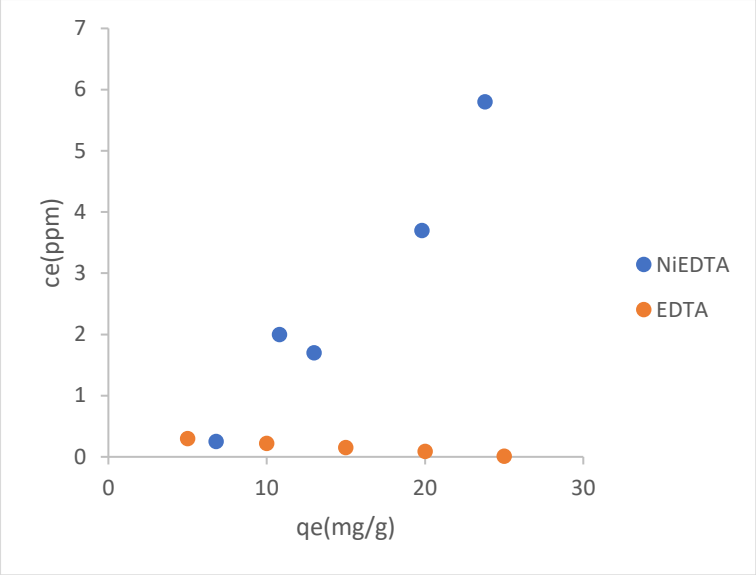

Figure. 3.69: Henry adsorption isotherm plot of EDTA and NiEDTA by EtOH-cys-AgNPs

3.13 The influence of magnesium, sodium ions on the adsorption of lead in a binary system containing magnesium and sodium ions by EtOH-cys-AgNPs

3.13.1 Effect of initial concentration

The adsorption of lead was investigated in the presence and absence of Na and Mg ions, given their likely presence in low concentrations in most water samples. As can be seen from Table 3.16, the qe values for lead adsorption remain relatively constant in the presence or absence of Na+ and Mg^{2+}. Thus it is unlikely that the presence of these ions will have much influence in the analysis of real freshwater samples. in the activities. Shown in the table 3.16.

Metal	**Pb(II)**	**Mg(II)**	**Pb containing Mg**	**Pb containing sodium**	**Na(I)**
qe(mg/g)	9.4	9.4	9.35	9.82	9.4

Table. 3.16: Effect of Na^{+} and Mg^{2+} on the adsorption of lead and lead by EtOH-cys-AgNPs.

3.13.2 Effect of contact time

The qe values increases for all the Pb(II), Mg(II), Na(I), (Pb+Mg) and (Na+Pb) and the adsorption reaches equilibrium at 40 minutes for all the ions examined and remained constant to 1440 minutes with similar values of qe suggesting that there is no possible interference on the adsorption of Pb(II) by Mg(II) and Na(I) ion in the binary systems. (Figure. 3.70). the

adsorption of Na+Pb increases with time and reached equilibrium at 40 minutes and stable till 60 minutes, similar observations is observed with Mg+Pb.

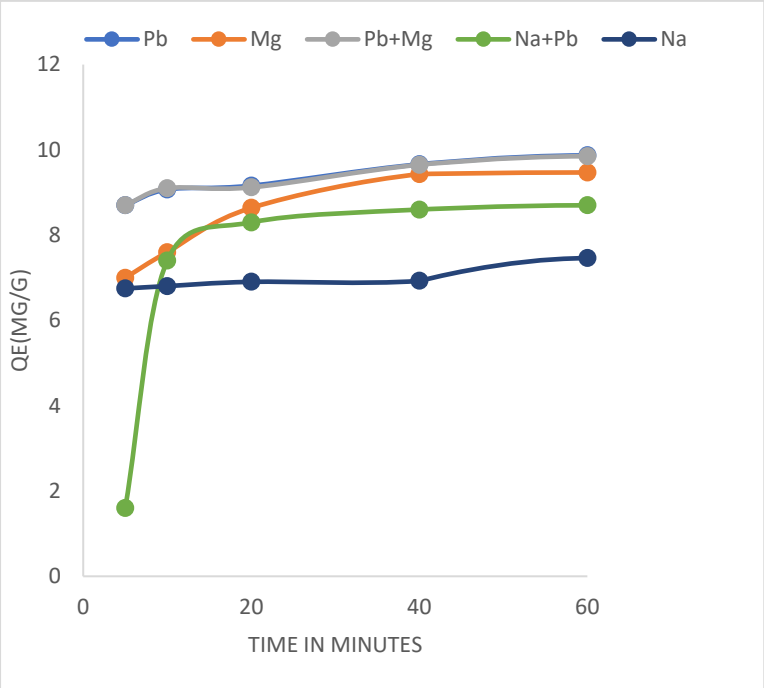

Figure. 3.70: Effect of contact time of adsorption of lead, sodium, magnesium, and lead containing sodium or magnesium ions by EtOH-cys-AgNPs

3.13.3 Effect of dose

The adsorption of Pb(II), Mg(II), Na(I) and (Pb+Mg) by EtOH-cys-AgNPs decrease with an increase in dose of EtOH-cys-AgNPs suggesting that the presence of a high vacant site at low doses. except for Na+Pb whose qe values increase with the doses of EtOH-cys-AgNPs and ended up with qe of 5.1 mg/g. Thus, it can be justified that there exists a possible influence of Na(I) ions in the adsorption of the binary system of Pb (II) ions (Figure. 3.71).

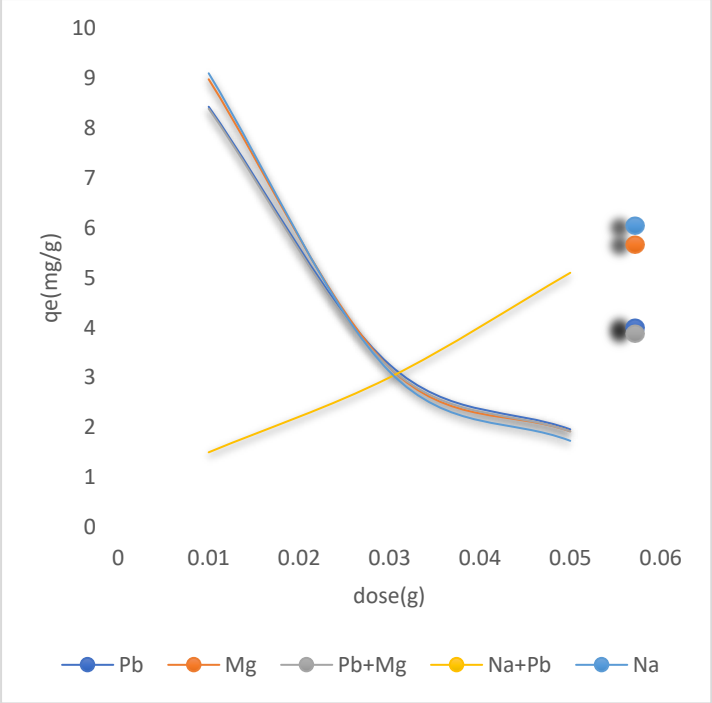

Figure. 3.71: Effect of dose of adsorption of lead and lead containing sodium or magnesium ions by EtOH-cys-AgNPs.

3.13.4 Effect of pH

The qe values increases for all the metal ions examined as expected, albeit slightly. Again, the Na/Pb system is different in that there is a more significant increase in adsorption over the pH range, with a similar qe value at the highest pH (Figure. 3.72).

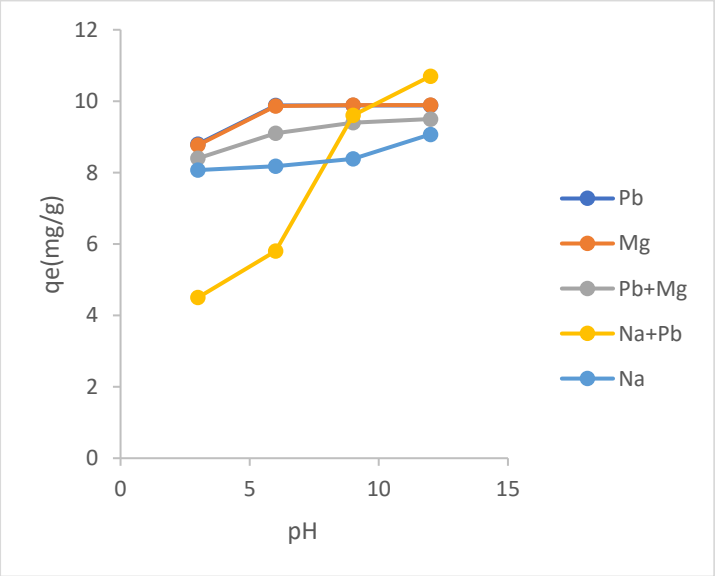

Figure. 3.72: Effect of pH of adsorption of lead and lead containing sodium or magnesium ions by EtOH-cys-AgNPs.

3.13.5 Effect of temperature

The qe values of Pb(II), Mg(II), Na(I), (Mg+Pb) and (Na+Pb) adsorption by EtOH-cys-AgNPs increases with temperature and the qe values for the adsorption of (Na+Pb) ions were quite slow as the temperature increase but later gave a qe values of 9.8 mg/g similar to the previous metal cations examined. (Figure. 3.73).

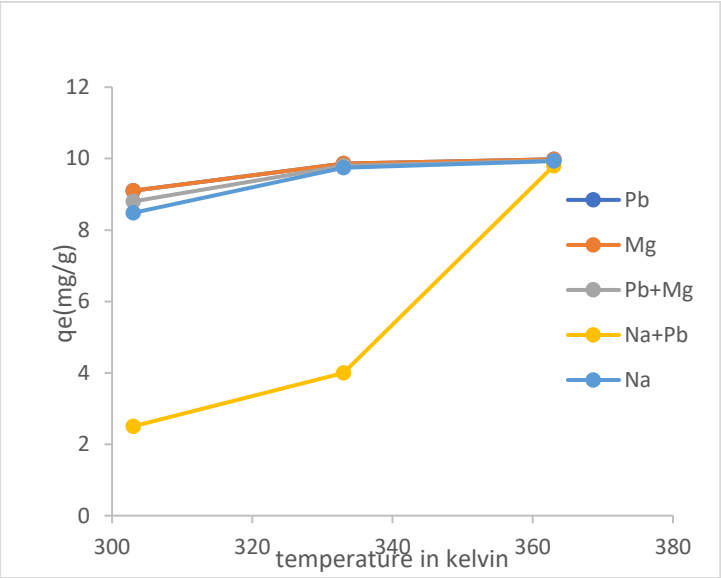

Figure. 3.73: Effect of temperature of adsorption of Lead and Lead contain sodium and magnesium ions by EtOH-cys-AgNPs.

3.13.6 Adsorption thermodynamic

Adsorption process suggest a spontaneous process for all metal examined with an exothermic process except for Pb(II) with a non-spontaneous positive Gibbs free energy and endothermic heat of reaction. (Table. 3.17) and figure. 3.74.

Metals	$\Delta G(\frac{kJ}{mol})$	$\Delta H(\frac{kJ}{mol})$	ΔS(J/mol/S)	slope	intercept
Pb (II)	10.0	208.78	666.87	25113	-80.211
Na+Pb	-88.2	-45.23	148.48	-5440	17.595
Na(I)	-138.8	-68.5	236.1	-3922	16.812
Mg(II)	-73.95	-32.6	138.77	-8245.2	28.399
Mg+Pb	-80.15	-35.78	148.48	-4304.1	17.86

Table. 3.17. Adsorption thermodynamic parameters of of lead, sodium, magnesium and lead containing sodium and magnesium ions adsorption by EtOH-cys-AgNPs

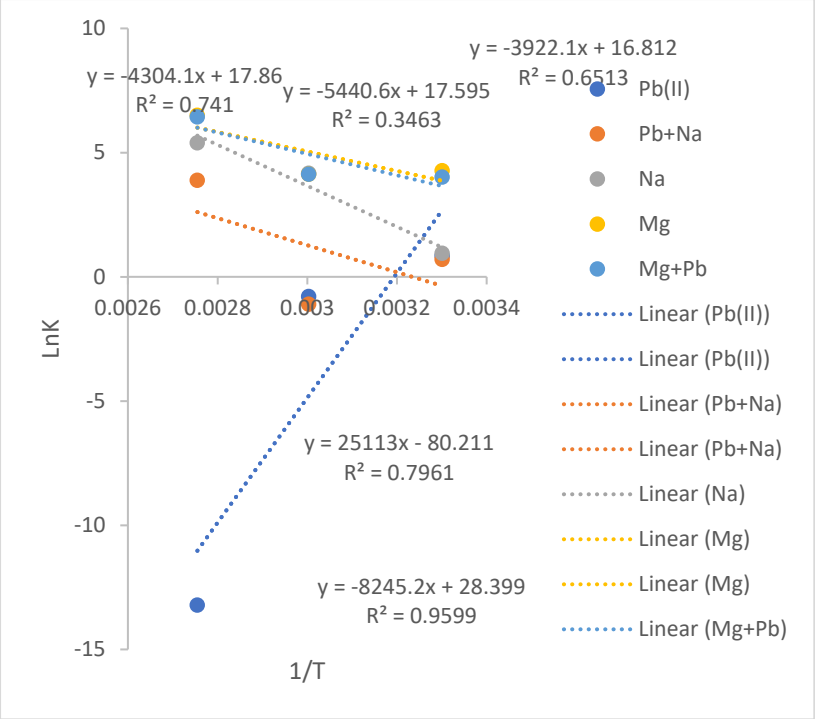

Figure. 3.74: Adsorption thermodynamics of lead, sodium, magnesium and lead containing sodium and magnesium ions adsorption by EtOH-cys-AgNPs at 5-1440 minutes

3.14 Demonstration of maximum adsorption capacity of EtOH-cys-AgNPs with some selected heavy metals

The adsorption of $NiCl_2$, $Ni(NO_3)_2$ and $Cd(NO_3)_2$ by EtOH-cys-AgNPs was investigated at an initial concentrations ranging from 100 ppm- 800 ppm in order to know the maximum extent of adsorption.

100-800 ppm of $NiCl_2$, $Ni(NO_3)_2$ and $Cd(NO_3)_2$ were prepared and shaken with 0.01g of the EtOH-cys-AgNPs and agitated for 2 hours, after which the solution were filtered and analysed using uv-visible spectroscopy. The adsorption behaviour was similar in their adsorptive mode and this shows that optimal adsorption occurs at 400 ppm and drops when the adsorption reaches 800 ppm. (Figure.3.75).

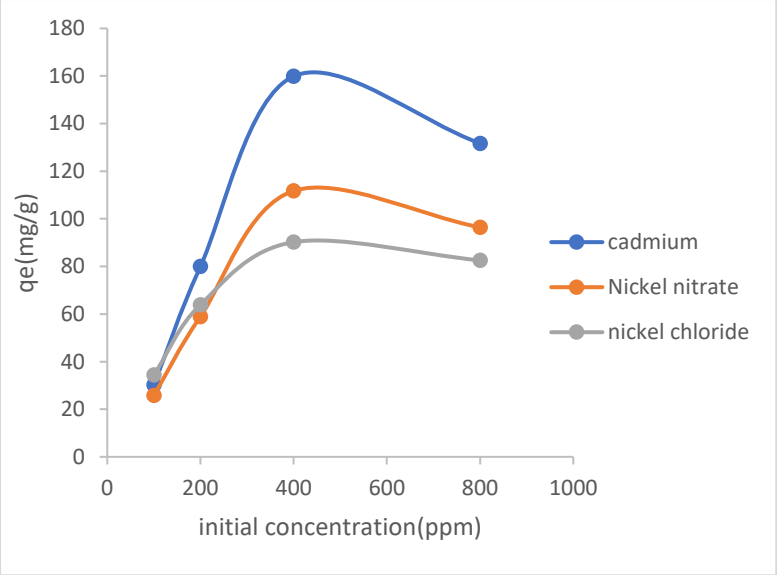

Figure 3.75: Effect of initial concentration of $NiCl_2$, Ni $(NO_3)_2$ and $Cd(NO_3)_2$

3.15 Conclusion to chapter 3.

From the preceding, it can be concluded that AgNPs can be produced from the borohydride reduction of $AgNO_3$, and can be stabilized by the attachment of cysteine via an Ag-S bond. The amount of surface coverage by cysteine is much higher when the synthesis is conducted in aqueous medium as opposed to ethanol. The NPs formed in ethanol are smaller (ca 5 nm) compared to those formed in water (40-50 nm, albeit with some evidence of a second population of 3-5 nm). Adsorption of a range of metal ions at ppm levels was successful, and the NPs showed excellent efficiency in adsorbing the ions present. The presence of additional common species such as Na^+, Mg^{2+} and EDTA generally had little impact on adsorption behaviors, and generally, if anything, tended to improve behavior. Kinetic and thermodynamic analysis both suggested a strong chemisorption type behavior, likely involving electrostatic ion pairing between carboxylate and the ion in question, but possibly also N ligation, both arising from the surface-bound cysteine.

While there was some shift in LSPR and this varied to an extent from ion to ion, it is hard to envisage that UV-vis could reliably detect which metals were in a specific water sample, and thus future efforts could be directed towards a different sensing method (e.g., an electrochemical based approach may be able to distinguish.)

Chapter 4

Synthesis, characterization and application of cysteine-based gold nanoparticles (cys-AuNPs) towards the detection and removal of heavy metal from aqueous solution.

4.1 Synthetic methodology

The synthesis of cys-AuNPs was coined using the method developed by Turkevich [123] which involves the refluxing of gold(III) chloride with sodium citrate tribasic, leading to a characteristic ruby-red colouration suspension of gold nanoparticles. At this point cysteine was added leading to a more intense coloration. L-cysteine is known to have a strong effect on UV-Visible spectra of gold nanoparticle solutions, more than other amino acids, for instance lysine [151]. In this work, the authors demonstrate that a 10^{-3} M solution added to the colloidal gold solutions results to a rapid broadening of the adsorption peak, and a bathochromic shift. And this is as a result of the coupling of the SPR of two adjacent NPs. [152]This kind of colour change as an effect of aggregation is a well-understood phenomenon [153] When the interparticle distance in the aggregates decreases to less than about the average particle diameter, the electric dipole–dipole interaction and coupling between the plasmons of neighbouring particles in the aggregates results in the bathochromic shift of the absorption band These results support the observations about the interaction of cysteine with gold nanoparticles[154], where, based on the analysis of Fourier transform infrared spectra these affirms the existence of covalent interaction of sulphur and gold. The formation of a covalent bond Au-S is also proposed by other literature report [155,156.] Furthermore, it was suggested[157] assemblies of NPs are formed by electrostatic interaction between the amino group and the negative charge group in the other NPs. Also, the synthesized gold nanoparticles findings agree with reported data on the adsorption of homocysteine on gold nanoparticles [158].

4.2 Characterisation of the cys-AuNPs

4.2.1 Physical appearance of cys-AuNPs

On addition of gold (III) chloride to the boiled sodium citrate tribasic solutions, the solution changes to ruby-red, characteristic of gold nanoparticles. Addition of cysteine to the solution causes the intensity of colour to increase (Figure. 4.0).

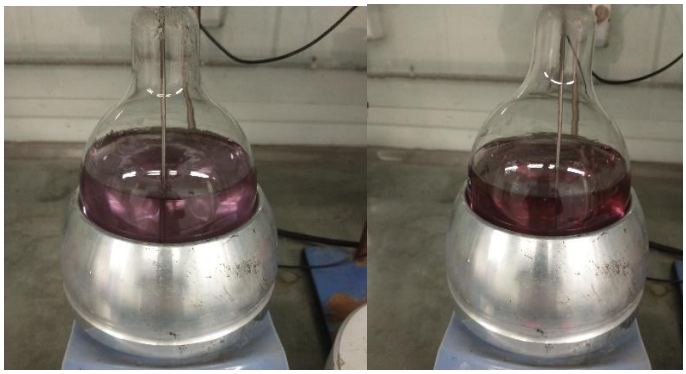

Figure. 4.0: Image of gold nanoparticles (left) and cys-AuNPs (right)

4.2.2 UV/Visible characterization of cys-AuNPs

The UV–Vis absorption spectra of cysteine-capped gold nanoparticles synthesized were recorded immediately after the complete synthesis of the nanoparticles. The appearance of a broad band LSPR was found in the absorption spectrum of the cys-AuNPs which was absent in the spectrum of the gold chloride, sodium citrate tribasic showing the formation of the cys-AuNPs (Figure.4.1-4.2). All the spectra obtained display an absorption wavelength peak at approximately 536 nm which is attributed to the localized surface plasmon resonance mode of spherical gold nanoparticles (Figure. 4.2), Their stability was investigated over 100 minutes at 10-minute intervals (Figure 4.2). The initially formed cys-AuNPs were thus shown to be relatively unstable, with a significant drop in LSPR intensity over around 1 hour, but then the resultant NPs appear to be stable subsequently. (Figure.4.2-4.3)

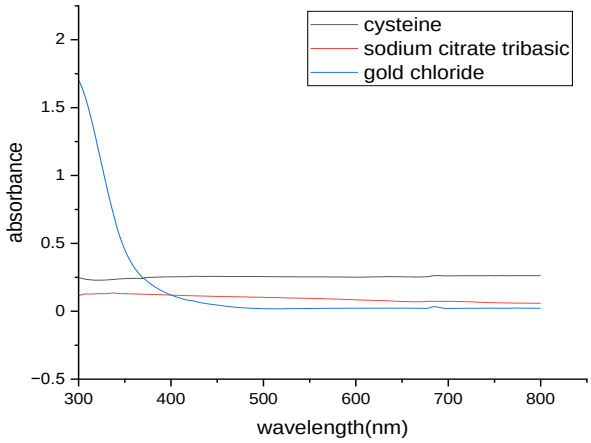

Figure. 4.1: UV/Visible spectra of cysteine, sodium citrate tribasic and gold chloride

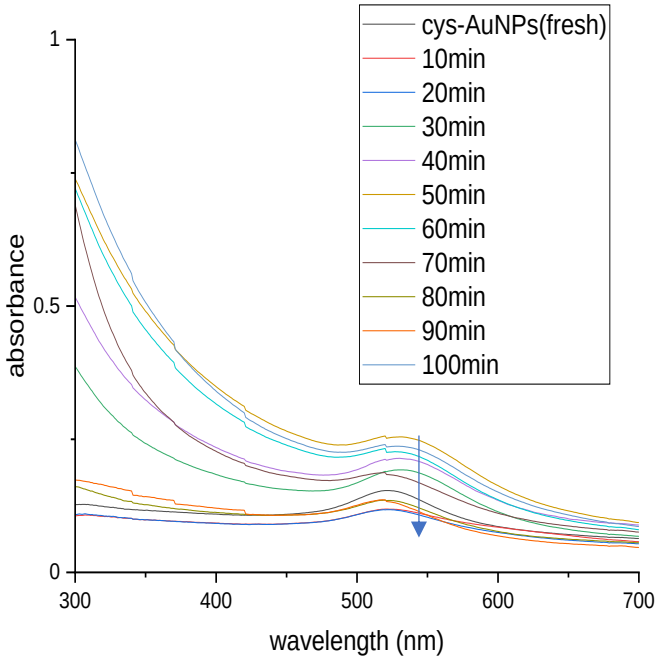

Figure. 4.2: UV/Visible spectra of cys-AuNPs and its absorbance stability measurements with times

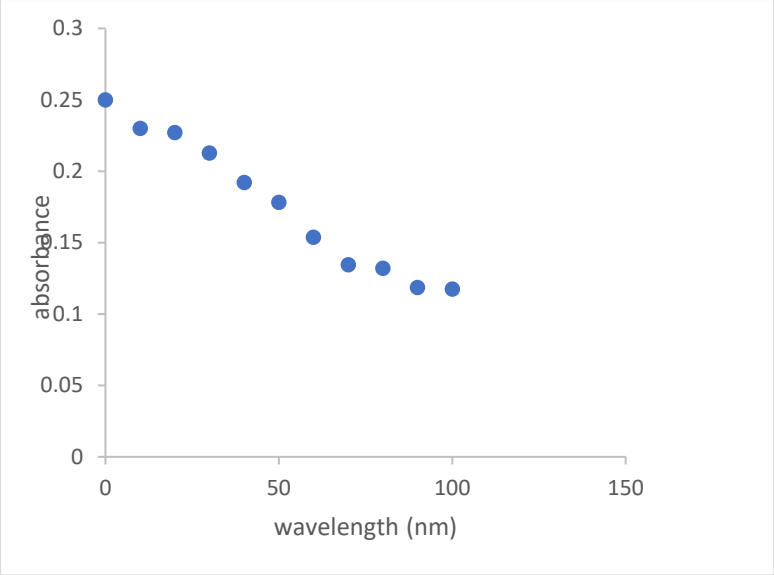

Figure.4.3: A plot of LSPR absorbance vs time of cys-AuNPs

4.2.3 Fourier transform infrared spectroscopy of cys-AuNPs

The FTIR spectra were run on a dried sample of colloidal cys-AuNPs solution which had been freeze dried for 24 hrs.

The Fourier transform infrared spectra of cysteine, cys-AuNPs in the absence of, and in the presence of sodium citrate tribasic are shown below. Bands observed in the Fourier transform infrared spectra of l-cysteine are identified as the following: 1550–1650 cm^{-1} (C=O) peak of the acids and carboxylate anion, and the corresponding symmetric stretches 1393 cm^{-1} carboxylate symmetric stretching, 1200–1250 cm^{-1} (C–O), 3158cm^{-1} (O–H / N-H), 2958 cm^{-1} (C–H), 1066 cm^{-1} (C–NH_2), 600–800 cm^{-1} (C–S) and 2547 cm^{-1} (S–H).[158,159] The spectrum of the cys-AuNPs indicates very little evidence for the presence of cysteine. As confirmed by thermal analysis of the nanoparticles, there is very little organic material present in the material. The major features seen in the NP spectrum are likely to be residual water and some contamination. (Figure.4.4).

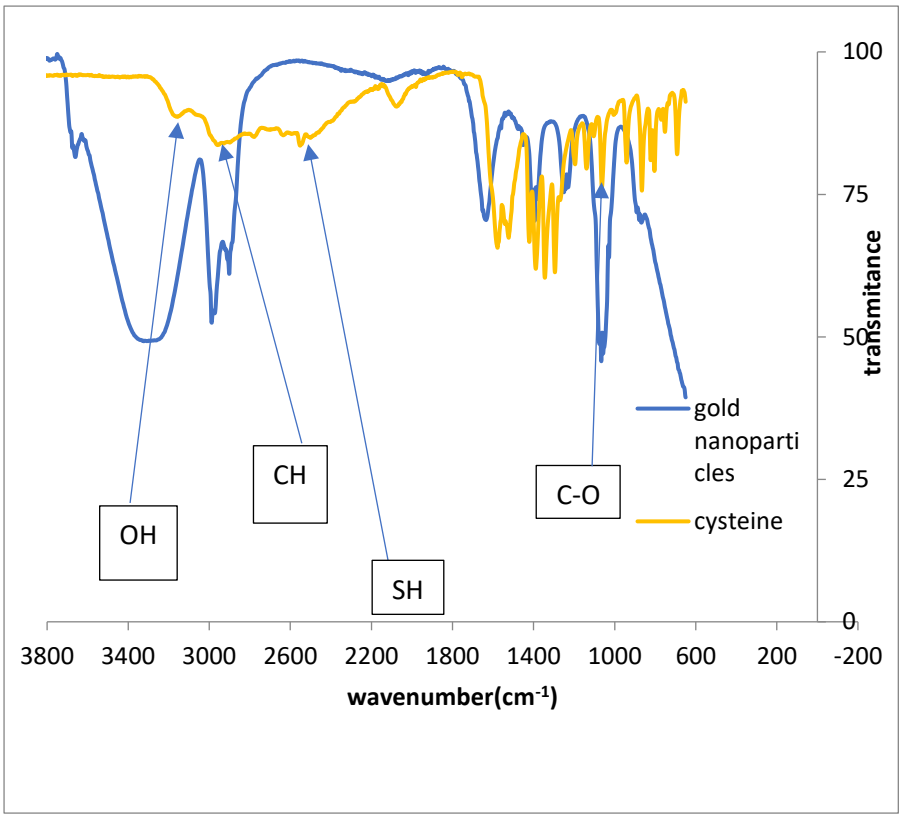

Figure. 4.4: Fourier transform IR spectra of cys-AuNPs

4.2.4 Powder x-ray diffraction data of cys-AuNPs

The indexed X-Ray Diffraction pattern for gold nanoparticles synthesized using the Turkevich method[160,161] is shown in Figure.4.5 below. For gold nanoparticles, the characteristic peaks appearing at 2 theta = 38.06, 44.31, 64.70 and 77.88 corresponding to the (111), (200), (220) and (311) crystal planes of gold nanoparticles agree with the data reported in JCPDS 00-001-1172. The average crystallite size, determined by the Scherrer method, was observed to be 17 nm. The x-ray diffraction diffractogram was compared with that of gold as described by the International Centre for Diffraction Data (ICDD) from the JCPDS file (04-0784) (Gopalakrishnan and Raghu, 2014).[162] These results showed that the synthesized gold nanoparticles were crystalline in nature. Similar diffraction angles were observed by Choi et al. (2014)[163]with the use of catechin as a reducing agent. The unassigned peaks were similar to those observed in a study by (Philip et al. 2011)[164] which suggest that the stabilization of the nanoparticles occur at the surface of the NPs. The sharpness and intensity of the peak (111) suggests that the orientation of the synthesized nanoparticles occurs predominantly in the (111) crystal lattice plane. Similar diffraction angles have been reported for gold nanoparticles

formed using cumin and gum Arabic (Shalaby et al. 2015).[165](Figure.4.5)

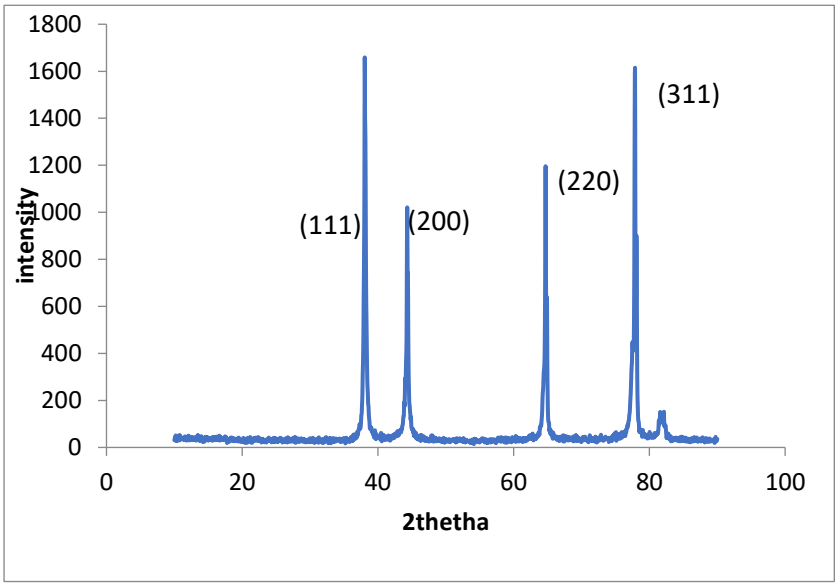

Figure. 4.5: Powder x-ray diffraction patter of cys-AuNPs

4.2.5 Transmission electron microscopy of cysteine capped gold nanoparticles

Transmission electron microscopy (TEM) of the cys-AuNPs has been measured by TEM imaging software. From the sizes of a great number of particles, measured on the TEM images, the following characteristics were estimated: average size (diameter): 10-20 nm, in very good agreement with the pXRD data (17 nm average). TEM images for cys-AuNPs show aggregates of nanoparticles (Figure.4.6). As a characteristic for the cys-AuNPs, it is to be observed that the nanoparticles are mostly linearly arranged, but also united in a more ordered rather complex network and are found to be spherical in appearance. Gold nanoparticles synthesized at elevated temperature are not exclusively spherical but also triangular, hexagonal and trapezoid gold nanoparticles have been observed.[166]Reaction times of 20–30 min have also been observed to form spherical, triangular, hexagonal, and trapezoid gold nanoparticles. Siddiqi and Husen, 2017).[166] The structure of the cysteine stabilized gold nanoparticles appears to be mono-distributed which might be as a result of the lesser number of organic molecules at the surface of the nanoparticles (see sections 4.2.3, 4.2.7 and 4.2.8), therefore the cysteine stabilized gold nanoparticles are majorly dominated by gold centre.

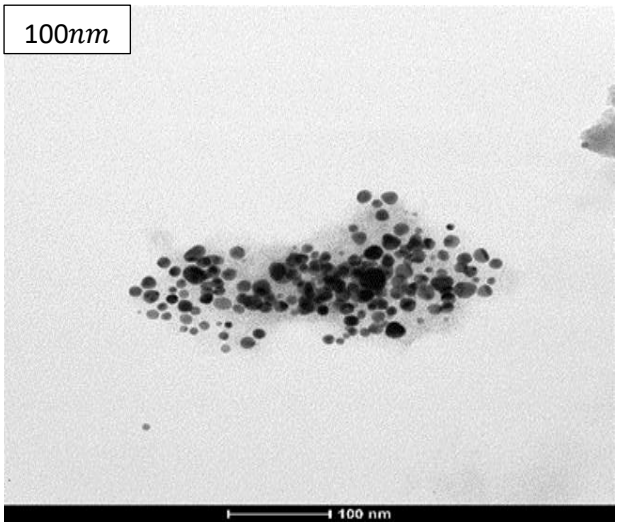

Figure. 4.6: TEM images of cys-AuNPs (100nm)

4.2.6 Scanning electron microscopy of cys-AuNPs

SEM images of the as synthesized gold nanoparticles are shown in Figure 4.7 below. SEM image shows roughly spherical clusters of gold nanoparticles with an average size of about 200 nm. After the reduction of gold ions, the gold nanoparticles are aggregated into fairly uniform clusters in the solid state. The morphologies of the synthesized gold nanoparticle are in good agreement with those synthesized by Mohsen et al. 2015.[167]

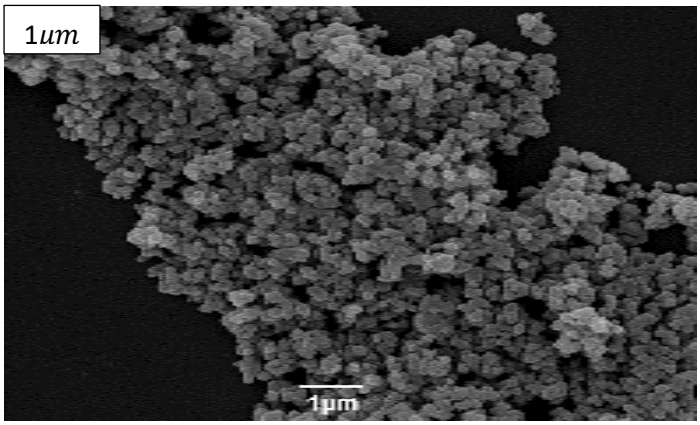

Figure. 4.7: SEM images of cys-AuNPs

4.2.7 Thermal analysis of cys-AuNPs

The thermal stability of the synthesized gold nanoparticles was determined by monitoring the weight loss over time with increasing temperature. Overall, very little mass is lost (slightly less

than 1 %, in comparison to the 6 % and 66 % lost in the case of cysteine stabilized AgNP. The information provided by the TGA suggest few organic compounds at the surface of the nanoparticles and this is consistent with the Fourier transform infrared spectra of the synthesized gold nanoparticles. (Figure. 4.8)

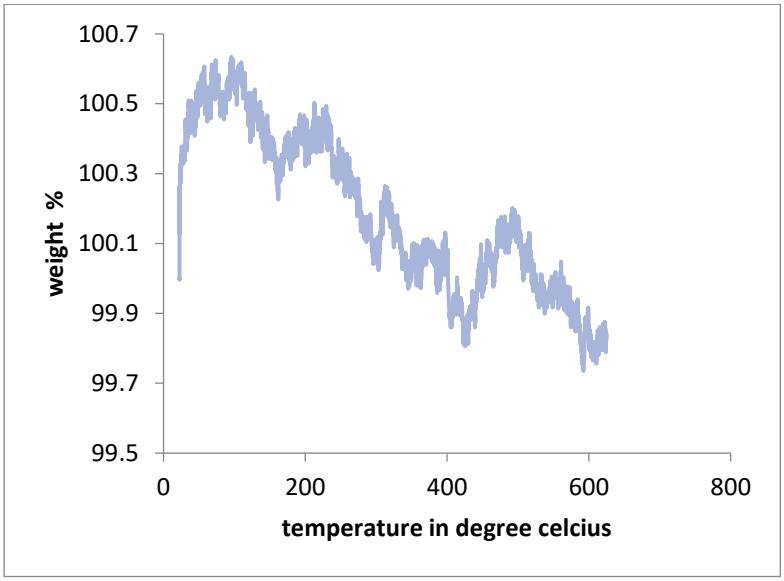

Figure. 4.8: Thermogravimetric analysis of cys-AuNPs

4.2.8 Micro analysis of cysteine stabilized gold nanoparticles

The elemental analysis results revealed that there are only trace amounts of organic molecules at the surface of the cysteine stabilized gold nanoparticles, this result agrees with the thermal analysis result and the Fourier transform infrared spectroscopy results. (Table 4.1**)**

sample	%C	%H	%S	%N	%Inorganic
cys-AuNPs	1.62	0	-	-	98.39

Table. 4.1: microanalysis of cys-AuNPs

4.2.9 Structural summary for cys-AuNPs

TEM images show well defined and roughly spherical gold nanoparticles have successfully been formed. Their diameters are in the range 10-20 nm. pXRD confirms crystallinity of the gold core, and an average size of 17 nm, in excellent agreement with the TEM imaging. In contrast to the Ag systems, there is no detectable cysteine on the surface. The nanoparticles are not stabilised by cysteine to any significant extent - these fits with the reduction in LSPR intensity over 100 minutes too. So, the structure is only the metal NP Given the alternative

routes to AuNPs covered in the following chapters, the name cys-AuNPs will be retained, to indicate the synthetic route.

4.3 Interaction of metal ions with cys-AuNPs

4.3.1 Interaction of copper, nickel and silver with cys-AuNPs

The interaction of copper by cys-AuNPs produces a bathochromic shift in the LSPR from 524 nm to 533 nm and new, relatively weak peaks were also observed at 409 nm and 695 nm. (Figure. 4.9).

The interaction of nickel with cys-AuNPs causes a slight bathochromic shift in the LSPR from 522 nm to 525 nm, an additional peak was also observed in one sample at 708 nm. (Figure. 4.10)

The interaction of silver by cys-AuNPs exhibit a LSPR at 533 nm and additional peak of silver (Ag) was also observe at 413 nm. (Figure. 4.11)

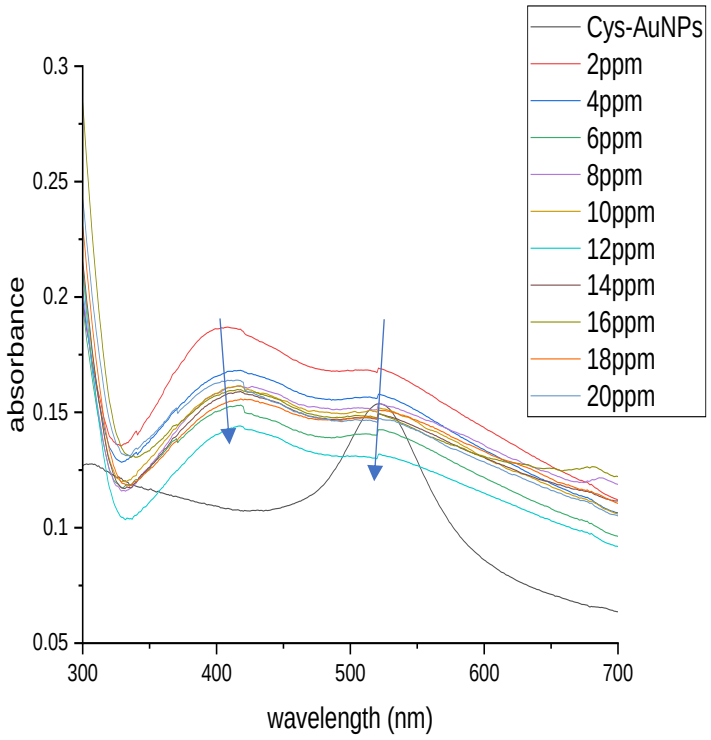

Figure. 4.9: UV/Visible spectra of detection of copper (2-20 ppm) by cys-AuNPs

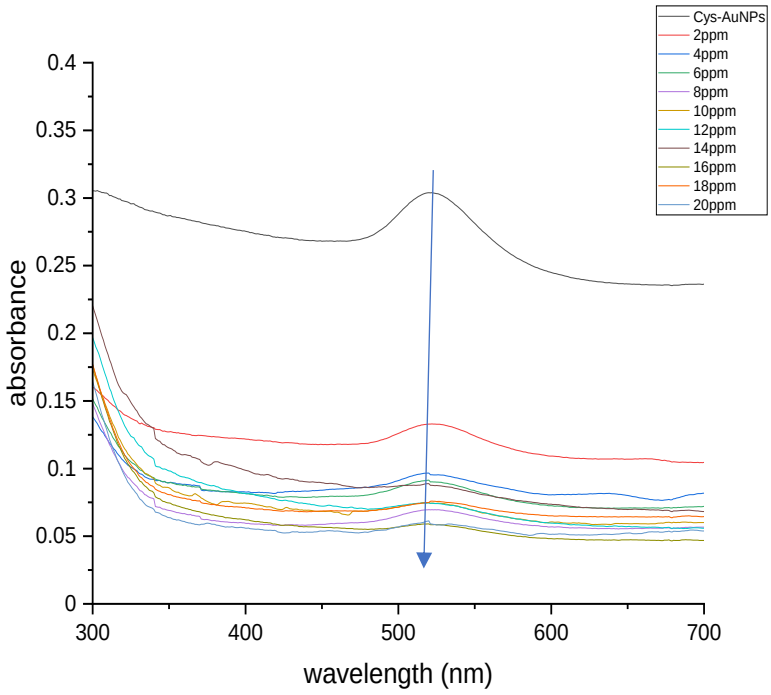

Figure. 4.10: UV/Visible spectra of detection of nickel by cys-AuNPs and nickel (2-20 ppm)

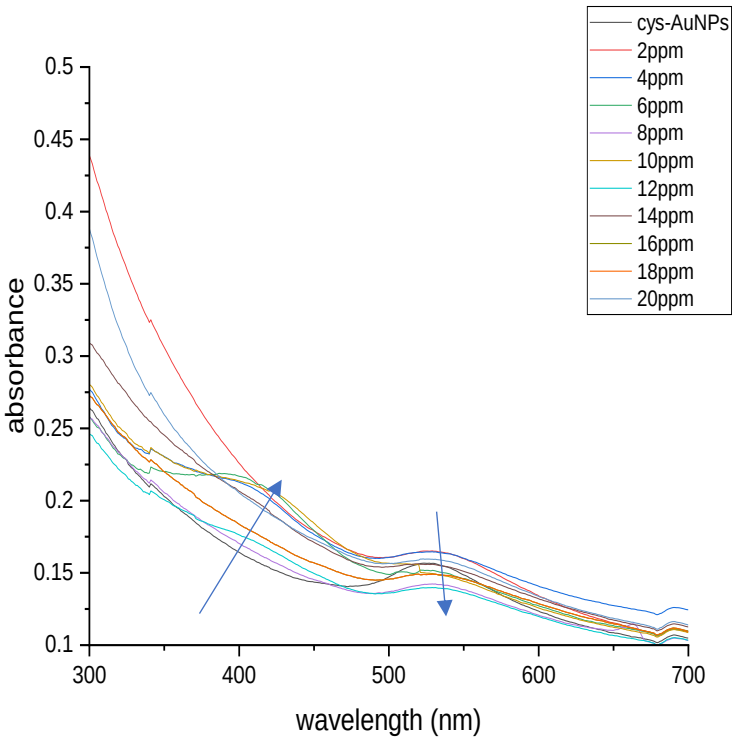

Figure. 4.11: UV/Visible spectra of Ag(I) ions interacting with cys-AuNPs

4.3.2 Results and discussion on the adsorption of Cd(II),Cu(II) and Pb(II) by cys-AuNPs

4.3.2.1 Effect of initial concentration

The adsorption of Cd(II), Cu(II) and Pb(II) shows similar behaviour as those obtained in EtOH-cys-AgNPs, the qe obtained for each metal ion increases as the initial concentration increase at the stage there is availability of vacant sites on the cys-AuNPs and the metal ions are able to adsorbed onto the surface, thereby leading to an increase in the value of qe. (Figure 4.12)

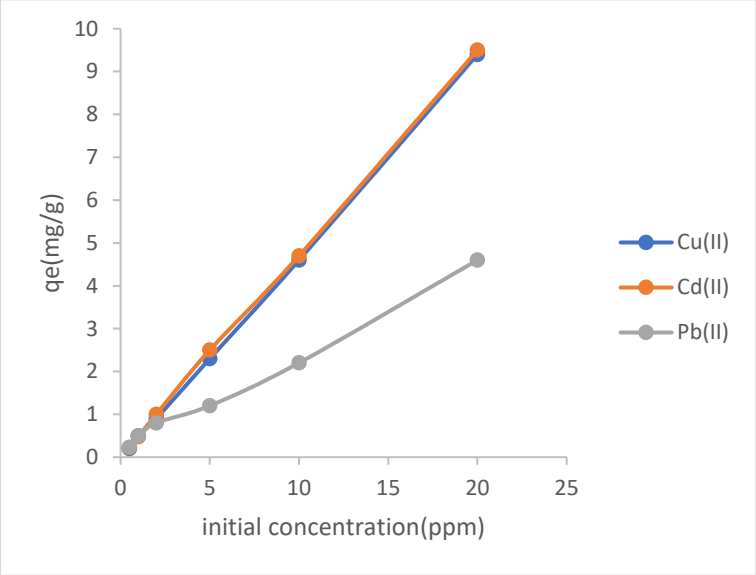

Figure. 4.12: Effect of initial concentration plot of adsorption of Cu(II), Cd(II) and Pb(II) by cys-AuNPs

4.3.2.2 Effect of contact time

The adsorption of Cd(II) and Pb(II) by cys-AuNPs shows adsorption reaches equilibrium at 40 minutes and Cu(II) at 60 minutes remains constant from then till 1440 minutes. Similar adsorption equilibrium time was also observed for EtOH-cys-AgNPs. This is also attributed to the availability of vacant sites on gold and silver NPs and their ability to adsorb the metal ions quickly, though the value of the qe for each metal ion varied for the two adsorbents. The qe values obtained for Cu(II), Cd(II) and Pb(II) ions by cys-AuNPs are 7.58 mg/g, 3.52 mg/g and 3.46 mg/g respectively. The qe values obtained for the Cu(II), Cd(II) and Pb(II) ions adsorption by EtOH-cys-AgNPs were 6.4 mg/g,4.62 mg/g, 4.52 mg/g respectively. (Figure. 4.13-4.14)

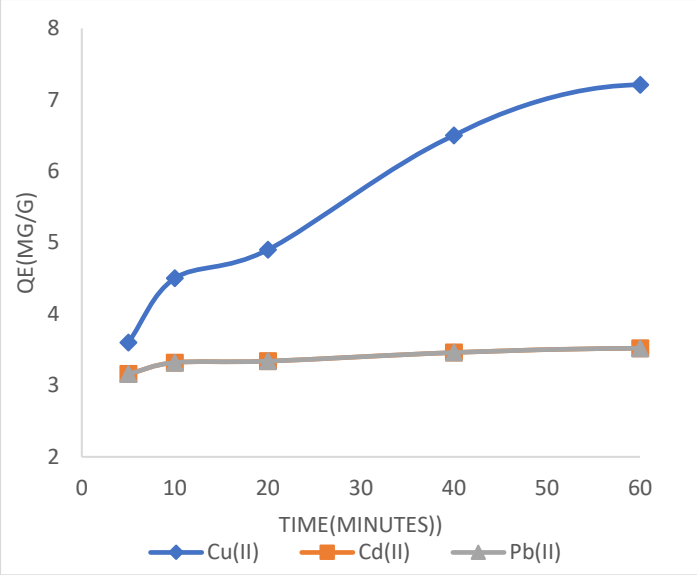

Figure. 4.13: Effect of contact time plot of Adsorption of Cu(II), Cd(II) and Pb(II) by cys-AuNPs at 5-60 minutes

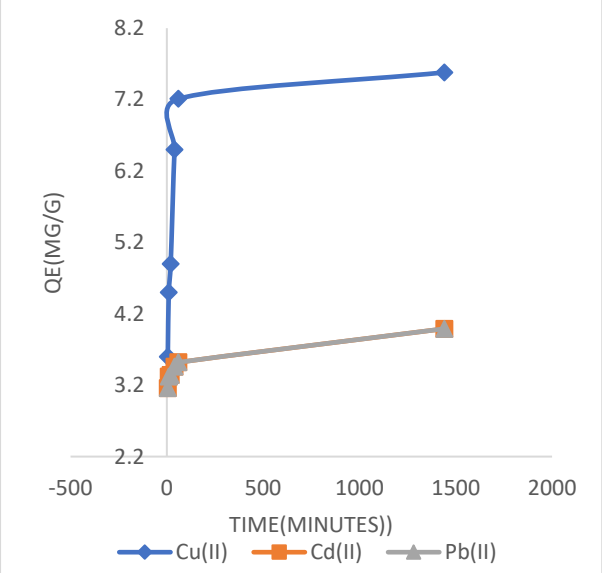

Figure. 4.14: effect of contact time plot of Adsorption of Cu(II), Cd(II) and Pb(II) by cys-AuNPs at 5- 1440 minutes

4.3.2.3 Effect of Dose

The qe for Cu(II), Cd(II) and Pb(II) ions adsorbed by cys-AuNPs decreases as the dose of cys-AuNPs rises, and this can be as a result of the nanoparticles having enough capacity at 0.01 g to adsorb all the metal in the system and thereby, as the doses increases to 0.05 g, no more ions can be adsorbed. Similar observation is also observed with EtOH-cys-AgNPs. (Figure. 4.15)

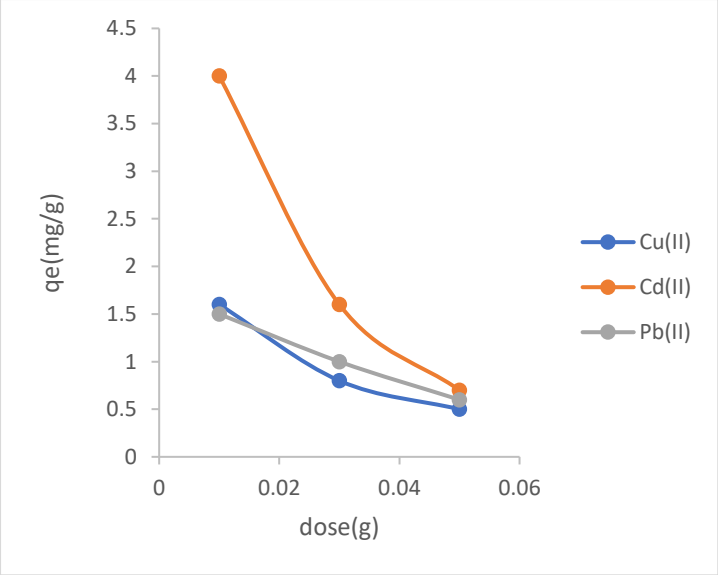

Figure. 4.15: effect of dose plot of Adsorption of Cu(II), Cd(II) and Pb(II) by cys-AuNPs

4.3.2.4 Effect of pH

The quantity of Cu(II) ions adsorbed by cys-AuNPs increase with pH and this might be due to the higher electrostatic interaction between ions of unlike charges. There is a slight decrease in the qe values for Cd(II) as the pH increases ,while for Pb(II) similar observation was observed and there has been a gradual increase in the qe values for Cu(II) has the pH increases.at a pH of 12 there exist significant amounts of hydroxide ions in solution which might have contributed to the adsorption results This might also relate to the large amount of cysteine in the Ag system meaning that even at acidic pH, there are free amine sites - Cu binds very well with amines. . Here, with far fewer cysteine molecules, the charge on the NP and the Cu species may well play a more important part (qe is also a bit lower, which also fits with the cysteine N playing a significant role. (Figure. 4.16)

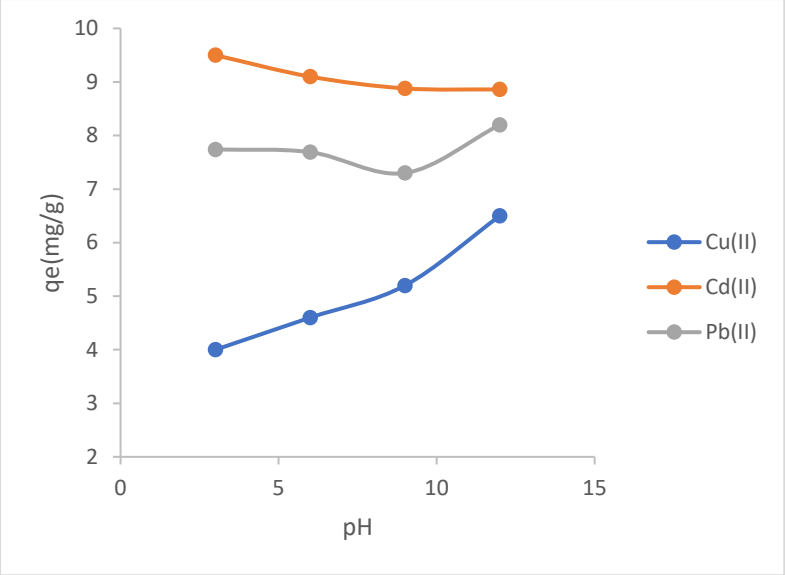

Figure. 4.16: Effect of pH on adsorption of Cu(II), Cd(II) and Pb(II) by cys-AuNPs

4.3.2.5 Effect of temperature

The qe values increases for Cd(II) and Pb(II) ions adsorption by cys-AuNPs as the temperature increases over the range of 303-363 K, The adsorption of Cu(II) by cys-AuNPs decreases with increasing temperature. (Figure. 4.17)

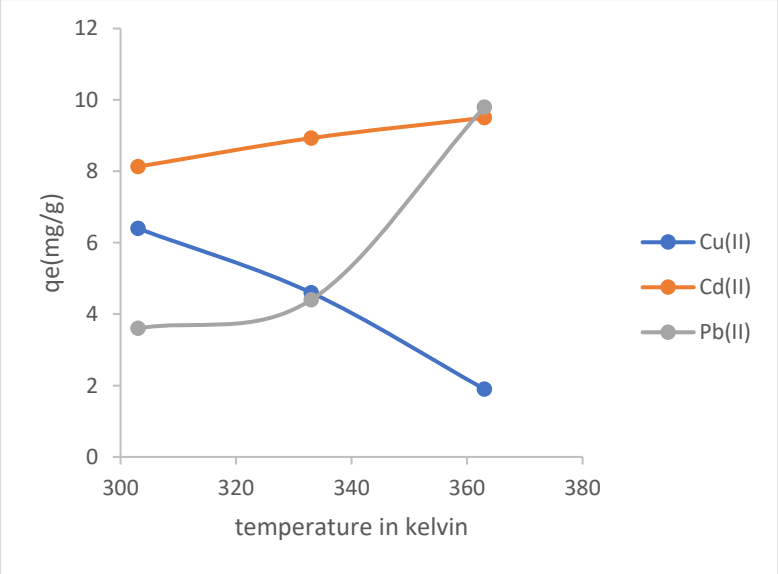

Figure. 4.17: Effect of temperature on adsorption of Cu(II), Cd(II) and Pb(II) by cys-AuNPs

4.3.2.6 Adsorption kinetics

The concept of adsorption kinetic model has been fully explained in Chapter 1 of the thesis ,all adsorption experiments by cys-AuNPs follows pseudo second order kinetic and a plot of t/qt vs time gave good R^2 values of 1 for all the three metal ions adsorbed by cys-AuNPs and thus is consistent with the adsorption of Cu(II),Cd(II) and Pb(II) by cys-AuNPs occurring vial chemisorption .Low R^2 values are obtained for the pseudo first order kinetic model, with the exception of lead with a value of 0.91. Similar adsorption kinetic pattern is also obtained for EtOH-cys-AgNPs. (Table.4.2 and Figure 4.18 and 4.19)

Metal	**Pseudo first-order R^2**	**Pseudo second-order R^2**
Cu (II)	0.2	1
Cd (II)	0.39	1
Pb (II)	0.91	1

Table. 4.2: R^2 values for the adsorption kinetics of Cu (II), Cd (II) and Pb (II) by cys-AuNPs

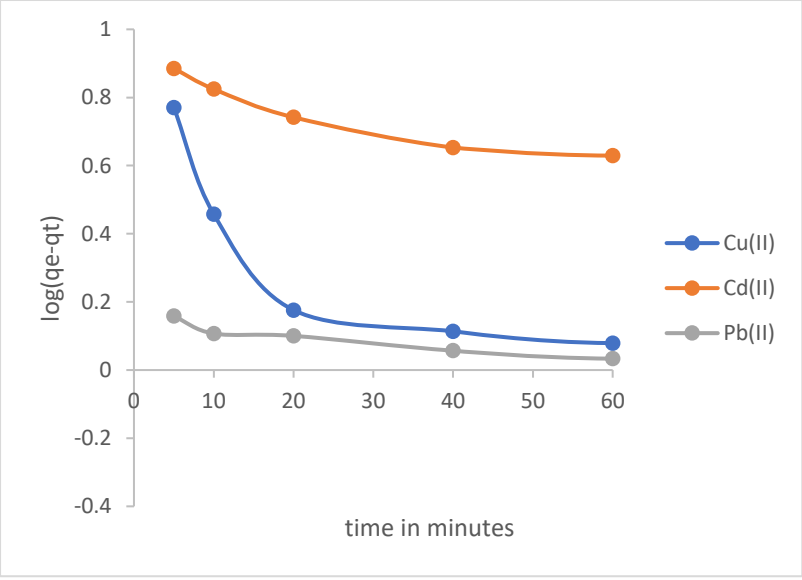

Figure. 4.18: pseudo first order plot of adsorption of Cu(II), Cd(II) and Pb(II) by cys-AuNPs at 5-60 minutes

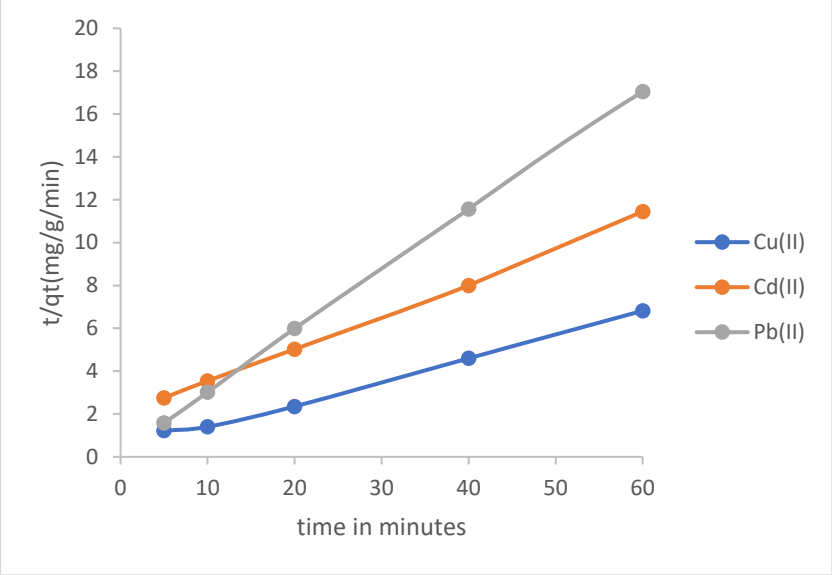

Figure 4.19: Pseudo second order plot of adsorption of Cu(II), Cd(II) and Pb(II) by cys-AuNPs at 5-60 minutes

4.3.2.7 Adsorption isotherm of Cu(II), Cd(II) and Pb(II) ions adsorbed by cys-AuNPs

The adsorption of Cu(II), Cd(II) and P(II) ions adsorbed by cys-AuNPs follows the Henry isotherm model best and this can be as a result of the low concentration ranges of the metal ions examined. The Henry isotherm is considered to be more suitable for solutes of low concentration ranges. (Table 4.3 and Figure. 4.20).

metal	Henry isotherm R^2	Langmuir Isotherm R^2	Temkin isotherm R^2	Freundlich Isotherm R^2	D-R isotherm R^2
Cu (II)	0.999	0.76	0.90	0.90	0.87
Cd (II)	0.92	$5E^{-6}$	0.72	0.86	0.72
Pb (II)	0.97	0.49	0.79	0.66	0.75

Table.4.3: Adsorption isotherm R^2 values of adsorption of Cu(II), Cd(II) and Pb(II) by cys-AuNPs

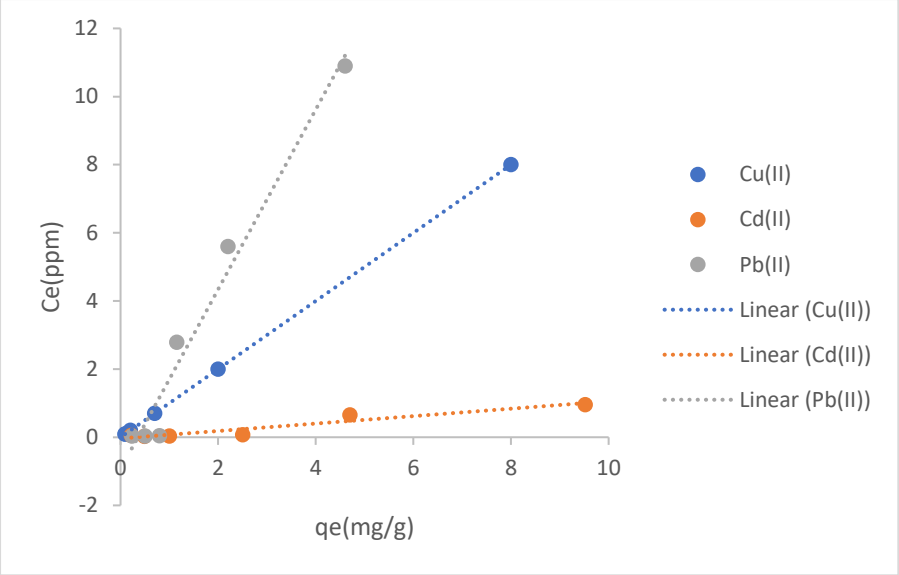

Figure 4.20: Henry isotherm plot of adsorption of Cu(II), Cd(II) and Pb(II) by cys-AuNPs

4.3.2.8 Adsorption thermodynamics

The thermodynamics of Cu(II) and Pb(II) adsorption by cys-AuNPs shows that the adsorption process occurs endothermically with a negative value of entropy suggests decrease in degree of disorder in the adsorption process. This is significantly different to what was seen with Ag, and may suggest a different mechanism of adsorption (possibly reflecting the very low amounts of organics on the surface of the Au system). The adsorption of Cd(II) by cy-AuNPs suggests a spontaneous process and there is an increase in the disorder overall, more similar to the majority of systems investigated with the cys-AgNPs. (Figure. 4.21 and a highlight of the values from the adsorption thermodynamics parameters are listed in Table 4.4)

metals	**ΔG (kJ/mole)**	**ΔS(J/Mol / K)**	**ΔH (kJ/mole)**	**slope**	**intercept**
Cd (II)	-47.2	81.6	-22.89	-2754.5	9.8172
Pb (II)	38.6	-61.69	20.24	2435.7	-7.4211
Cu (II)	24.1	-38.2	12.79	1539.4	-4.693

Table. 4.4: Adsorption thermodynamics of adsorption of Cu(II), Cd(II) and Pb(II) by cys-AuNPs

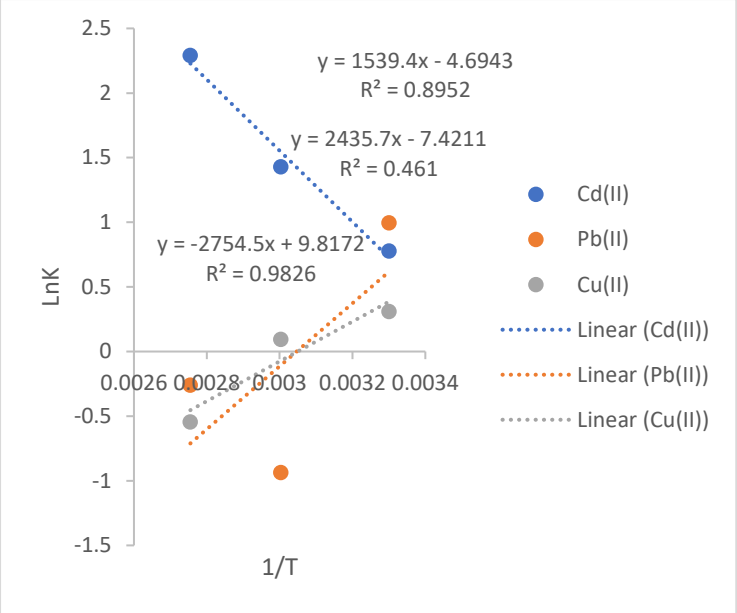

Figure. 4.21: Adsorption thermodynamics of Cu(II), Cd(II) and Pb(II) by cys-AuNPs

4.4 Results and discussion on the role of chelating agents in the adsorption of Ni{NO_3^-, SO_4^{2-}, Cl^-} and Ni{NO_3^-, SO_4^{2-}, Cl^-}-EDTA by cys-AuNPs

4.4.1 Effect of initial concentration

The adsorption of the Ni{NO_3^-, SO_4^{2-}, Cl^-} and Ni{NO_3^-, SO_4^{2-}, Cl^-}-EDTA by cys-AuNPs increase with the initial concentration; the value of qe for Ni{NO_3^-, SO_4^{2-}, Cl^-} adsorption by cys-AuNPs are 9.4 mg/g, 9.6 mg/g and 9.3 mg/g respectively, and this suggests that the adsorption of Ni{NO_3^-, SO_4^{2-}, Cl^-} by cys-AuNPs is not significantly influenced by the other anions present in the ..-, The adsorption of Ni{NO_3^-, SO_4^{2-}, Cl^-}-EDTA by cys-AuNPs show clearly that there is a significant influence of EDTA on the adsorption of Ni(II) by cys-AuNPs and this is very similar to what was observed with cys-AgNPs in organic solvent involving the adsorption of EDTA and NiEDTA by EtOH-cys-AgNPs.(Fig.4.22)

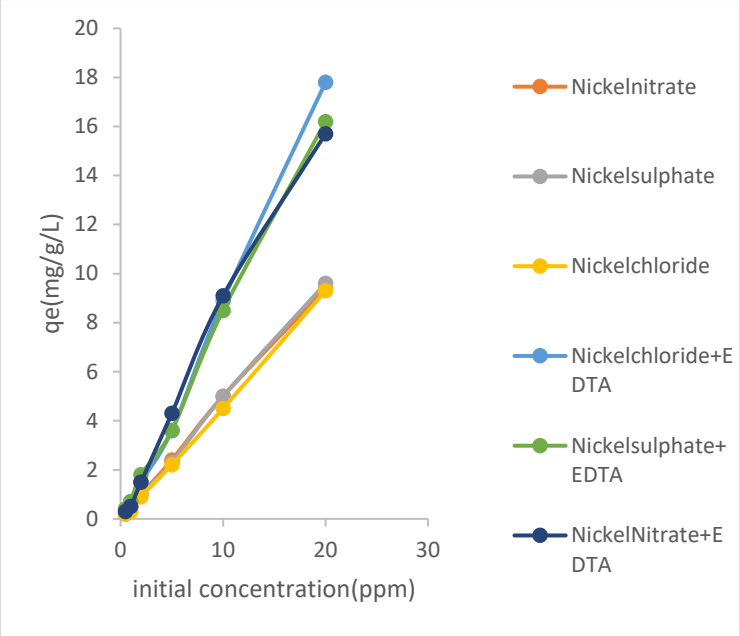

Figure. 4.22: Effect of initial concentration on adsorption of Ni {NO_3^-, SO_4^{2-}, Cl^-} and Ni { NO_3^-, SO_4^{2-}, Cl^-}-EDTA by cys-AuNPs

4.4.2 Effect of contact time

The adsorption of Ni{NO_3^-, SO_4^{2-}, Cl^-} by cys-AuNPs reaches equilibrium at 60 minutes and remains constant to 1440 minutes with qe value7.5 mg/g and 9 mg/g,8.5mg/g, and the difference in the adsorption equilibrium time might be attributed to the different sorption behaviours of the other anions in solution. The adsorption of Ni{NO_3^-, SO_4^{2-}, Cl^-}-EDTA by cys-AuNPs show the qe value to be significantly higher than the adsorption of Ni{NO_3^-, SO_4^{2-}, Cl^-} by cys-AuNPs, although the rate of adsorption is not significantly altered. Depicted in Figure 4.23, Similar behaviour was also observed with EtOH-cys-AgNPs.

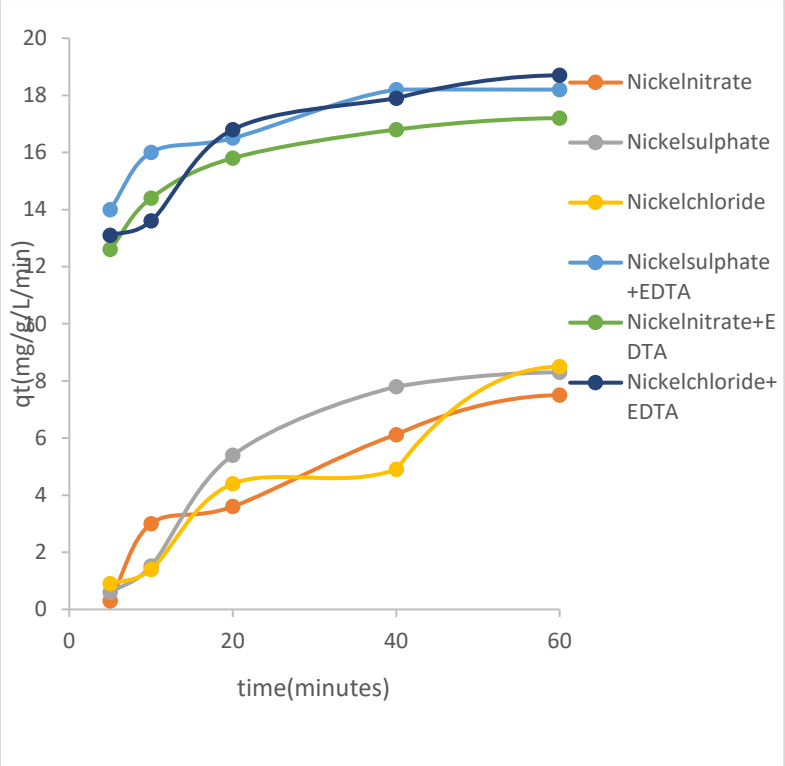

Figure. 4.23: effect of contact time on adsorption of Ni{NO_3^-, SO_4^{2-}, Cl^-} and Ni{NO_3^-, SO_4^{2-}, Cl^-}-EDTA by cys-AuNPs

4.4.3 Effect of dose

The quantity of Ni{NO_3^-, SO_4^{2-}, Cl^-}and Ni{ NO_3^-, SO_4^{2-}, Cl^-}-EDTA by cys-AuNPs again decreases with the dose of cys-AuNPs .Similar trends with the EtOH-cys-AgNPs. However, while this phenomenon generally relates to the ability of 0.01g of NP to completely adsorb the soluble metal species – meaning qe drops by a factor of 3 and 5 respectively at the higher doses – this is less obviously the case here (Figure. 4.24). The adsorption of Ni{NO_3^-, SO_4^{2-}, Cl^-}-EDTA complex decreases with the dose(g) of cys-AuNPs and there is a dramatic increase in the qe values of Ni{NO_3^-, SO_4^{2-}, Cl^-}-EDTA complex showing a possible co-adsorption of Ni and EDTA by cys-AuNPs.

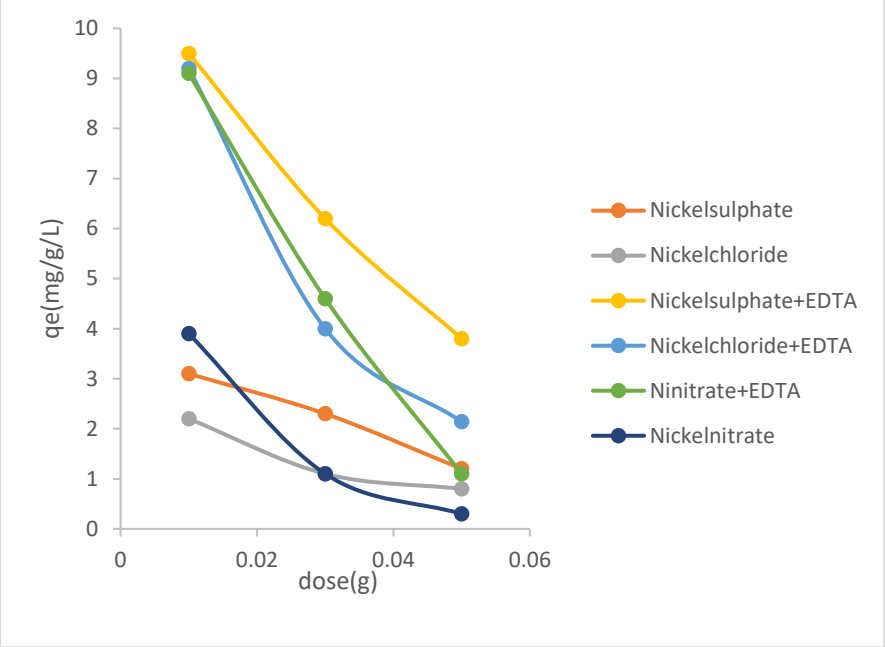

Figure. 4.24: Effect of dose on adsorption of Ni{NO_3^-, SO_4^{2-}, Cl^-} and Ni{NO_3^-, SO_4^{2-}, Cl^-}-EDTA by cys-AuNPs

4.4.4 Effect of pH

The qe values of adsorption of Ni{NO_3^-, SO_4^{2-}, Cl^-} and Ni{NO_3^-, SO_4^{2-}, Cl^-}-EDTA by cys-AuNPs are displayed in Figure. 4.25. The low adsorption values of qe obtained at lower pH values can be attributed to the higher protonation present at the adsorbent surface and thus lower attraction to the cationic species. Broadly, the EDTA complexes are anionic over the whole range, and thus have a flatter profile. Higher pH values yield more significant metal adsorption, likely due to a more favourable electrostatic interaction due to fewer protons, more substantial negative ligands on the surface, and decreased competition between the H^+ and metal cations. The qe values of adsorption of Ni{NO_3^-, SO_4^{2-}, Cl^-}-EDTA by cys-AuNPs shows the pH values maxima at a pH of 9 and remains constant for Ni{NO_3^-, Cl^-}-EDTA with qe values of 15.2 mg/g and 17.3 mg/g respectively and a sharp Increase For Ni{SO_4}-EDTA at a pH of 12 of the system, with qe values of 16.2 mg/g.(Fig 4.25) .

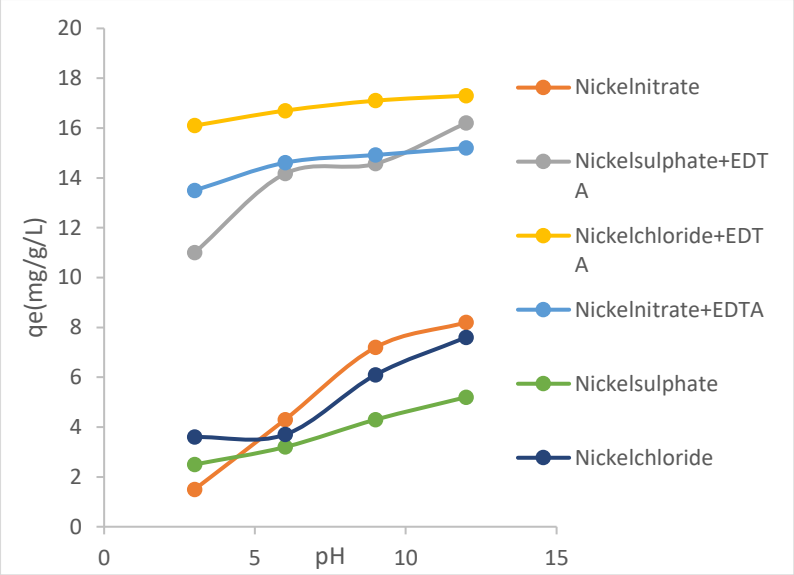

Figure. 4.25: effect of pH on adsorption of Ni{NO_3^-, SO_4^{2-}, Cl^-} and Ni{NO_3^-, SO_4^{2-}, Cl^-}-EDTA by cys-AuNPs

4.4.5 Effect of temperature

The qe values of adsorption of Ni{NO_3^-, SO_4^{2-}, Cl^-} and Ni{NO_3^-, SO_4^{2-}, Cl^-}-EDTA by cys-AuNPs increase with the temperature of the system. A similar trend is also observed in cys-AgNPs in organic solvent. (Figure. 4.26).

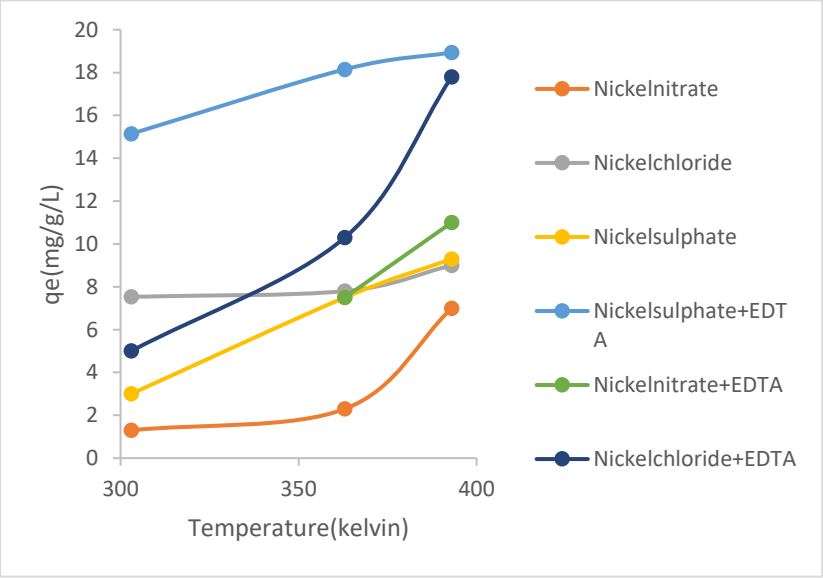

Figure. 4.26: Effect of temperature on adsorption of Ni{NO_3^-, SO_4^{2-}, Cl^-} and Ni{NO_3^-, SO_4^{2-}, Cl^-}-EDTA by cys-AuNPs

4.4.6 Adsorption thermodynamics

The Gibbs free energy and the heat of formation for adsorption of Ni {NO_3^-, SO_4^{2-}, Cl^-} and Ni {NO_3^-, SO_4^{2-}, Cl^-}-EDTA by cys-AuNPs are all negative for all the adsorption experiments and this indicate a spontaneous reaction process. List of values are depicted in table 4.5, while a plot of lnK versus 1/T are shown in figure. 4.27.

Metals	ΔG**(kJ/mole)**	ΔH**(kJ/mole)**	Δ***S*** **(J/Mol/ K)**	**slope**	**intercept**
NO_3	-68.77	-38.25	102.42	-4597.2	12.328
NO_3-EDTA	-57.7	-29.96	94.38	-3604.5	11.352
SO_4,	-5.56	-4.05	5.121	-487.96	0.6167
SO_4-EDTA	-48.72	-22.96	86.46	-2762.7	10.398
Cl_2	-32.33	-16.05	54.872	-1931.6	6.6624
Cl_2-EDTA	-84.87	-44.430	135.62	-5344.8	16.3131

Table. 4.5: Adsorption thermodynamics of adsorption Ni {NO_3^-, SO_4^{2-}, Cl^-} and Ni{NO_3^-, SO_4^{2-}, Cl^-}-EDTA by cys-AuNPs

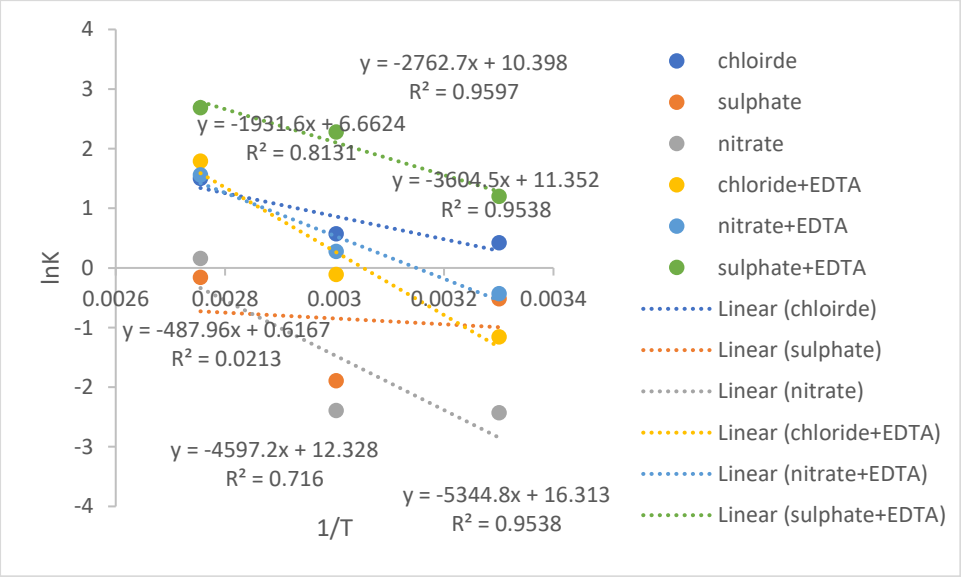

Figure. 4.27: Adsorption thermodynamics of Ni{NO_3^-, SO_4^{2-}, Cl^-} and Ni{NO_3^-, SO_4^{2-}, Cl^-}-EDTA by cys-AuNPs

4.4.7 Adsorption kinetics

The adsorption kinetic model works best with pseudo second-order kinetic model for adsorption of Ni{NO_3^-, SO_4^{2-}, Cl^-} and Ni{NO_3^-, SO_4^{2-}, Cl^-}-EDTA by cys-AuNPs ,table of

R^2-values are depicted in Table. 4.6 and figure. 4.28. The pseudo-first-order model again fits very poorly. Given these results it is suggested that the adsorption data are well represented by pseudo-second-order and the rate-limiting step of Ni{NO_3^-, SO_4^{2-}, Cl^-} and Ni{NO_3^-, SO_4^{2-}, Cl^-}-EDTA ions onto cys-AuNPs may be chemical adsorption or chemisorption and not physical sorption.

Metal-Ni (II)	**Pseudo first-order kinetic**	**Pseudo second order kinetics**
NO_3	0.458	0.9999
SO_4	0.5	0.9979
Cl_2	0.79	0.991
NO_3-EDTA	0.097	1
SO_4-EDTA	0.0157	1
Cl_2-EDTA	0.031	1

Table. 4.6: R^2-values adsorption kinetic model of Ni{NO_3^-, SO_4^{2-}, Cl^-} and Ni{ NO_3^-, SO_4^{2-}, Cl^-}-EDTA adsorption by cys-AuNPs

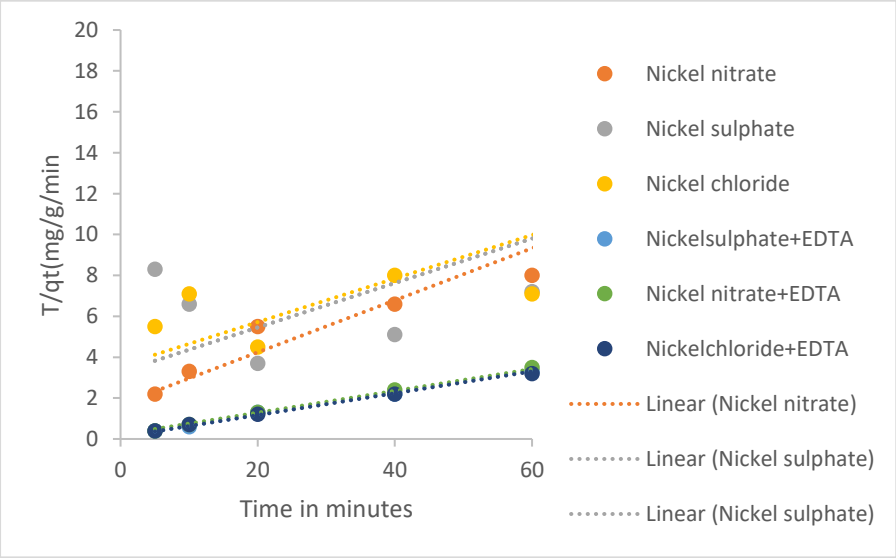

Figure. 4.28: A plot of pseudo second-order kinetics on adsorption of Ni {NO_3^-, SO_4^{2-}, Cl^-} and Ni {NO_3^-, SO_4^{2-}, Cl^-}-EDTA by cys-AuNPs at 5-60 minutes

4.4.8 Adsorption Isotherm

The R^2 values obtained from different adsorption isotherm are itemized in the table. The values obtained shows that the adsorption fits best with the Henry Isotherm for all the metals ion examined except for Ni$(NO_3)_2$}-EDTA which fits best with both Henry and the Temkin

isotherm model. Temkin isotherm model considers the effects of indirect adsorbate/adsorbate interactions on the adsorption process; it is also assumed that the heat of adsorption of all molecules in the layer decreases linearly as a result of increase surface coverage [168]. (Table 4.7 and Figure 4.29)

Metals	Henry isotherm	Freundlich isotherm	Temkin isotherm	D-R isotherm	Langmuir Isotherm
Cl_2	0.93	0.55	0.77	0.41	0.098
SO_4	0.96	0.79	0.86	0.70	0.33
NO_3	0.91	0.79	0.89	0.82	0.0768
Cl_2-EDTA	0.97	0.69	0.42	0.53	0.21
SO_4-EDTA	0.99	0.89	0.85	0.84	0.057
NO3-EDTA	0.94	0.68	0.95	0.67	0.388

Table. 4.7: R^2-values of adsorption isotherm of Ni {NO_3^-, SO_4^{2-}, Cl^-} and Ni{NO_3^-, SO_4^{2-}, Cl^-}-EDTA adsorption by cys-AuNPs

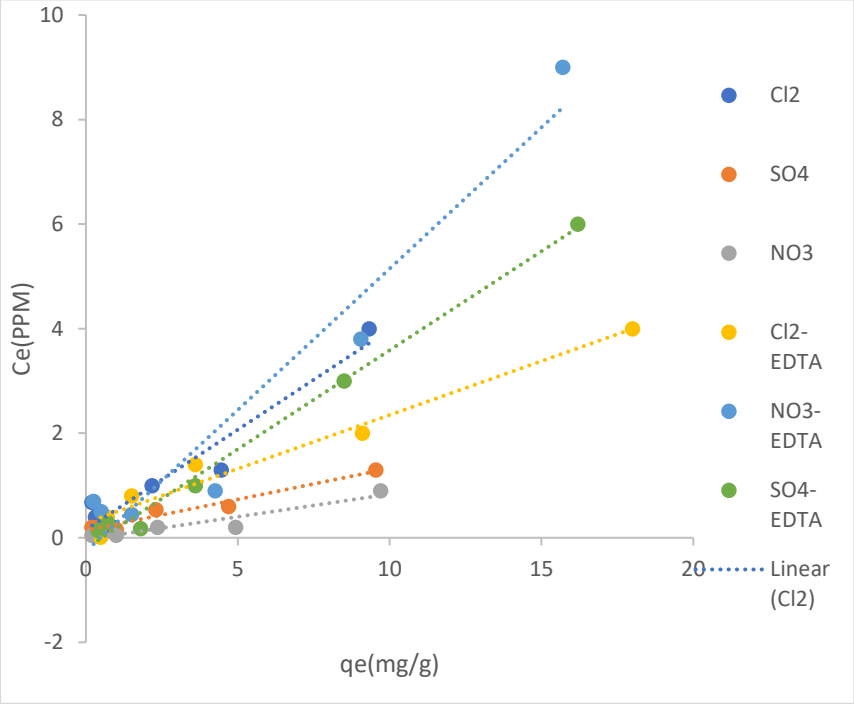

Figure. 4.29: Henry adsorption isotherm of adsorption Ni {NO_3^-, SO_4^{2-}, Cl^-} and Ni{NO_3^-, SO_4^{2-}, Cl^-}-EDTA by cys-AuNPs

4.4.9 UV/Visible spectroscopy of Ni{SO_4} and Ni{SO_4}-Na

The UV/Visible spectroscopy of $NiSO_4$ and $NiSO_4$- in the presence of sodium ions were measured in order to investigated any possible influence of the Na counterions of EDTA in the adsorption process .500ppm initial concentration of $NiSO_4$ were prepared with deionized water and another 500 ppm of $NiSO_4$ were prepared in 0.01M Na_2SO_4. The uv-visible spectra of the two systems suggest at most minimal involvement of the Na ions in the adsorption experiments. (Figure.4.30 and 4.31).

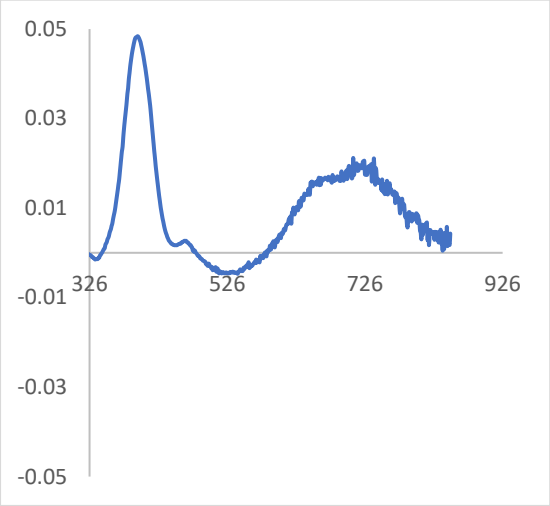

Figure.4.30: UV/Visible spectroscopy of nickel sulphate (500ppm)

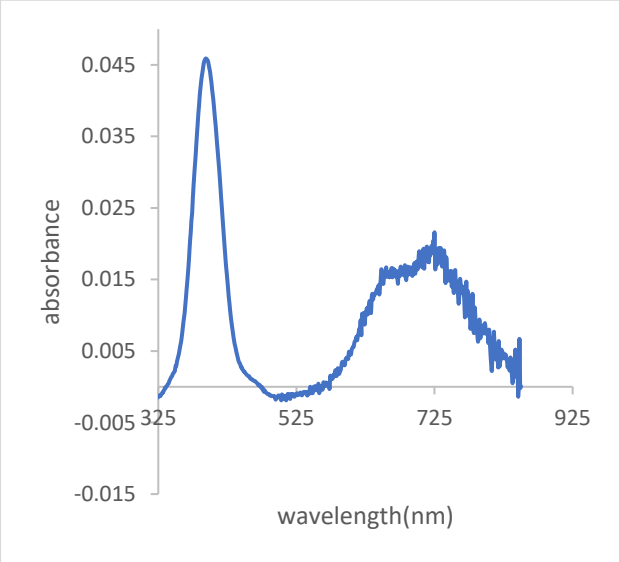

Figure 4 31:UV/Visible spectroscopy of nickel sulphate -sodium (500ppm)

4.5 Conclusion to Chapter 4

Gold nanoparticles have successfully been synthesised by reduction of Au(III) by citrate, in the presence of cysteine. While the role of cysteine was expected to be a stabiliser, and by analogy to the Ag systems in Chapter 3, would decorate the surface, this appeared not to be the case, and it was not possible to detect anything but traces of organics (whether citrate-derived or cysteine) on the surface of the nanoparticles. Despite this, stable AuNPs were formed, although the initially formed system showed a significant (ca 40%) reduction in LSPR intensity over ca. 1 hour, being stable subsequently. the adsorption behaviour is broadly similar to what was observed with the Ag system. The adsorption of Cu(II),Cd(II) and Pb(II) by cys-AuNPs ,the effect of dose suggest that 0.01g of the dose of cys-AuNPs is sufficient enough to adsorbed all the metals and this is similar to what we have in aq-cys-AgNP and ET-OH-cys-AgNPs. Similar adsorption behaviour is found in effect of pH with ET-OH-cys-AgNPs which all the three metal ions increase with the pH except for cadmium whose qe values decreases with pH.

The adsorption fits best in henry adsorption isotherm and this is similar to the ETOH-cys-AgNPs adsorption isotherm results, which suggest the adsorption energy being independent of the coverage (lack of inhomogeneities on the surface). The adsorption Kinetic fits best with Pseudo second order kinetics suggesting the adsorption process progress via a physisorption adsorption process.

CHAPTER FIVE

Result and discussion on the green synthesis, structure characterization of metal nanoparticles obtained from Jasmine green tea extracts and application towards the detection of heavy metals from aqueous solution

5.0 Green tea silver nanoparticles (GT-AgNPs)

5.1. Results and discussion on GT-AgNPs

In comparison to the conventional routes to metal NPs, which typically involve reducing agents such as $NaBH_4$ and other reagents, green routes for the synthesis of metal nanoparticles have emerged as a promising pathway, avoiding such reductants and relying on low cost, abundant natural reductants and stabilisers. In green methods, natural agents such as plant extracts, tea leaves extracts, peels and biomolecules are employed for the fabrication of nanoparticles.[169-176] These bio-directed approaches are non-toxic, reliable, cost-effective, efficient, bio-compatible, and eco-friendly. Amongst the green methods, the uses of Tea leaves extract in fabrication of metal nanoparticle is coveted process since it is simple, rapid, scalable and high yielding as the synthesis of the metal nanoparticles with tea leaves yielded a high amounts of the nanoparticles in a single pots.[177]Many researchers have reported the successful synthesis and applications of a wide variety of metal and metal oxide nanoparticles from the extract of different plants and plant parts.[178-182] The extract of green tea leaves is a popular beverage due to its flavour and anti-oxidant properties. The main constituents of tea leaves are polyphenols, caffeine, organic acids, amino acids, terpenes, and flavanols. The anti-oxidant properties of the green tea extract are accredited to the tea polyphenols, predominantly the catechins (including epicatechin, epigallocatechin, epicatechin-3-gallate, and epigallocatechin-3-gallate)[183]. and these makes them an excellent candidate for the reduction and stabilization of metal to it nano sized state.

5.1.1 Physical appearance

The colour of the GT-AgNPs is similar to the colour of cysteine stabilized silver nanoparticles (in aqueous solvent) which is a vibrant yellow. The initial colour of the extract is brown and addition of silver nitrate to the extract the solution turns yellow. (Figure.5.0)

Figure.5.0: Physical appearance of a) jasmine green tea leaves bag b) jasmine green tea extracts c) GT-AgNPs

5.1.2 FT-IR spectroscopy of GT-AgNPs

Fourier transform infrared spectra of GT-AgNPs and dried green tea powder are depicted (Figure.5.2). The spectra were explained by the linking of the absorption bands to the respective functional group presents in the compounds which are responsible for the reduction and capping of silver nanoparticles. The spectra of green tea Ag nanoparticles dried powder showed a very broad peak stretching from ca.3500 cm $^{-1}$ to almost 2100 cm^{-1} as well as sharper peaks at, 2971, 2851, 1740, 1360, 1218, 1191, and 1000 cm$^{-1.}$ As discussed earlier, green tea extracts consist of a range of molecules such as polyphenols, amino acids, organic acids such as gallic acid, catechins and caffeine. he very broad band is assigned to the O–H stretching of alcohol in polyphenols, acids and N–H stretching in amines. The bands representing sp^3 C–H stretching appear at 2971 and 2851 cm$^{-1.}$ The strong sharp bands at 1740 and 1360 cm^{-1} are assigned to C=O and C-O bonds of gallate esters or free acids found in the green tea extracts respectively; [184] the 1191 and 1000 cm^{-1} peaks represent C–O–C stretching, and the strong band at 973 cm^{-1} is assigned to aromatic C=C bending.

Changes in the spectral of chemical components of green tea dried powder and GT-AgNPs can be recognized by comparing their respective infrared spectra. All the vibrational peaks in the Green Tea dried powder spectrum were shifted in the GT-AgNPs spectrum, they tend to be narrower after reducing and stabilizing of the nanoparticles. Literature study revealed that it likely the presence of flavonoid in the green tea plays a significant and has help in reducing the silver from +1 states to zero states which is due to the abundance of the hydroxyl group which makes epigallocatechin gallate (epigallocatechin-3-gallate) a powerful antioxidant and a strong reducing agent for the nanoparticles fabrication[185],after the nanoparticles synthesis, the colloid

were dried in the oven and the powder are washed with ethanol and deionized water and further dried at 103 ^{0}C at this stage the epigallocatechin would have dissolved away.

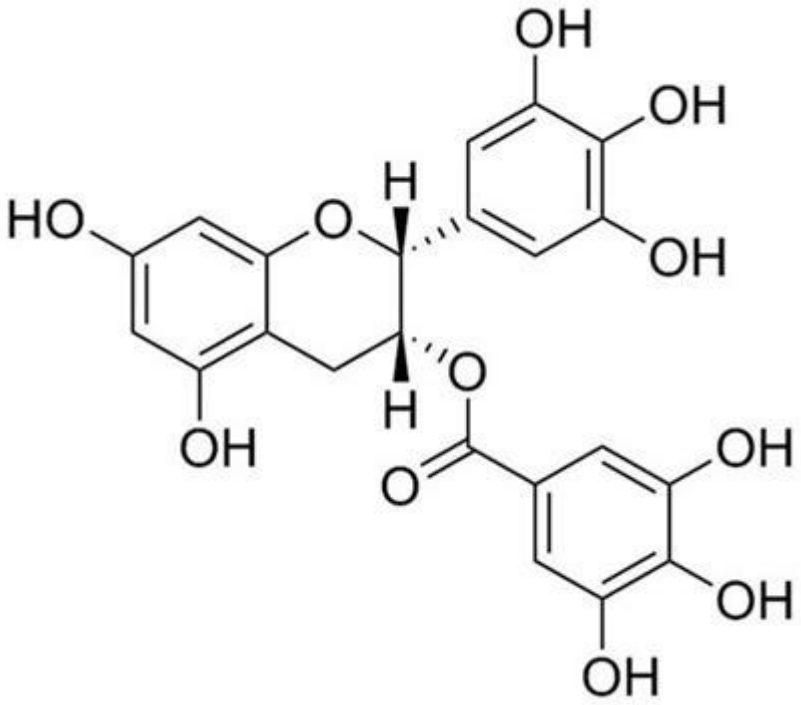

Figure.5.1: Chemical structure of epigallocatechin gallate

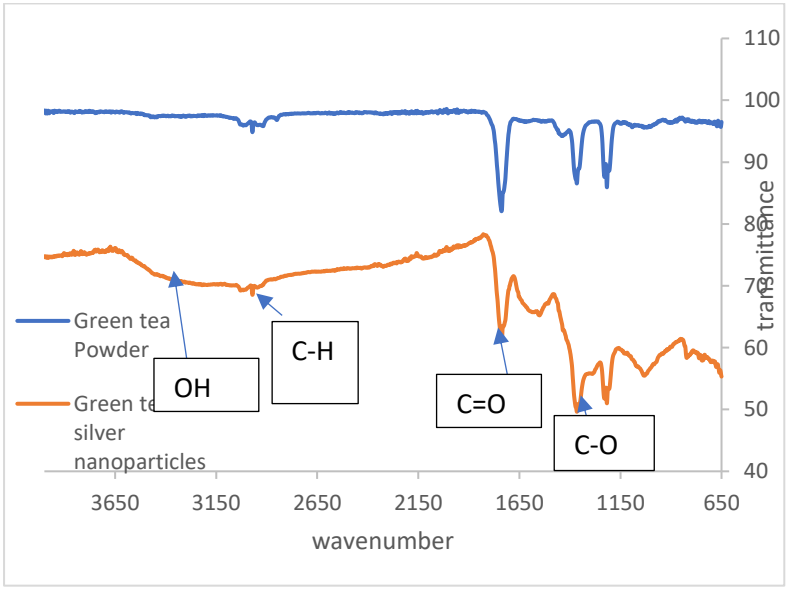

Figure.5.2: Fourier transform infrared spectra of GT-AgNPs and green tea dried powder

5.1.3 UV/Visible spectroscopy of GT-AgNPs

The LSPR was observed at 452 nm and remains stable with time. Image depicted in the figure 5.3. The silver nanoparticles absorption band are affected by the size of particles, dielectric effect, and immediate chemical environments.[186-189] Nanoparticles sized between 2 and 100 nm, is identified with a characteristic localized surface plasmon peaks.[190-192] A study published by Nazima et al.,[193] concluded that the average peak for silver nanoparticles was noticed at the range of 370- 430 nm. A research study conducted by Alomar et al., [194]focused on the use of a green chemistry technique to produce eco-friendly metal nanoparticles using Peganum harmala leaves. UV−Visible spectroscopy was employed to analysed the synthesized silver nanoparticles, and a sharp peak was detected at 350 nm for neem, aloe vera, Indian mint, and guava leaves, Alex et al.,[195]observed localized surface plasmon resonance bands of silver nanoparticles at 446, 456, 443, and 347 nm, respectively. In another study, in which Al Masoud et al., [196] prepared silver nanoparticles from ginger, an absorbance peak was observed at 434 nm, A study carried out by Rani et al., [197]saw the use of a green approach to synthesize highly stable spherical silver nanoparticles. This study involved the use of UV−Visible spectroscopy to examine the stability of nanoparticles over three months, where a sharp band between 420 and 430 nm was detected. Parit et al., [198] conducted a further green study and reported the existence of two distinct peaks at 363 and 426 nm when synthesizing non-spherically shaped silver nanoparticles. In this research, the localized surface plasmon resonance was observed at 441 nm which confirms the complete synthesis of the silver nanoparticles by the green tea extracts.

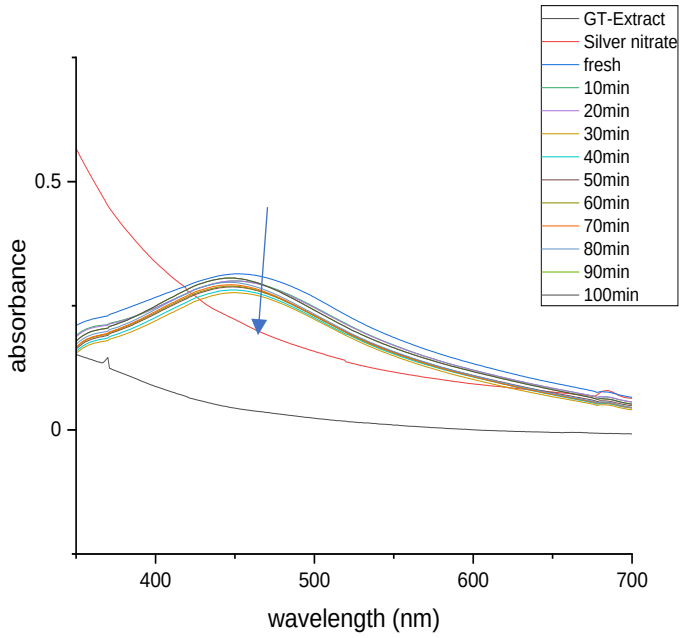

Figure.5.3: UV/Visible spectra of GT-extract, silver nitrate and GT-AgNPs and its absorbance stability measurements with time (10-100 min) at 10 minutes interval.

5.1.4 Thermal analysis of GT-AgNPs

TGA of green tea extracts and GT-AgNPs were run under nitrogen at a heating rate of 10 ^{0}C / min, and the thermogram curve of the GT-AgNPs is depicted in Figure.5.4 The TGA trace of the extracts consisted of a three-stage decomposition (after a very small water loss) leading to a residue of 17% at 600 ^{o}C. The GT-AgNPs lose around 6% by mass over the same temperature range, suggesting that the GT-AgNPs contain around 6-5% organic material, similar to the EtOH-cys-AgNPs.The thermogram of GT-extracts shows a thermal decomposition of organics compound in two stages with the first decomposition associated with decarboxylation and the second decomposition accounting for loss of organic compounds.

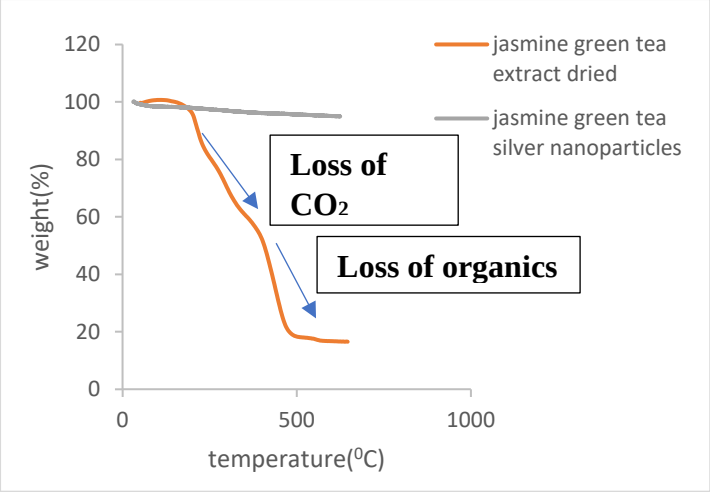

Figure.5.4: Thermal analysis of *jasmine* green tea silver nanoparticle

5.1.6 Microanalysis of GT-AgNPs

The C, H and N contents of the green tea powder and the green tea silver nanoparticles are shown in Table.5.0, the percentage carbon hydrogen and nitrogen of the green tea silver nanoparticle revealed that 18 % of the fabricated nanomaterials are organic and 82 % is the remainder component and oxygen contents. These results are in best agreement with the Powder x-ray diffraction analysis of the GT-AgNPs which suggest 84% GT-AgNPs. The PXRD software using match and find the percentage metal present in the examined sample. The discrepancies in the TGA and microanalysis data might be as a result of selective adsorption of some of the carbon rich organic compounds to the exclusion of others

Analysis	**Remainder (%)**	**%C**	**%H**	**%N**
GT-extracts	53.13	42.21	4.66	<0.3
GT-AgNPs	84	13.85	1.2	0.65

Table.5.0: Microanalysis GT-AgNPs

5.1.7 Powder X-ray diffraction of GT-AgNPs

The Powder X-ray diffraction pattern of the GT-AgNPs is depicted in the Figure 5.5 The XRD peaks at 2θ degree of 38.1, 44.3, 64.4 and 77.4 can be attributed to the (1 1 1), (2 0 0), (2 2 0), and (3 1 1) crystalline planes of the face centred cubic crystalline structure of metallic silver (JCPDS file No. 01-071-4613). Besides, the peak near 31.9 implied the possible existence of Ag_2O [198]. The difffractogram of the dried GT-AgNPs and green tea there are appearance of

peaks which are not in the diffractogram of the latter.The XRD of jasmine green tea AgNPs looks strong which is consistent with low organics comtents.

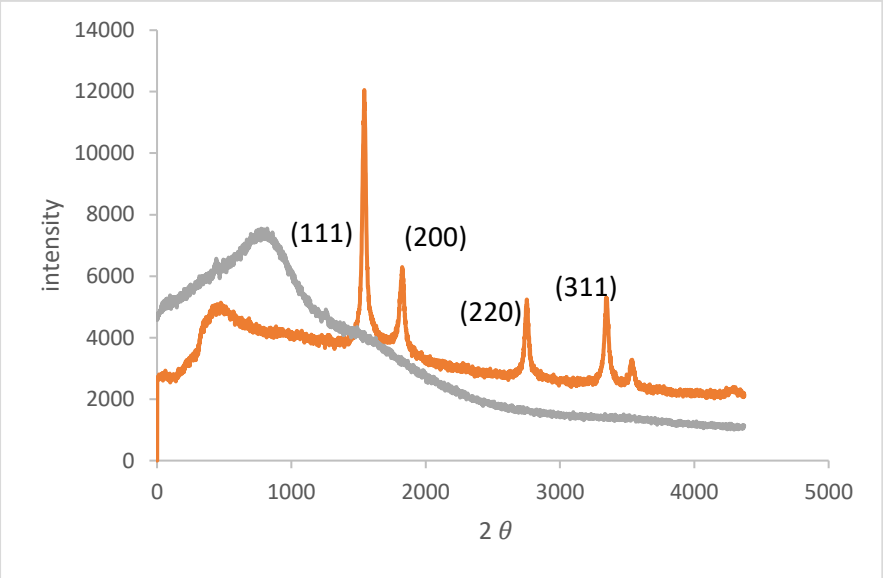

Figure.5.5: Powder x-ray diffraction of dried jasmine green tea (grey line) and GT-AgNPs (orange line)

5.1.8 Scanning electron microscopy of *jasmine* green tea silver nanoparticle

The SEM images of GT-AgNPs are shown in Figure.5.6-5.7 and the SEM of GT-AgNPs are made up of clusters of nanoparticles which are predominantly dispersed in the form of spheres. The nanoparticles were very close to each other within the formed spherical range, which may be due to the high stabilizing power of the green tea extracts. Similarly, SEM image of EtOH-cys-AgNPs is also made of clusters of NPs.

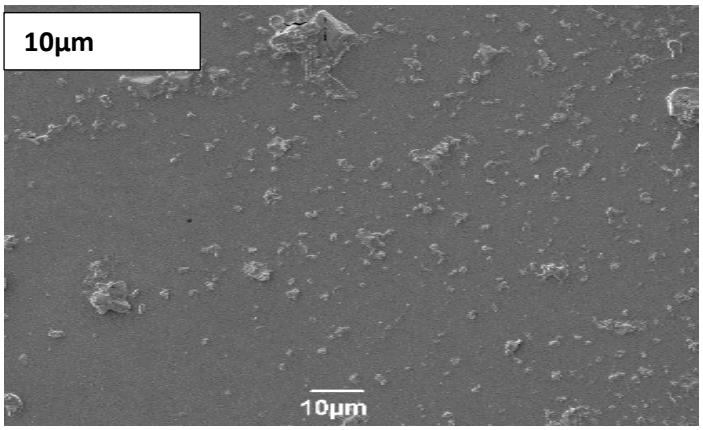

Figure.5.6: SEM images of GT-AgNPs (10µm)

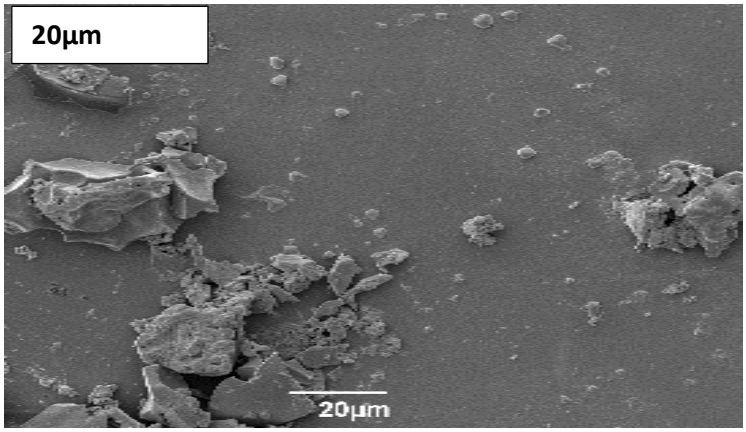

Figure.5.7: SEM images of GT-AgNPs (20µm)

5.1.9 TEM of GT-AgNPs

TEM was employed to further complement the scanning electron microscope results in order to characterize the size, shape and morphology of the GT-AgNPs. The TEM images of GT-AgNPs depicted in Figure.5.8-5.9, shows a mixture of spherical and some diamond forms. Green tea silver nanoparticles have particle sizes ranging from 20 to 90 nm. (Figure 5.8-5.9)

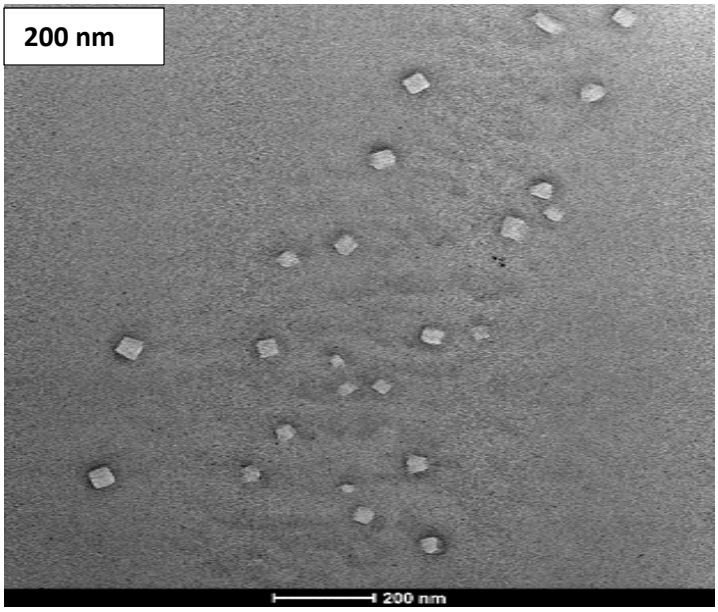

Figure.5.8: TEM images GT-AgNPs (200 nm)

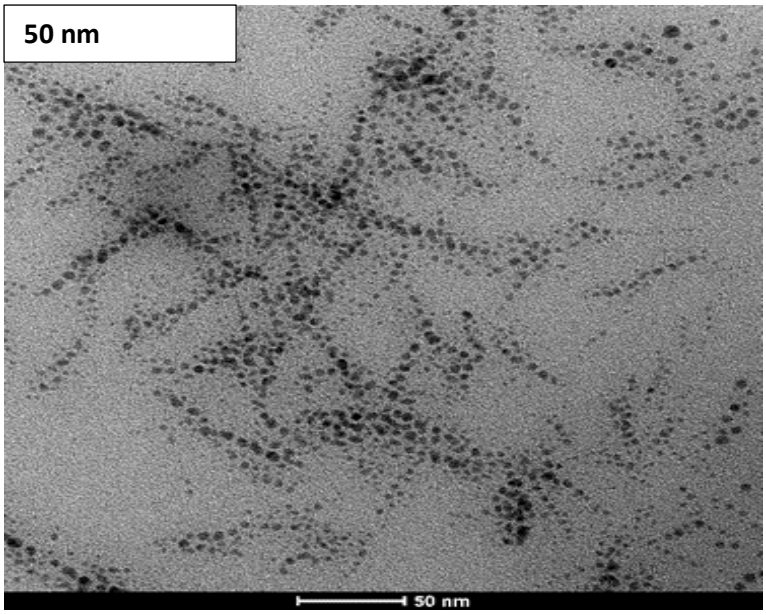

Figure.5.9: TEM images GT-AgNPs (50 nm)

5.2 Application of green tea metal nanoparticles toward the detection of heavy metals from aqueous solution

5.2.1 Detection of Ni(II) by GT-AgNPs

The interaction of Ni(II) ions with GT-AgNPs induces a slight bathochromic shift with a change in the shape of the LSPR indicating the possible detection of Ni(II) by GT-AgNPs, similar observation was made with aq-cys-AgNPs (Figure.5.10)

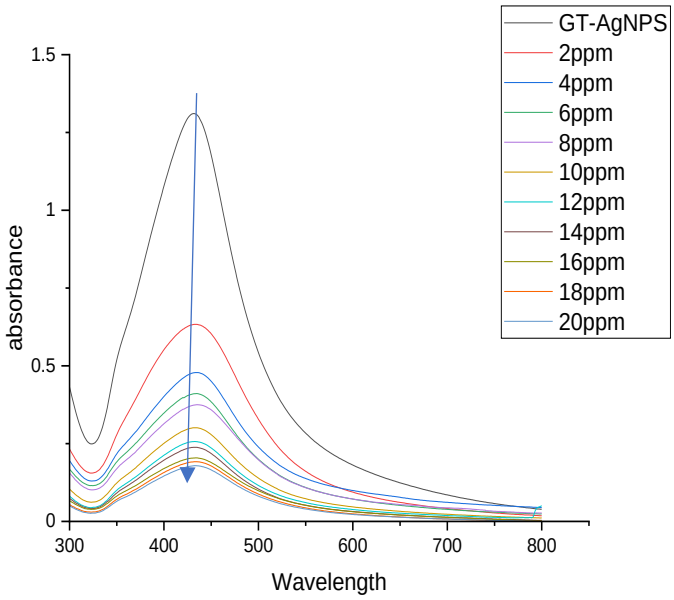

Figure.5.10:UV/Visible spectroscopy of detection of nickel (2-20 ppm) by GT-AgNPs

5.2.2 Detection of Au(III) by GT-AgNPs

the interaction of Au(III) by GT-AgNPs show a bathochromic shift in the LSPR. The visual colour observation changes from yellow to light brick red colour, the LSPR shifted from 424 nm to 446 nm. (Figure.5.11)

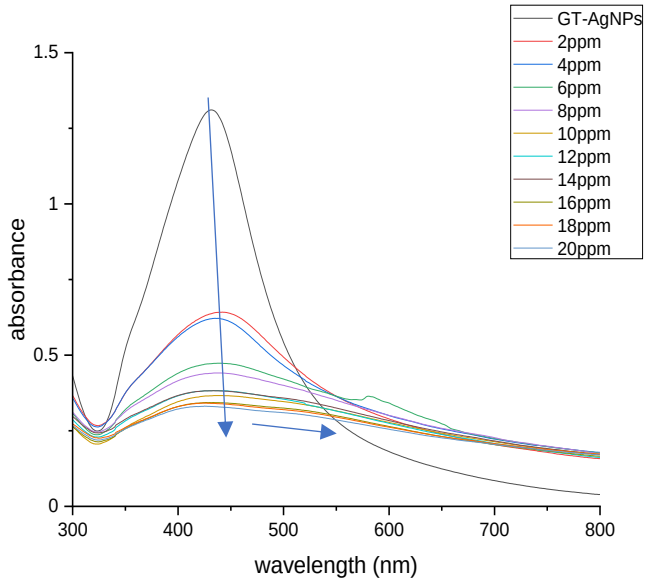

Figure.5.11: UV/Vis spectroscopy of detection of gold (2-20 ppm) by GT-AgNPs

5.3 Adsorption of Cu(II) by GT-AgNPs

5.3.1 Effect of initial concentration

The effect of initial concentration was tested on the concentration ranges between 20-800 ppm and 0.1g pf the adsorbents agitated for 2 hours after which the adsorbents were separated from the supernatant using filtration methods, the supernatant solution is analysed using UV/Visible spectroscopy. The quantity of Cu(II) ions adsorbed increased with initial concentration till 400 ppm and tends to desorbed at 800 ppm.(Figure.5.12)

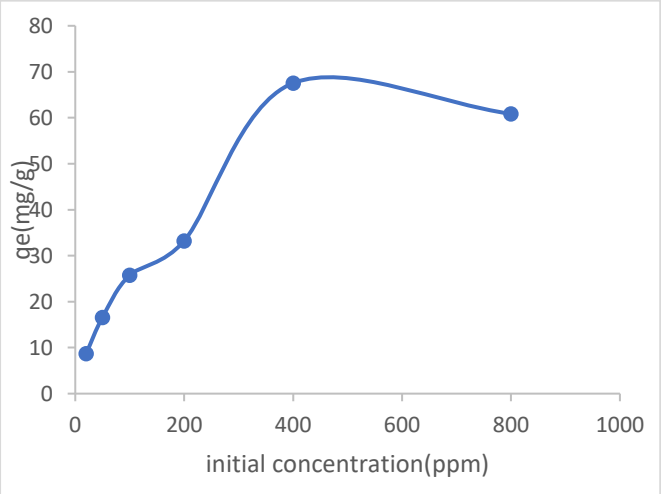

Figure.5.12: Effect of initial concentration of Cu(II) by GT-AgNPs

5.3.2 Effect of contact time at optimal dose

The quantity of Cu(II) adsorbed by GT-AgNPs was rapid at instant and reaches optimal time at 60 minutes with qe values 75mg/g at 400 ppm of Cu(II) concentration.(Figure.5.13).

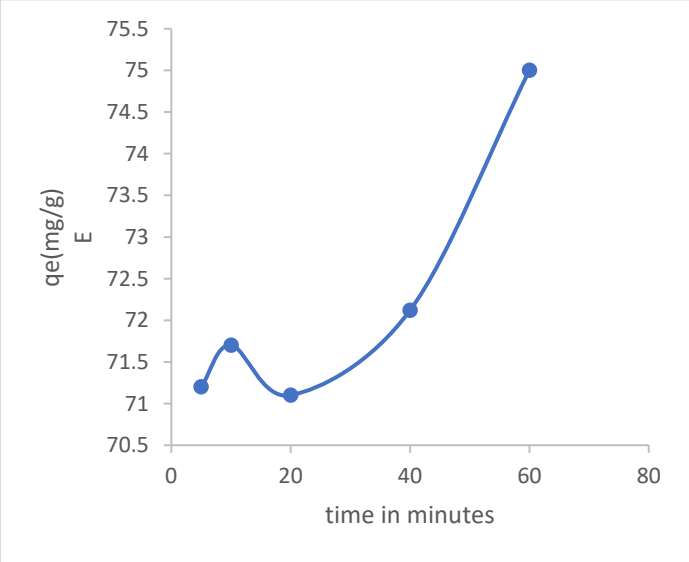

Figure.5.13: Effect of contact time of Cu(II) by GT-AgNPs

5.3.3 Effect of dose at optimal initial concentration and time

The qe of Cu(II) ions decreases with the dose of GT-AgNPs, similar trends observed in PL-AgNPs and cys-AgNPs in organic solvents. (Figure.5.14).

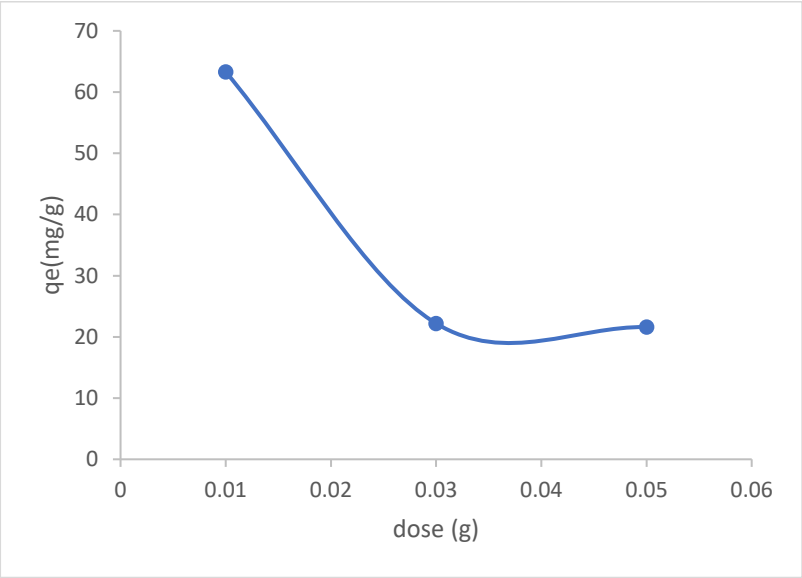

Figure.5.14: Effect of dose of Cu(II) by GT-AgNPs

5.3.4 Effect of pH at optimal initial concentration, optimal time and dose

The qe values increases for Cu(II) ions examined as expected, the reason can be attributed as a result of the high pH is been dominated by negative charge and the surface of the GT-AgNPs is also negatively charged and there exist a strong electrostatic attraction of the metal cations and the GT-AgNPs as a result of these. Depicted in Figure. 5.15. Similar trends are observed in GT-AgNPs and EtOH-cys-AgNPs.

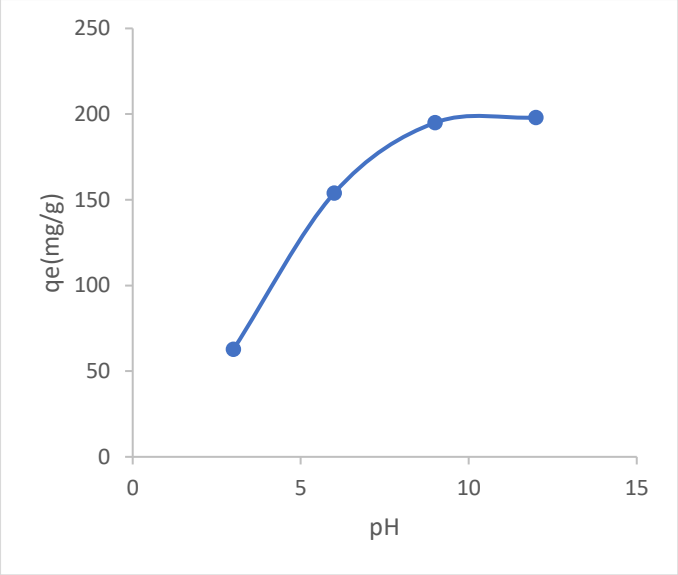

Figure.5.15: Effect of pH of Cu (II) by GT-AgNPs

5.3.5 Effect of temperature at optimal initial concentration, time, dose and pH

The qe values increases for Cu(II) ions adsorbed by GT-AgNPs increases with the temperature. Depicted in Figure. 5.16. Similar trends are observed in PL-AgNPs and EtOH-cys-AgNPs.

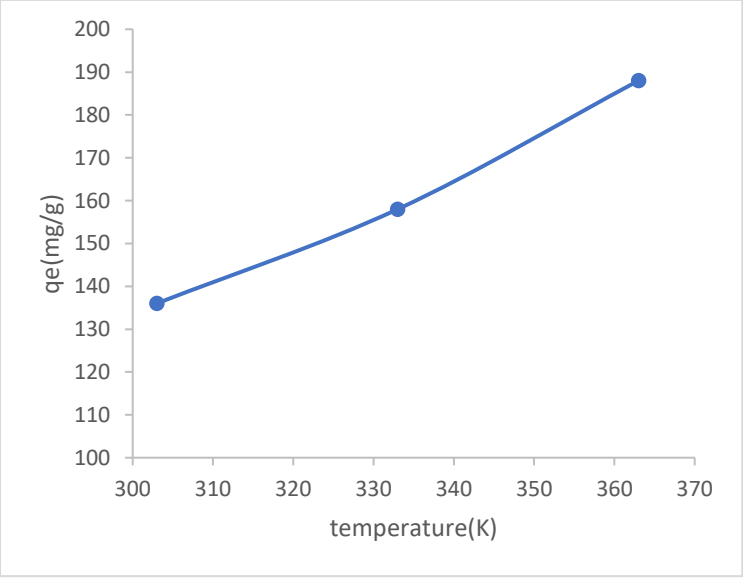

Figure.5.16: Effect of temperature of Cu(II) by GT-AgNPs

5.3.6. Adsorption isotherm

The adsorption isotherm fits best with Henry Adsorption isotherm and follow with competition with Temkin and Freundlich adsorption Isotherm. (Figure.5.17 -5.19 and Table.5.1)

Adsorption isotherm	Langmuir isotherm	Henry Isotherm	Temkin isotherm	D-R isotherm	Freundlich Isotherm
Cu (II)	0.5448	0.999	0.9498	0.6011	0.9498

Table.5.1: Adsorption Isotherm R^2 of adsorption of Cu(II) by GT-AgNPs

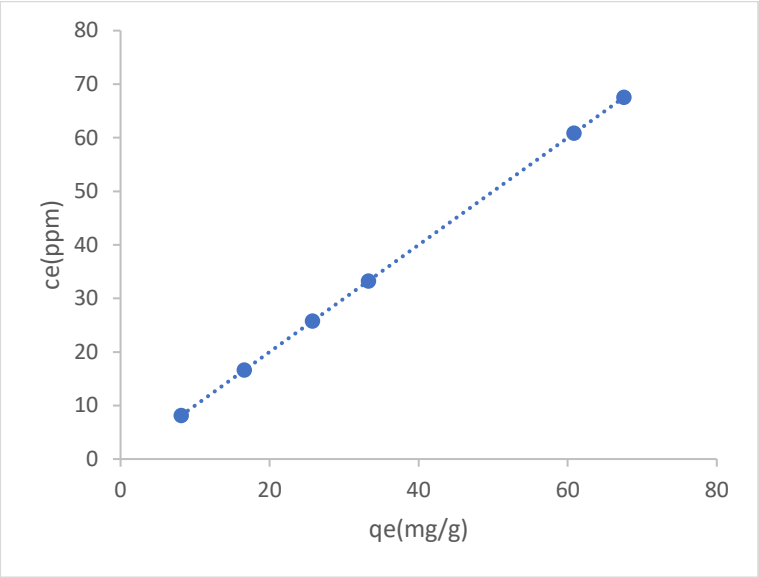

Figure.5.17: Henry adsorption isotherm of adsorption of Cu(II) by GT-AgNPs

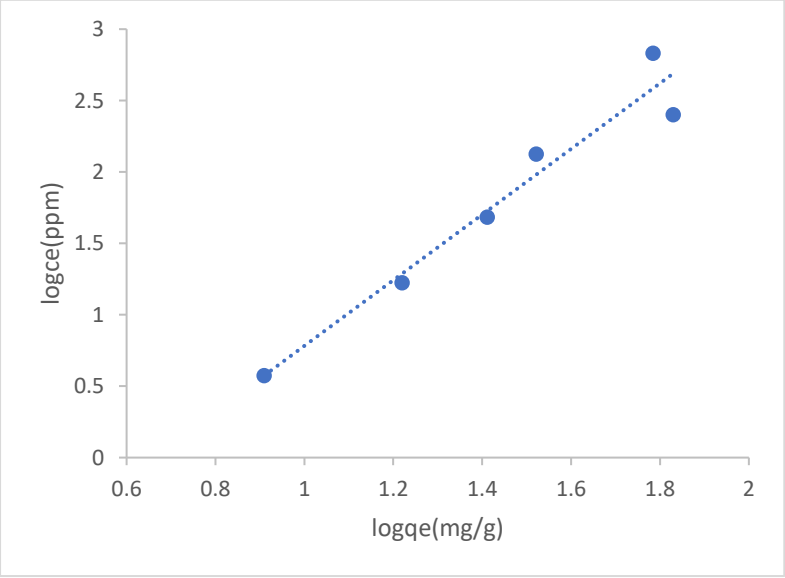

Figure.5.18: Freundlich adsorption isotherm of adsorption of Cu(II) by GT-AgNPs

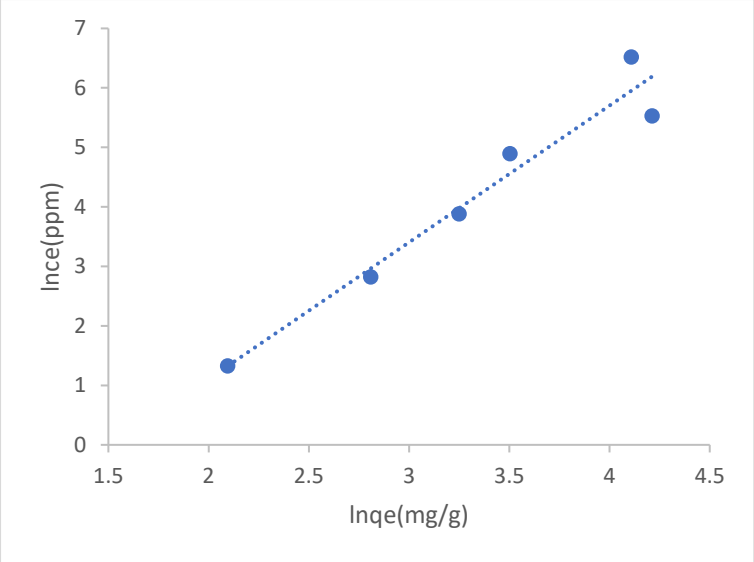

Figure.5.19: Temkin adsorption isotherm of adsorption of Cu(II) by GT-AgNPs

5.3.7 Adsorption kinetic

The adsorption fits best using Pseudo second-order kinetic model. (Figure.5.20-5.21.)

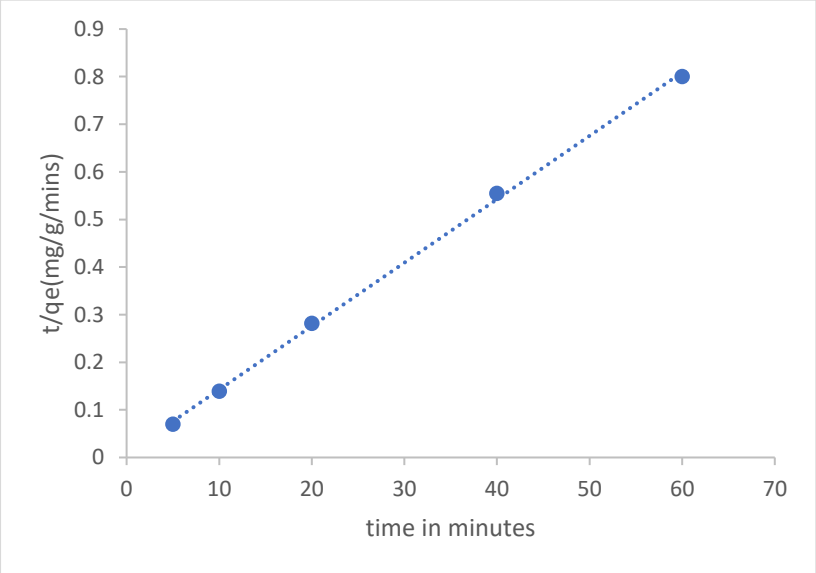

Figure.5.20: Pseudo second-order of adsorption of Cu(II) by GT-AgNPs

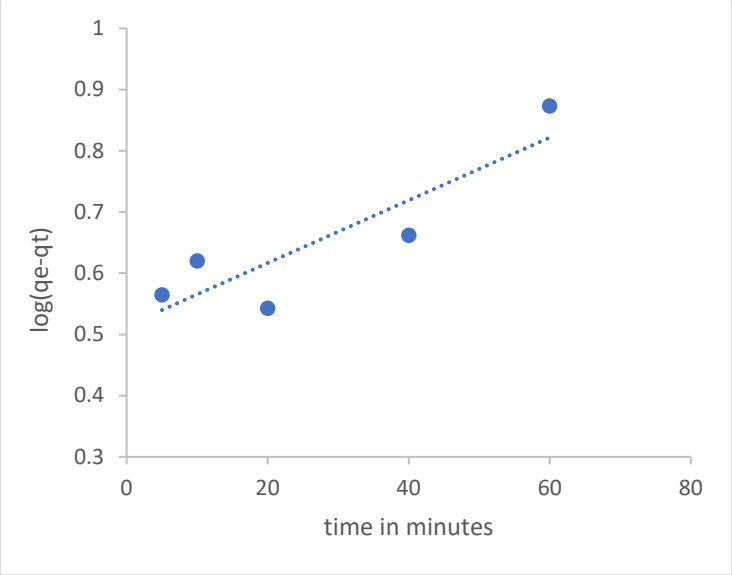

Figure.5.21: Pseudo first -order plot of Cu(II) adsorption by GT-AgNPs

5.3.8. Adsorption thermodynamic

The change in enthalpy values at -29.88 kj/mole, the change in entropy values at 97.98 J/Mol/ K and the change in Gibbs free energy give -59.08kj/mole. The adsorption of Cu(II) by GT-AgNPs suggests a spontaneous process and there is an increase in the disorder overall. (Figure.5.22).

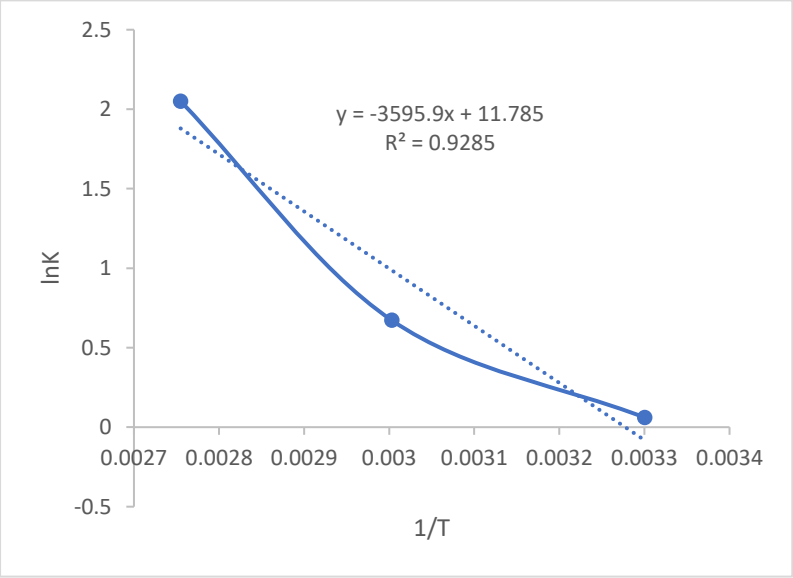

Figure.5.22: Adsorption thermodynamics of Cu(II) adsorption by GT-AgNPs

5.4 Conclusion to chapter 5

The synthesis of metal nanoparticles using jasmine green tea extracts shows the ability of the extract to reduce and capped the metal nanoparticles as this is evidenced by the various analytical tools used in the characteristics of the metal nanoparticles.

The metal nanoparticles synthesized were exposed to various metal ions at low (2-20 ppm) concentrations. In the majority of cases there was a clear change to the LSPR, which often diminished in intensity, and also shifted as is depicted in the following,

The detection of Ni(II) by GT-AgNPs Detection of Au(III) over the range 6 ppm- 20 ppm by GT-AgNPs shows a change in the yellow colour of GT-AgNPs to a reddish brown and there exists a change in the LSPR of the GT-AgNPs with a red shift.

Detection of Au(III), Cu(II) and Ni(II) by GT-AgNPs and ETOH-cys-AgNPs and aq-cys -AgNPs shows a suitable interaction with the heavy metals examined and thus no signals of gold were shown in the uv-visible spectra and thus shows the potential of the Green tea synthesized Ag-NPs and GT-AuNPs to be utilized for interaction with heavy metals.

Detection of Ag(I), Cu(II) and Ni(II) by GT-AuNPs and cys-AuNPs shows an excellent interaction property towards the detection of heavy metals and both give a better result and can be used as greener alternative to detect heavy metals.

Adsorption of Cu(II) by GT-AgNPs shows the potential to remove heavy metals from aqueous solutions.

Chapter six

Results and discussion on synthesis and structural characterization of jasmine green tea gold nanoparticles (GT-AuNPs) and application towards a portable sensor for the detection of heavy metal from aqueous solution

6.1 Physical appearance

The GT-AuNPs appears purplish-red after the synthetic process suggesting the formation of GT-AuNPs. Depicted Figure.6.0.

Figure.6.0: physical appearance of a) *jasmine* green tea bag b) *jasmine* green tea extract c) GT-AuNPs

6.1.1 Fourier transform infrared spectroscopy of GT-AuNPs

The Fourier transform infrared spectra of green tea powder and colloidal solution of GT-AuNPs was obtained immediately after the synthesis process. In order to investigate the nature of interaction between the tea extract and gold (III) ions, Fourier transform infrared spectra were carried out. Depicted in figure 6.0, it could be observed that the green tea powder consists of a weak broad peak in the region of 3454 cm^{-1} corresponding to the O–H stretch and the peaks at 2971, 2907 and 2785 cm^{-1} are assigned to the sp^3 C–H stretching vibrations of the organic constituents of the *jasmine* green tea. A band at 1739 cm^{-1} could be attributed to the C=O stretch of the acid and ester groups present in green tea powder and the peak at 1366 cm^{-1} could be assigned to the stretching vibration of carboxylate ion (–COO–). A peak at 1217 cm^{-1} shows the C-O- stretching vibration in the polyphenolic compounds and peaks at 1220 and 1000 cm^{-1}

could be attributed to the C–O and C–OH single-bond vibrations. The peaks present at 813 and 631 cm^{-1} confirm the presence of aromatic-substituted rings. In the spectra of GT-AuNPs, some changes are seem: a new peak at 1708 cm^{-1} and a slight shift in the C=O stretch from 1739 cm^{-1}, the appearance of a broad band of -OH—band in the region of 3312 cm^{-1} .The rest of the fingerprint region is broader and weaker ,but no clearly new peaks appear compared to that of green tea gold nanoparticles after the reaction with tea extract as shown below. The new peak at 1708 cm^{-1} could be due to coordinated acids and possibly also to the conversion of C–OH group to C=O group during the reduction reaction of $Au^{3+} \rightarrow Au$. A very weak intensity of the peak also mean the C-OH groups is present in a small fraction and only a tiny amount is converted to C=O group which confirms the fact that a large amount of the tea aliquot is used for the reactions.

The FT-IR spectra of GT-AgNPs and GT-AuNPs looks very similar and this can be attributed to the reduction and stabilization pattern of flavonoids present in the *jasmine* green tea.

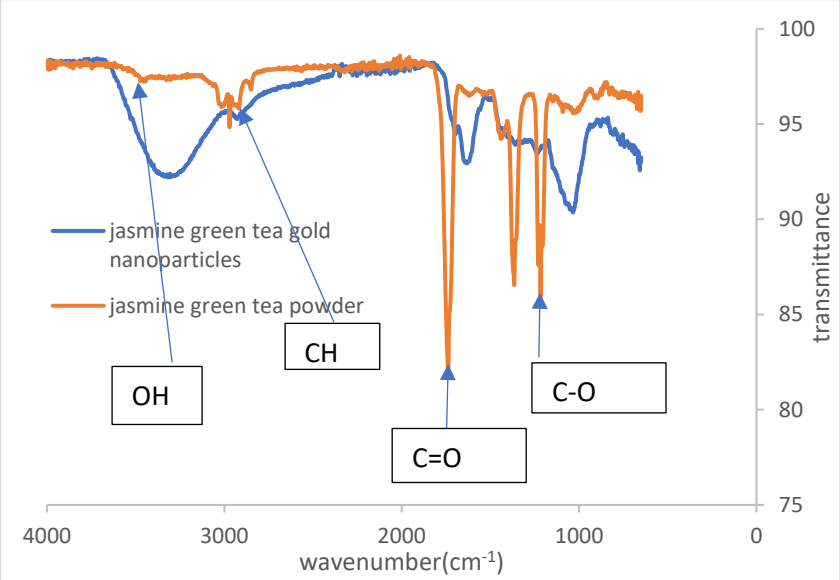

Figure.6.1: FT-IR of *jasmine* green tea(dried) and GT-AuNPs

6.1.2 UV/Visible spectroscopy of GT-AuNPs

Absorption spectra of the GT-AuNPs (Figure.6.3) reveals the existence of surface plasmon resonance wavelength at 535 nm. Presumably the flavonoids components embedded in the green tea are likely candidates for the effective reduction of gold ions to zero oxidation state gold nanoparticles, their chemical topologies permit effective encapsulation around the gold nanoparticles thus retarding aggregation and agglomeration of the nanoparticles. The recent discovery on the distinct feature of phytochemicals components in tea in initiating nanoparticle

formation is of significant value in the fabrication of greener gold nanoparticles and this has makes it useful for medical and technological applications under safe conditions.[199-205] The LSPR of the synthesized GT-AuNPs was observed at 533 nm and remain stable with time certainly and then drops.

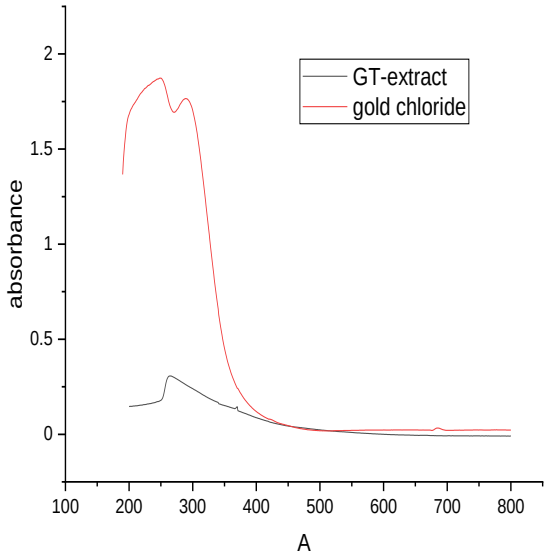

Figure.6.2: UV /Visible spectra of green tea extracts and gold chloride

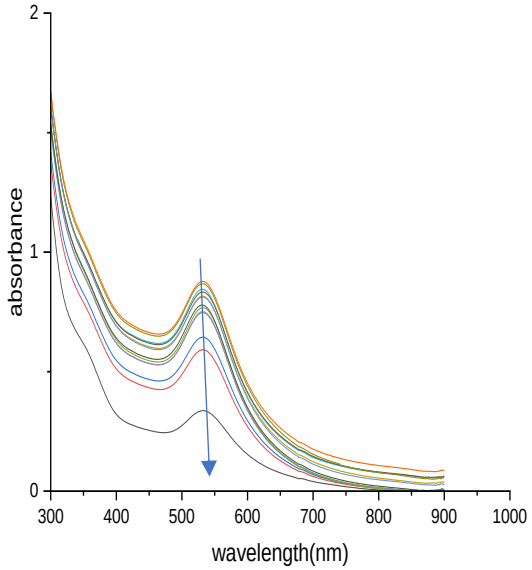

Figure.6.3: UV/Visible spectra of GT-AuNPs (10-100 minutes) at 10 minutes interval

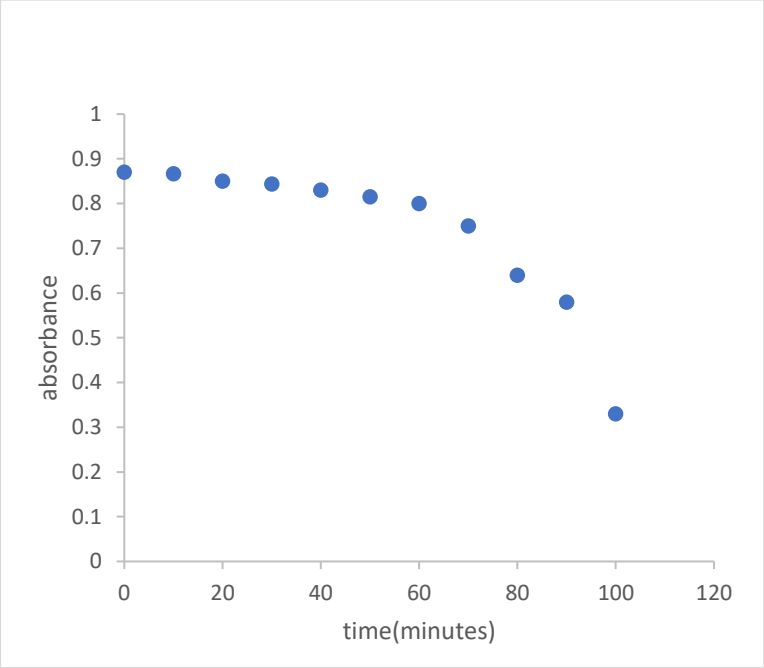

Figure.6.4: A plot of absorbance stability measurements of GT-AuNPs versus time

6.1.3 Thermal analysis of GT-AuNPs

Thermogravimetric analysis shows that the GT-AuNPs are homogenous in nature and contain a significant number of organic constituents. The first weight loss for the GT-AuNPs occurred at 180-190 °C and shows a steady weight loss in the temperature range from 180–620 °C with a total weight loss up to 650 °C which is about 50 % percent weight loss and the breakdown of the loss is as follows ,22.2.2 % and occurred at 190 °C (13 %), 200-390 °C, (10 %), and 640 °C (31.71 %). The thermograph of the GT-AuNPs is in best agreement with the research published by Hojat et al.,2018 [206]. As there is no expected weight loss over this range for gold, and it is likely that the organics decompose partly to volatiles and partly to involatile carbonaceous deposits, it appears that the organic content is at least 50 %. The thermolysis jasmine green tea extract(dried) suggest it contains 15 % water and also volatiles components. Similar decomposition behaviour at high temperature was observed with cys-AgNPs (synthesised in both aqueous and organic solvents). (Figure.6.5)

The cys-AuNPs contained 1 % of organic components at the surface of the nanoparticles, here we have a much higher number of organic components at the surface of the GT-AuNPs which suggest the excellent reducing ability of flavonoids present in the jasmine green tea to reduced and stabilize the synthesized gold nanoparticles.

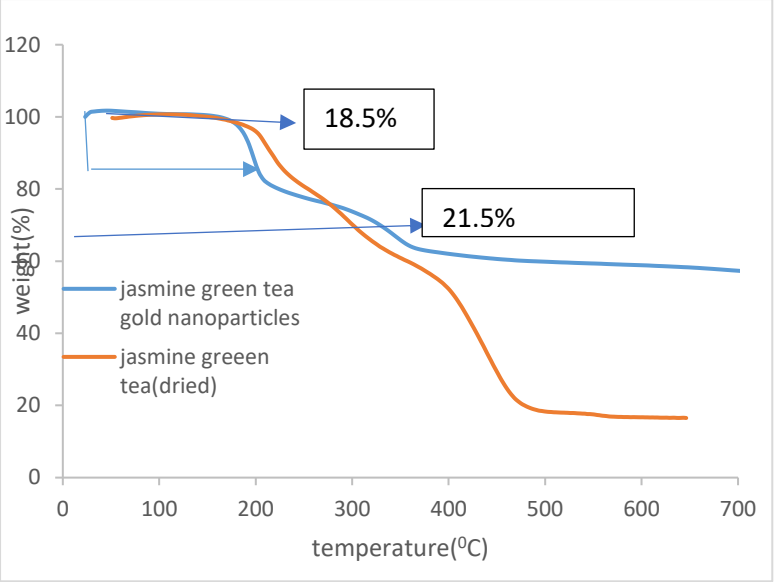

Figure.6.5: TGA of jasmine green tea extract(dried) and GT-AuNPs

6.1.4 Microanalysis of GT-AuNPs

The CHN analysis of jasmine GT-AuNPs shows that there exists a total of 66.6 % inorganics and 33 % organic compounds and this is in best agreement with the TGA data obtained for GT-AuNPs. Depicted in table.6.0.

Analysis	Remainder (%)	%C	%H	%N
GT-extracts	53.13	42.21	4.66	<0.3
GT-AuNPs	66.56	29.4	2.82	1.22

Table.6.0: Microanalysis of GT-AuNPs

If we assume that the extracts retain their overall composition after NP formation, then the 66.56% remainder in the GT-AuNPs should consist of [53.13 / 42.21]x29.4 = 37.0% oxygen from organics. If we also assume that the residual mass in the GT-AuNPs is composed of the same proportion of residual mass from the extracts themselves, plus all the gold, then the residual 66.56% is 7.52% O and 59.15% Au. Again, we see the presence of N in the AuNPs (as was also observed in the Ag system (Section 5, Table.4.0). This suggests that there may be selective adsorption of some components form the extracts onto the NP surface (e.g., protein) and thus the above calculation can only be an approximation

6.1.5 Powder X-ray diffraction of GT-AuNPs

The crystalline feature of GT-AuNPs was confirmed with an X-ray pattern (Figure.6.6) with diffraction peaks at 38.07, 44.22, 64.29, and 77.59 in a 2θ range 10^0–80° relating to (111), (200), (220), and (311) facets of a face centred cubic crystal structure (JCPDS. No. 004-0784) and showed the crystalline structure of prepared gold nanoparticles with green tea extract. The PXRD of GT-AuNPs obtained is quite similar to those obtained from cys-AuNPs,

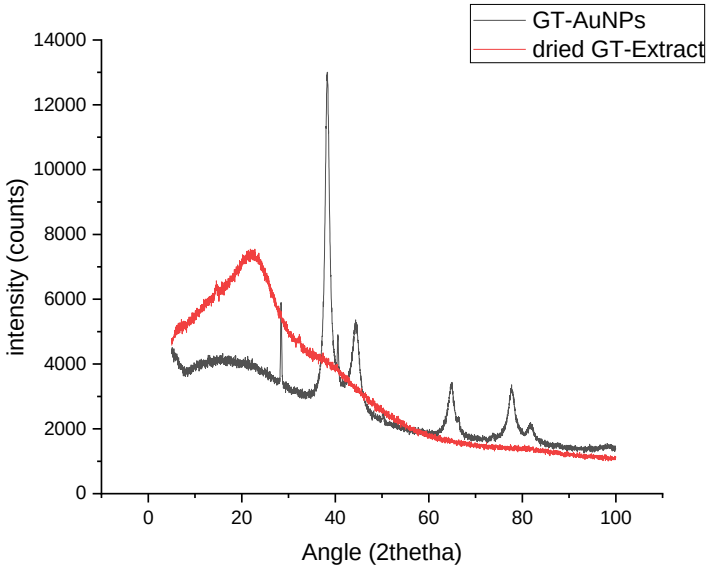

Figure.6.6: PXRD of GT-AuNPs and GT-extracts(dried)

6.1.6 TEM of GT-AuNPs

High resolution TEM was applied to determine the dimension and shape and morphology of the nanoparticles. The TEM images obtained for the synthesized green tea gold nanoparticles are depicted below (Figure.6.7-6.8). Based on the image, the synthesized nanoparticles tend to be spherical in nature, it is obvious that GT-AuNPs have roughly spherical morphology, with some more angular NPs also visible, with a great distribution of particles with sizes between 30 and 50 nm. The result of the TEM suggest the existence of lattices fringes which evidenced the excellence crystallinity. The crystalline nature of the particles was clearly indicated by the lattice structures shown in image. (Figure.6.6)

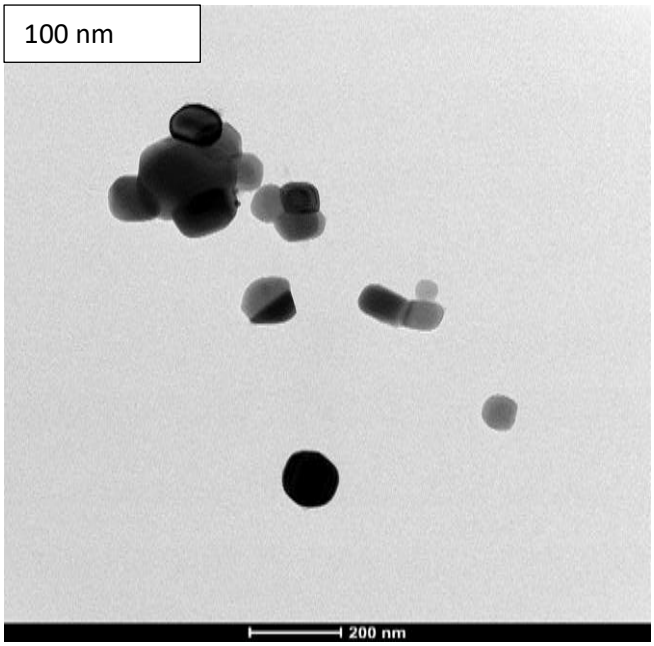

Figure.6.7: TEM of GT-AuNPs (100 nm)

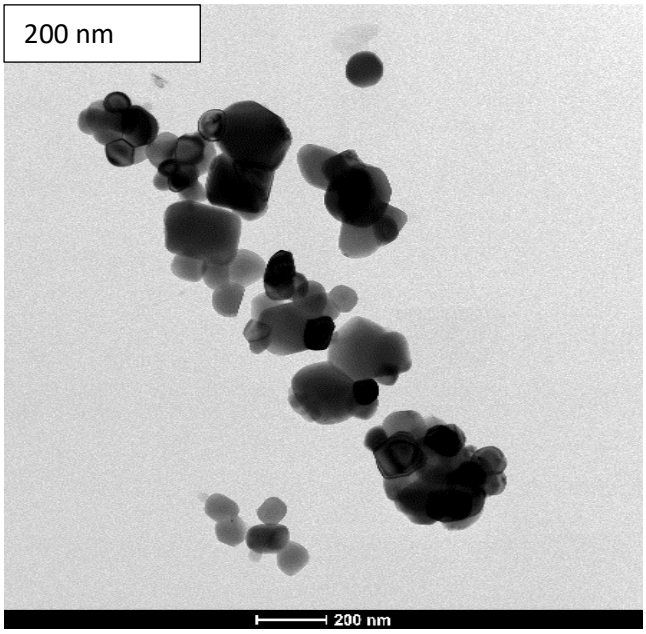

Figure.6.8: TEM of GT-AuNPs (200 nm)

6.1.7 Scanning electron microscopy of GT-AuNPs

SEM images of the GT-AuNPs synthesized showed the existence of clusters. The particles comprise of nearly spherical and some occluded shapes of nanoparticles. This variety of

geometrical shapes is typical of green synthesis of gold nanoparticles and has been described in the literature.[207-210](Figure.6.9-6.10).

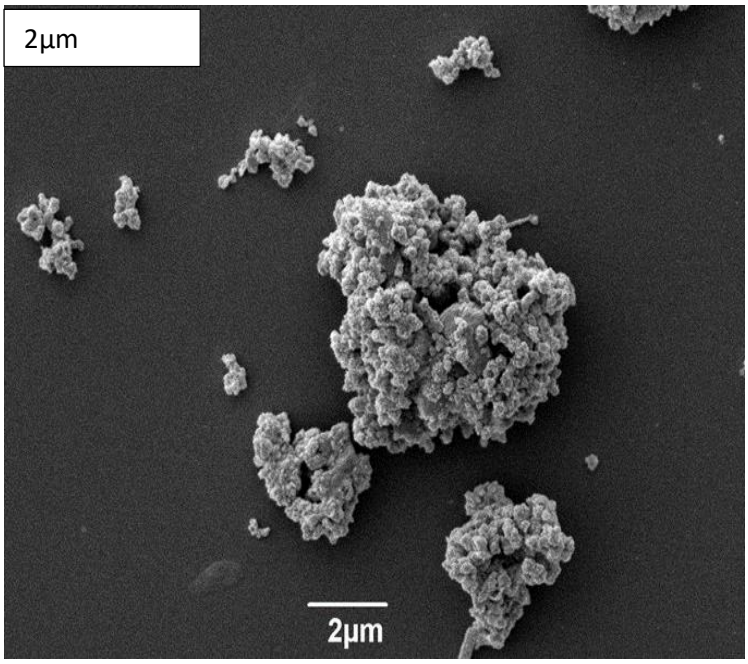

Figure.6.9:SEM images of GT-AuNPs(2µm)

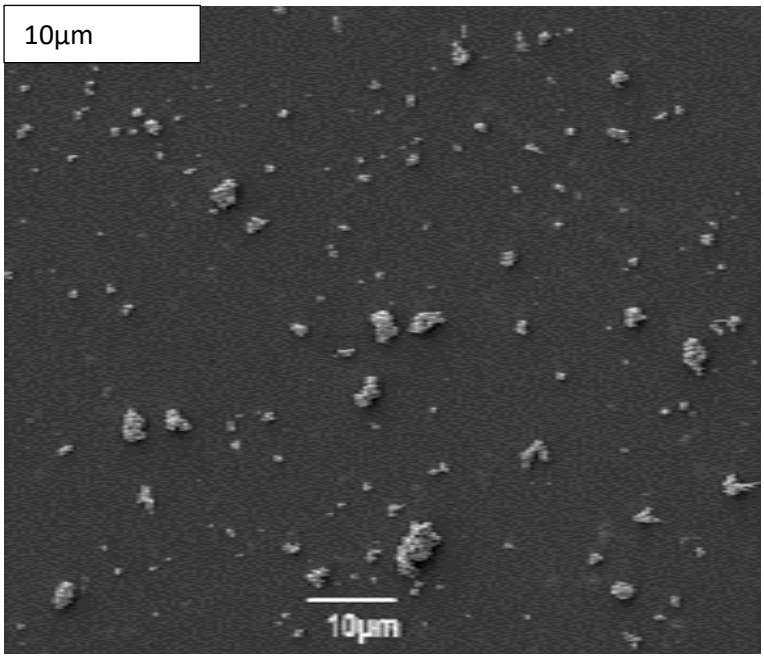

Figure.6.10:SEM images of GT-AuNPs(10µm)

6.2 Interaction of heavy metal with GT-AuNPs

6.2.1 Interaction of nickel with GT-AuNPs

The interaction of heavy metals by GT-AuNPs shows a distinct pinkish red colour after 5 minutes contact time, The LSPR tends to remain the same with shape of the LSPR. (Figure .6.11)

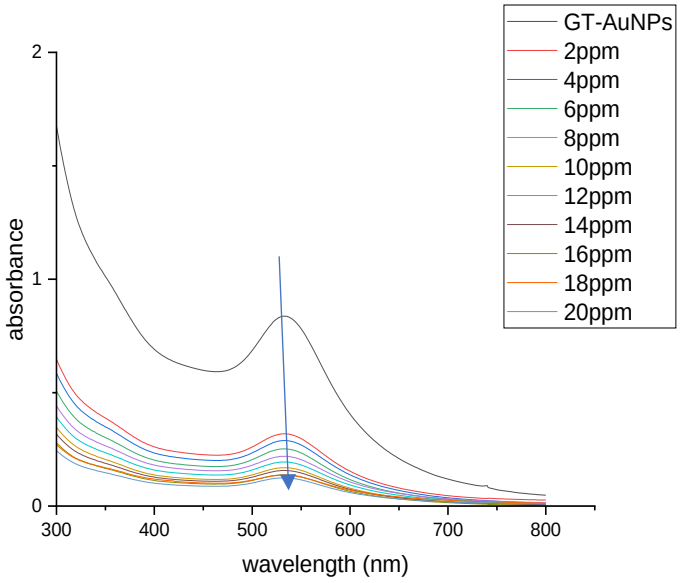

Figure.6.11: UV/Visible spectra of GT-AuNPs and nickel(2-20ppm)

6.2.2 Detection of copper by GT-AuNPs

The interaction of copper by GT-AuNPs shows that the initial pink colour changes after the 5 minutes contact times and the intensities of the colour decrease as the concentration of the copper increases. The LSPR suffers a slight blue shift from 537 nm to 534 nm**.** (Figure.6.12).

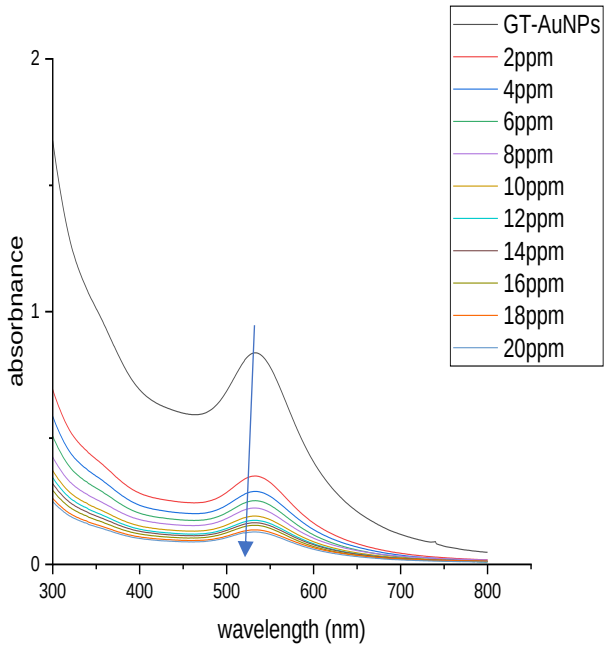

Figure.6.12: UV/Visible spectra of copper and GT-AuNPs

6.2.3 Detection of silver by GT-AuNPs

The interaction of silver by GT-AuNPs appear to change from purple red to pinkish purple and the quenching of the silver by GT-AuNPs appears to have shift the LSPR from 537 nm to 571 nm with the change in the shape of the LSPR. (Figure 6.13)

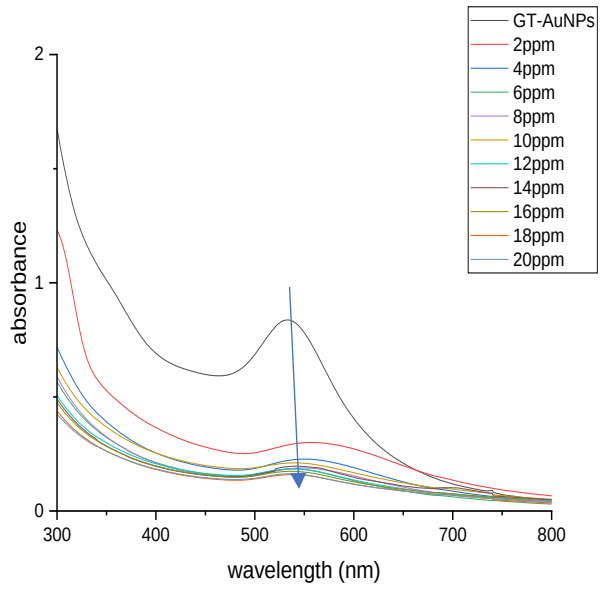

Figure.6.13: UV/Visible spectra of Silver and GT-AuNPs

6.3 Conclusion

The synthesis of metal nanoparticles using jasmine green tea extracts shows the ability of the extract to reduce and capped the metal nanoparticles as this is evidenced by the various analytical tools used in the characteristics of the metal nanoparticles.

The metal nanoparticles synthesized were exposed to various metal ions at low (2-20 ppm) concentrations. In the majority of cases there was a clear change to the LSPR, which often diminished in intensity, and also shifted as is depicted in the following,

Detection of Ag(I) by GT-AuNPs shows a colour change from, brick red to pinkish colour over the concentration range examined and there exist a shift in LSPR from 537 nm to 571 nm. Gold was shown in the UV/Visible spectra and thus shows the potential of the green tea synthesized Ag-NPs and GT-AuNPs to be utilized for interaction with heavy metals.

Detection of Ag(I), Cu(II) and Ni(II) by GT-AuNPs and cys-AuNPs shows an excellent interaction property towards the detection of heavy metals and both give a better result and can be used as greener alternative to detect heavy metals.

Chapter seven

7.0 Results and discussion on the synthesis and structural characterization of metal nanoparticles with the aid of cassava extracts.

7.1 Extraction of cassava flesh

Cassava extracts was choice due to the abundance of cassava in southern area of Nigeria and the ease of availability of the cassava biowaste to be used in the production of the metal nanopartilcles.50 g of chopped cassava flesh are weighed into 500 ml round bottom flask and boiled at 100 ^{o}C till it boils after which the extracts are decanted and left to cooled down. Raw cassava is 60% water, 38% carbohydrates, 1% protein, and has negligible fat.[211]

7.1.1 Gold nanoparticles obtained using citric acids, ascorbic acids and cassava flesh extracts

Production of metal nanoparticles from the cassava flesh extracts alone proved not to be successful, therefore ascorbic acid was used to co -synthesize the metal nanoparticles. In one set of experiments, ascorbic acid alone was used to reduced metal nanoparticles and, in another set of experiments, ascorbic acid and cassava flesh extracts were used to reduce and stabilize metal nanoparticles A comparative study was carried out on the synthesized AA-metal nanoparticles and the metal nanoparticles obtained from AA and cassava flesh extracts nanoparticles**.**

A parallel study was carried out using citric acid in place of ascorbic acid.

Metal nanoparticles obtained from these chapter were characterized using UV/Visible spectroscopy, FTIR, TGA and PXRD

7.1.2 UV/Visible spectroscopy of cit-AuNPs and cit-Au-cas-NPs

LSPR peaks were observed for the cit-AuNPs and cit-Au-cas-NPs at 533 nm and 547 nm respectively, the latter system gave the broader peaks, indicating a larger particles size. The absorbance stability measurements of cit-Au-cas-NPs prove to be stable with time compared to the cit-AuNPs. (Figure .7.0 and 7.1).

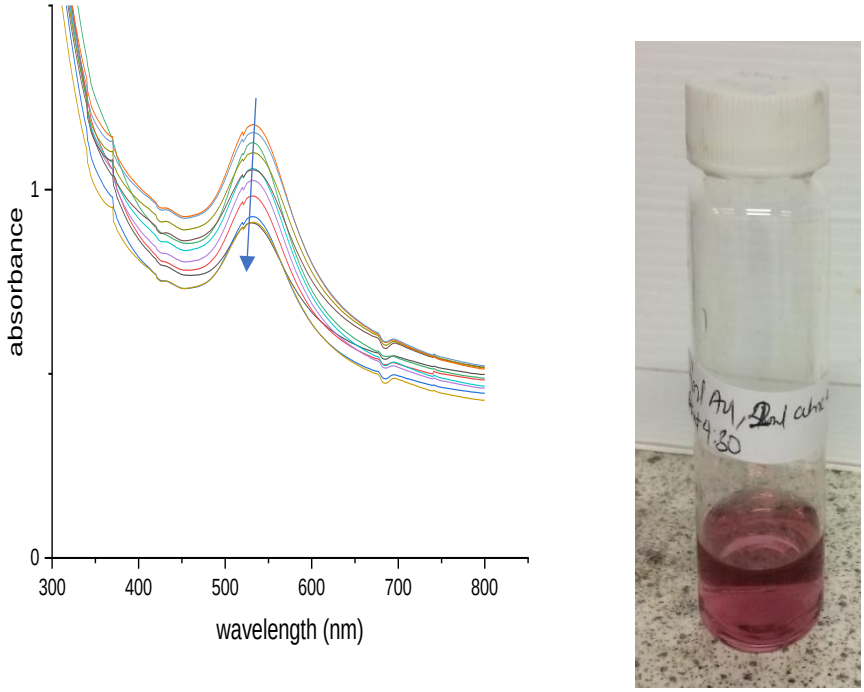

Figure 7.0: UV-Visible spectra of cit-AuNPs and it absorbance stability measurements with time (10-100 mins) at 10 mins interval and jpeg of Cit-AuNPs

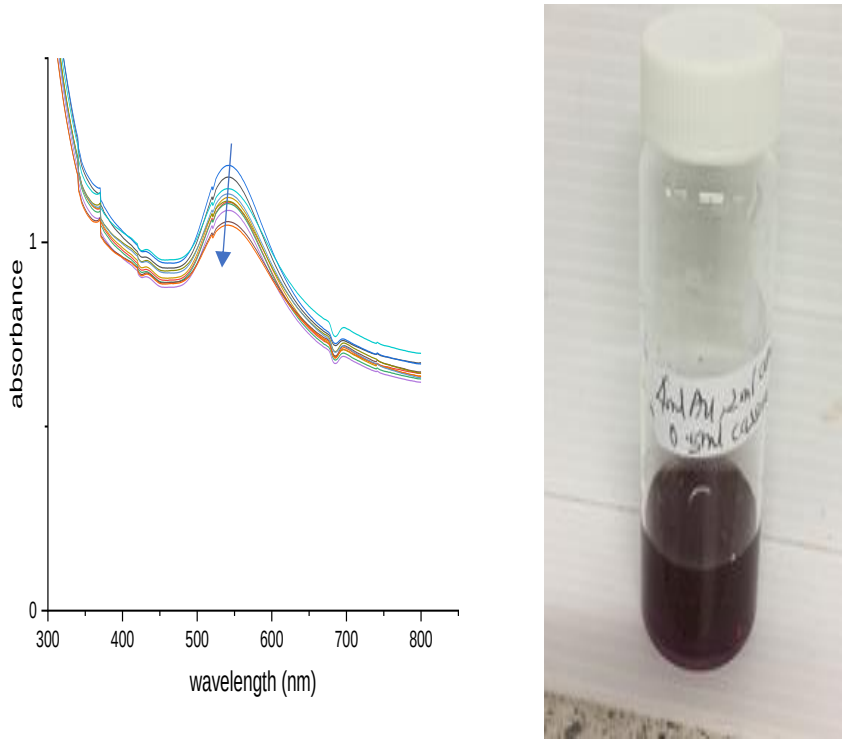

Figure 7.1: UV-Visible spectra of cit-Au-cas-NPs and its absorbance stability measurements with time (10 -100 mins) at 10 mins and jpeg Cit-Au-cas-NPs

7.1.3 UV-Visible spectroscopy of AA-AuNPs

The LSPR was observe at 547 nm for AA-AuNPs and tends to be stable with time to some extents, With a pinkish red appearance. The LSPR observed for AA-Au-cas-NPs at 541 nm. The LSPR observed for AA-AuNPs and AA-Au-cas-NPs tends to be stable with time, in compared with those obtained from citric acids, The AuNPs obtained are mainly dominated by large particle size as regards the broadness of the shape of the LSPR which relates to the size of the material. depicted in Figure.7.2 and 7.3

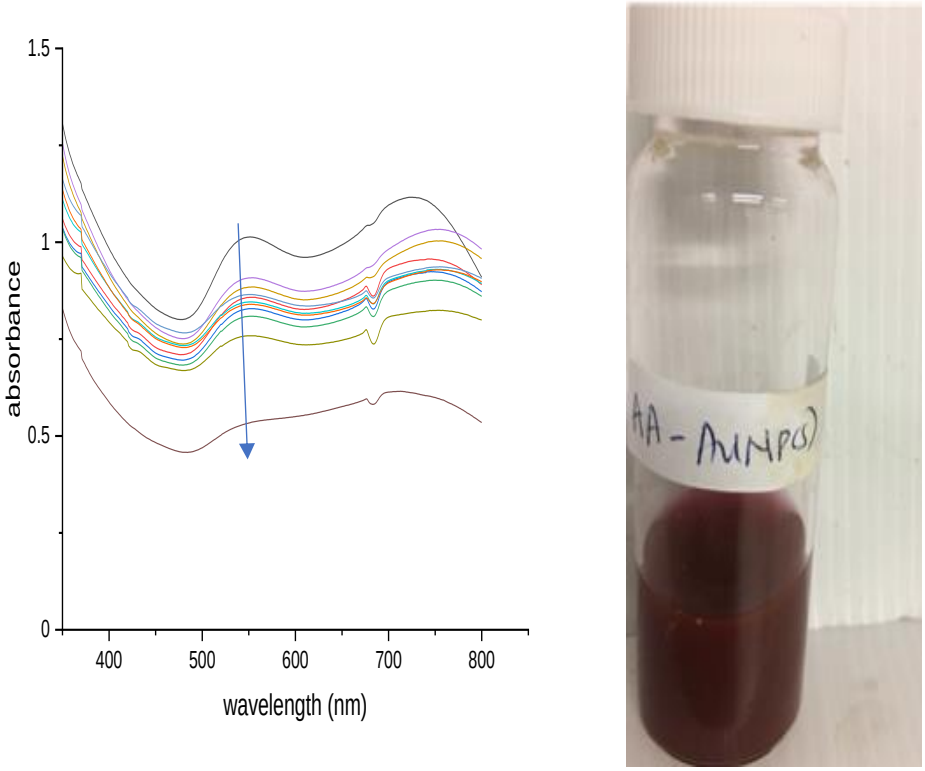

Figure.7.2: UV/Visible spectra of AA-AuNPs and its absorbance stability measurements with time (10-100 mins) at 10 mins interval

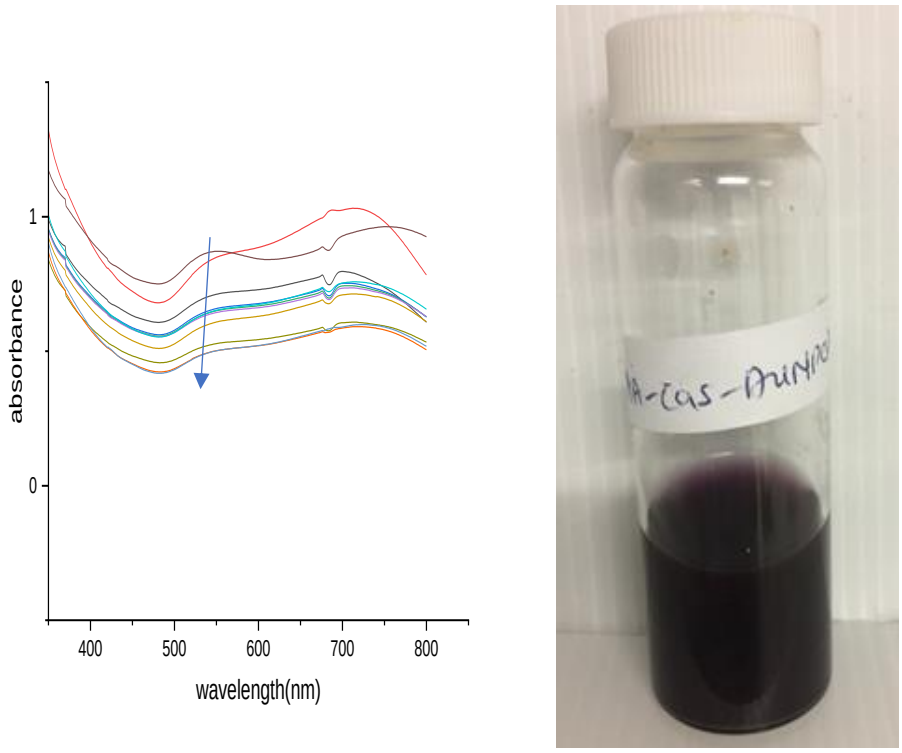

Figure.7.3: UV-Visible spectra of AA-Au-cas-NPs and its absorbance stability measurements with time (10-100 mins) at 10 mins interval and its jpeg image

7.1.4 FTIR spectra of AA-AuNPs and AA-Au-cas-NPs

The FT-IR spectrum for pure L-ascorbic acid is shown in figure 7.5. The stretching vibration of the carbon-oxygen double bond and the peak of enol hydroxyl were observed at 1674 cm^{-1} and 1322 cm^{-1}, respectively. After the formation of the AuNPs These peaks disappeared and new peaks were seen at 3481 cm^{-1}, 1718 cm^{-1}, and 1681 cm^{-1} (Figure.7.4). These peaks correspond to the hydroxyl, oxidized carbonyl groups, and conjugated carbonyl groups, respectively. These results indicate the presence of the polyhydroxy structure on the surface of the silver nanoparticles. The existence of polyhydroxy structure in the gold nanoparticles shows a great dispersion effect on the synthesized gold nanoparticles.[212](figure 7.4)

To understand the nature of binding mode by citric acids, cassava flesh extracts on AuNP surfaces, we studied the FTIR spectra. The FTIR spectra of cit-AuNPs and cit-Au-cas-NPs are shown in Figure.7.5. It is evident from Figure 7.5. that the characteristic peaks of cit-AuNPs are at 1696 cm^{-1}(vC=O) and 1320cm^{-1}(υs, C−O), and a broad peak around 3200−3420cm^{-1}(O−H). The FTIR spectra of cit-Au-cas-NPs (Figure.7.6) are similar to those of cit-AuNPs. However, the difference is due to the weak appearance of the O-H peak in cit-

Au-cas-NPs peaks at 3404cm^{-1} and the intensity of the C=O and C-O- bond of the cit-Au-cas-NPs tends to be stronger in compared to the Cit-AuNPs at 1704cm^{-1} and 1015cm^{-1} respectively suggesting the possible complexation of more material at similar spots.

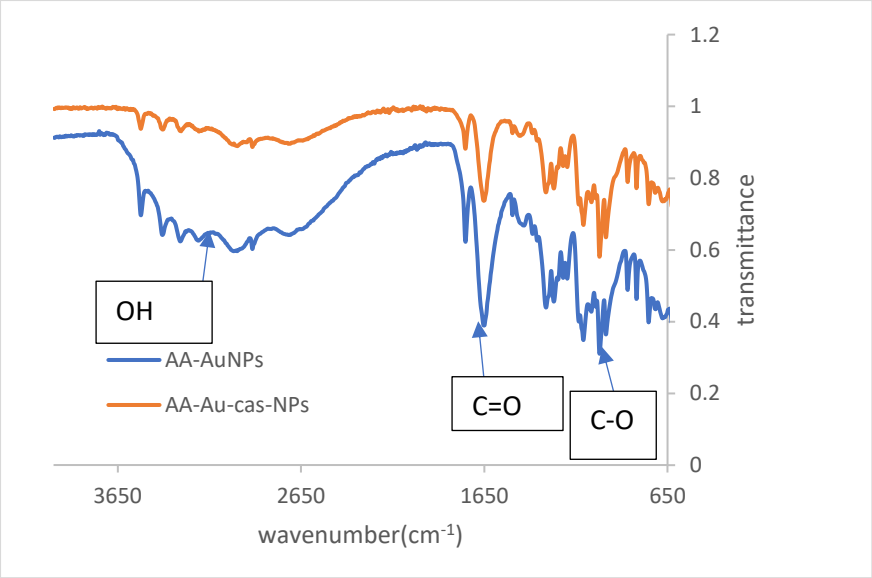

Figure.7.4: FTIR spectra of AA-AuNPs and AA-Au-cas-NPs

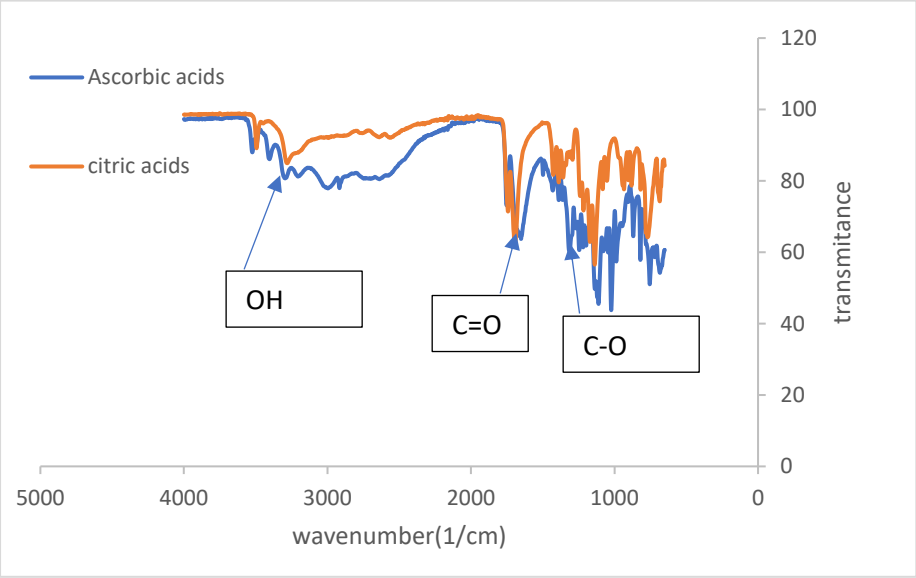

Figure.7.5: FTIR spectra of ascorbic acids and citric acids

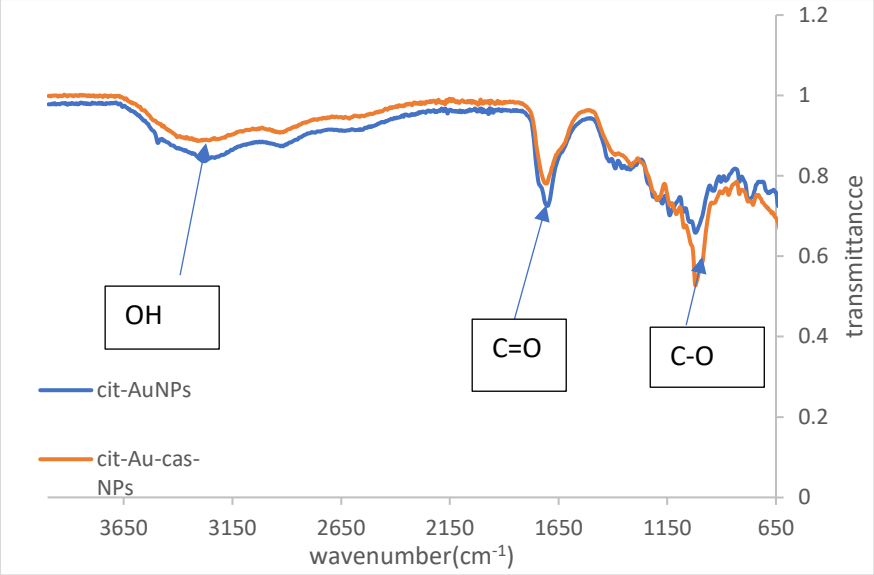

Figure.7.6: FTIR spectra of cit-AuNPs and cit-Au-cas-NPs

7.1.5 Scheme of reaction of ascorbic acids and AuNPs

Ascorbic acid is a good reducing agent and can reduce, and thereby neutralize, reactive oxygen species leading to the formation of ascorbate radical and an electron. This free electron reduces the Au^{3+} ions to or Au^{0} as can be seen in scheme 1 of figure7.7.

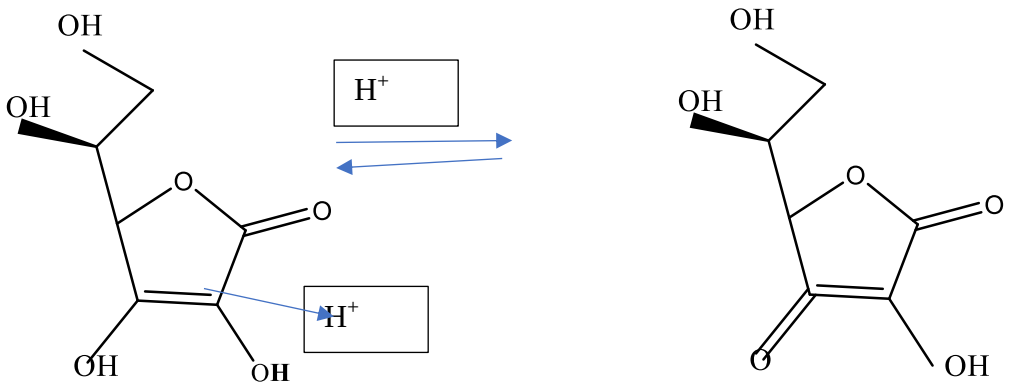

Ascorbic acid **Ascorbate radical**

$2HAuCl_4 \rightarrow 2Au^{+}+HCL$

$e + Au^{+} \rightarrow Au^{0}$

Figure.7.7: scheme of reaction of ascorbic acids and AuNPs

7.1.6 Scheme of reaction of citric acids with gold

Citric acids have been an employed as a co reducing agent in the synthesis of gold nanoparticles and thus the gold chloride got reduced to its elemental state. (Figure.7.8).

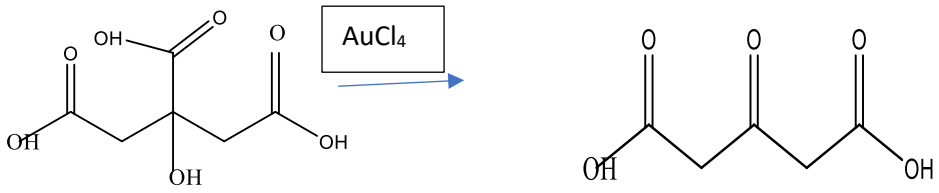

$AuCl_4 \longrightarrow AuCl + H^+ + 3Cl^- + CO_2$

$3AuCl + Cl \longrightarrow 2Au^0 + AuCl_4$

Figure.7.8: Scheme of reaction of citric acids and AuNPs

7.1.7 Powder x-ray diffraction of AuNPs

The PXRD of cit-Au-cas-NPs shows a 2θ values at $20.44\,\theta$,$28.44^0\,\theta$,$38.46^0\,\theta$,$44.70^0\,\theta$,$64.67^0\,\theta$ and $77.56^0\,\theta$ and the last four values correspond to the (111), (200), (220), and (311) planes of gold The broad peaks at 2 θ 20.440 and 28.44^0 are from the amorphous structure of the organics presents. (Figure 7.9). The PXRD of AA-AuNPs are also characterized by strong intense signals and also peaks of AuNPs which corresponds to the Face centre cubic crystal structures.

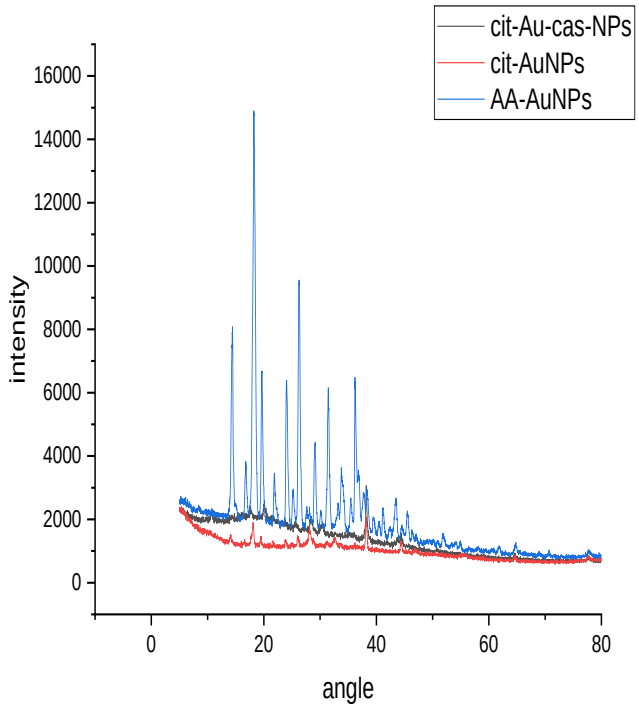

Figure.7.9: PXRD of cit-Au-Cas-NPs, cit-Au-cas-NPs and AA-AuNPs

7.1.8 Thermal analysis of cit-AuNPs,cit-Au-cas-NPs, AA-AuNPs and AA-Au-cas-NPs

The thermal analysis results show that the decomposition for the AA-AuNPs, AA-Au-cas-NPs and cit-AuNPs samples are of three stages the first stage implies the loss of loosely bound water in the samples, the second and third decomposition implies the breakdown of organic component in the samples The residues includes the inorganic component along with any residues from the organics.(Figure.7.10) The thermal decomposition of cit-Au-cas-NPs is of two stage decomposition the first stage involves the loss of physically bonded water and the second stage decomposition of the organic contents in the sample with 84 percent remnants

and 16 percent total organic contents present in the samples. Depicted in(figure.7.9)

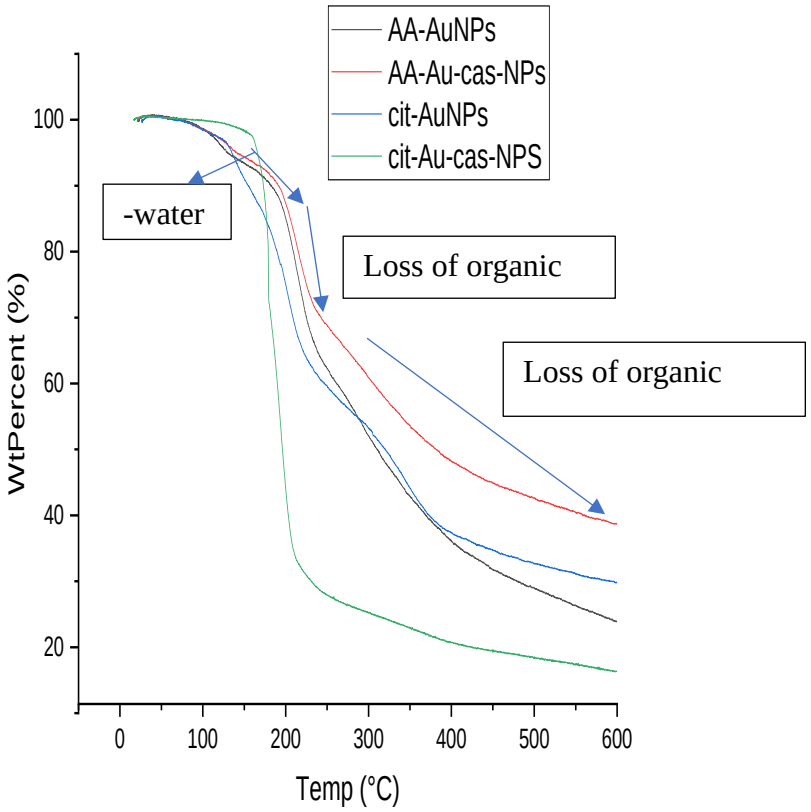

Figure.7.10: thermal analysis of AA-AuNPs, AA-Au-cas-NPs, cit-AuNPs and cit-Au-cas-NPs

7.2 Conclusion

Gold nanoparticles produced with the aid of citric acids and cassava flesh extracts are mainly dominated by small particles sized compared to those of ascorbic acids and cassava flesh based on the shape and appearance of LSPR in the absorption spectrum, there exist a face centred crystal structure for all the gold nanoparticles. The stability measurement of absorbance of the absorption spectra shows that the AuNPs produced via citric acids and cassava flesh extracts are stable with time compared to those produced using ascorbic acids and cassava flesh extract.

Chapter eight

8.0 Silver nanoparticles obtained using citric acids, ascorbic acids and cassava flesh extracts

Silver nanoparticles are obtained using citric acids and, in another experiment, citric acids and cassava flesh extracts were used in the production of AgNPs. The same procedure was used with the ascorbic acids and cassava flesh extracts. The synthesized silver nanoparticles obtained from each fraction were characterized using uv-visible spectroscopy, PXRD, FTIR and TGA.

8.1 UV/Visible spectroscopy of Cit-AgNPs, cit-Ag-cas-NPs,AA-AgNPs and AA-Ag-cas-NPs

The LSPR appear at 433 nm and the shape of the LSPR tends to be narrow , comparatively the cit-AgNPs and cit-AuNPs seems to contain smaller particle size compared to their counter-part cit-Ag-cas-NPs and cit-Au-cas-NPs,the LSPR observed for the cit-Ag-cas-NPs are at 434 nm ,similar shapes of LSPR was observed for the cit-AgNPs and cit -Ag-cas-NPs,citric acids reduction of the silver nanoparticles to its zero valency are quite weak and slow and these can be confirmed by the appearance of the LSPR of the AgNPs produced by the co reduction and stabilization of silver by citric acids and cassava flesh extracts .Depicted in (figure8.0-8.1) The LSPR was observed at 424 nm and 452 nm for AA-AgNPs and AA-Ag-cas-NPs respectively and appear to be vibrant in colour the reduction and stabilization of AgNPs by AA seems to be fast and rapid in compared to the citric acids system this can be as a result of the strength of the organic acids. this can also be confirmed by the similarity in the jpeg appearance of the AgNPs produced from the two fractions. the AA-AgNPs and AA-Ag-cas-NPs are characterized by traces of yellowish precipitates and cit-AgNPs are mainly clear solution which tends to produced reddish- brown after 8 hours of reaction Depicted in figure (8.2-8.3)

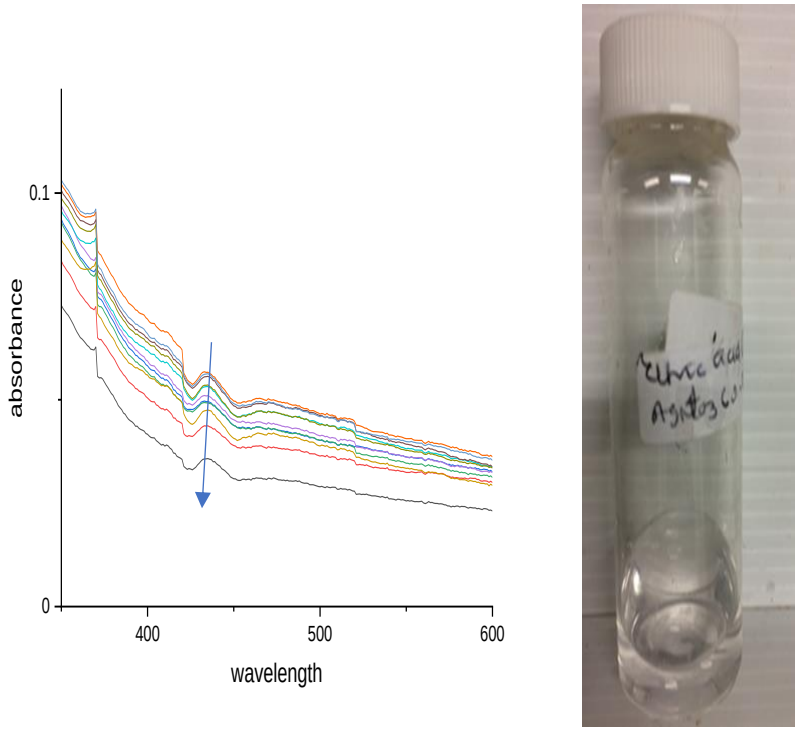

Figure.8.0: UV/Visible spectra cit-AgNPs and its absorbance stability measurements with time (10-100 mins) at 10 mins interval and is jpeg image

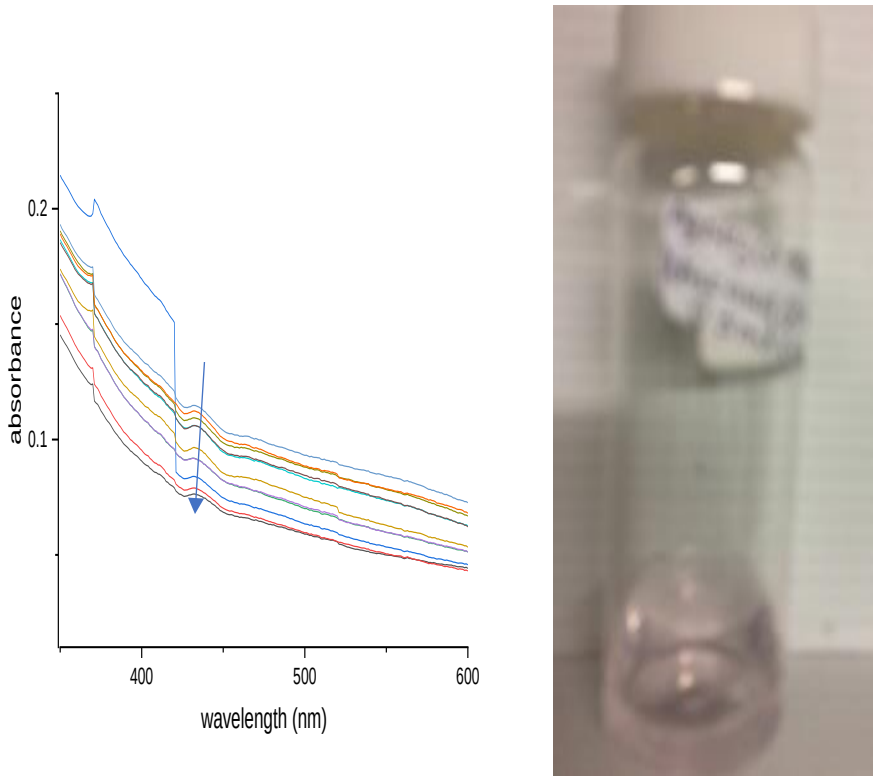

Figure.8.1: UV/Visible spectra of cit-Ag-cas-NPs, its absorbance stability measurements with time (10-100 mins) at 10 mins interval and its jpeg image

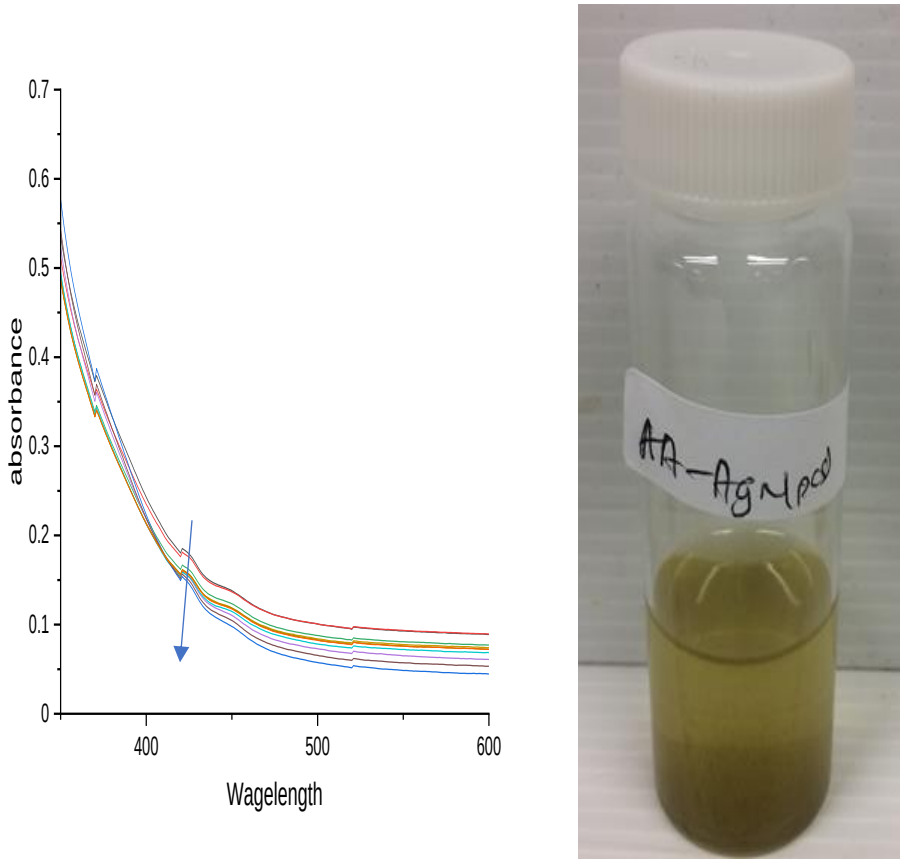

Figure.8.2: UV/Visible spectra of AA-AgNPs and its absorbance stability measurement with time (10-100 mins) at 10 mins interval, its jpeg image

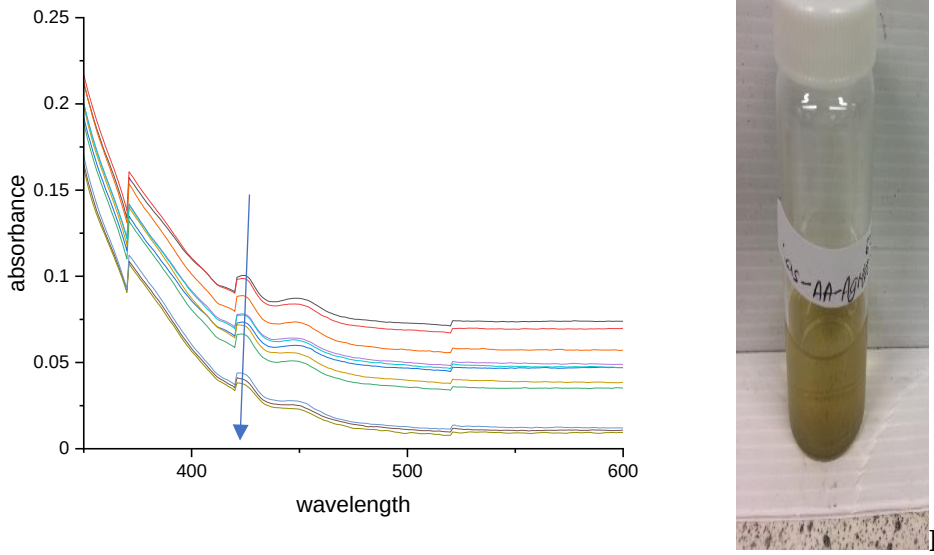

Figure.8.3: UV/Visible spectroscope of AA-Ag-cas-NPs, its stability measurement and its jpeg image.

8.1.2 PXRD of AA-AgNPs, AA-Ag-cas-NPs ,cit-AgNPs and cit-Ag-cas-NPS

The PXRD of AA-AgNPs and AA-Ag-cas-NPs exhibit a similar diffractogram with different intensity and in good agreement with the literature report on XRD of ascorbic acids stabilized silver nanoparticles. The crystalline nature of biogenic AA-AgNPs and AA-Ag-cas-NPs nanoparticles was confirmed by X-ray diffraction pattern. The PXRD pattern of biosynthesized AA-Ag-cas-NPs (Fig. 8.4) shows several peaks, where the four main peaks are located at 38.33°, 44.4°, 64.95°, and 82.62°, corresponding to the (111), (200), (220), and (311) reflection planes, respectively, to the structure of face-centered cubic (FCC) crystal of silver (JCPDS, No. 04–0783). In addition to Braggs peaks for silver nano-crystal, additional peaks were observed at 16.29°, 30.48°, and 34.7°. The presence of these additional peaks might be due to AA and its oxidation product on the surface of AgNPs. On the basis of Bragg's diffraction angle (2θ) and the full width of half maximum (β) for more intense peaks (111), for AA-AgNPs similar diffractogram pattern was observed with four distinct signals corresponding to the crystal structure of Face centred cubic crystal structure. The two main peaks are located at 38.24°, 45.52°, 64.78°, corresponding to the (111) and (200) reflection planes, respectively depicted in (figure 8.4).

The PXRD diffractogram of cit-AgNPs shows three main peaks are located at 37.5°, 43.24° and 63.32°, corresponding to the (111), (200) and (220) reflection planes, respectively, with several other peaks contributing from citric acids or Ag_2O. similar peaks were also observed with cit-Ag-cas-NPs though with strong intensity, four distinct peaks of AgNPs was observed in the diffractogram of the cit-Ag-cas-NPs with the fourth one extremely low frequency he four main peaks are located at 38.03°, 44.2°, 64.52°, and 84.72°, corresponding to the (111), (200), (220), and (311) reflection planes, respectively. (Figure.8.5)

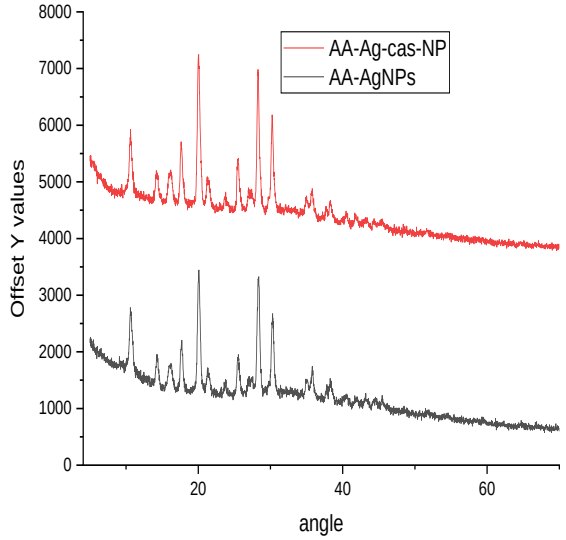

Figure.8.4: PXRD of AA-AgNPs and AA-Ag-cas-NPs

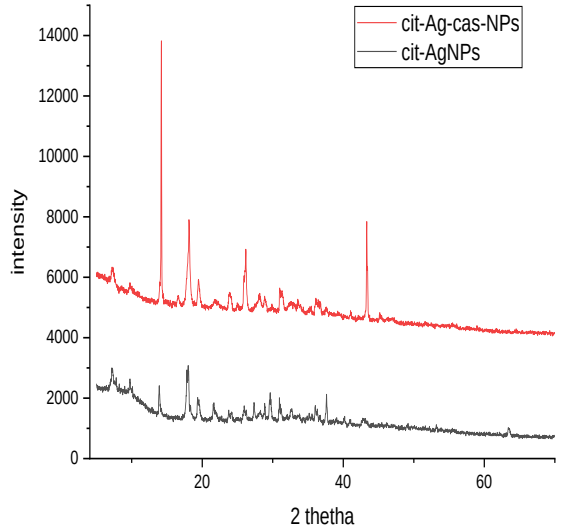

Figure.8.5: PXRD of cit-AgNPs and cit-Ag-cas-NPs

8.1.3 Thermal analysis of cit-AgNPs, cit-Ag-cas-NPs, AA-AgNPs and AA-Ag-cas-NPs

The thermal analysis of the cit-AgNPs and cit-Ag-Cas-NPs shows decomposition pattern and the complete decomposition of the samples occur at 300-400 ^{0}C with 43 % remnants for the cit-Ag-cas-NPs and 33 % remnants (residue from organics) with cit-AgNPs. The thermal analysis of AA-AgNPs shows a completed decomposition at 450 ^{0}C with 36 % remnants

containing inorganics and residue from the organic and 70% organic parts in the sample. AA-Ag-cas-NPs shows similar decomposition with 31% remnants in the samples. (Figure.8.6).

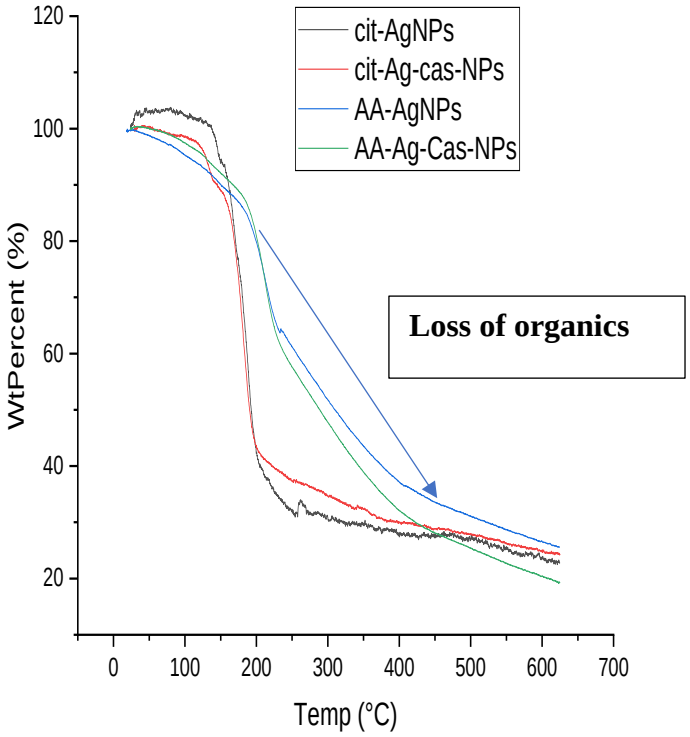

Figure.8.6: Thermal analysis of AA-AgNPs, AA-Ag-cas-NPs, cit-AgNPs and cit-Ag-cas-NPs

8.1.4 FTIR spectroscopy of cit-AgNPs, cit-Ag-cas-NPs,AA-AgNPs and AA-Ag-cas-NPs

The FTIR of cit-AgNPs and cit-Ag-cas-NPs shows a relative characteristics band with band shifting and deformation. There were prominent peaks at 1695 and 1145cm^{-1} from citric acid and a craggy array between 1145 and 950 cm^{-1} associated with aggregation of the strong absorbances from each of the sugars. For example, the absorbance at 1695 cm^{-1} is associated with stretching of the C=O bond in the carboxylate groups of citric acid, while 1021 cm^{-1} is indicative of the α-anomeric linkage between glucose and fructose in sucrose. The region between 1140 and 904 cm^{-1} contains C-C and C-O stretching modes, while O-C-H, C-C-H and

C-O-H bending vibrational modes are assigned to the region between 1415 and 1135 cm^{-1}.Depicted in figure.8.7.

The FT-IR spectrum for pure L-ascorbic acid. The stretching vibration of the carbon-carbon double bond and the peak of enol hydroxyl were observed at 1674 cm^{-1} and 1322 cm^{-1}, respectively. These peaks disappeared after the reaction and new peaks were observed at 3481 cm^{-1}, 1718 cm^{-1}, and 1681 cm^{-1} (Figure.8.8). These peaks correspond to the hydroxyl, oxidated carbonyl groups, and conjugated carbonyl groups, respectively. These results indicate the presence of the polyhydroxyl structure on the surface of the silver nanoparticles. (Figure 8.8-8.9)

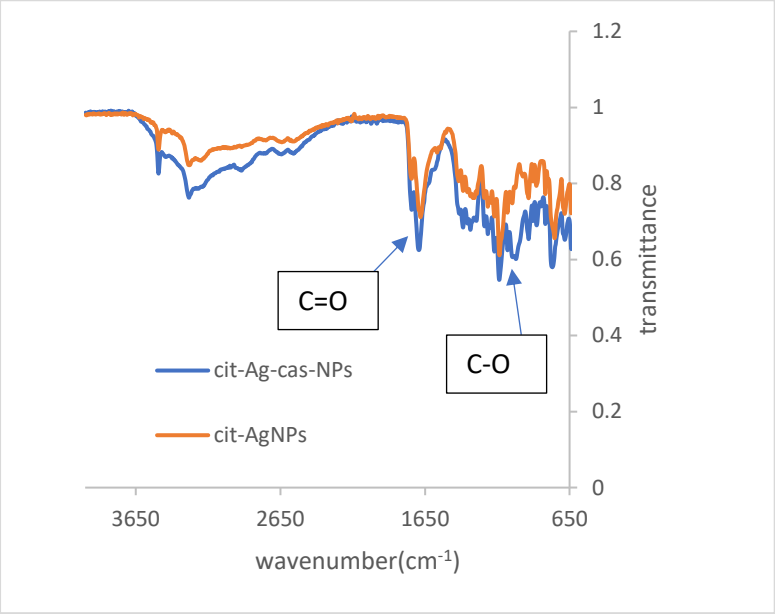

Figure.8.7: FTIR spectra of cit-AgNPs and cit-Ag-cas-NPs

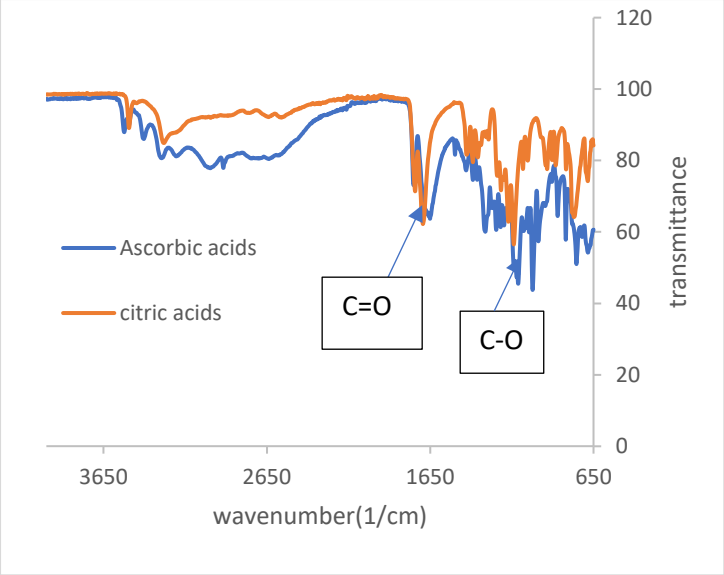

Figure.8.8: FTIR spectra of citric acids and ascorbic acids

.

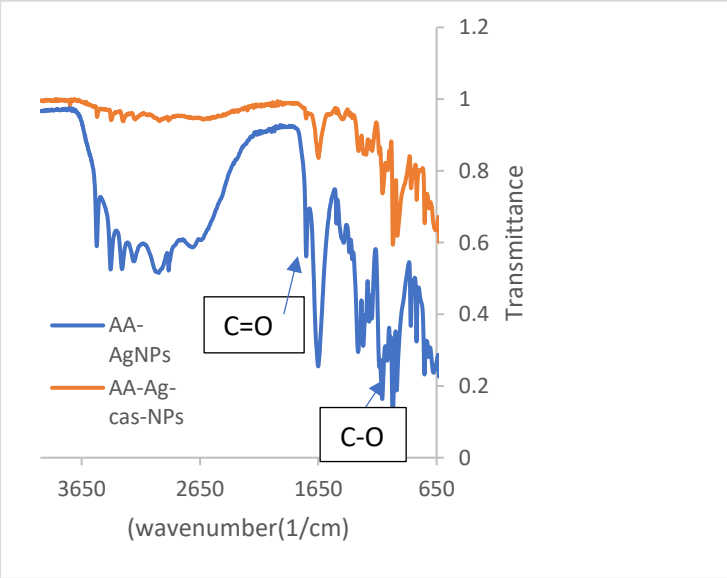

Figure.8.9: FTIR spectra of AA-AgNPs and AA-Ag-cas-NPs

8.2 Conclusion to chapter 8

Silver nanoparticles were successfully synthesised with the aid of citric acids and ascorbic acids, synthesis of silver and gold nanoparticles with the cassava flesh extracts could not reduce the silver and gold to its elemental form possibly due to weak reducing ability of the cassava extracts there limiting its ability to reduce the metal to its free state. Successful; synthesis is achieved with the aid of citric acids and ascorbic acids.

CHAPTER NINE

9.0 Result and discussion on the synthesis and structural establishment of metal nanoparticles using cassava peels waste and cassava flesh

Nigeria produces about 15 million tons of wet peels annually from the processing of cassava for foods and industry[213]. These peels are usually dumped in an open space to dry enough to be burned or rot. The peels biogas releases methane into the atmosphere and also leads to the stinking effluents that contaminates the nearby underground water and river ,the burning of the cassava peels leads to the generation of acid smoke which has detrimental effect on the life of aquatic and humans living in the environments, However the wet cassava peels can be utilized in the product on of metal nanoparticles, the presence of sugars in the form of glucose in the cassava peels can be used in the reduction of the metal ions and the fatty acids components can acts an effectives stabilizers for the metal nanoparticles. This method of synthesis is a benign approach which tailors towards the sustainable synthesis of Metal nanoparticles such as Ag and Au are produced from cassava peel and cassava Flesh extracts, other sets were produced using the aqueous components of each extract that have undergo some purification treatments such as washing with ethyl acetate and freeze drying the purified extracts termed the aqueous component(aq) in this chapter. The respective metal nanoparticles formed were characterized using UV-Visible spectroscopy, FTIR, TGA, PXRD, and proton NMR.

This chapter synthesizes the metal nanoparticles using the wet cassava peel and cassava flesh. FL are used for flesh cassava, PL are used for peel cassava, aq-FL represents the aqueous component of the flesh cassava and aq-PL represents the aqueous component of the peel cassava.

9.1 Silver nanoparticles produces from cassava

9.1.1 UV/Visible spectroscopy

The visual inspection of the colour changes for the formation of AgNPs indicate a chocolate brown for the FL-AgNPs and yellow for the aq-FL-cassava AgNPs, the uv-visible spectrum of the coloured suspension was recorded for further confirmation of the NPs. The maximum uv-visible absorption peak for FL-AgNPs sample was found at 461 nm and appears to be broader in nature, the LSPR was observed at 438nm for the aq-FL-cassava AgNPs and tends to be narrow and could be attributed to the particles sizes of each nanoparticle produced from each

fraction[214]. (Depicted in figure .9.0-9.9) The AgNPs formed from the cassava Flesh extracts appears to be bigger in size than those formed from the aqueous phase of the extracts, according to the UV-vis results. The UV/Visible spectroscopy of FL-AgNPs was recorded from 200-900 nm and depicted in figure.9.1.

Comparing the colour of the AgNPs from each fraction, the aqueous phase cassava flesh AgNPs are yellow and is in agreement with the work of Sallaudeen et al.[100] who also produced AgNPs under acidic conditions .it is worth noting that the aqueous phase is mainly dominated by organic acids present in the cassava extracts, leading to a solution of yellow and could have result in the reduction of the silver ion by the organic acids molecules to the free silver atom. The colour of AgNPs produced from the cassava flesh extracts were brown and this could be explained by the reduction of the silver ions by the flavonoids and organic components present in the crude cassava extracts rather than by the organic acids alone. The colour of silver nanoparticles obtained from the cassava flesh extracts is mostly in support of the research published on the synthesis of silver nanoparticle by plant extracts.

The solution of FL-AgNPs contains a large amount of precipitates meaning that the silver nanoparticles produces from the cassava Flesh Extract are mainly dominated by larger particle size nanoparticles in comparison with the aq-FL-AgNPs which contains a small clear solution an these are in best agreement with the shape of their LSPR in their respective uv-visible absorption spectra.

The AgNPs synthesized using the crude cassava peel extract changes colour from cream to reddish brown and contains less precipitate the LSPR appears at 429 nm and tends to be narrow. The AgNPs synthesized from the aqueous phase of the cassava extracts changes colour from light cream to a light brown and exhibit a broad LSPR at 448 nm in the uv-visible spectrum.

Comparatively, the AgNPs obtained using the cassava peels mainly composed of average nanoparticles sized in compared to the one obtained using the cassava flesh extracts, reversal observation is also observed with the AgNPs obtained using the aqueous phase of each cassava extracts. Depicted in figure 9.0-9.9.

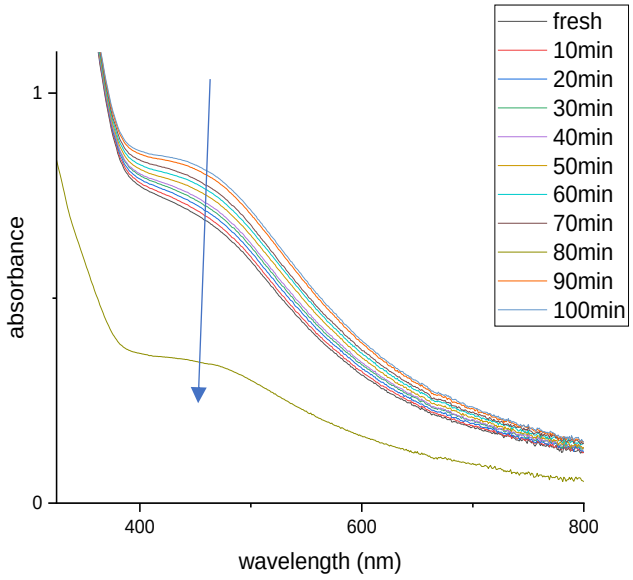

Figure. 9.0:UV/Visible spectra of Fl-AgNPs and its absorbance stability over time (10-100 mins) at a 10minutes interval

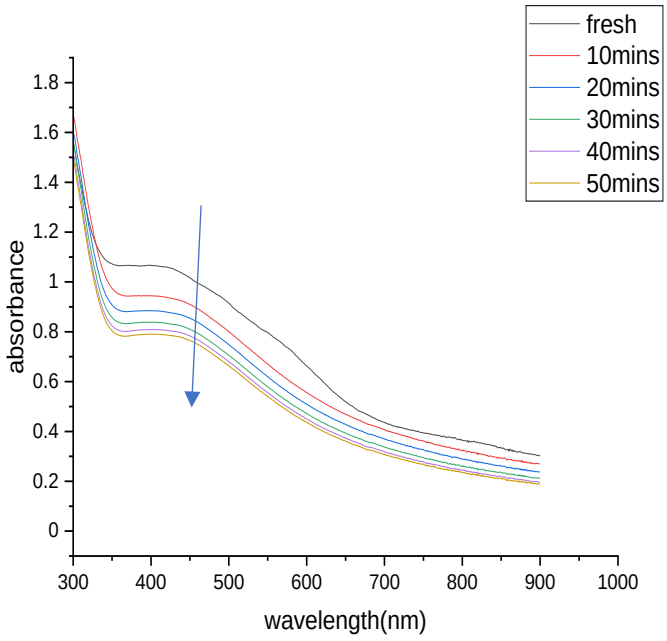

Figure.9.1: UV/Visible spectra of Fl-AgNPs and its absorbance stability over time (10-50 mins) at a 10 minutes interval

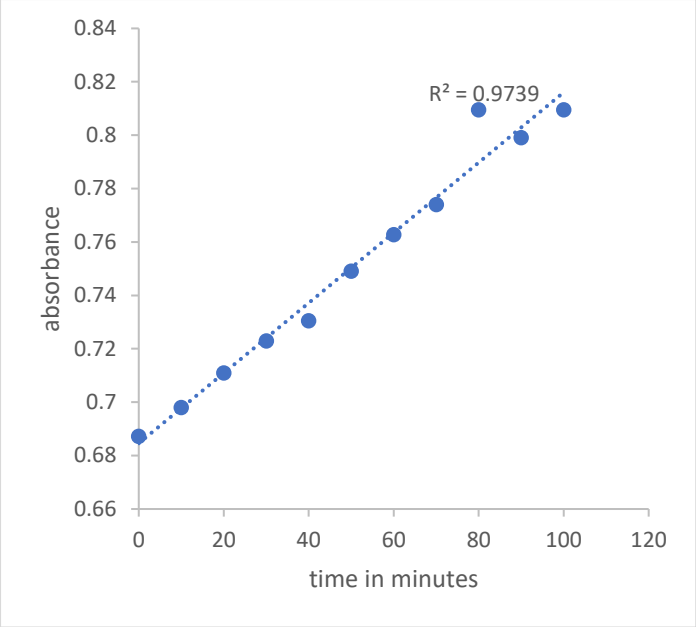

Figure.9.2: A plot of absorbance of FL-AgNPs over time at 10minutes interval

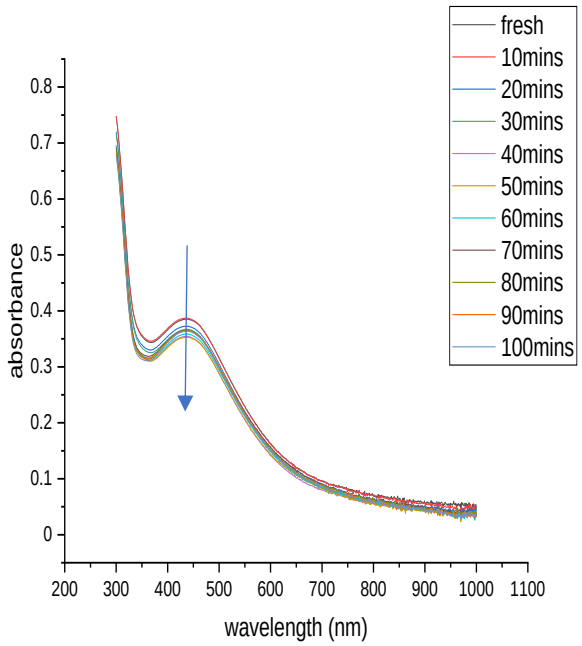

Figure.9.3: UV/Visible spectra of aq-FL-AgNPs and its absorbance stability over time at a 10 minutes interval

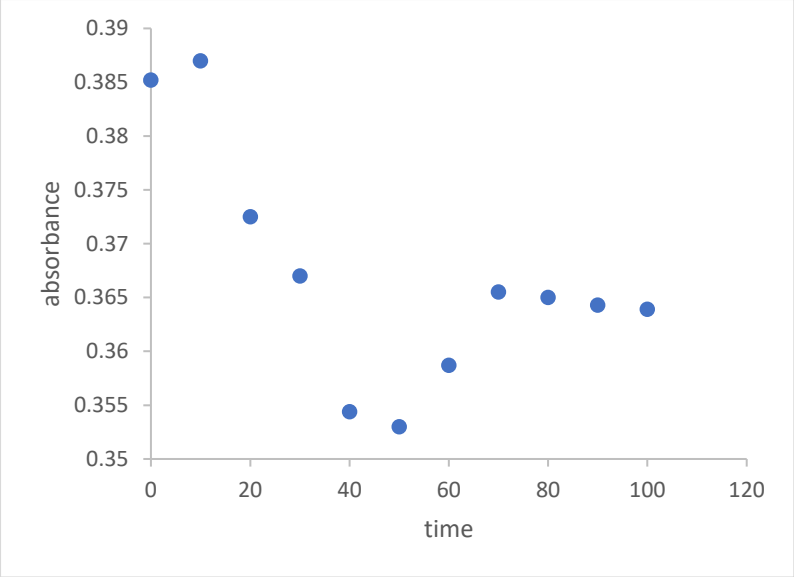

Figure.9.4: A plot of absorbance of aq-FL-AgNPs over time at 10minutes interval

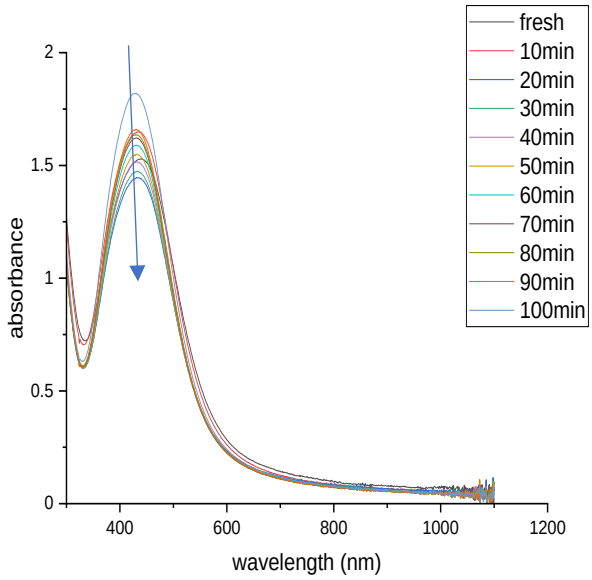

Figure.9.5: UV/Visible spectrum of PL-AgNPs and its absorbance stability measurement over time at a 10 minutes interval

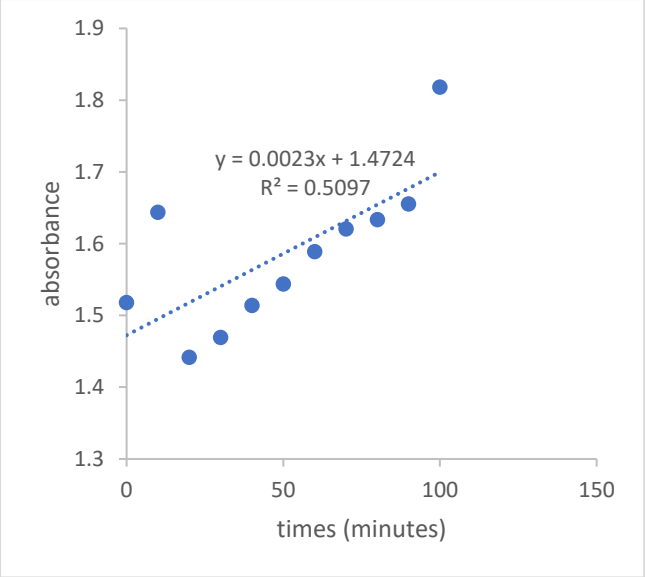

Figure.9.6: A plot of absorbance of -PL-AgNPs over time at 10minutes interval

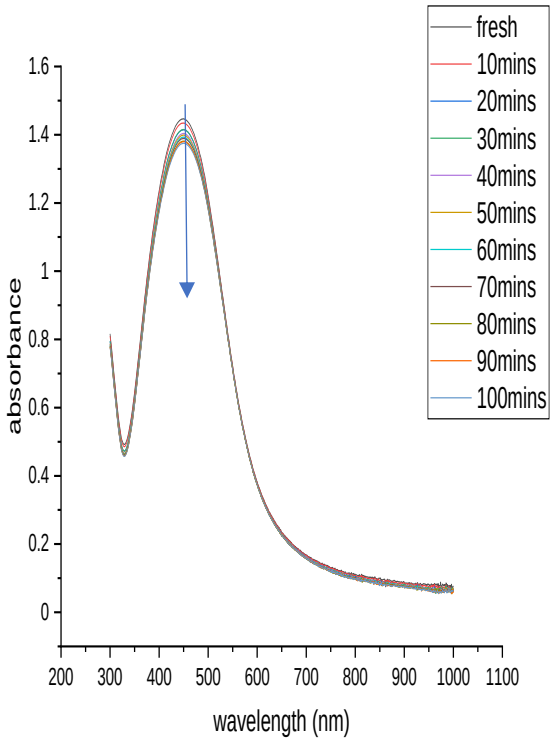

Figure.9.7: UV/Visible spectrum of aqueous phase of crude cassava peel silver nanoparticles and its degradation over time

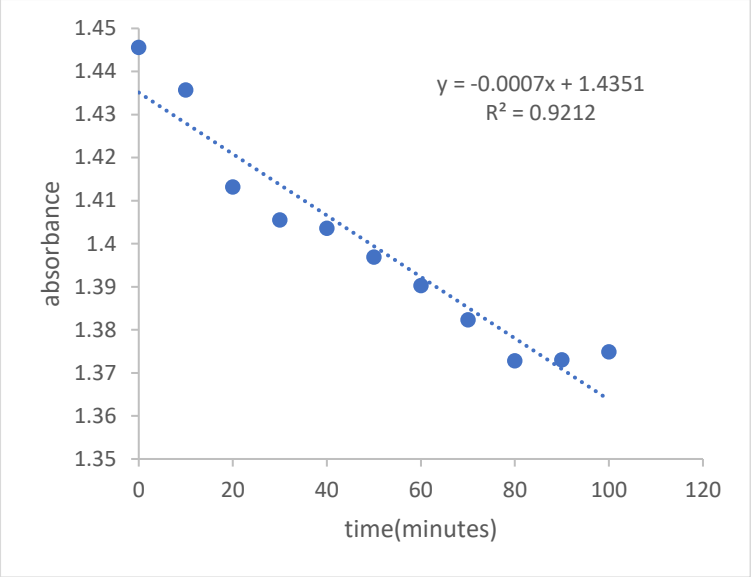

Figure.9.8: A plot of absorbance of -aq-PL-AgNPs over time at 10minutes interval

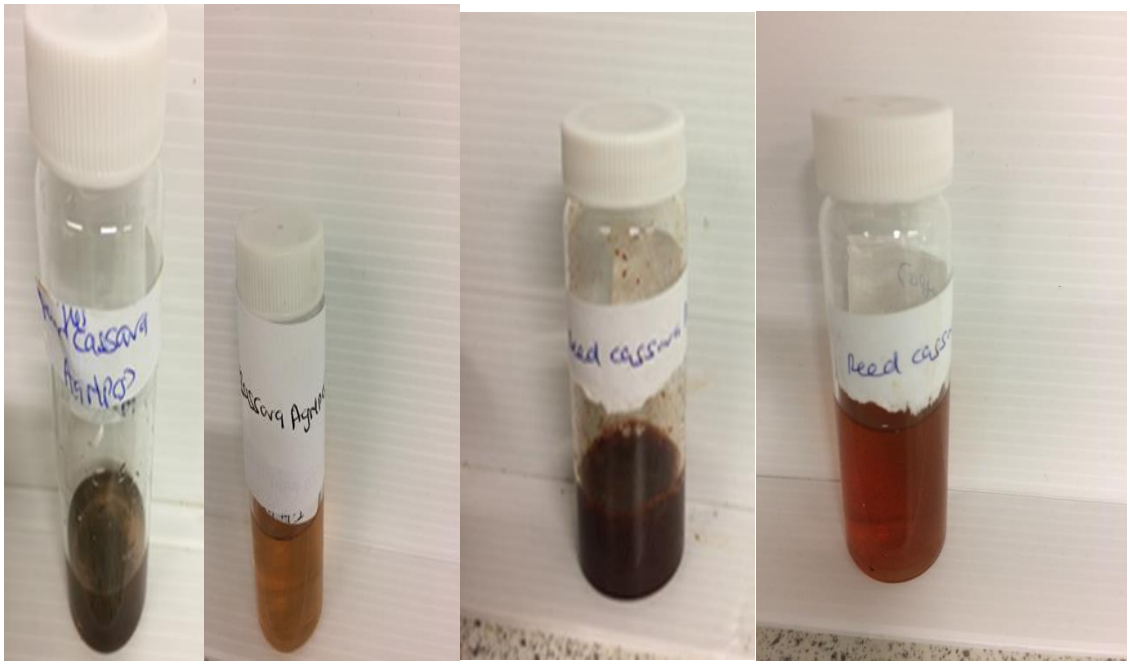

Figure.9.9: Jpeg image of A) FL-AgNPs ,b)aq-FL-AgNPs c)PL-AgNPs ,d)aq-PL-AgNPs

9.1.2 FTIR spectroscopy of cassava silver nanoparticles

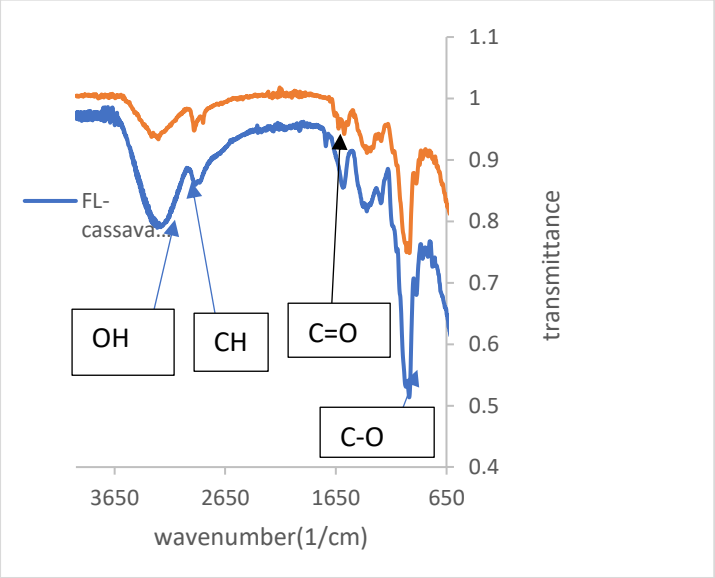

Figure.9.10: FTIR spectra of cassava flesh extracts (dried) and cassava Flesh AgNPs

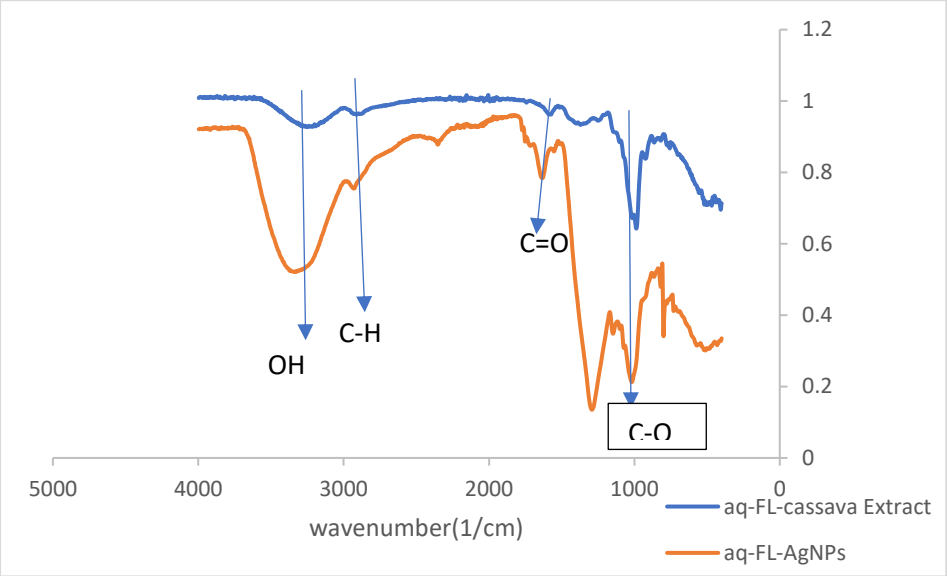

Figure.9.11: FTIR spectra of aqueous phase of cassava flesh extracts and aqueous phase cassava Flesh AgNPs

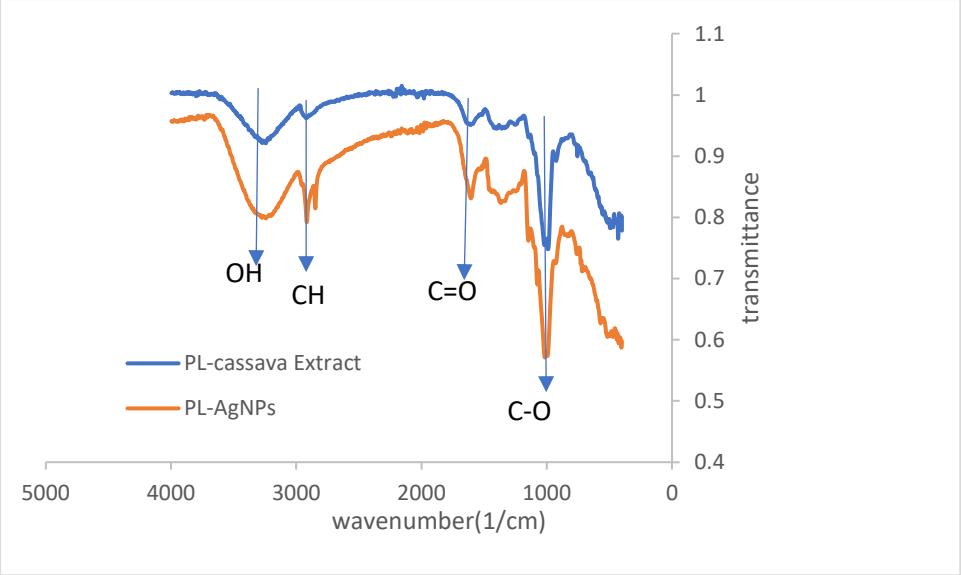

Figure.9.12: FTIR spectra of cassava peel extracts (dried) and cassava peel AgNPs

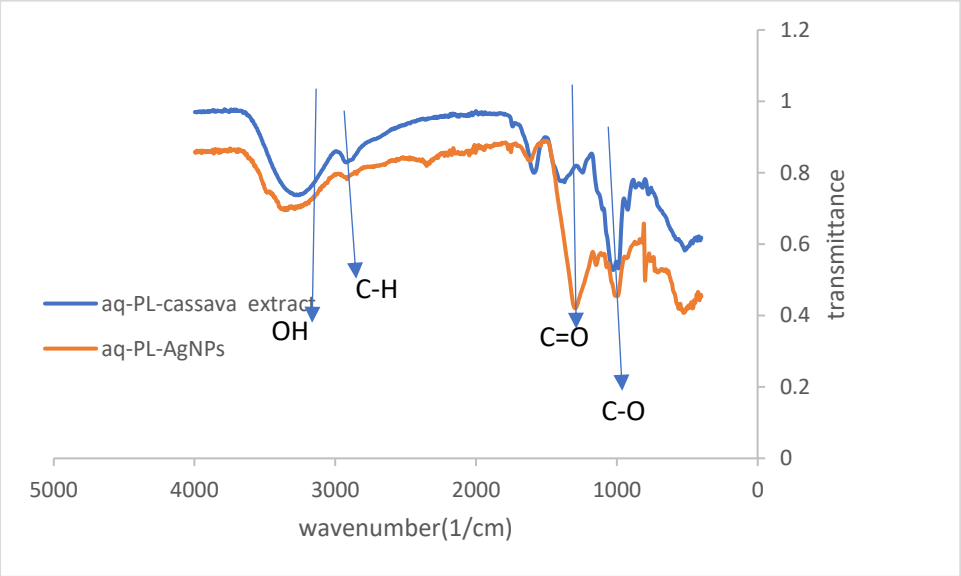

Figure.9.13: FTIR Aqueous phase of crude cassava peels extracts (dried) and aqueous phase cassava peel AgNPs.

The IR spectra of cassava flesh extracts showed a -OH- band at 3283cm^{-1} and a carbonyl stretch at 1743 cm $^{-1,}$ indicatives of carboxylic acids. Additional peaks are present at 2923 cm $^{-1}$ and 1250 cm $^{-1}$ are also present, corresponding to aliphatic C-H str and C-O str respectively. The spectrum of the corresponding NPs is broadly similar, although peaks are shifted somewhat, consistent with them being coordinated to the surface of the NP. For example the carbonyl stretch is now centred at 1631cm suggestive of a change from free acid to a coordinated carboxylate group. (Figure.9.10.)

In the spectra of aqueous phase cassava flesh extracts, there are characteristics band of -OH- band at 3298cm^{-1},-CH_3- band at 2953cm^{-1} ,OH- bend band at 1580cm^{-1} and -C-O- band at 1347cm^{-1} which stretches and defame in the spectra of the aqueous phase cassava flesh AgNPs to 3356cm^{-1} for the -OH-band, 2940cm^{-1} for the -CH_3 band and 1644cm^{-1} for the -C=O- band ,and 1019cm^{-1} ,1293cm^{-1} are characteristics band of -C-O- respectively. (Figure.9.11)

Comparatively, there appear to be similar characteristics bands in the spectra of both FL-AgNPs and aq-FL-AgNPs. The -OH-band in the FL-AgNPs tends to be narrow and shorth compared to the aq-FL-AgNPs whose band tends to broad and long, the same trend is observed in the -C=O band of the spectra of Fl-AgNPs (broad and short) and aq-FL-AgNPs (narrow and long) suggesting the possible influence of organic fraction of the cassava flesh extracts in the FL-AgNPs. (Figure 9.10-9.11).

The FTIR spectra of crude cassava peels extracts(dried) and the aqueous phase of crude cassava peels extracts(dried) there appear to be less organic components in the aqueous phase fraction of the FTIR spectra of crude cassava peel extracts (dried),in The FTIR of crude cassava peel extracts and cassava PL-AgNPs showed a characteristics spectra of the crude cassava peel extracts and their appear to be band shifting and deformation in the spectra , the -OH – band in the crude cassava peel extracts shifted from 3286cm^{-1} to 3321cm^{-1} in the spectra of PL-AgNPs ,the-CH- band shift from 2927cm^{-1} to 2917cm^{-1},the -C=O- band also shifted from 1701 cm^{-1} to 1601cm^{-1} and the -C-O- band shifted from 1074cm^{-1} to 1017cm^{-1}.Depicted in figure.9.12 and 9.13.

The FTIR spectra of aqueous phase of crude cassava peels extracts and the aqueous phase cassava AgNPs shows spectra characteristics of the aqueous phase crude cassava peel extracts. Absorption band of 3308 cm^{-1} corresponding to −OH-stretching of aqueous phase of cassava peel extract, and shifted to 3296cm^{-1} in the aq-PL-AgNPs spectra. The C–H stretching at 2948 cm^{-1} in the spectra of aq-pl-cassava extracts shifted to 2921cm^{-1} in the aq-PL-AgNPs with band defamation. C=O stretching vibration at 1615 cm^{-1} in the spectra of aq-PL-cassava peel extracts shifted to 1627 cm^{-1}in the spectra of aq-PL-AgNPs, represented a carbonyl group which may be from carboxylic acid groups present in the aqueous phase. The bands at 1050 cm^{-1} in the spectra of aq-PL-cassava extracts corresponded to -C-O- and has shifted to 1009 cm^{-1} in the spectra of aq-PL-AgNPs. The figure below shows the FTIR spectra of the each set of nanoparticles with its cassava fractions.

Comparatively, the spectra of PL-AgNPs contains less carboxyl group while in the spectra of aq-PL-AgNPs appears to contain large amount of carboxyl group of mildly or strong organic acids which is as a result of the present of higher fraction of this organic acids in the aqueous phase of the cassava peel extracts.

Comparing the cassava peel extracts and the aqueous phase of the cassava extracts, the spectra of the aqueous phase contain a higher numbers of carbonyl band and -C-O- band while the spectra of the cassava peel extracts tend to be dominated by both the organic and the aqueous fraction. Depicted in Figure.9.12 and 9.13.

9.1.3 Powder X-ray diffraction techniques

In order to establish the crystalline phase of the synthesized cassava AgNPs and further confirmation of the AgNPs formation, the synthesized material was subjected to XRD analysis and from the corresponding diffraction patterns. The synthesized material was identified as face centre cubic structure of silver. The XRD patterns displayed two characteristic peaks at 33.44°and 43.08°, corresponding to the crystal planes of (111) and (200) respectively. In addition to these the XRD structure of the crude cassava flesh extracts suggest an amorphous crystal structure. Further, the crystallite size of the material was also calculated from the XRD patterns using Debye-Scherrer approximation and the value was found as 30nm. (Figure.9.14)

The XRD of aqueous phase cassava flesh extracts and aq-FL-AgNPs patterns displayed four characteristic peaks of AgNPs at 35.92°, 43.89°, 62.84°, and 80.58° corresponding to the crystal planes of (111), (200), (220) and (222), , XRD patterns also show some unknown peaks (marked with stars) at 46.11°, 54.72°, 57.31° and 85.52° which may be due to the crystallization of bioorganic phase on the AgNPs surface originating from the organic acids present In the aqueous phase of the cassava extracts. Depicted in Figure.9.16.

The PXRD of the crude cassava peel extracts show a Braggs plane at 21.59^0 is due to the low crystallinity of the cassava extracts(dried), and the silver peaks with almost a little intensity could be attributed to AgNPs covered by cassava extracts, significant Braggs planes are found at 22.22^0,38.22^0,64.45^0,77.83^0 are attributed to the 111,200,220,311 diffraction planes of silver. It is evidence that the PL-AgNPs exhibited a structure which are face centre cubic crystal structures. Calculation from debyle Scherrer equation suggest 14.40nm of the particle size of PL-AgNPs. Depicted in Figure.9.17.

The powder x-ray diffraction peaks of the aqueous phase crude cassava peel extracts ,crude cassava peel and both cassava fraction AgNPs were studied, the crude cassava peel and aqueous phase of crude cassava peel extracts exhibit an amorphous structure, while the silver nanoparticles made from the aqueous phase of crude cassava peel extracts exhibit brags reflection at 37.07^0,46.35^0,62.07^0 and 70.43^0 corresponding ro to (111),(200),(220) and (311) planes respectively which are attributed to a face centred cubic crystal structure .depicted in figure.9.17- 9.18.

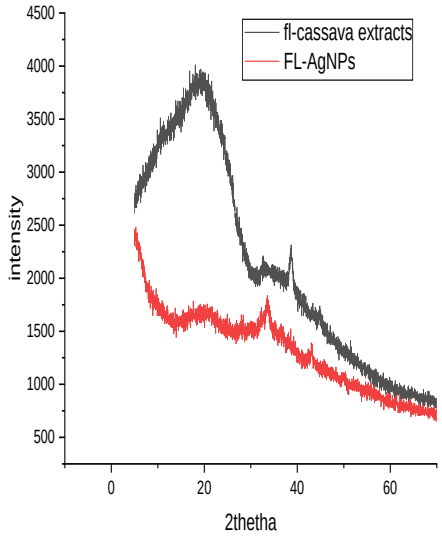

Figure.9.15: PXRD of crude cassava flesh extract and FL-AgNPs

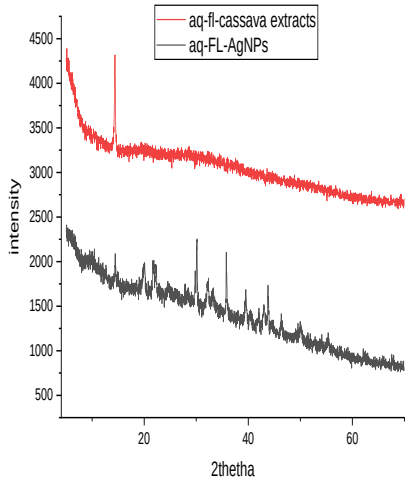

Figure.9.16: PXRD of aqueous phase of crude cassava flesh extracts and aq-FL-AgNPs

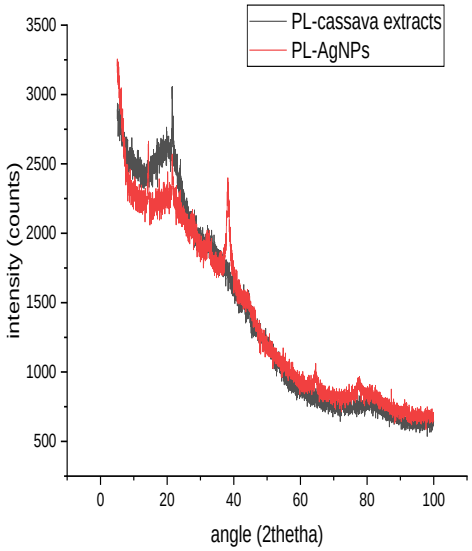

Figure.9.17: PXRD of crude cassava peel extracts (dried) and cassava peel AgNPs

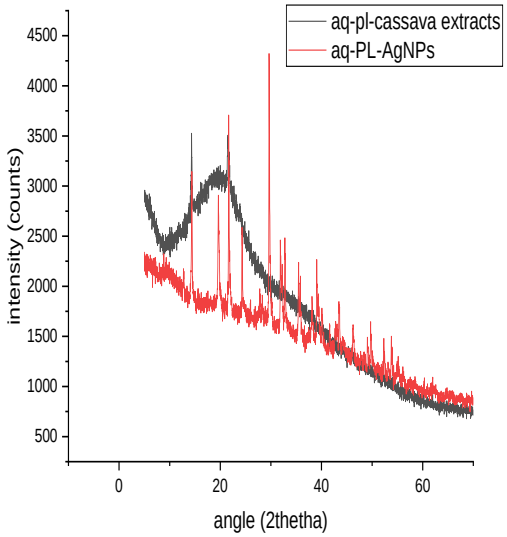

Figure.9.18: PXRD Aqueous phase of crude cassava peels extracts and aqueous phase cassava silver nanoparticles

9.1.4 Thermogravimetric (TGA) analyser

TGA were employed to analyse the decomposition temperature of AgNPs with both fraction of the cassava extracts. As shown below, the thermal stability of AgNPs synthesized from both crude cassava flesh extracts and aqueous phase of cassava flesh extracts and different fraction of the cassava starch were determined in the temperature range of 25–625 °C. The result from figure 9.19.-9.24 and shown that the FL-cassava extracts and FL-AgNPs exhibit a weight loss at 80-90 °C corresponding to residual water in the sample, another dramatic decomposition is observed between 150-216 °C in FL-AgNPs .The thermal stability of the two extracts is broadly similar with a two-stage mass loss after loss of residual water ,with the cassava flesh extracts being somewhat more stable in terms of temperature of breakdown and also a higher level of residual mass.(Figure.9.19).

The decomposition of the aq-PL-AgNPs is faster and rapid compared to the PL-AgNPs. similar decomposition pattern was observed in each cassava extract, aqueous phase fraction and the corresponding AgNPs produce from each fraction. (Figure.9.19-9.24).

TGA thermogram of the aq-PL-AgNPs showed single identical and continuous weight loss of stages (Fig.9.23). these discrepancies could be as a results of sample sizes not enough. The first decomposition stage occurs from room temperature to 161 °C with 1.65% weight loss indicating the removal of water containing impurities in the aq-PL-AgNPs. The second stage was observed between the temperatures 160–171 °C with 31.68% weight loss, attributed to the decomposition of the capping organic compounds (such as carbonyl and the reducing sugar) agents acting as the core–shell. Similar amount of inorganic and organic components present in the FL-AgNPs is observed in the PL-AgNPs with PL-AgNPs having 46% inorganics. Depicted in Figure.9.22 and 9.23. The thermogram of aq-FL-AgNPs suggest 68 percent remnants and 32 percent organic compounds. (Figure.9.24)

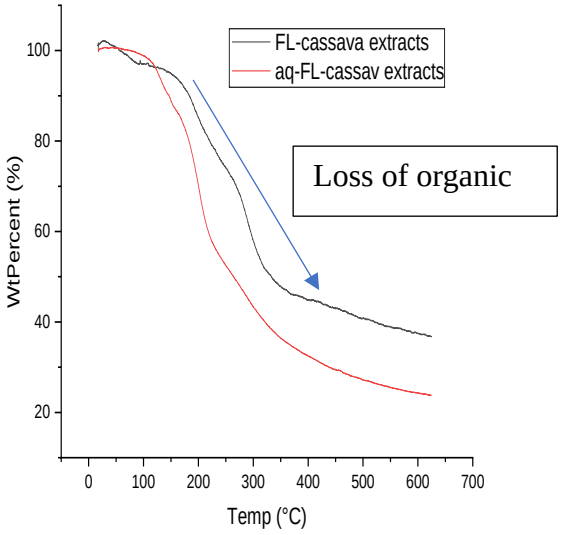

Figure.9.19: Thermal analysis of FL-cassava extracts (dried) and aq-FL-cassava extracts

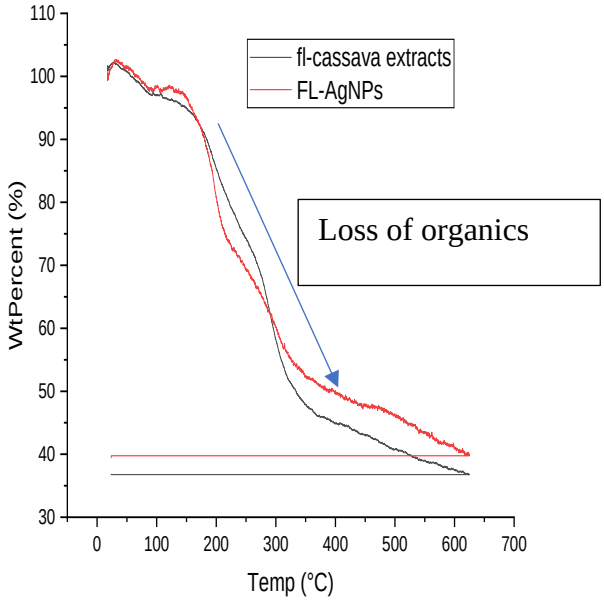

Figure.9.20: Thermal Analysis of FL-cassava extracts(dried) and FL-AgNPs

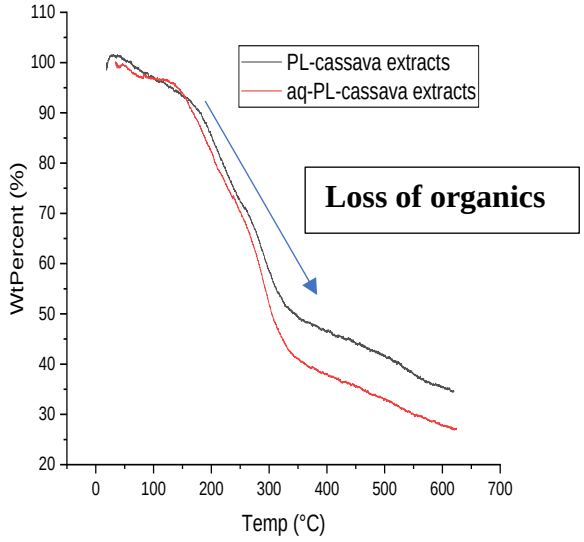

Figure.9.21: Thermal analysis of aq- PL-cassava extracts(dried) and aq-PL-cassava extracts(dried)

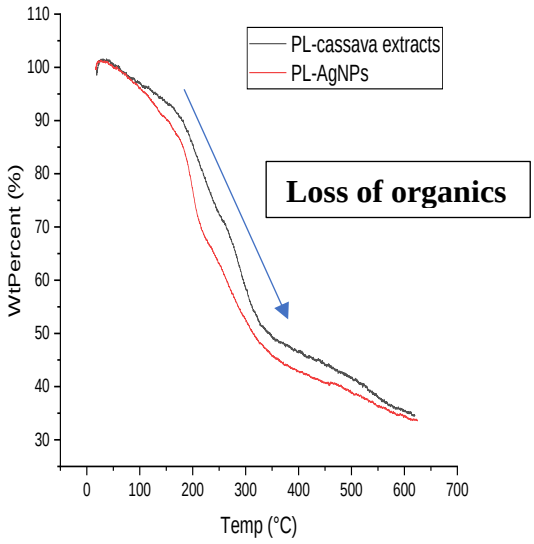

Figure.9.22: Thermal analysis PL-cassava extracts(dried)and PL-AgNPs

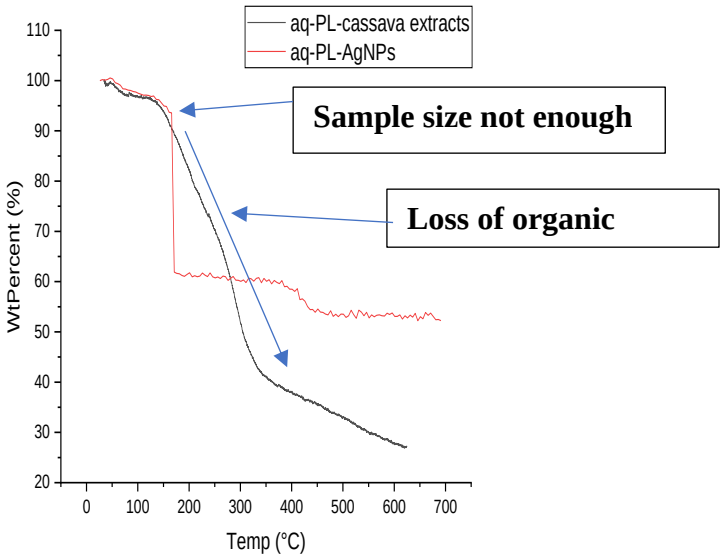

Figure.9.23: Thermal analysis of aq-PL-cassava extracts(dried) and aq-PL-AgNPs

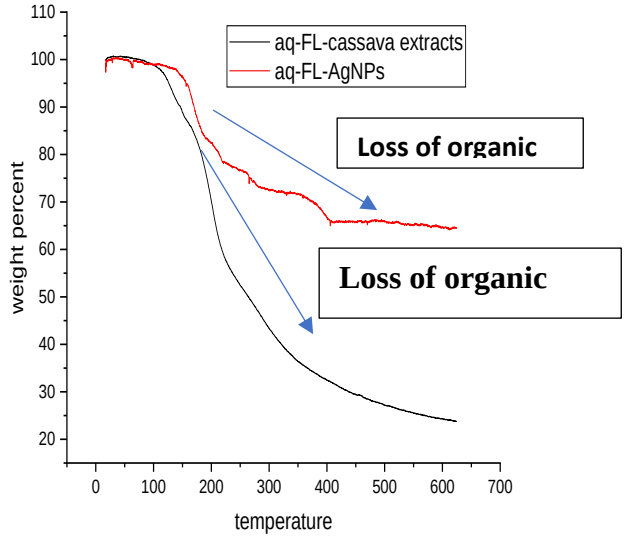

Figure.9.24: Thermal analysis of aq-FL-cassava extracts(dried) and aq-FL-AgNPs

9.1.7 HPLC analysis of the cassava extracts (Dried) and aqueous phase

The HPLC analysis confirms the abundance of glucose and xylose in both cassava extracts(dried) and the aqueous phase of both extracts, the product of hydrolysis, degradation of glucose and xylose are also observed in low amounts in the aqueous phase of both cassava extracts. Depicted in Table .9.0.

Ret time (min)	**Compound found**	**Aq-FL-cassava extracts(dried)**	**PL-cassava extracts(dried)**	**Aq-PL-cassava extracts(dried)**	**FL-cassava extracts(dried)**
8.488	cellobiose	$5.39E^{-3}$	$1.69E^{-2}$	-	-
9.023	glucuronic acids	-	$3.34E^{-3}$	-	$3.47E^{-5}$
9.530	galacturonic acids	-	-	-	-
9.887	glucose	$2.47E^{-2}$	$8.94E^{-2}$	$4.69E^{-3}$	$1.32E^{-2}$
10.607	xylose	$9.88E^{-3}$	$8.212E^{-3}$	$3.07E^{-3}$	$8.58E^{-3}$
10.850	mannitol	-	-	-	-
11.293	arabinose/rhamnose	-	-	-	-
12.947	levoglucosan	$2.7E^{-3}$	$9.35E^{-4}$	-	$1.98E^{-3}$
13.557	lactic acid	$2.06E^{-3}$	$2.45E^{-3}$	-	-
14.463	formic acid	$2.82E^{-3}$	-	-	-
15.710	acetic acid	$5.47E^{-1}$	-	-	$1.46E^{-2}$
17.127	levullinic acids	$3.47E^{-3}$	$2.51E^{-3}$	$4.77E^{-3}$	$6.99E^{-4}$
33.621	HMF	$1.32E^{-3}$	-	$9.81E^{-3}$	$8.99E^{-4}$

50.490	furfural	$3.78E^{-4}$	$2.5E^{-4}$	$4.55E^{-4}$	-

Table.9.0: HPLC profile of the of flesh cassava extracts(dried)

9.2 Application of PL-AgNPs as an interaction and adsorption of Cu(II) from aqueous solution

9.2.1 Interaction of Cu (II) by PL-AgNPs

2-20 ppm of Cu(II) were prepared,2 ml of each concentration are kept in a separate vial,2 ml of PL-AgNPs were added and left for 5minutes after which the solution are analysed using UV-Visible spectroscopy. (Figure.9.25). No significant changes were observed in the LSPR of PL-AgNPs and after the 5 minutes reaction times.

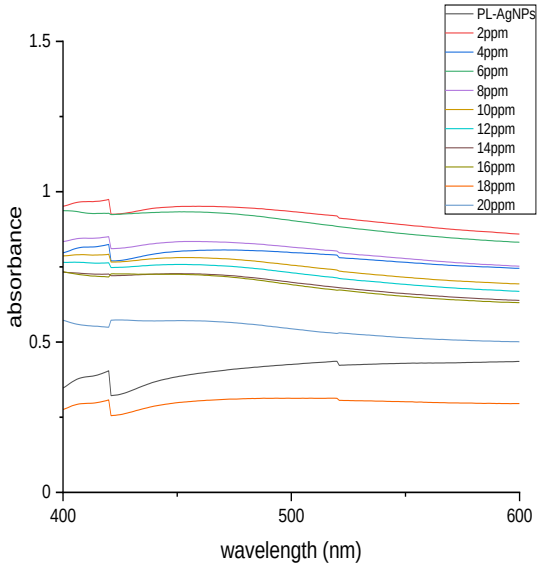

Figure.9.25: Interaction of Cu(II) by PL-AgNPs

9.3 Adsorption results

9.3.1 Effect of initial concentration

The result of adsorption of copper by PL-AgNPs shows the same trend in their adsorption pattern with Ni(II) and Cd(II) adsorption by EtOH-cysAgNPs and the quantities of each metal ion are adsorbed by increases approximately linearly till 400 ppm and decreases at 800 ppm. o (Fig.9.26).

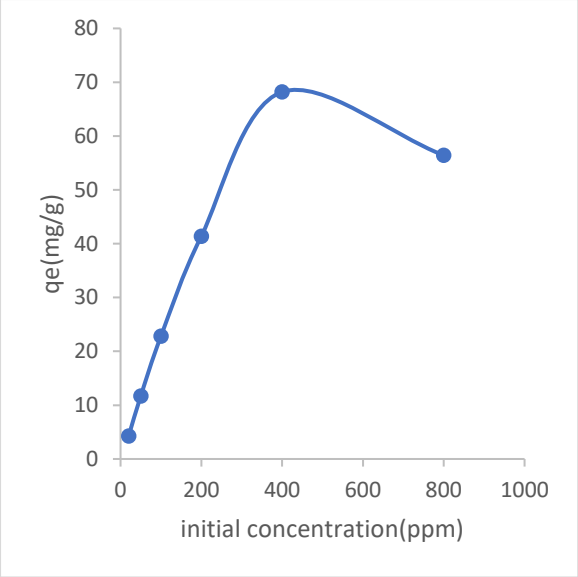

Figure.9.26: Effect of initial concentration of Cu(II) adsorbed by PL-AgNPs

9.3.2 Effect of contact time at optimal initial concentration

The adsorption of copper by PL-AgNPs is fast at the beginning and reaches equilibrium at 40 minutes for all the metal ions and tends to be stable subsequently from 60 minutes At 40 minutes, the value of qe became stables till 60 minutes, suggesting that the adsorption has reached equilibrium. (Figure. 9.27).

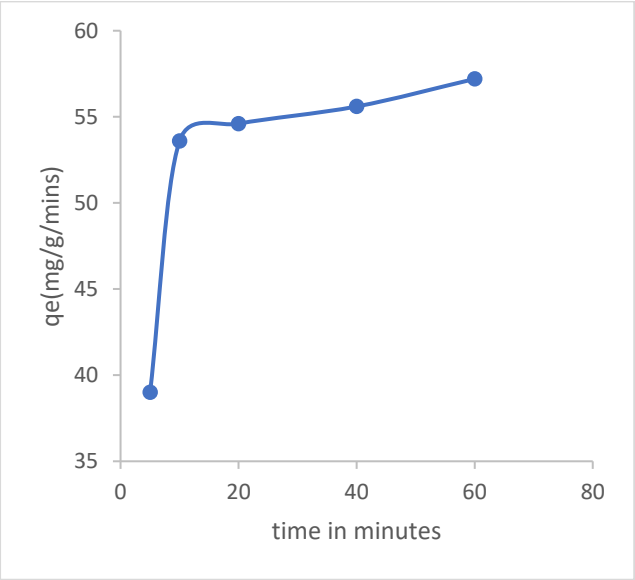

Figure.9.27: Effect of contact times of Cu(II) adsorbed by PL-AgNPs

9.3.3 Effect of dose at optimal initial concentration, optimal contact time

The quantity of Cu(II) ions adsorbed by PL-AgNPs again decreases with the dose of PL-AgNPs. Similar trends with the EtOH-cys-AgNPs. However, while this phenomenon generally relates to the ability of 0.01g of NP to completely adsorb the soluble metal species – meaning qe drops by a factor of 3 and 5 respectively at the higher doses – this is less obviously the case here (figure.9.28),0.01g of ET-OH-cys-AgNPs is sufficient enough to adsorbed Cu(II) at 400ppm.

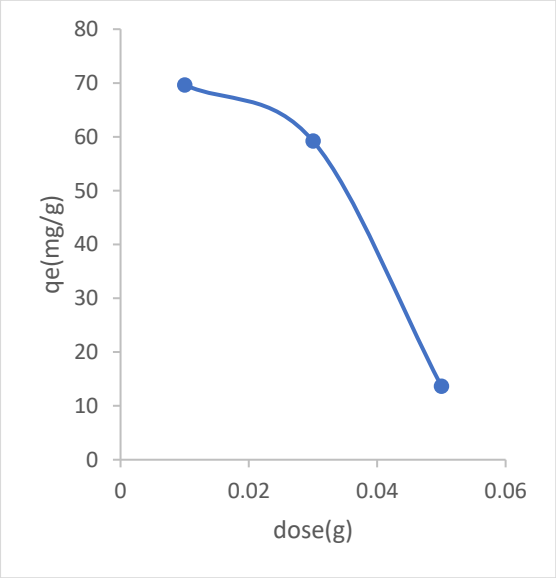

Figure.9.28: Effect of dose of Cu(II) adsorbed by PL-AgNPs

9.3.4 Effect of pH at optimal initial concentration, optimal contact time and dose

The qe values increases for Cu(II) ions examined as expected, the reason can be attributed as a result of the high pH is been dominated by negative charge and the surface of the PL-AgNPs is also negatively charged and there exist a strong electrostatic attraction of the metal cations and the PL-AgNPs as a result of these. Depicted in Figure.9.29. Similar trends are observed in GT-AgNPs and EtOH-cys-AgNPs.

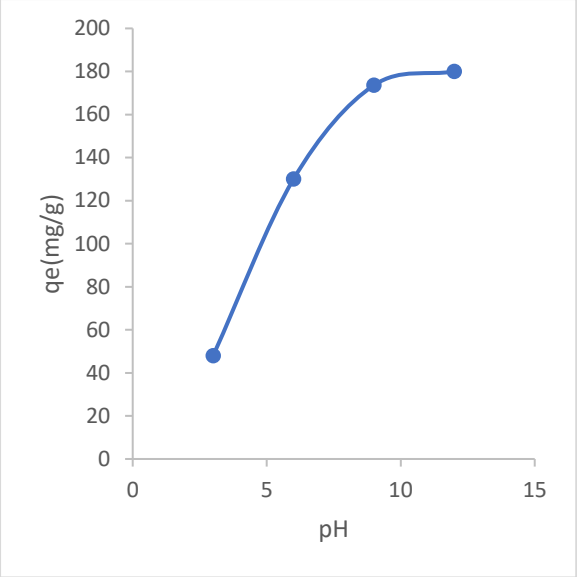

Figure.9.29: Effect of pH of Cu(II) adsorbed by PL-AgNPs

9.3.5 Effect of temperature at optimal initial concentration, optimal contact time, optimal dose and optimal pH

The qe values of adsorption of Cu(II) ions by PL-AgNPs increase with the temperature of the system. A similar trend is also observed in cys-AgNPs in organic solvent and GT-AgNPs. (Figure. 9.30).

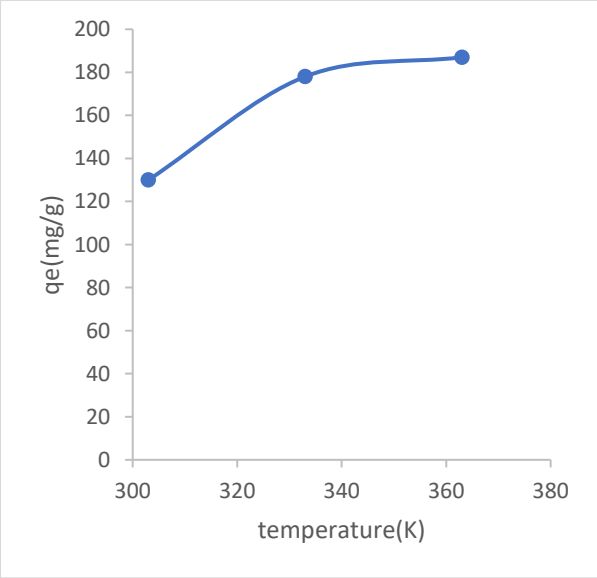

Figure.9.30: Effect of temperature of Cu(II) adsorbed by PL-AgNPs

9.3.6 Adsorption isotherm

The adsorption isotherm fits best with Freundlich Isotherm suggesting the heterogeneous nature of the adsorption sites. (Figure.9.31-9.32). The table of the R^2 value are highlighted in table.9.1.

Adsorption isotherm R^2	Freundlich Isotherm R^2	Temkin Isotherm R^2	Henry Isotherm R^2	Langmuir Isotherm R^2	D-R Isotherm R^2
Cu(II)	**0.723**	**0.723**	**0.398**	**0.2658**	**0.151**

Table.9.1: Adsorption Isotherm R^2 of adsorption of Cu(II) by PL-AgNPs

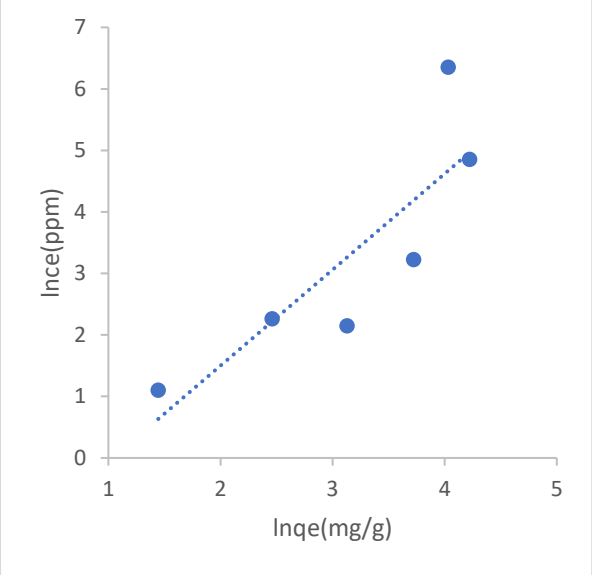

Figure.9.31. Temkin adsorption isotherm of Cu(II) adsorption by PL-AgNPs

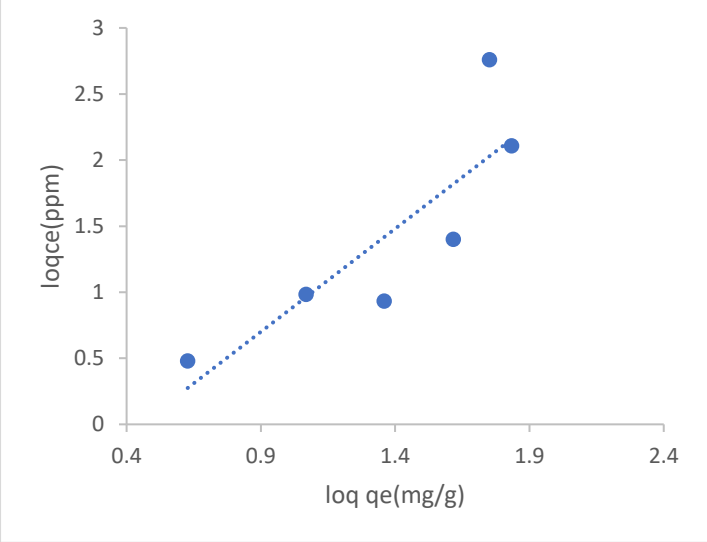

Figure.9.32: Freundlich adsorption isotherm of Cu(II) adsorption by PL-AgNPs

9.3.7 Adsorption Kinetics

The adsorption fits best using Pseudo second order kinetics. (Figure.9.33-9.34)

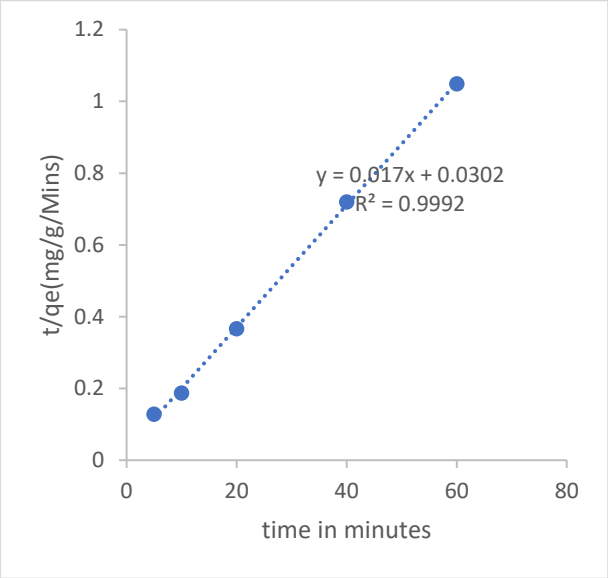

Figure.9.33: Pseudo second-order Kinetics of Cu(II) adsorption by PL-AgNPs

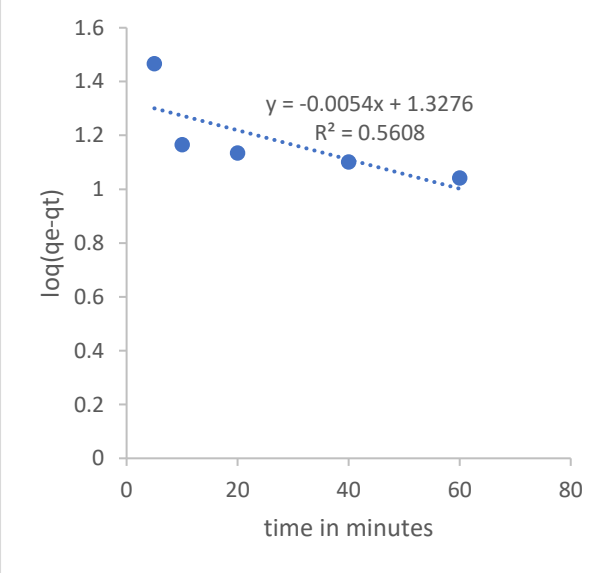

Figure.9.34: Pseudo first order Kinetics of Cu(II) adsorption by PL-AgNPs

9.3.8 Adsorption thermodynamics

The plot of adsorption thermodynamics parameter for Cu(II) adsorption parameters are $\Delta H = -31.33 kj/mole, \Delta S = 103.74 \text{J/Mol/ K})$ and $\Delta G = -62.2 kj/mol$ suggesting a spontaneous adsorption process characterized by an increased in disorderliness of the molecules.(Figure.9.35)

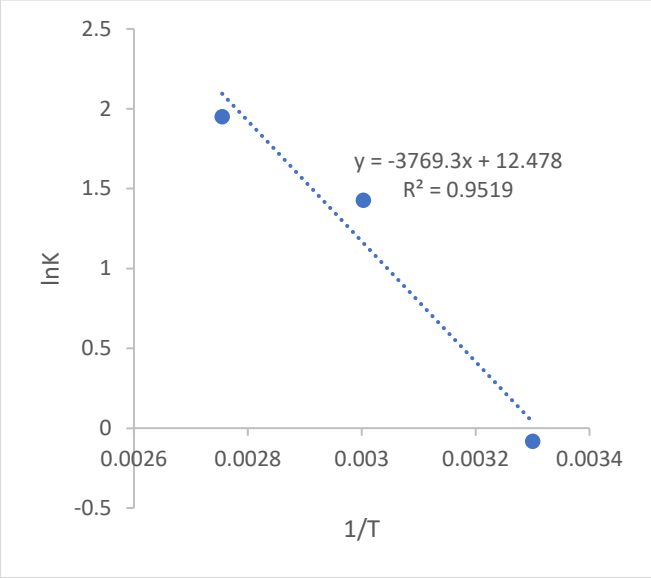

Figure.9.35: Adsorption thermodynamics of Cu(II) adsorption by PL-AgNPs

9.4 Conclusion to chapter 9

AgNPs were successfully synthesized using the aqueous phase and the complete extract of the cassava waste peels and cassava Flesh as demonstrated from the information obtained from the structural establishment from several analytical techniques. The formation of AgNPs was greatly enhanced using the aq-PL-cassava extracts and aq-FL-cassava extracts and this is obtained by the rapid formation and stability of the LSPR over time. The existence of LSPR in the UV/Visible spectra of of FL-AgNPs, aq-FL-AgNPs and aq-PL-AgNPs are characterized by bigger sizes particle size and stable over time, with exception to PL-AgNPs whose particles size are smaller compared to the other.

The interaction of Cu(II) by PL-AgNPs shows little of fair changes in the absorption of spectra of the before and after the interaction. It also shows the potential to remove heavy metals from aqueous solution.

CHAPTER TEN

10.0 Gold nanoparticles from cassava

10.1 FTIR spectra of gold nanoparticles from cassava

As expected from the HPLC and NMR data the FTIR of AuNPs produced from the various faction and FL-cassava extracts consist essentially of the expected bands from sugars. Table.10.0 and Figure.10.1

Band position (Cm^{-1})	3322	2974	1574	1368	1000
Functional group	OH str	CH def	OH def	CH def	C-O- str

Table.10.0: FTIR band assignation of cassava AuNPs

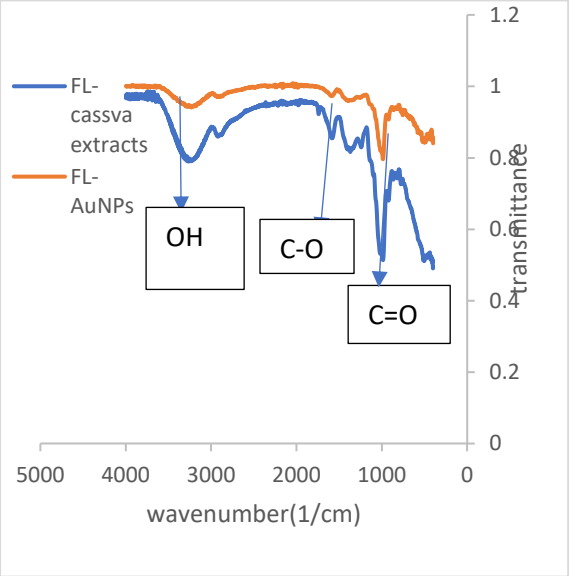

Figure.10.0: FTIR spectra of cassava flesh and cassava flesh AuNPs

The spectra of aq-FL-cassava extracts and aq-FL-AuNPs are broadly similar to before and consistent with the presence of saccharides (Fg.10.1). A new signal appeared at $1701cm^{-1}$ C=O stretching vibration, this carbonyl signal (C=O) can possibly be attributed to an aldehyde group (from an open chain sugar) or a carboxylic acid from oxidation of sugar during NP formation, or from a fatty acid coordinated to the surface.

The FTIR spectra of PL-cassava extracts and PL-AuNPs are presented in Figure.10.2 and are found to be consistent with the presence of sugars. same observation with the aq-PL-cassava

extracts(dried) and the aq -PL-AuNPs(Figure.10.3). Similar mode of vibrations is found in the

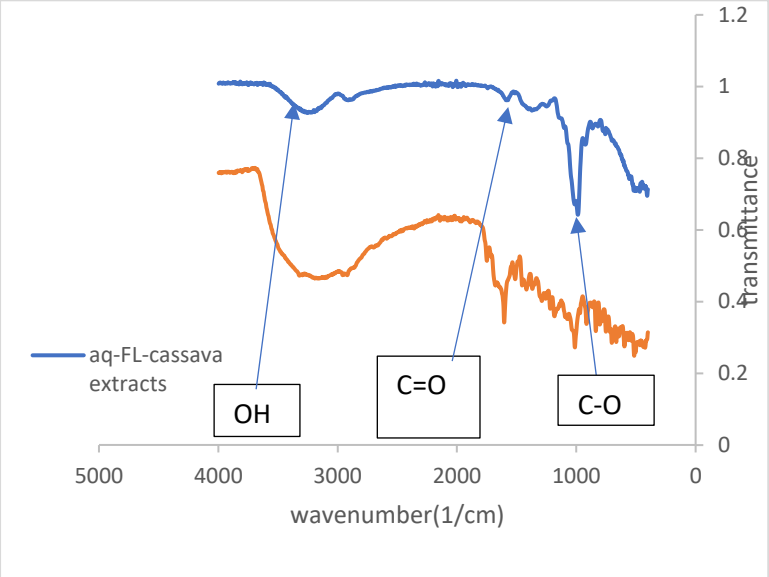

Figure.10.1: FTIR spectra of aqueous phase cassava flesh and cassava flesh AuNPs

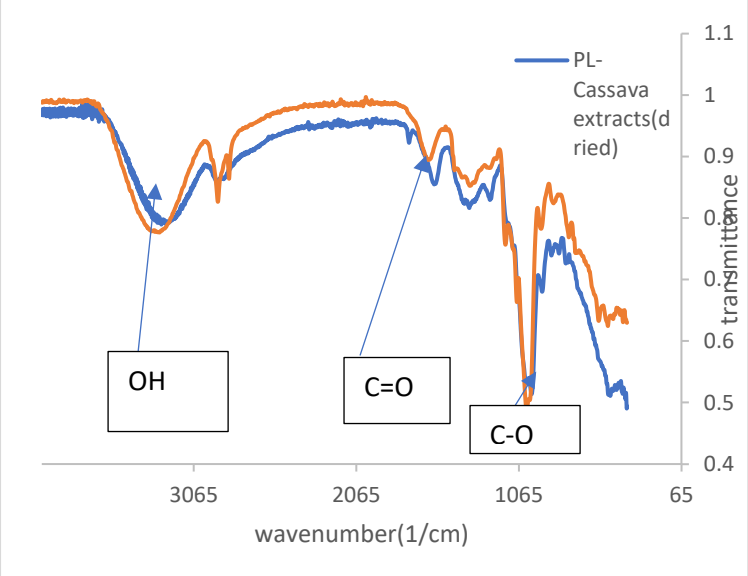

Figure.10.2: FTIR spectra of cassava peels and cassava peel AuNPs

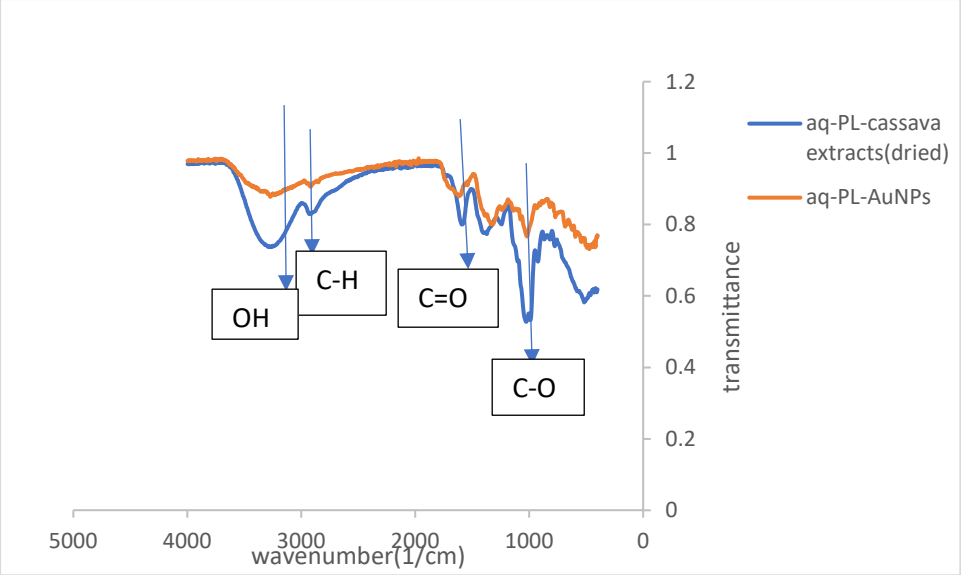

Figure.10.3: FTIR spectra of aqueous phase cassava peels and aqueous phase cassava peel AuNPs

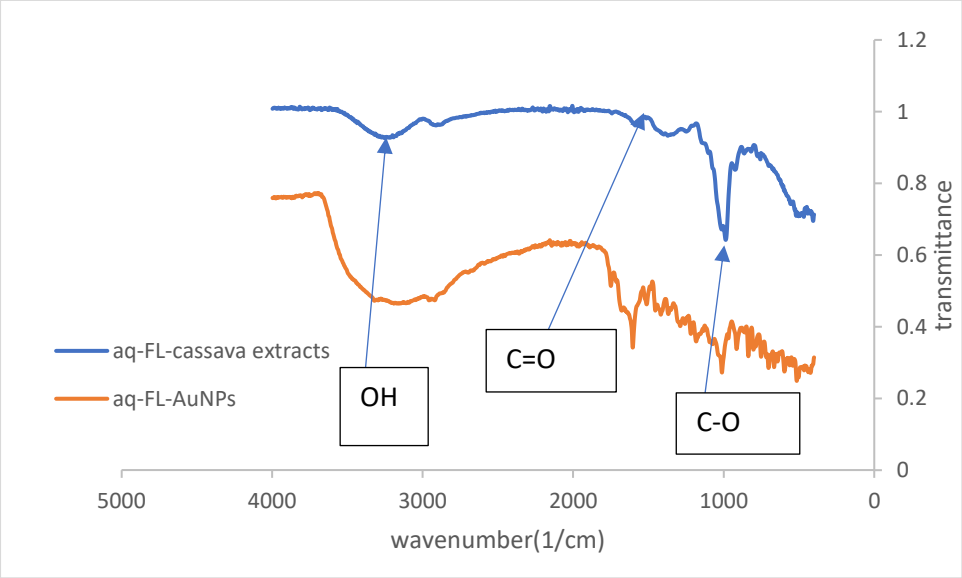

Figure.10.4: FTIR spectra of aqueous phase cassava flesh and cassava flesh AuNPs

10.2 UV/Visible spectroscopy

Figure.10.5 shows the photographs and the UV–Vis spectra of AuNPs synthesized by PL-cassava Extracts and of $AuCl_3$. The addition of aqueous $AuCl_3$ resulted in a colour change from pale yellow to purplish red after 20minutes of reaction, indicating the formation of AuNPs.

depicted in figure.10.5. The surface plasmon resonance was observed at 550nm. The stability in absorption intensity of the peaks with time indicate the presence of stable of AuNPs in the solution. There was no obvious change in SPR peak even after 100 min, indicating the complete synthesis of AuNPs by PL- cassava extracts. (Figure.10.5)

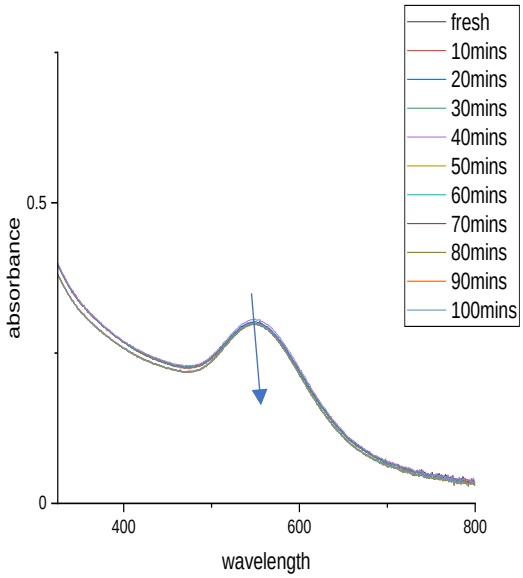

Figure.10.5: UV/Visible spectra of PL-AuNPs and its absorbance stability measurements with time (10-100 mins) at 10 mins interval

Figure.10.6 show the UV/Visible spectra of the FL-AuNPs, the LSPR was observed at 575nm and tends to be narrow in shape compared to hoe synthesized using the PL-cassava extracts implying that the size of the PL-AuNPs tend to be bigger compared to the FL-AuNPs.The obtained FL-AuNPs displays excellent time stability measurements.

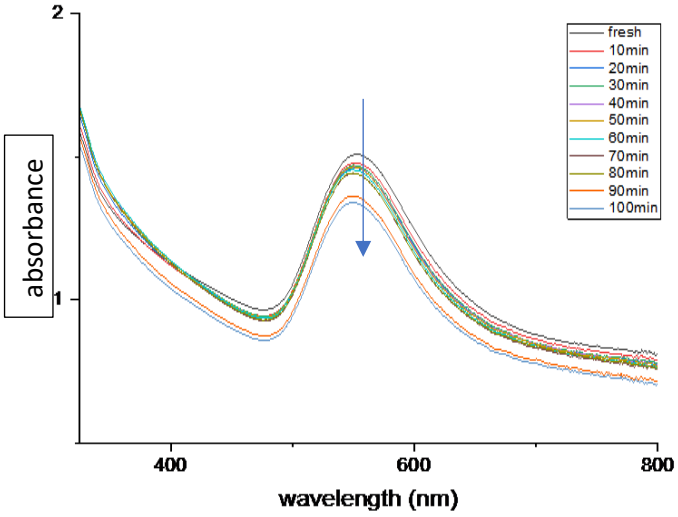

Figure.10.6: UV/Visible spectra of FL-AuNP and its absorbance stability measurement with time (10-100 mins) at 10 mins interval

Figure.10.7 shows the UV/Visible spectra of PL-AuNPs, the LSPR were observed at 556nm, there appear to be a red shift compared with aq-the PL-AuNPs (fig.10.8) as the synthesis of aq-Pl-AuNPs are primarily done by the sugars the aq-PL-AuNPs also tends to comprise of bigger particle as the broadness of the spectra implies a bigger particles size, the broadness of the LSPR tends to increases with time. (Figure.10.7-10.8)

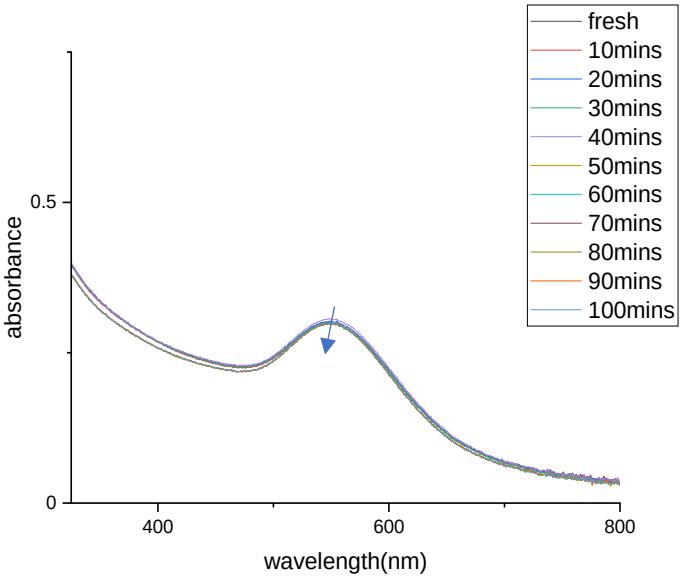

Figure.10.7: UV/Visible spectra of PL-AuNPs and its absorbance stability measurements with time (10-100 mins)

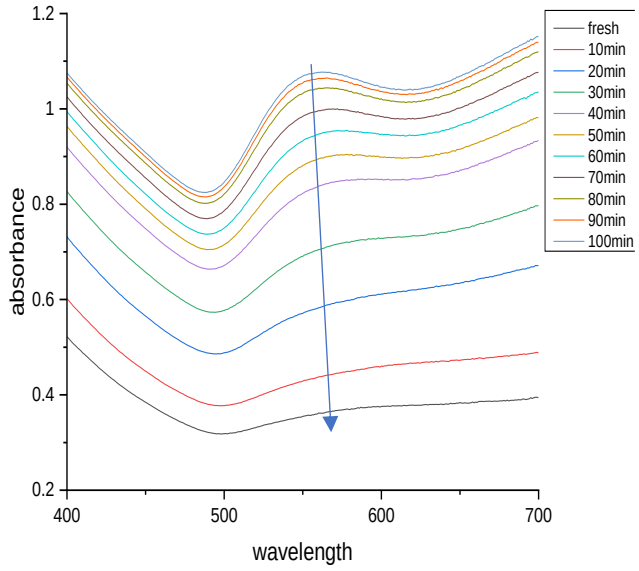

Figure.10.8: UV/Visible spectra of aq-PL-AuNPs and its absorbance stability measurements with time (10-100 mins)

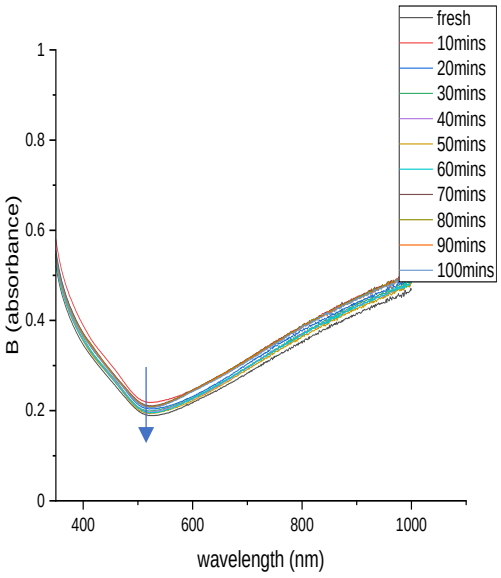

Figure.10.9: UV/Visible spectra of aq-FL-AuNPs and its absorbance stability measurements with time (10-100 mins)

Figure.10.9 depicts the UV/Visible spectra of aq-FL-AuNPs the spectra reveal that no LSPR were observed throughout the sample time, the UV/Visible spectra of the FL-AuNPs displays an excellent LSPR at 575 nm compared to the aqueous phase fractions of the FL-cassava extracts

Figure.10.8 and 10.9 represent the UV/Visible spectra of aq-PL-AuNPs and aq-FL-AuNPs synthesized using the original methods of synthesis, no signs of LSPR was observed. The condition used for the synthesis of aq-PL-AuNPs and aq-FL-AuNPs does not lead to the production of AuNPs and thus the UV/Visible spectra of both fractions suggest the presence of Au(III) which might be as a result of the absence of the organic component present in the extracts and thus could not reduce the Au(III) to Au(0) nor stabilized it.

Figure.10.10 represent the UV/Visible spectra of aq-FL-AuNPs and aq-PL-AuNPs synthesized using the optimized methods, no signs of LSPR was observed.

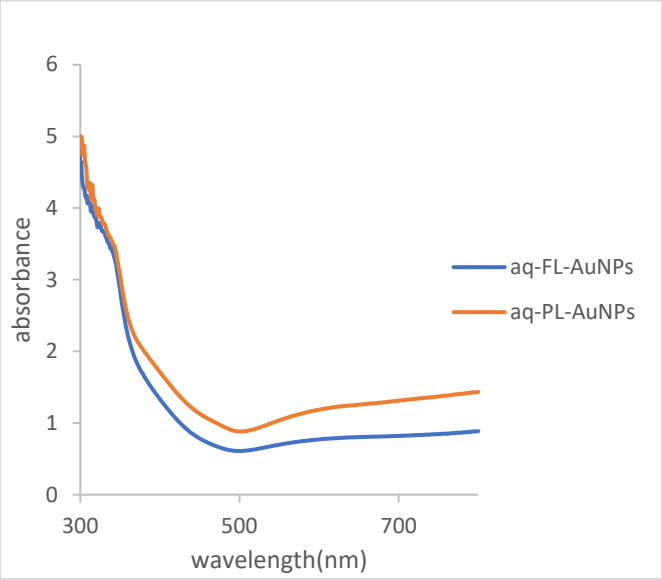

Figure.10.10: UV/Visible spectra of optimized aq-FL-AuNPs and aq-PL-AuNPs

The AuNPs produced from the PL-cassava extracts and FL-cassava extracts resulted into purplish colourations which is characteristics of AuNPs, the AuNPs produced from the Aqueous faction of PL-cassava extracts yield purplish coloration of AuNPs, while the aqueous faction of FL-cassava extracts yields a greenish black coloration of AuNPs with no LSPR. (Figure.10.11)

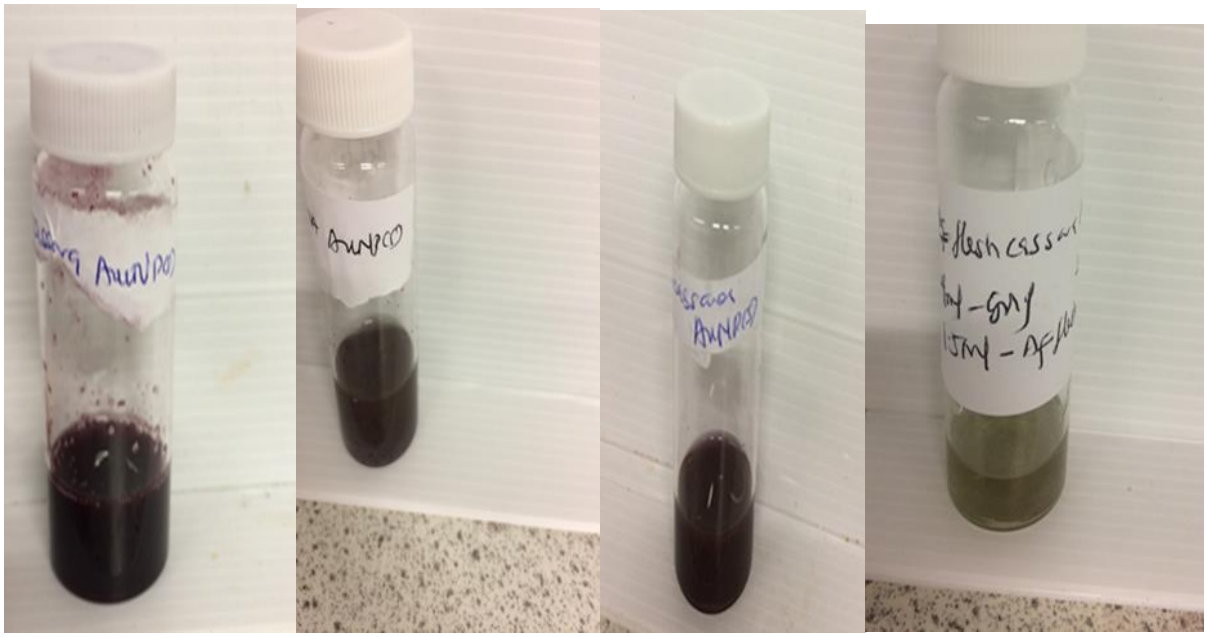

Figure.10.11: Jpeg image a) PL-AuNPs, b) aq-PL-AuNPs, c) FL-AuNPs, d) aq-FL-AuNPs

10.3 PXRD techniques of cassava gold nanoparticles

Figure 10.12 shows the XRD patterns of the PL-cassava starch and the PL-AuNPs and cassava starch and both exhibited a similar diffractogram. The PL-AuNPs shows a five characteristic peaks at 21.42^0,39.2^0,43.2^0,63.5^0 and 78.6^0 corresponding to the (1 1 1), (2 0 0), (2 2 0), (3 1 1) and (2 2 2) facets of gold. The peaks demonstrated that the PL-AuNPs obtained is crystalline gold with face-centred cubic (FCC) structure.[3]

The Figure 10.13 shows PXRD diffractogram of aq-PL-AuNPs with four weak characteristics peaks at 38.07^0,44.5^0,65.2^0 ,77.9^0 and 81.68^0 correspond to the (111), (200), (220), (311), and (222) facets of metallic Au in face-centred cubic structure (JCPDS File No. 04-0784), respectively.[3] This data demonstrated that the Au^{3+} was reduced to form crystallized AuNPs, which was consistent with the results reported for Au nanoparticles.

The diffractogram of FL-AuNPs show a characteristics peak of 38.2^0,44.59^0,64.76^0 and 77.77^0 which also corresponds to the corresponding to the (1 1 1), (2 0 0), (2 2 0) and (3 1 1) facets of gold. The peaks demonstrated that the FL-AuNPs obtained is crystalline gold with face-centred cubic (FCC) structure. Depicted in figure.10.14.

The PXRD of the aq-FL-AuNPs shows peaks at 37.8^0,44.2^0,64.4^0,77.99^0 and 81.65^0 which correspond to the (111), (200), (220), (311), and (222) facets of metallic Au in face-centred

cubic structure. All the AuNPs made using the cassava extracts and the Aqueous phase of each fraction result into a face centred cubic crystal. depicted in figure.10.12-10.15.

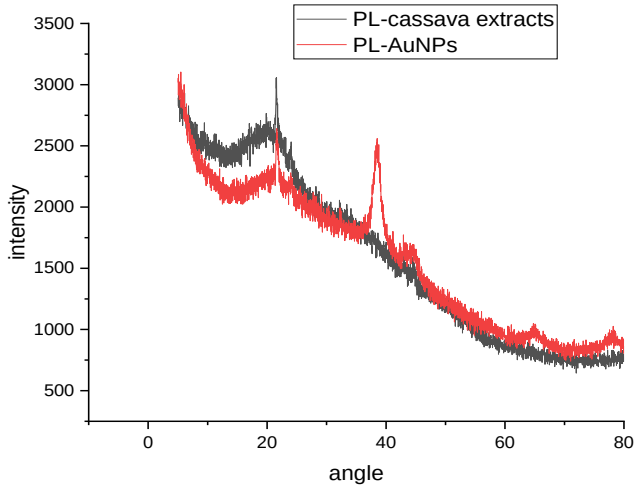

Figure.10.12: PXRD of cassava peel extracts and -PL-AuNPs

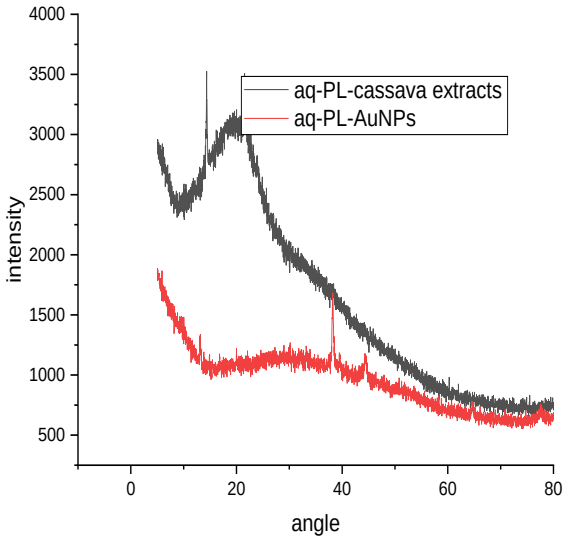

Figure.10.13: PXRD of aqueous phase cassava peel extracts and aq-PL-AuNPs

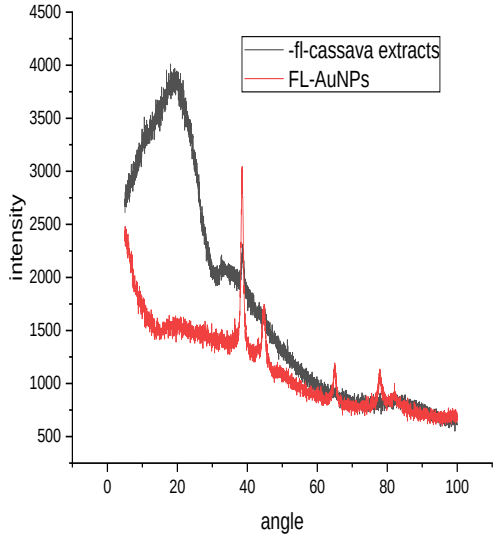

Figure.10.14: PXRD of cassava flesh extracts and FL-AuNPs

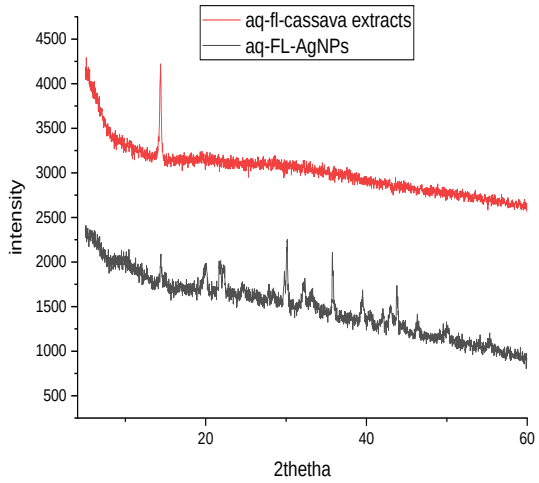

Figure.10.15: PXRD of aq- cassava flesh extracts and aq-FL-AuNPs

10.4 Thermal analysis of the Cassava AuNPs

TGA thermogram of the FL-cassava extracts and corresponding AuNPs are generally similar with two or three stage weight loss and few unusual features, the AuNPs have a higher residual mass due to the gold and the residues from the extracts contains both inorganic and carbonaceous organic compound .the decomposition profile is minimally influenced by the metal and therefore the gold content can be estimated based on the organic residue plus the

additional residue from the Au except aq-FL-AuNPs which has a huge influenced decomposition suggesting the Au has a more active role ,and making the estimation of Au content more difficult. The thermal analysis of all the AuNPs synthesized from the both aqueous components and the two extracts have decomposition pattern similar to the decomposition of saccharides.

10.5 Conclusion to chapter 10

The synthesis of gold nanoparticles was achieved using the total cassava waste peels and flesh extracts and there exist no formation of gold nanoparticles using the aqueous phase of both extracts as evidence by the absence of LSPR in the UV/Visible spectroscopy of the aq-FL-AuNPs and aq-PL-AuNPs, the PXRD results obtained for both Pl-AuNPs and FL-AuNPs are in relatives with the literature study. The formation of the LSPR were quite rapid and prominent in the PL and FL-cassava extracts.

11.0 General Summary

Silver nanoparticles were successfully synthesised using the sodium borohydride and cysteine, green tea extracts also show potential to synthesized silver nanoparticles without the aid of auxiliary reactants such as ascorbic acids and citric acids, it evident that cassava flesh extracts on its own cannot reduce the silver ion to it elemental form at room temperature, it requires the aid of co reductants to successfully achieved the synthesis of silver nanoparticles. Cassava Peel extracts, cassava Flesh extracts and the aqueous components of both extracts successfully produced silver nanoparticles and it evident by the presences of LSPR on the absorption spectra of the respective silver Nanoparticles.

Silver nanoparticles produced from sodium borohydride and cysteine shows potential to interacts with heavy metals and also removed it from contaminated waste water, silver nanoparticles made from green tea and cassava extracts also shows potential to interact with the heavy metals and removed it from aqueous solution as evidence from the adsorption results and the interaction results.

Adsorption of Ni(II) in the presence of EDTA by ET-OH-cys-AgNPs shows some possible co-adsorption of EDTA when compared to the adsorption of Ni(II) Adsorption results and 0.01g of cys-AgNPs could potentially remove all the heavy metals with optimal metal capacity at 400 ppm.

The adsorption of Pb(II) in the presence of Na(I) and Mg(II) ion by ET-OH-cys-AgNPs shows possible contribution in the adsorption of Pb(II) in a single system and when compared to it in a binary system.

Synthesis of AuNPs by sodium citrate tribasic, green tea extracts and cassava peel extracts, cassava flesh extracts and aqueous components of the two extracts were successfully achieved except in the case of synthesis of AuNPs by cassava flesh extracts at room temperature which requires the aid of co-reductants such as ascorbic acids and citric acids. There exists some variation in the shape and values of the LSPR among the synthesized gold nanoparticles.

Adsorption isotherm Tends to fit best with Henry adsorption Isotherm and adsorption kinetic fit best with pseudo second -order kinetic for all the metal ion examined.

11.1 General conclusion

Silver Nanoparticles particles produced using the traditional way shows a positive interaction towards set of heavy metal ions examined and demonstrate the ability to remove the heavy metal ion analysed in the thesis, The effect of the high amount of cysteine on the silver nanoparticles is less pronounced in the adsorption experiment as both have the optimal adsorption at 0.01g of the adsorbents. In the interaction experiments, the ET-OH-cys-AgNPs shows a colour change in response to Cu(II) and Ni(II),red and dark-grey respectively, while aq-cys-AgNPs shows a fair yellowish change in response to Cu(II) and Ni(II) and both shows a red shift for Cu(II) and Ni(II).The changes in the interaction pattern might be attributed to the quantity of cysteine at the surface of the nanoparticles. Results obtained from the rest of the other heavy metals analysed shows they could be potentially be used as an interactive tool to detect heavy metal from waste water. The silver nanoparticles obtained from peel fractions of the cassava extracts shows an excellent adsorption performance and also have optimal dose of 0.01g of the PL-AgNPs and also shows a positive interaction results towards Cu(II) in waste water. The silver nanoparticles produced from green tea extracts shows potential to be used in the removal of heavy metals and also have optimal dose at 0.01g of the adsorbents which is similar to aq-cys-AgNPs, ET-OH-cys-AgNPs and PL-AgNPs. Due to the abundance of cassava peel in southern region Nigeria and also the presence of toxic heavy metals in the southern region of Nigeria, Silver nanoparticles obtained from cassava can be a better alternative to the other silver Nanoparticles produced from the traditional routes and green tea.

Gold nanoparticles obtained from the traditional routes shows an excellent sensing and adsorption results towards the heavy metal analysed and could be used an interactive tool and adsorbents for the removal of heavy metals from waste water. Green tea demonstrates the ability to reduced gold ion to it free states and the ability to stabilized it surfaces as demonstrate by the characterization results, The interaction of heavy metals with green tea stabilized gold nanoparticles shows a positive interactive result towards the range of heavy metal analysed and could be used as an interactive tool for the detection of heavy metals from waste water. Due to the cost of gold no adsorption experiments were caried out on gold. Out of the fractions of cassava extracts used in the production of gold nanoparticles, excellent results were obtained from 2 fractions of the cassava extracts (cassava peel and cassava flesh extracts) and the aqueous components of the cassava peel and cassava flesh could not reduce the gold ions to its free state and no evidence of LSPR was observed in the aqueous components of the cassava flesh while that of the cassava peel the LSPR got diminished with time.

Conclusively, silver nanoparticles obtained from cassava extracts prove to be choice as metal nanoparticles owing to the abundance of cassava in Nigeria and availability of the cassava peel waste in the Southern region of Nigeria, it also benign, greener, cost effectives and shows an excellent adsorption result towards heavy metal ions examined.

11.2 Recommendation

Successful synthesis of noble metal nanoparticles was achieved in this research thesis, and also it evident that the metal nanoparticles can interact with the heavy metal ions examined using UV/Visible spectroscopy but UV/Visible spectroscopy can't distinguish which metal is which it will be suitable if a more sensitive analytical equipment's such as ICP-OES or electrochemical studies can be use in replacement of the UV/Visible spectroscopy.

11.3 Future work

Cheap metal nanoparticles such as copper, nickel and molybdenum disulphides Nanoparticles were synthesised using the cassava peel extracts and the cassava flesh extracts, no evidence of successful synthesis was achieved it which might be attributed with the reducing ability of the cassava extracts. Synthesis involving GT-extracts, citric extracts and ascorbic acids produced mixed results. Greener extracts possessing a stronger reducing components can be used in replacements. which might have the potentials to reduce the metal easily.

References

1. M. Auffan, J. Rose, J.-Y. Bottero, G. V. Lowry, J.-P. Jolivet and M. R. Wiesner, *Nat. Nanotechnol*., 2009, **4,** 634–641

2. G. Walters, I. P. Parkin, R. Palgrave, I. P. Parkin, S. W. Han, C. Goyes, Y. Jestin, M. L. Mattarelli, M. Montagna, G. N. Conti, S. Pelli, G. C. Righini, C. Tosello and K. C. Vishunubhatla, *J. Mater. Chem*., 2009, **19**, 574–590

3. J.-Y. Bottero, J. Rose and M. R. Wiesner, *Integr. Environ. Assess. Manag*., 2006, **2**, 391–395

4. D. F. Emerich and C. G. Thanos, *Biomol. Eng.*, 2006, **23**, 171–184

5. A. K. Gupta and M. Gupta, *Biomaterials.*, 2005, **26**, 3995–4021

6. S. Eustis and M. A. El-Sayed, *Chem. Soc. Rev*., 2006, **35**, 209–217

7. www.nanowerk.com (accessed October,2024)

8. B. Khlebtsov, V. Zharov, A. Melnikov, V. Tuchin and N. Khlebtsov, *Nanotechnology*., 2006, **17**, 5167

9. S. Link and M. A. El-Sayed, *J. Phys. Chem. B*, 1999, **103**, 4212–4217

10. J.J. Mock, D.R. Smith and S. Schultz, *Nano Lett*.,2003,**3**,485

11. G.C. Schatz, L.J. Sherry, R.C. Jin, C.A. Mirkin and R.P. Van Duyne, *Nano Lett*.,2006,**6**, 2060

12. M.D. Malinsky, K.L. Kelly, G.C. Schatz, R.P. Van Duyne, *J. Am. Chem. Soc*. ,2001,**123**, 1471

13.. L.J. Sherry, S.H. Chang, G.C. Schatz, R.P. Van Duyne, B.J. Wiley and Y.N. Xia, *Nano Lett.*,2005**,5**,2034

14. C.L. Nehl, H.W. Liao and J.H. Hafner, *Nano Lett*.,2006,**6**, 683

15. S.M. Marinakos, S. Chen and A. Chilkoti, *Anal. Chem*.,2007,**79**,5278

16. J.F. Wang, H.J. Chen, X.S. Kou, Z. Yang, and W.H. Ni, *Langmuir*.,2008,**24**,5233

17. E.M. Larsson, J. Alegret, M. Kall and D.S. Sutherland, *Nano Lett*.,2007,**7**, 1256

18. Y.G. Sun and Y.N. Xia, *Anal. Chem*.,2002,**74** 5297

19. N. Nath and A. Chilkoti, *Anal. Chem*.,2002,**74**,504

20. J. Zhao, L. Jensen, J. Sung, S. Zou, G. C. Schatz and R. P. Van Duyne, *J. Am. Chem. Soc*., 2007, **129**, 7647 —7656

21. J. Xiong, Y. Wang, Q. Xue and X. Wu, *Green Chem*,2011,**13**,900-904

22. W. Yu, H.Q. Xie, L.F. Chen, Y. Li and C. Zhang,*Nanoscale Res. Lett*.,2009,**4**,465-470

23. C.Cameron ,F.W.Crane,L.Jun,T.,Jing ,Z.Yimei ,and C.Jingyi, *J .Phys. Chem. C* .,2017, **10**, 5684–5692

24. K.G. Mithun,S. Sanjay ,G. Indersh and K.G.Tanmay *RSC Adv*., 2020, **10**, 22027

25. W. Shuang, R.Shanmugam,M. Malini and M.Vanaja , *Art.cells,nanomedicine and biotechnology*,2020 ,**1**, 1153-1158

26. M.S. Daniel, 2012, Proyecto fin de Carrera Universidad de Cantabria.

27. V.A.G. Rivera, F.A. Ferri and E. Marega, 2012, Plasmonics -Principles and Applications, Dr. Ki Young Kim (Ed.), InTech, DOI: 10.5772/50753

28. H. S. Desarkar P. Kumbhakar and A. K. Mitra, *Appl Nanosci*.,2012,**2**,285291, 285-291

29. N.D.Jaji. M.H.Bisyrul. L. Lee., and M. H. Hussin, *Nanotechnology*., 2021,318–329

30. S.P.Govinder, E.Ameen, P.Bala , T.A.Asif Ali, K.M.Tapas, *International Journal of Hydrogen Energy*.,2019, **2,** 578-586

31. A.Asad, A.M.Farhana, C. Xiaolin, D.Yiwen , C. Kui ,X. Xiaoliang ,X. Ruixiang and Z. Lixin *Nanoscale*., 2019, **11**, 7813

32. E.B.Mohamed, A. Abdellatif ,M. Abdellah ,. *Optik*., 2018, **171**,237-246

33. J. Rick, M.C. Tsai, and B.J. Hwang, *Nanomaterials*.,2015, **6,** 5–30.

34. M.B. Tahir, M. Sohaib, M. Sagir, and M. Rafique, *Ref. Modul. Mater. Sci. Mater. Eng*., 2020, 1-12

35. T.A. Saleh and V.K. Gupta, Environ. *Sci. Pollut. Res. Int*. 2012,**19**, 1224–1228

36. I. Saiqa, *Nano Res Appl*., 2016, **2,** 1–10

37. M. Tanveer and G. Tezcanli Guyer, *Renew. Sustain. Energy Rev*., 2013, **24**, 534–543

38. P. Peralta-Zamora, A. Kunz, S. Gomes de Moraes, R. Pelegrini, P. De Campos Moleiro, J. Reyes, and N. Durán, *Chemosphere*.,1999, **38**, 835–852

39. F. Banat, S. Al-Asheh, M. Al-Rawashdeh and M. Nusair, Desalination., 2005, 181, 225–232

40. S.K. Kansal, M. Singh and D. Sud, *J. Hazard. Mater*., 2007, **141**, 581–590

41. The Brownfields and Land Revitalization Technology Support Center. Archived from the original on 2008-02-18. Retrieved 2009-12-21

42. "absorption (chemistry)". Memidex (WordNet) Dictionary/Thesaurus. Archived from the original on 2018-10-05. Retrieved 2010-11-02.

43. Atkins, P. W.; De Paula, Julio; Keeler, James (2018). Atkins' Physical chemistry (Eleventh ed.). Oxford, United Kingdom. ISBN 978-0-19-876986-6. OCLC 1020028162. [page needed}

44. Ferrari, L.; Kaufmann, J.; Winnefeld, F.; Plank, J. (2010). "Interaction of cement model systems with superplasticizers investigated by atomic force microscopy, zeta potential, and adsorption measurements". *J. Colloid Interface Sci.* 347 (1) 15–24

45. S.A Khosrowshahi, A. Mobin. Mohammad, E. Mashhadimoslem, Khakpour, H.B.M. Emrooz, S. Sadeghzadeh, and A. Ghaemi, The role of surface chemistry on CO_2 adsorption in biomass-derived porous carbons by experimental results and molecular dynamics simulations, Scientific Reports. 12 (1): 8917,2022

46. Carroll, T. Gregory Jongejan, G.M. Mahthild, F. Pijper, Dirk and L. Ben, Chemical Science.,2010, 4 469

47. K. Czelej, K. Cwieka and K.J. Kurzydlowski, *Catalysis Communications.*,2016, **5**,33–38

48. K. Czelej, K. Cwieka, J.C. Colmenares and K.J. Kurzydlowski, Langmuir.,2016,**30**,7493–7502

49. Czepirski, L.; Balys, M. R.; Komorowska-Czepirska, E. (2000). "Some generalization of Langmuir adsorption isotherm". Internet Journal of Chemistry. 3 (14). ISSN 1099-8292. Archived from the original on 2017-01-13. Retrieved 2013-11-19

50. N. Ayawei, A. N. Ebelegi and D. Wankasi, *J. Chem*., 2017, **11**, 3039817

51. A. A. Inyinbor, F. A. Adekola and G. A. Olatunji, *Water Resour. Ind*., 2016, **15**, 14 —27

52. F. Batool, J. Akbar, S. Iqbal, S. Noreen and S. N. A. Bukhari, *Bioinorg. Chem. Appl.*, 2018, 2018, 3463724

53. A. O. Dada, F. A. Adekola and E. O. Odebunmi, *Appl. Water Sci*., 2017, **7**, 1409 —1427

54. M. Dubinin the potential theory of adsorption of gases and vapors for adsorbents with energetically nonuniform *surfaces Chem. Rev*., 1960,**60**,235-241

55. Q. Hu, Z. Zhang Application of dubinin-radushkevich isotherm model at the solid/solution interface: a theoretical analysis J. Mol. Liq.,2019, 277,646-648

56. Alberti et al., 2012 G. Alberti, V. Amendola, M. Pesavento, R. Biesuz, *Coord. Chem. Rev*., 2012,**256**,28-45

57. H.Y. Erbil Surface Chemistry of Solid and Liquid InterfacesBlackwell Pub, Oxford eMAMalden MA 2006

58. S. Y. Lagergren, *Handlingar* 1898, 24 1–39

59. T.A. Saleh, *Interface Science and Technology*,2022,**34**, 65-97

60. Y. S. Ho and G. McKay, *Process Saf. Environ. Prot*., 1998, **76**, 332 —340

61. S. Azizian, *J. Colloid Interface Sci*., 2004, **276**, 47 —52

62. W. Rudzinski and W. Plazinski, *J. Phys. Chem. B*, 2006, *110*, 16514 —16525

63. D. Kiani, Y. Sheng, B. Lu, D. Barauskas, K. Honer, Z. Jiang and J. Baltrusaitis, *ACS Sustainable Chem. Eng*., 2018, **7**, 1545 —1556

64. J. Zhou, S. Yang and J. Yu, *Colloids Surf. A.*, 2011, **379**, 102 —108

65. P. Xia, X. Wang, X. Wang, J. Song, H. Wang and J. Zhang, *Colloids Surf.A.*, 2016, **506**, 220 —227

66. D. Kiani, M. Silva, Y. Sheng and J. Baltrusaitis, *J. Phys. Chem. C*, 2019, **123**, 25135 —25145

67. J. Lin, S. He, Y. Zhan and H. Zhang,*Environ. Technol.*, 2020, **41**, 586 —602

68. J. Chen, L. G. Yan, H. Q. Yu, S. Li, L. L. Qin, G. Q. Liu, Y. F. Li and B. Du, *Chem. Eng. J.*, 2016, **287**, 162 —172

69. G. Blanchard, M. Maunaye and G. Martin, *Water Res.*, 1984, **18**, 1501 —1507

70. B. Lu, D. Kiani, W. Taifan, D. Barauskas, K. Honer, L. Zhang and J. Baltrusaitis, *J. Phys. Chem. C*, 2019, **123**, 8908 —8922

71. K. L. Tan and B. H. Hameed, *J. Taiwan Inst. Chem. Eng.*, 2017, **74**, 25 —48

72. S. P. D. Monte Blanco, F. B. Scheufele, A. N. Módenes, F. R. Espinoza-Quiñones, P. Marin, A. D. Kroumov and C. E. Borba, *Chem. Eng. J.*, 2017, **307**, 466 —475

73. Y. Tong, P. J. McNamara and B. K. Mayer, *Environ. Sci.: Water Res. Technol.*, 2019, **5**, 821 —838

74. Y. S. Ho, J. C. Y. Ng and G. McKay,*Sep. Purif. Methods.*, 2000, **29**, 189 —232

75. É.C. Lima, M.H. Dehghani, A. Guleria, F. Sher, R.R. Karri, G.L. Dotto, H.N. Tran, CHAPTER 3 - Adsorption: Fundamental aspects and applications of adsorption for effluent treatment, in: M. Hadi Dehghani, R. Karri, E. Lima (Eds.) Green Technologies for the Defluoridation of Water, Elsevier, 2021, pp. 41–88.

76. E.C. Lima, A.A. Gomes, H.N. Tran, *J. Mol. Liq.*, 2020, **311,**113315

77. J. Debord, M. Harel, B. Cheknane, J.-C. Bollinger and O. Bouras, *RSC Adv.*, 2016, **6**,66266-66274

78. E.C. Lima, A. Hosseini-Bandegharaei, J.C. Moreno-Piraján and I. Anastopoulos *J. Mol. Liq.*, 2019, **273**, 425-434

79. S. Zhuang, E. S. Lee, L. Lei, B. B. Nunna, L. Kuang and W. Zhang, *Int. J. Energy Res.*, 2016, **40**, 2136–2149

80. C. J. Johnson, E. Dujardin, S. A. Davis, C. J. Murphy and S. Mann, *J. Mater. Chem*., 2002,**12**, 1765–1770

81. P.Atkins,J. de Paula 2002, Physical Chemistry (7th ed.). New York: W.H.Freeman. p. 513. ISBN 0-7167-3539-3. |quote=the electric dipole moment of the molecule must change when the atoms are displaced relative to one another

82. Chromatography/Fourier transform infrared spectroscopy and its applications, by Robert White, p7

83. B.D. Cullity, Addison Wesley Mass., 1978, ISBN 0-201-01174-3

84. Klug, Harold, Alexander and Leroy, X-ray diffraction Procedures, (2nd ed.). Canada,1954

85. B.R. Stephen, C. Christopher, C.B. Scott, E. Peter, H. Li, S.E. David, B.S. Aleksandr, B. John, E.V. András,R.H.W. Angela, Z. Jiwen, S. Catherine ,S. Arnold ,Y. Jia and A.G. Eric , *Metrologia*., 2013 ,**50**, 663-678

86. B.Akbari, M. PirhadiTavandashti and M. Zandrahimi, *Iranian Journal of Materials Science and Engineering*., 2011, **8**

87. G.D. Danilatos, *Scanning*., 1986, **9** ,8–18

88. A.W. Coats, J.P. Redfern, *Analyst*.,1963, **88** ,906–924

89. D.Q. M. Craig and M. Reading, CRC Press.,2007, 0-8247-5814-5

90. K. Caswell, C. M. Bender and C. J. Murphy, *Nano Lett*., 2003, **3**, 667 —669

91. A. Ben Moshe and G. Markovich, *Chem. Mater*., 2011, **23**, 1239 —1245

92. G. S. Métraux and C. A. Mirkin, *Adv. Mater*., 2005, **17**, 412 —415

93. D. Zhang, L. Qi, J. Yang, J. Ma, H. Cheng and L. Huang, *Chem. Mater*., 2004, **16**, 872 —876

94. M. Pérez, R. Moiraghi, E. Coronado and V. Macagno, *Cryst. Growth Des*., 2008, **8**, 1377 —1383

195. S. Banerjee, K. Loza, W. Meyer-Zaika, O. Prymak and M. Epple, *Chem. Mater*., 2014, **26**, 951 —957

96. P. Sahoo, S. Kamal, T. J. Kumar, B. Sreedhar, A. Singh and S. Srivastava, *Def. Sci. J*., 2009, **59**, 447—455

97. K. Shameli, M. Bin Ahmad, S. D. Jazayeri, S. Sedaghat, P. Shabanzadeh, H. Jahangirian, M.Mahdavi and Y. Abdollahi, *Int. J. Mol. Sci*., 2012, **13**, 6639 —6650

98. Y. Yang, S. Matsubara, L. Xiong, T. Hayakawa and M. Nogami, *J. Phys. Chem. C*., 2007, **111**, 9095 —9104

99. U. Nickel, A. Zu Castell, K. Pöppl and S. Schneider, *Langmuir*., 2000, **16**, 9087 —9091

100 M. A. Raza, Z. Kanwal, A. Rauf, A. N. Sabri, S. Riaz and S. Naseem, *Nanomaterials*., 2016, **6**, 74

101. L. Ge, Q. Li, M. Wang, J. Ouyang, X. Li and M. M. Xing, *Int. J. Nanomed*., 2014, **9**, 2399 —2407

102. I. Washio, Y. Xiong, Y. Yin and Y. Xia, *Adv. Mater*., 2006,**18**, 1745 —1749

103. M. Rycenga, C. M. Cobley, J. Zeng, W. Li, C. H. Moran, Q. Zhang, D. Qin and Y. Xia, *Chem. Rev*., 2011, **111**, 3669 —3712

104. Z. S. Pillai and P. V. Kamat, *J. Phys. Chem*. B., 2004, **108**, 945 —951

105. M. N. Nadagouda and R. S. Varma, *Cryst. Growth Des*., 2007, **7**, 2582 —2587

106 C. Han, V. Nagendra, R. Baig, R. S. Varma and M. N. Nadagouda, *Appl. Sci*., 2015, **5**, 415 —426

107 N. G. Bastús, F. Merkoçi, J. Piella and V. Puntes, *Chem. Mater*., 2014, **26**, 2836 —2846

108. S. Chen, G. Wang, W. Sui, A. M. Parvez and C. Si, *Green Chem*., 2020, **22**, 2879 —2888

109. J. J. Giner-Casares, M. Henriksen-Lacey, M. Coronado-Puchau and L. M. Liz-Marzán, *Mater. Today*., 2016, **19**, 19 —28

110. J. A. Creighton, C. G. Blatchford and M. G. Albrecht, *J. Chem. Soc., Faraday Trans*., 1979, 75, 790 —798

111. D. L. Van Hyning and C. F. Zukoski, *Langmuir*., 1998, **14**, 7034 —7046

112. M. Wuithschick, B. Paul, R. Bienert, A. Sarfraz, U. Vainio, M. Sztucki, R. Kraehnert, P. Strasser, K. Rademann and F. Emmerling, *Chem. Mater*., 2013, **25**, 4679 —4689

113. G. Mie *Ann. Phys.*, 1908, **330**, 377 —445.

114. J. Turkevich, P. C. Stevenson and J. Hillier, *Discuss. Faraday Soc.*, 1951, **11**, 55 —75

115. G. Frens *Nat. Phys. Sci.*, 1973, **241**, 20 —22

116. M. Brust, M. Walker, D. Bethell, D. J. Schiffrin and R. Whyman, *J. Chem. Soc., Chem. Commun.*, 1994, **0**, 801 —802

117. N. Li, P. Zhao and D. Astruc, *Angew. Chem., Int. Ed*., 2014, **53**, 1756 —1789

118. J. Wiesner and A. Wokaun, *Chem. Phys. Lett*., 1989, **157**, 569 —575

119. N. R. Jana, L. Gearheart and C. J. Murphy, *Adv. Mater*., 2001, **13**, 1389 —1393

120. C. J. Murphy *Science.*, 2002, **298**, 2139 —2141

121. A. P. Alivisatos *Science., 1996*, **271**, 933 —937

122.P. Sallahuddin, S.H. Syeda, B.M. Rasool, C. Ali, Sirajuddin and A. Munazza Arain, *Journal of Inorganic and Organometallic Polymers and Materials*. ,2018,**28,**863–870

123. J. Turkevich, P.C. Stevenson, J. Hillier, *Discuss. Faraday Soc.*,1951, **11**, 55

124.B. Ajitha, Y. Ashok Kumar Reddy, S. Shameer, K. M. Rajesh, Y. Suneetha and P. Sreedhara Reddy, *J. Photochem. Photobiol.B.*, 2015, **194**, 84 —92

125.M. PR. Hemlata, A.P. Singh and K.K. Tejavath, ACS *Omega*.,2020,**5**,5520–5528

126. I.A. Adelere, and A. Lateef, *Nanotechnol Rev*. ,2020,**2**, 567–587

127. K. Joanna and A. Townshend, *Encylopedia of Anal.Sci*., 2005, **3**,105-113

128. D. Paramelle, A. Sadovoy, S. Gorelik, a P. Free, J. Hobleya and D. G. Fernigb, *RSC Analyst*,2014, **139**, 4855

129. M.T. Alula, L. Karamchand, N.R. Hendricks, J.M. Blackburn, *Anal Chim Acta.* ,2018,**1007**,40–49

130. F. Chai, C. Wang, T. Wang, et al., Nanotechnology.,2010, **21** ,25501

131.IM Weiss, C. Muth, R. Drumm, H.O.K. Kirchner, BMC, *Biophysis*.,2018,**11**,2

132. D. Philip, *Spectrochim. Acta Part. A*., 2010,**75**, 1078–1081

133. V. Kathiravan, S. Ravi, S. Ashokkumar, *Spectrochim. Acta A Mol. Biomol. Spectrosc*.,2014,**130**, 116–121

134. K.J. Chen, Y. Shi, Q. Cheng. *Adv. Sci*., 2018, ***5***, 1700179

135.D. Vilela, M.C. González and A. Escarpa, Anal. Chim. Actai., 2012, 751, 24–43

136.Y. Yao, D. Tian, and H.Li, ACS Appl. Mater. Interfaces.,2010, 2, 684–690

137.J. Gong, G. Li and Z. Tang, Nano Today., 2012, 7, 564–585

138.H.K. Sung, S.Y. Oh, C. Park and Y. Kim, Langmuir., 2013, 29, 8978–8982

139.J. Sangeetha and J. Philip, *RSC Advances* ,2013,**3**, 8047–8057

140. H.M. Freundlich, *The Journal of Physical Chemistry A*.,1906, **57**, 385-470.

141. Czepirski, L.; Balys, M. R.; Komorowska-Czepirska, E. (2000). "Some generalization of Langmuir adsorption isotherm". Internet Journal of Chemistry. 3 (14). ISSN 1099-8292. Archived from the original on 2017-01-13. Retrieved 2013-11-19

142. Erbil, 2006H.Y. ErbilSurface Chemistry of Solid and Liquid Interfaces Blackwell Pub, Oxford eMAMalden MA 2006

143.N. Ayawei, A. N. Ebelegi and D. Wankasi, *J. Chem*., 2017, **11**, 3039817

144. Dubinin, 1960, M. Dubinin the potential theory of adsorption of gases and vapours for adsorbents with energetically nonuniform *surfaces Chem. Rev*., 1960,**60**,235-241

145.P. Prakash, P. Gnanaprakasam, R. Emmanuel, S. Arokiyaraj and M. Saravanan, *Colloids and Surfaces B: Bio interfaces*., 2013 **,108,** 225–59

146.K. Yoti, M. Baunthiyal, and A. Singh, *Journal of Radiation Research and Applied Sciences*., 2016, 2**,** 17–27

147.M. Khan, S Kumar, M Ahamed and M.S. Alsalhi, *Mater. Lett.*,2012, **68,**497-500

148. A. Ozer, M.S. Tanyıldızı, F. Tumen, *Environ. Technol*., 1998,**19**, 1119-1125

149.A.K. Bhattachary, C. Venkobachar, *J. Environ. Eng*., 1984,**110**, 110-122

150.T. Mathialagan, T. Viraraghava, *J. Hazard. Mater*., 2002,**94**,291-303

151**.** O. Horovitz, A. Mocanu, Gh. Tomoaia, L. Bobos, D. Dubert, I. Dăian, T. Yupsanis and M. Tomoaia-Cotisel, *Studia Univ. Babes-Bolyai, Chem.*,2007 **,52,** 97

152. N. R. Jana, L. Gearheart, S. O. Obare and C. J. Murphy, *Langmui*r.,2002, **18** ,922

249. K. S. Mayya, V. Patil and M. Sastry, *Langmuir.*, 1997, **13,** 3944

153. S. Aryal, B. K. C. Remant, N. Dharmaraj, N. Bhattarai, C. H. Kim, H. Y. Kim, *Spectrochim. Acta A.*, 2006 ,**63,** 160

154. Z. P. Li, X. R. Duan, C. H. Liu and B. A. Du, *Anal. Biochem.*, 2006,**351,** 18

155.P. K. Sudeep, S. T. S. Joseph and K. G. Thomas, *J. Am.Chem. Soc*., 2002, **127** ,6516

156.U. Kreibig and L. Genzel, *Surface Sci.*, 1985, **156,** 678

157. I. S. Lim, W. Ip, E. Crew, P. N. Njoki, D. Mou, C. J. Zhong, Y. Pan and S. Zhou, *Langmuir*.,2007, **23,** 826

158.H. Fenghua, L. Yaling and C. Peifeng, *J. Mater. Sci*., 2011 **,46** ,573

159.Z. Jindal and N. K. Verma, *J. Mater. Sci*., 2008, **43** ,6539

160. J. Turkevich, P.C. Stevenson, J. Hillier, Discuss. Faraday Soc.,1951, **11**, 55

161.J. Turkevich, *Gold Bull.*, 1985**, 18,** 86

162. R. Gopalakrishnan and K. Raghu, *journal of nanoscience*.,2014

163.Y. Choi, M Choi, S. Cha, Y.S. Kim, S. Cho and Y. Park, *Nanoscale Res Lett.*, 2014,**9,** 103

164. D. Philip, C. Unni, S.A. Aromal and V.K. Vidhu, *Spectrochim. Acta A Mol. Biomol. Spectrosc*., 2011,**78,** 899–904

165. T.I. Shalaby, R.S. S. El-Dine and S.A.A. El-Gaber, *Nanosci. Nanotechnol*., 2015,**5,** 89–96

166. K.S.Siddiqi and A. Husen ,*Nanoscale Res. Lett.*, 2017, **12,** 1–18

167. A. Mohsen, Soheila, Dehfuly, F. Daryoush, S. Ronak and M. Korujid, *RSC Advance*., 2015, **5,** 104621

168. N. Ayawei, A. N. Ebelegi and D. Wankasi, *J. Chem*., 2017, **11**, 3039817

169. S. Venkateswarlu, Y. S. Rao, T. Balaji, B. Prathima, N. V. V. Jyothi, Mater. Lett. 2013, 100, 241–244

170.L. Du, H. Jiang, X. Liu, E. Wang, Electrochem. Commun. 2007, 9, 1165–1170

171.G. Rajakumar, A. A. Rahuman, S. M. Roopan, V. G. Khanna, G. Elango, C. Kamaraj, A. A. Zahir, K. Velayutham, *Spectrochim. Acta - A: Mol. Biomol. Spectrosc*.,2012, 91, 23–29

172.F. Arsiya, M. H. Sayadi, S. Sobhani, *Mater. Lett*.,2017, **186**, 113–115

173.R. Genç, G. Clergeaud, M. Ortiz, C. K. O'Sullivan, *Langmuir* 2011, **27**, 10894–10900

174.F. Ameen, *Appl. Nanosci*., 2022, **12**, 1384

175.S. Al-Nadhari, N. M. Al-Enazi, F. Alshehrei, F. Ameen, *Environ. Res*., 2021, **194**, 110672.

176.M. Isacfranklin, T. Dawoud, F. Ameen, G. Ravi, R. Yuvakkumar, P. Kumar, S. I. Hong, D. Velauthapillai, B. Saravanakumar, *Ceram. Int*., 2020, **46**, 25915–25920

177.S. Ahmed, M. Ahmad, B. L. Swami and S. Ikram, *J. Adv. Res.*,2016, **7**, 17–28

178.M. F. Zayed, W. H. Eisa, S. M. El-Kousy, W. K. Mleha and N. Kamal, *Spectrochim. Acta-A: Mol. Biomol. Spectrosc.*,2019, **214**, 496–512

179.P. Pawliszak, D. Malina, A. Sobczak-Kupiec, Mater. Chem. Phys. 2019, 234, 390–402.

180.S. N. A. M. Sukri, K. Shameli, M. M. T. Wong, S. Y. Teow, J. Chew and N. A. Ismail, *J. Mol. Struct*.,2019, **1189**, 57–65

181.R. Majumdar, B. G. Bag and P. Ghosh, *Appl. Nanosci*. 2016, **6**, 521–528

182.M. A. Khalilzadeh and M. Borzoo, *J. Food Drug Anal*.,2016, **24**, 796–803

183. A. Y. Yashin, B. V. Nemzer, E. Combet and Y. I. Yashin, *J. Food Res.* 2015, **4**, 56–87

184.D. A. Selvan, D. Mahendiran, R. S. Kumar and A. K. Rahiman, J. Photochem. Photobiol., B, 2018, 180, 243– 252

185.H. Al Rashid, A. Kundu, V. Mandal, P. Wangchuk, and S. C. Mandal, *Herbal Medicine in India*, 2020, DOI: 10.1007/ 978-981-13-7248-3_39

186. S. Link and M.A. Ei-Sayed, Annu. *Rev. Phys. Chem.*, 2003,**54**,331–366

187.M.A. Noginov, G. Zhu, M. Bahoura, J. Adegoke, C. Small, B.A. Ritzo, V.P. Draciiev and V.M. Siialaev, *Appl. Phys. B*, 2007,***86,***455–460

188.S.S. Nath and D.G. Gope, *Nano Trends.*, 2007,**2**,20–28

189.A. Taleb, C. Petit and M.P. Pileni, J. *Phys. Chem. B.*, 1998,**102**,2214–2220

190.M. Sastry, V. Patil and S.R. Sainkar, J. *Phys. Chem. B.*, 1998,**102**,1404–1410

191.A. Henglein, *J. Phys. Chem.*, 1993,**97**,5457–5471

192.M. Sastry, K.S. Mayya and K. Bandyopadhyay, *Colloids Surf. A Physicochem. Eng. Asp.*, 1997,**127**,221–228

193. N. Sultana, P.K. Raul, D. Goswami, D. Das, S. Islam, V. Tyagi, B. Das, H. K. Gogoi, P. Chattopadhyay and P.S. Raju, *RSC Adv.*, 2020, **10,** 9356−9368

194. T.S. Alomar, N. AlMasoud, M.A. Awad, M.F. El-Tohamy and D.A. Soliman, *Mater. Chem. Phys.* 2020, **249**, 123007

195.A.K. Varghese, P. Tamil, R. Rugmini, P.M. Shiva, K. Kamaksh and K.C. Sekhar, *ACS Omega* 2020**, 5**, 13123−13129

196.N. A. Masoud, T.S. Alomar, M.A. Awad, M.F. El-Tohamy and D.A. Soliman, *Green Chem. Lett. Rev.*, 2020, **13**, 316−327

197.P. Rani, V. Kumar, P.P. Singh, A.S. Matharu, W. Zhang, K.H. Kim, J. Singh and M. Rawat, *Environ. Int.*, 2020, **143**, 105924

198 S.B. Parit, V.C. Karade, R.B. Patil, N.V. Pawar, R.P. Dhavale, M. Tawre, K. Pardesi, U.U Jadhav, V.V. Dawkar, R.S. Tanpure, J.H. Kim, J.P. Jadhav and A.D. Chougale, *Mater. Today Chem*. ,2020, **17**, 100285.

199. A. Pimpin and W. Srituravanich, *Eng. J*., 2012, **16**, 37 —56

200. Z. Szabó, J. Volk, E. Fülöp, A. Deák and I. Bársony, *Photonics Nanostruct*., 2013, **11**, 1 —7

201. Y. Yin, B. Gates and Y. Xia, *Adv. Mater*., 2000, **12**, 1426 —1430

202. C.-W. Kuo, J.-Y. Shiu, Y.-H. Cho and P. Chen, *Adv. Mater*., 2003, **15**, 1065 —1068

203. K. Xu and J. Chen, *Appl. Nanosci*., 2020, **10**, 1013 —1022

204. R. Matsumoto, S. Adachi, E. H. S. Sadki, S. Yamamoto, H. Tanaka, H. Takeya and Y. Takano, *ACS Appl. Electron. Mater*., 2020, **2**, 677 —682

205. V. Amendola and M. Meneghetti, *Phys. Chem. Chem. Phys*., 2009, **11**, 3805

206. V. Hojat, F. Maliheh, H. Mona and H. Saba, *RSC Advance.*,2018,67

207.J.A. Ascencio, M. Pérez and M. José-Yacamán, *Surf Sci.*, 2000,**447**,73–80.

208.R. Chen, J. Wu, H. Li, G. Cheng, Z. Lu and C.M. Che, *Rare Metals.*, 2010,**29**,180–186

209.D. Cornejo-Monroy L.S., Acosta-Torres, A. Moreno-Vega, C. Saldana, V. Morales-Tlalpan and V.M. Castaño, *J Nanosci Lett.* ,2013,**3**,25.

210.C.A. Foss, Jr, G.L. Hornyak, J.A. Stockert and C.R. Martin, J *Phys Chem.*, 1994,**98**,2963–2971.

211.Manihot esculenta Crantz, Rei Herb. 1: 167 (1766)". Plants of the World Online. Board of Trustees of the Royal Botanic Gardens, Kew. 2022. Archived from the original on 11 November 2022. Retrieved 11 November 2022

212. J. Xiong, Y. Wang, Q. Xue and X. Wu, *Green Chemistry*., 12011,**3**, 900-904

213.J.M. Fang, P.A. Fowler, J. Tomkinso and C.A.S. Hill, Carbohydr. *Polym.*, 2002, **47**, 245–252

214. O. Sevenou, S.E. Hill, I.A. Farhat and J.R. Mitchell, Int. *J. Biol. Macromol.*,2002, **31**, 79–85